UNIVERSITAT DE BARCELONA

Photoswitchable ligands targeting beta-adrenoceptors for *in vitro, in vivo* and structural studies

Anna Duran Corbera

Photoswitchable ligands targeting beta-adrenoceptors for *in vitro*, *in vivo*, and structural studies

ANNA DURAN CORBERA

2022

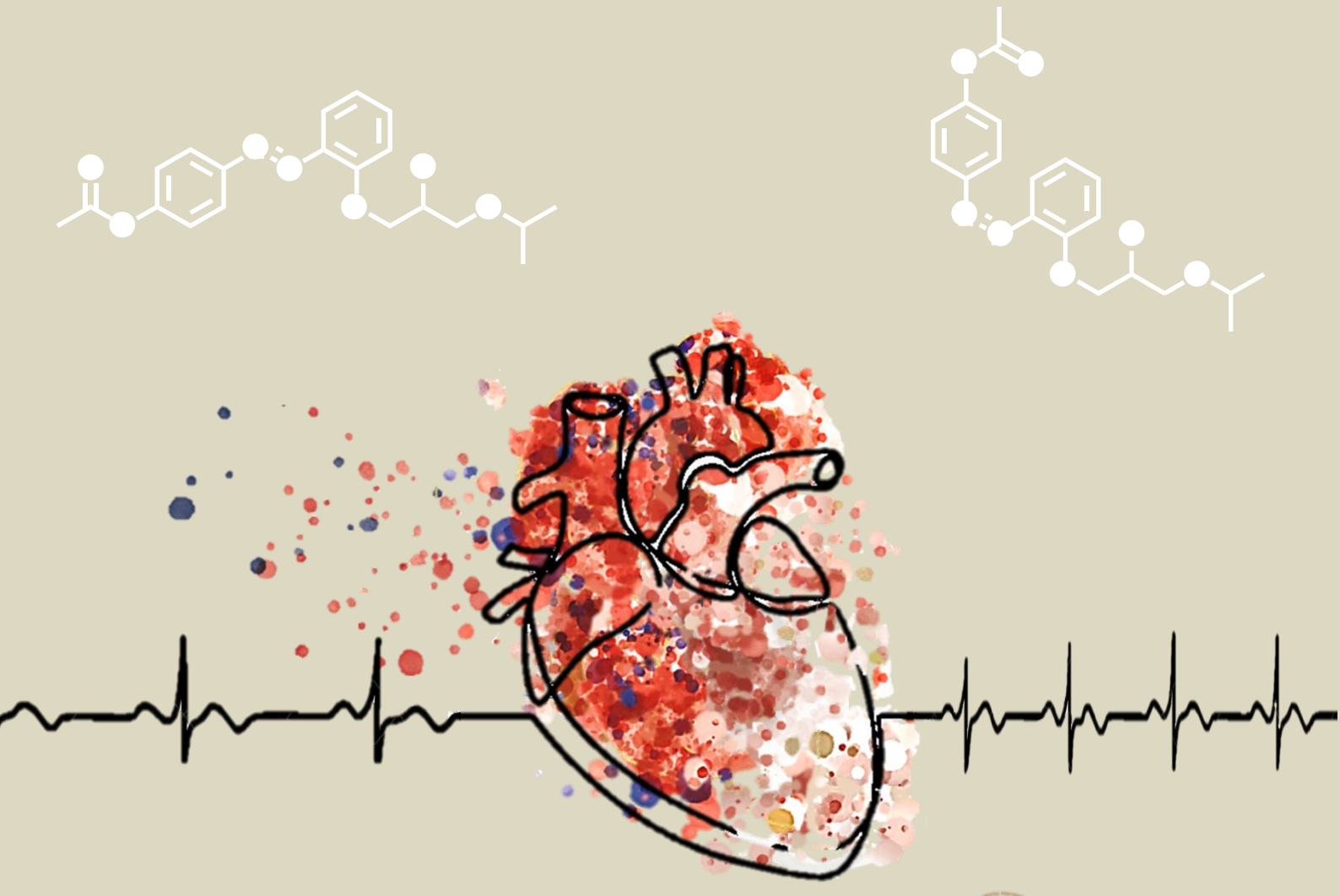

UNIVERSITAT DE BARCELONA

Universitat de Barcelona
Facultat de Farmàcia i Ciències de l'Alimentació
Programa de Doctorat en Biotecnologia

Photoswitchable ligands targeting beta-adrenoceptors for *in vitro*, *in vivo,* and structural studies

Anna Duran Corbera

2022

Memòria presentada per Anna Duran Corbera per optar al títol de doctor per la Universitat de Barcelona

Directors

Dr. Amadeu Llebaria Soldevila
Medicinal Chemistry & Synthesis (MCS)
Institute for Advanced Chemistry of Catalonia (IQAC-CSIC)

Dr. Xavier Rovira Algans
Medicinal Chemistry & Synthesis (MCS)
Institute for Advanced Chemistry of Catalonia (IQAC-CSIC)

Tutor UB

Prof. Josefa Badia Palacin
Integrative Biochemistry
University of Barcelona

Acknowledgements

Tal y como dice el refrán: “es de bien nacido ser agradecido”. Por ello, siento que esta tesis doctoral no puede empezar de otra manera que agradeciendo a todas las personas que han formado parte de ella, tanto a nivel profesional como a nivel personal. Estoy segura de que sin vuestras aportaciones y apoyo hubiera sido mucho más difícil, por no decir imposible, completar esta etapa. Una etapa de más de 4 años que ha estado llena de buenos momentos, pero también repleta de temporadas difíciles y de mucho sacrificio. Sin embargo, la palabra que para mí mejor define esta etapa es aprendizaje.

Primer m’agradaria donar les gràcies a les dues persones que han supervisat i guiat aquesta tesi. Amadeu, moltes gràcies per a ser com un pare (“father thesis”), per a inspirar-me amb la teva passió per la ciència i la teva capacitat de generar noves idees. Gràcies també per a confiar en mi i deixar-me escollir camins que tu sabies que eren erronis, per a que pogués aprendre i créixer per mi mateixa. Xavi, moltes gràcies per introduir-me al món de la farmacologia, que ara m’apassiona. Per tot el que m’has ensenyat, a nivell científic i personal, i per les bones discussions científiques que tant ens agraden. De veritat, ha estat un plaer poder compartir aquesta aventura amb vosaltres.

Por otro lado, dar las gracias a la gente que ha formado parte del MCS durante estos años. Empezando por Juanlo, gracias por acompañarme y guiarme durante todo el camino, con tus grandes conocimientos sintéticos y tu sentido del humor. Carmeta, gràcies per ser com una mare, de les que sempre es preocupen, però que mantenen un ampli somriure i transmeten alegria i bon humor. Lourdes, gracias por tu ayuda incesante con los diferentes equipos, análisis de datos etc., que ha sido esencial. Teresa, por compartir conmigo buenos, y no tan buenos, momentos haciendo residuos. Carol, gracias por tu energía, las risas que nos has proporcionado, tu cariño infinito y por ser pesada a veces (de forma necesaria). Xavi Greg, gràcies per a ser el millor gestor-quimiotecari-boticari del món! Joanet, gràcies per ensenyar-me i ajudar-me en el projecte dels caged, pels pitis compartits (subministrats per tu) i pels moments fora del CSIC. Xavi Gómez, gràcies per les lliçons que em donaves a l’inici, amb dibuixos a la vitrina inclosos. Alessia, por las risas y momentos compartidos a altas horas de la noche, cuando ya no debíamos estar en el laboratorio. Silvia, por esos días tan bonitos en Urbino y enseñarme que no hay nada mejor que un gelato italiano con panna! Sandra, que estuviste con nosotros un tiempo breve, pero te convertiste en una pili para siempre. Laia, per els bons moments que hem passat juntes fent activitats de divulgació. Aleix, mi calvo de confianza, por hacerme reír con tus gifs, tus imitaciones y tu inglés de Liverpool. Roser, gràcies per obrir-te poc a poc, ensenyar-me el teu costat carinyós i convertir-te en una amiga. Por último, gracias Maria y Gloria. Me llevo a dos grandes amigas conmigo de esta etapa de mi vida. Maria, desde el principio hubo conexión, gracias por estar siempre, incluso en la distancia; por nuestras infinitas charlas científicas y personales. Pero especialmente, gracias por tu luz. Gloria, gracias por enseñarme lo valioso que es mantener la sonrisa, incluso en los momentos difíciles. Por las infinitas risas que hemos compartido que han hecho de las largas horas de trabajo, momentos memorables. Sois muy especiales para mí.

Por otro lado, agradecer al grupo de Demetrio Raldúa, por enseñarme a hacer ensayos con larvas de zebrafish. Gracias Melissa y Eva, por vuestra paciencia, buen rollo y ayuda constante.

I would also like to thank all the people I met during my research stay at PSI. Firstly, thanks Jörg for giving me the opportunity to work and learn under your supervision. I would also like to thank Steffen, for his patience supervising me and teaching me in the lab when I started. And for taking care of me outside of the lab, inviting me to mountain hikes, ski trips etc. Robin, it was very special meeting you and working alongside with you. Even with all the stress, we managed to share good moments and drink some melone schnapps shots. Thank you, Gabriella, for being a friend, listening to my problems and making me laugh. Also, thanks for all your lessons on structural biology and cryo-EM. Thanks to Antonia, for the shared after-work beers and her knowledge on practical aspects of the lab. Max, who always was on charge of organizing hikes and events, I hope I will see you soon. Cheers Hannah for your patience helping me with TSA and showing me how to shoot crystals and process data. Huge thanks to Lorenz, who gave me a to do list of things you must do in Switzerland (that I never managed to finish), thanks for all the good landscapes you showed me, for the day we swam in the Aare. I especially miss your non-political bias. A general thanks to all the people at LBR PSI who helped me at some point, Jonas, Ved, Matt, Oliver, Valentin etc. Finally, thanks to José, talking to you felt like being back home again.

Por otro lado, querría agradecer a la Fundación La Caixa, no solo por financiar mi doctorado sino por permitirme conocer a grandes personas; fuentes de inspiración que llevo pegaditas al corazón. A Javi y a Joan, por la conexión desde el inicio y por todo lo vivido después: chai lattes en el sandwichez, exposiciones de arte, conciertos etc. A Pablo, por ser auténtico, compartir conmigo risas, preocupaciones, ambiciones y planes de futuro. Andrés, que te ganaste un hueco muy especial en mi corazón desde el primer día. Por tus poemas, y por inspirarme con cada conversación.

A mis compañeros de piset, que entendían mis horarios extraños y mis cenas basadas en sopa de brick. Rebe, ets de tota la vida i sobren les paraules, però gràcies per cuidar-me com una mare, deixant-me menjar preparat i galetes quan arribava tard a casa després de dies infinits al lab. Santito con botas, por los desayunos contigo y tu buen rollismo. Iris, pel teu somriure constant i sentit de l'humor que tanta gracia em fa.

A les persones que sempre han format part d'aquesta història. Marta, ets com una germana, gràcies per ser-hi sempre i créixer al meu costat. Anna, ets el clar exemple de que a les amigues de veritat no cal veure-les amb freqüència, no importa el temps que passi, el sentiment de complicitat no canvia. Nuria, quant ha plogut des de que ens dèiem Star... i seguim sumant moments, ens posi on ens posi la vida. Gis, gràcies per ser i estar sempre, sé que puc comptar amb tu per a compartir bons i mals moments. I en general, a tots els amics de Vallromanes, per totes les històries viscudes, que ens han transformat en qui som avui... Clara, Lluís, Gonzalo, Jandro, Jaume, Marta, Marcos etc. Gràcies.

Hi ha una reflexió que sempre m'ha agradat: la vida és com un tren; hi ha persones que t'acompanyen durant tot el trajecte, altres baixen en un punt del trajecte i ja no tornen a pujar. Per última, algunes persones, fan una parada i es reenganxen més endavant en el trajecte. Gràcies Marina, per tornar al tren de la meva vida al final d'aquesta etapa, com si no hagués passat el temps. Et trobava a faltar.

Per últim, agrair a la meva família, suport incondicional i essencial de la meva vida.

Gracias Fer, por formar una familia conmigo y traer a Lou a nuestras vidas, para aportarnos más alegría y amor, si cabe. Gracias por hacerme enfadar y reír a partes iguales. Por los buenos momentos que hemos compartido en estos años juntos. Por tu infinita paciencia con mis momentos malos y por tu buena energía. Pero por encima de todo, por demostrarme tu amor de la manera más sincera, convirtiéndote en el pilar que sostenía mi vida en un año complicado, aún con la distancia que nos separaba. No te lo digo muy a menudo, pero GRACIAS, eres mi mayor apoyo.

Al meu pare, que de petita em va inculcar la passió per la lectura. Pels moments que hem compartit comprant llibres de Sherlock Holmes, de la Irène Némirovski etc. Tot i que no t'ho pensis, la teva aportació a la meva personalitat ha estat una part essencial del que m'ha fet arribar fins aquí. A mi madre, fuente de cariño y apoyo incondicional. Por ser la persona más positiva que conozco y dar los mejores abrazos del mundo, siempre en el momento necesario. Gracias por las risas que nos regalas con tus juegos de palabras y tu forma de ser. Eres muy especial, sin ti no lo hubiera conseguido. A la meva germana, que és possiblement la persona que millor m'entén, tant a nivell personal com professional. Tinc la sort de que no només és una germana, sinó també una amiga que m'ha acompanyat activament en gairebé totes les etapes de la meva vida. A més, comparteix amb mi la passió per la ciència, sent capaç d'entendre perfectament les frustracions i alegries que això comporta. Gràcies per la teva llum i per fer-me feliç. Finalment, voldria recordar a dues persones que van abandonar el món terrenal durant el transcurs d'aquesta tesi, les meves àvies. Gràcies per tant, us porto amb mi.

Abbreviations

7TM	Seven Transmembrane
7TMD	Seven Transmembrane Domain
aAB	Aminoazobenzene
AB	Azobenzene
Abs	Absorbance
AC	Adenylyl Cyclase
AC	Affinity Chromatography
ACN	Acetonitrile
AcOH	Acetic acid
ADME	Absorption, Distribution, Metabolism, Excretion
α-AR	Alpha Adrenoceptors
AR	Adrenergic Receptors
ATP	Adenosine Triphosphate
AUC	Area Under the Curve
β-AR	Beta Adrenoceptors
BLA	Basal Locomotor Activity
BODIPY	Boron Dipyrromethene
cAMP	Cyclic adenosine
C-C	Caged-Carvedilol
CFP	Cyan fluorescent protein
cGMP	Cyclic guanosine monophosphate
CMC	Critical Micelle Concentration
CNS	Central Nervous system
COPD	Chronic Obstructive Pulmonary Disease
CPM	(7-Diethylamino-3-(4'-Maleimidylphenyl)-4-Methylcoumarin)
CRD	Cystein-rich domain
Cryo-EM	Cryo-electron microscopy
DCM	Dichloromethane
DDM	n-Dodecyl-B-D-maltoside
DEACM	[7-(diethylamino)coumarin-4-yl]methyl
DMF	Dimethyl formamide
DMEM	Dulbecco's modified Eagle's medium
DMSO	Dimethylsulphoxide
Dox	Doxycycline
dpf	Days post-fertilization
DR	Dose-Response
DR	Dose Ratios
EC_{50}	Half maximal effective concentration
ECD	Extracellular domain
ECL	Extracellular loop
ECM	Extracellular matrix
E. Coli	*Escherichia Coli*

EDG	Electron donating group
E_{max}	Maximum agonistic effect
eNOS	Endothelial NO synthase
Eq.	Equivalents
EtOAc	Ethyl acetate
EWG	Electron withdrawing group
Fabs	Monoclonal Antibody Fragments
FACS	Fluorescence-Activated Cell Sorting
FEL	Free-electron Laser
FRET	Förster resonance energy transfer
GABA	gamma-Aminobutyric acid
GDP	Guanosine diphosphate
GFP	Green fluorescent protein
GI	Gastrointestinal
GPCR	G protein-coupled receptor
GRKs	G protein-coupled receptor Kinases
GTP	Guanosine triphosphate
h	Hours
HCOOH	Formic acid
HEK293	Human embryonic kidney cell line
HH	Hedgehog family of receptors
HPLC	High performance liquid chromatography
HPLC-MS	High performance liquid chromatography-mass spectrometry
HRV 3c	His-tagged human rhinovirus 3c
HTRF	Homogeneous time resolved fluorescence
IBMX	3-Isobutyl-1-methylxanthine
IC_{50}	Half maximal inhibitory concentration
ICL	Intracellular loop
IMAC	Immobilized metal ion affinity cromatography
IP_3	Inositol 1,4,5-trisphosphate
IP	Inositol monophosphate
λ	Wavelength
LABA	Long-acting Beta-Agonists
LC	Liquid chromatography
LCP	Lipidic Cubic Phase
LED	Light emitting diodes
LG	Leaving Group
m-AB	*Meta*- azobenzene
MAG	Monoacylglicerol
MeCN	Acetonitrile
MeOH	Methanol
mGlu	Metabotropic glutamate
mGluR	Metabotropic glutamate receptor
min	Minute
mM	Millimolar

MS	Mass spectrometry
MW	Microwave
NAM	Negative allosteric modulator
NaOH	Sodium Hydroxyde
nHex	Normal hexane
NIR	Near-infrared
nM	Nanomolar
nm	Nanometer
NMR	Nuclear magnetic resonance
NO	Nitric Oxide
o-AB	*Ortho*- azobenzene
***o*NB**	*Ortho*-Nitrobenzyl
OPE	One-Photon Excitation
pAB	Protonated-azobenzene
***p*-AB**	*Para*- azobenzene
PAM	Positive allosteric modulator
PBS	Phosphate buffered saline
PCL	Photochromic ligand
PDA	Photodiode array
PDE efficacy	Photoinduced difference of
PE	Photon excitation
PEG	Polyethylene glycol
PKA	Protein Kinase A
PKG	Protein Kinase G
PNGase F	Peptide N-glycosidase F
ppAB	Push-pull azobenzene
PPG	Photoprotecting Group
ppm	Parts per million
PPS	Photoinduced potency shift
pSB	Pseudostilbene
PSS	Photostationary state
PTL	Photochromic tethered ligand
PTM	Post-translational Modifications
PZL	Photoazolol
RGS	Regulators of G protein signaling
rt	Room temperature
r.t.	Retention Time
s	Seconds
SAR	Structure-activity relationship
SDS	Sodium Dodecyl Sulphate
SEC	Size Exclusion Chromatography
SEM	Standard error of the mean
Sf9	*Spodoptera frugiperda 9*
SFX	Serial Femtosecond Crystallography
SFX	Serial Microsecond Crystallography
T4L	T4 Lysozyme

$t_{1/2}$	Half-life time	**TSA**	Thermal Shift Assay
TEA	Triethylamine	**US**	Ultra-stable
TET	Tetracyclin	**UV**	Ultraviolet
THF	Tetrahydrofuran	**VFT**	Venus flytrap
Tm	Melting Temperature	**Vis**	Visible
TMD	Transmembrane Domain	**WNT**	Wingless/int1 family of receptors
toAB	tetra-*o*-substituted azobenzene	**WT**	Wild type
TPA	Two-Photon Absorption	**YFP**	Yellow fluorescent protein
TR	Time-resolved	**µM**	Micromolar

Summary

G protein-coupled receptors (GPCRs) are a large family of membrane proteins responsible for signaling transduction processes. Due to their roles in the modulation of important physiological functions, GPCRs are classical pharmacological targets and the focus of numerous research lines. Within this superfamily of receptors, beta-adrenoceptors (β-AR) have been widely studied. Their key contribution to the modulation of the cardiac output, among other physiological functions, has historically signaled these receptors as therapeutic targets. Many approved drugs have been reported to modulate the activation of β-AR, which evidences the high potential of these GPCRs in clinical and research applications. On the other hand, photopharmacology has arisen as an innovative approach with therapeutic potential and an enormous range of research applications. This technique uses synthetic light-regulated molecules to render light-controllable proteins.

In this context, the main objective of the present thesis was the development of light-sensitive molecules that allowed the modulation of beta-adrenoceptors through light application.

In the first chapter, we report the development of a caged analogue of carvedilol, an approved inhibitor of β-AR. Upon illumination at 405 nm, Caged-Carvedilol photolitically released the beta-blocker carvedilol. The caged ligand was used to explore light-dependent modulation of beta-adrenoceptors in a variety of physiological systems, including native cardiac tissues and living zebrafish larvae. Overall, this novel caged compound provides an innovative molecular tool to precisely control the activation state of β-AR in space and time. Therefore, C-C could be used in future studies to better understand the complex role of beta-adrenoceptors in physiology.

Caged ligands are certainly valuable molecular tools but present one main limitation, which is their irreversible nature; once the bioactive molecule is photolitically released, no compound deactivation is possible. To produce ligands that allow a reversible control of the target receptors with light, a series of azobenzene-based compounds were designed, synthesized, and photochemically characterized in Chapter 2. Additionally, we explored the light-dependent pharmacological properties of **Photoazolols 1-3** (**PZLs 1-3**) *in vitro* against two different receptor subtypes, β_1-AR and β_2-AR. The pharmacological results obtained for the first series of photochromic ligands guided the design of two additional azobenzenes to selectively modulate β_1-AR. Both ligands, based on a *para*-substituted azobenzene (*p*-AB) scaffold, displayed good light-dependent properties and an excellent β_1-AR selectivity profile. Additionally, *in vivo* assays were performed using zebrafish larvae. These experiments highlighted that light-dependent cardiac modulation was achieved when larvae were treated with *p*-AB **84** under different illumination conditions.

[redacted]

[redacted]

Finally, we intended to use the developed azobenzenes to perform structural studies on β-AR. The last chapter of this thesis describes the research conducted during a 6-months stay performed at the Paul Scherrer Institut (Switzerland), where a joint subproject was established with the Standfuss group. This subproject aimed to crystallize both, β_1-AR and β_2-AR, bound to one of the *trans*-on compounds from our library of photochromic ligands. After crystallization, we intended to perform conventional X-Ray Crystallography experiments with the obtained crystals in the dark and after illumination with the appropriate wavelength to evaluate the light-induced structural changes in our target receptors. Firstly, receptor expression and purification protocols were optimized and established for different constructs of β_1-AR and β_2-AR. Finally, crystallization trials were set up using purified protein bound to **PZL-1**, and preliminary crystals were obtained for the ultra-stable (US) construct of β_1-AR. However, we did not manage to obtain diffraction-quality crystals, required to perform X-Ray Crystallography experiments.

To sum up, the present thesis reports a variety of novel photopharmacological tools to study beta-adrenoceptors with spatiotemporal precision. *In vitro*, *in vivo*, and structural studies have been performed using different molecules from the developed library to demonstrate the possibilities offered by the described compounds in therapeutic and research applications.

Contents

Introduction

Results & Discussion contents

Materials & Methods contents

INTRODUCTION

Introduction contents

1 G Protein-Coupled Receptors

G Protein-Coupled Receptors (GPCRs) are the largest family of cell surface receptors. These proteins present a structurally similar core, with an extracellular N-terminus, seven transmembrane (7TM) α-helices and an intracellular C-terminus.[1,2] The main function of GPCRs is the mediation of intracellular signaling cascades in response to various stimuli, from light and odorants to neurotransmitters (Figure 1).[2] As a consequence of their roles in important physiological and pathological processes, this superfamily of receptors is one of the most pursued targets for drug development. Around one third of the marketed drugs nowadays are targeting these receptors.[3,4]

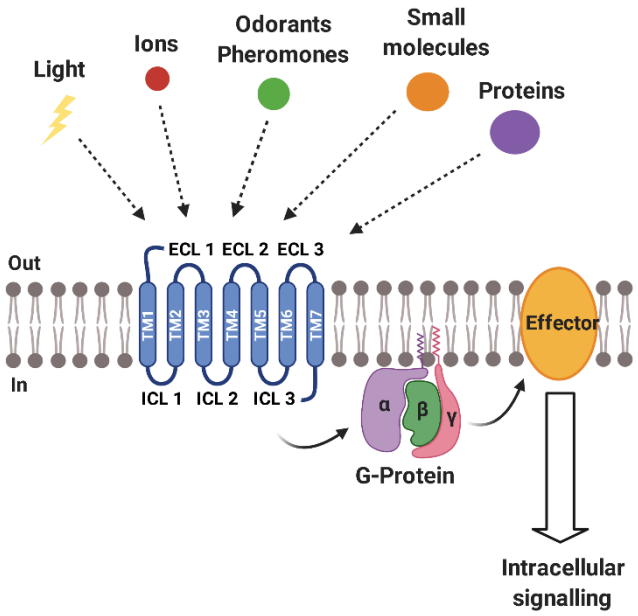

Figure 1. General topology and function of GPCRs. They all display a common core constituted by seven transmembrane α-helices (7TM) connected through three intracellular loops (ICLs) and three extracellular loops (ECLs). Adapted from Bockaert and Pin (1999) and created with BioRender.

1.1 Classification

Due to the large number of receptors embedded in the GPCR superfamily, several classification schemes have been proposed. Classically, GPCRs were divided in 6 classes (A-F) according to sequence homology and structural similarity.[5,6] More recently the GRAFS classification has appeared, where vertebrate GPCRs have been phylogenetically grouped in 5 main families: Glutamate, Rhodopsin, Adhesion, Frizzled and Secretin.[1]

1.1.1 Rhodopsin family

The rhodopsin family, which corresponds to the classic class A family, is the largest group of proteins within GPCRs. It is constituted by four groups (α, β, γ and δ) and 13 subgroups (Table 1). This class of receptors is very diverse and respond to a wide variety of stimuli, ranging from small molecules to proteins. Additionally, they can also bind to different types of G-proteins depending on receptor subtype or activate many G-protein independent signalling pathways, thus leading to complex and unique combinations of signalling transduction processes.

Many crystal structures of class-A GPCRs have been solved in the last 20 years, both in active and inactive conformations.[7] This has facilitated a better understanding of the structural similarities and particularities, as well as mechanisms of activation, within this large family of receptors. In fact, class-A-GPCRs share a seven-transmembrane (7TM) helices domain with highly conserved regions between the ligand-binding pocket and the G protein-coupling area. Additionally, they present a palmitoylated cysteine at the C-terminal tail. The orthosteric binding pocket of this family of receptors is generally located in the extracellular part of the helical bundle; however, some receptors present large extracellular domains at the N-terminus that allocate their ligands. Finally, some small-molecule-binding class A GPCRs have a vestibule in the entrance to the binding site that can accommodate parts of long orthosteric ligands or that can act as an allosteric binding pocket (Figure 2).[8–10]

Table 1. Summary of the human rhodopsin family (class A GPCRs), classified according to phylogenetic groups and subgroups.[1,11]

Group	Subgroup	Examples
α (Small molecules)	Prostaglandin	Prostaglandin and orphan receptors
	Amine	Serotonin, dopamine, muscarinic, histamine and adrenergic receptors
	Opsin	Rod and cone visual pigments and melanopsin receptors
	Melatonin	Melatonin and orphan receptors
	MECA	Cannabinoid, adenosine and melanocortin receptors
β (Peptides)	-	Hypocretin, neuropeptide FF, neuropeptide Y, tachykinin, bombesin-like receptors
γ (Peptides and small protein)	SOG	Opioid, galanin, kisspeptin, somatostatin receptors
	MCH	Melanin concentrating hormone receptor
	Chemokine	Classic chemokine, angiotensin and bradykinin receptors
δ (Peptide, proteins, small molecules)	MAS	MAS1 oncogene and MAS-related receptors
	Glycoprotein	Glycoprotein hormone receptors
	Purinergic	Formyl peptide, nucleotide and succinate receptors
	Olfactory	Many

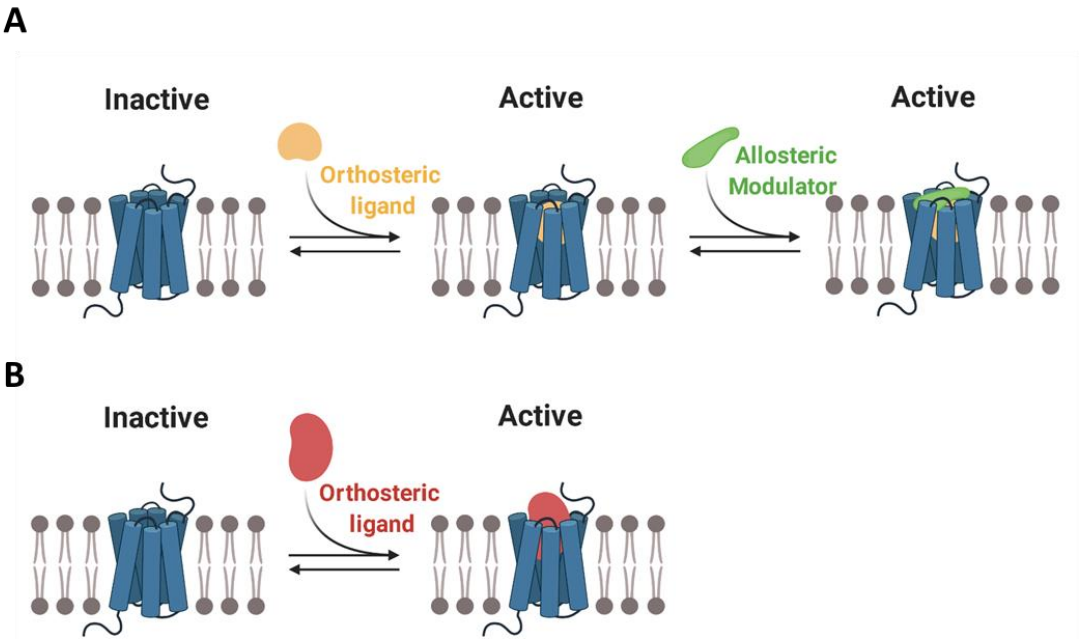

Figure 2. Topology of class A GPCRs. (A) Binding of a small molecule in the orthosteric pocket followed by the possible binding of an allosteric ligand in the vestibule present in the 7TMD. (B) Binding of a peptide to a class A GPCR. Created with Biorender.

1.1.2 Secretin family

The secretin family, also known as class B GPCRs, is constituted by 15 receptors that are activated by peptidic ligands (Table 2). Among the endogenous ligands for these receptors there are hormones and neurotransmitters. Their importance in the regulation of several physiological processes has highlighted them as therapeutic targets for type 2 diabetes, obesity or psychiatric disorders. A common structural feature of class B GPCRs is the presence of a large N-terminus extracellular domain (ECD). Peptidic ligands targeting class B GPCRs generally bind to the ECD through their C-terminal α-helix and the TMD through the N-terminus in a two-domain model (Figure 3). Signalling transduction in class B GPCRs is mainly mediated by the activation of Gsα; they can also activate Gqα and Giα, but activation of this pathways occurs with lower frequency.[12,13]

Table 2. Summary of the human secretin (family B), with phylogenetic subgroups classification.[1,11]

Subgroup	Examples
CRHRs/CALCRLs	Calcitonin and corticotropin-releasing hormone receptors
PTHRs	Parathyroid hormone receptors
GLPRs/GCGR/GIPR	Gastric inhibitory polypeptide, glucagon and glucagon-like peptide receptors
Secretin	Secretin, growth-hormone-releasing hormone and vasoactive intestinal polypeptide receptors

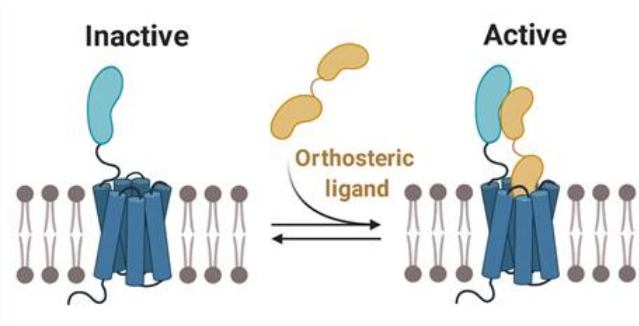

Figure 3. Topology of class B GPCRs. Binding mode of a peptide to a secretin-like receptor, adapted from Hoare (2005). Created with BioRender.

1.1.3 Glutamate family

The glutamate family (class C GPCRs) is constituted by 22 receptors classified in 4 subgroups (Table 3). They respond to the main excitatory (glutamate) and inhibitory (γ-aminobutyric acid) neurotransmitters of the central nervous system (CNS), but also to hormones, odorants and ions. Depending on the receptor subgroup they can bind different types of G proteins, leading to the activation of several intracellular signalling cascades.

Unlike other GPCRs, the glutamate family of receptors is constituted by three different domains. They present a 7 TMD that allocates the allosteric binding pocket. In the extracellular N-terminus they display a large domain named Venus flytrap (VFT). The VFT is constituted by two opposing lobes that form a cavity where endogenous or orthosteric ligands bind. This domain oscillates between open (active) and closed (inactive) conformations and binding of agonists or antagonists displace the equilibrium towards one of the two states. The third domain is the cysteine rich domain (CRD) and it links the VFT to the 7TMD (Figure 4).[14–16]

An additional particularity of class C GPCRs is that this type of receptors are constitutive dimers at the cell surface, either as homodimers (two identical units) or heterodimers (non-identical units).[16] Homodimers, such as mGlu receptors, are covalently bound through a disulphide bond between the VFT. On the other hand, heterodimers such as $GABA_B$ receptors are not covalently linked, but present an intracellular domain that strongly links their coiled coils.

Table 3. Summary of the human glutamate (family C), with phylogenetic subgroups classification.[1,11]

Subgroup	Examples
Glutamate	Metabotropic glutamate receptors
GABA-B	Gamma aminobutyric acid B receptors
T1/CaS	Taste 1, calcium sensing receptors
RAIG	Retinoic acid-inducible receptor

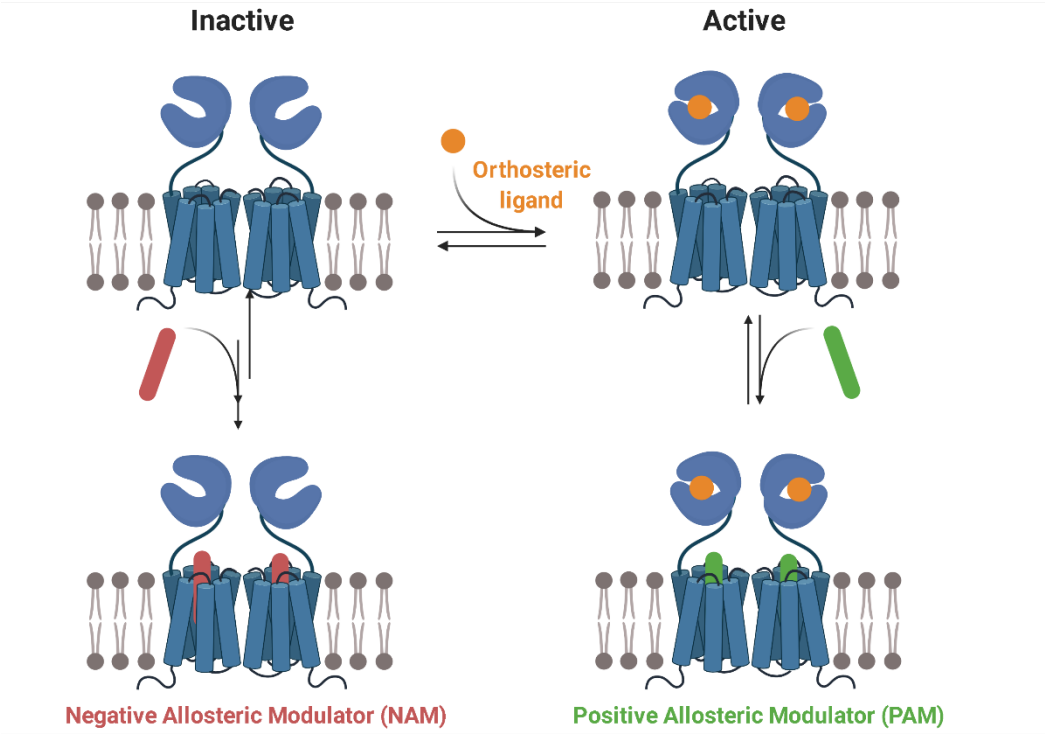

Figure 4. Topology of class C GPCRs. Binding mode of an orthosteric agonist or an allosteric modulator to a glutamate like receptor, adapted from Rondard *et al.* (2011). Created with BioRender.

1.1.4 Frizzled family

Class F GPCRs are a group of 11 receptors, mainly activated by lipoglycoproteins of the wingless/int1 (WNT) family or hedgehog family (HH) proteins. They have an important role in cellular communication, tissue homeostasis, regeneration and repair. It is known that these proteins mainly bind to G_O; however, mechanisms associated to activation of the frizzled family are not as well defined as for other families of GPCRs.[17,18]

Like the rest of GPCRs, these receptors include a domain with seven transmembrane-helices (TMD) with a C-terminus in the cytosol responsible for G-protein binding. The extracellular N-terminus displays a cysteine rich domain that has been proposed as the main ligand-binding region of the receptors. [19]

1.1.5 Adhesion family

The adhesion family is the second largest group of GPCRs, constituted by 33 receptors which are mainly orphan (endogenous ligands are not known). The few known ligands for this family of GPCRs are large macromolecules, either membrane proteins on neighboring cells or extracellular matrix (ECM) molecules. This suggests that this family of GPCRs contribute to cell-cell adhesive interactions and sense changes occurring in adjacent cells.[20] Signal transduction is mediated by several types of G proteins as well as the activation of non-G protein signaling cascades. A characteristic structural feature of adhesion proteins is the presence of a large extracellular N-terminus that can be cleaved from the 7TMD by autoproteolysis.[21]

1.2 GPCR Signaling

1.2.1 Signaling via G proteins

A schematic version of the signaling transduction processes initiated by GPCR activation is depicted in Figure 5. The receptor in its inactive state is initially bound to a heterotrimeric G protein complex composed by Gα, Gβ and Gγ subunits. When an extracellular ligand binds and activates a GPCR, it induces a conformational change in the transmembrane domain that leads to the activation of the heterotrimeric G protein in the cytosolic face. Signal transduction is thereafter initiated. A conformational change in the G protein promotes an exchange of GDP for GTP in the Gα subunit. This triggers the dissociation of GTP-bound Gα from the receptor and from the Gβγ dimer. Signal transduction is independently mediated by the two resulting G protein parts, as they promote activation of different downstream signaling cascades. Additionally, there are different families of G proteins ($G_s\alpha$, $G_{i/o}\alpha$, $G_q\alpha$, $G_{12/13}\alpha$ and Gβγ), which can inhibit or activate different signaling cascades. Upon activation, the different types of Gα modulate specific effector proteins. For instance, both $G_s\alpha$ and $G_i\alpha$ control the activation of adenylate cyclase (AC); however, while $G_s\alpha$ activates AC and causes an increase in cAMP concentration, $G_i\alpha$ inhibits this enzyme and reduces the amounts of the mentioned secondary messenger. On the other hand, $G_q\alpha$ activates the effector protein phospholipase C which leads to an increase on the calcium levels (Figure 5).

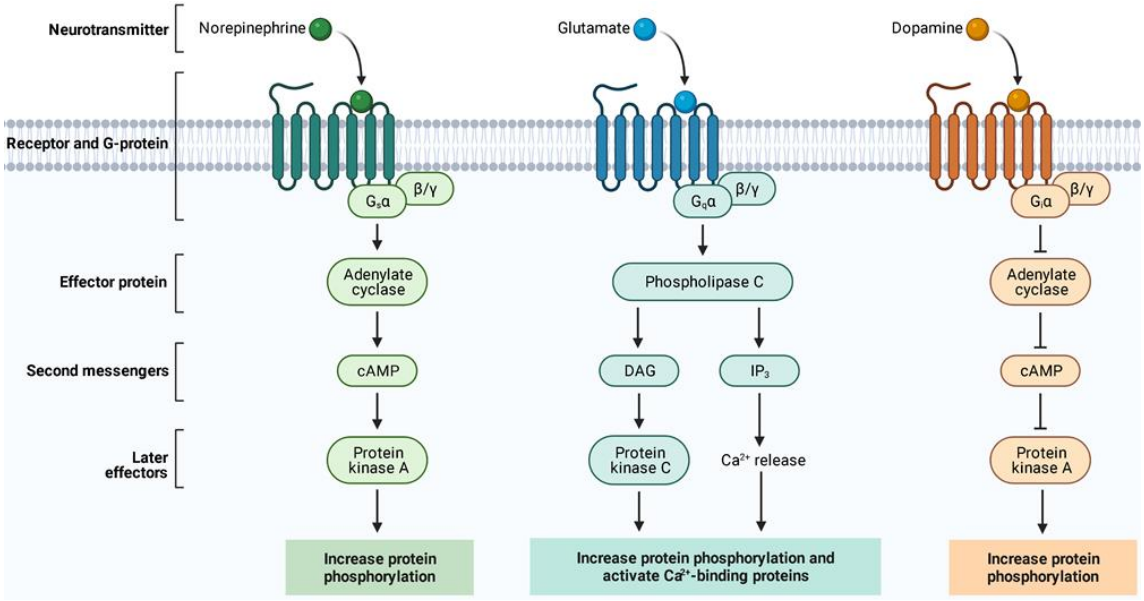

Figure 5. Ligand induced GPCR activation and signaling transduction through different types of Gα. Activation of the GPCR leads to G protein exchange of GDP for GTP. This causes the separation of the heterotrimeric form into two subunits. Different types of Gα can be activated by the GPCR, which are then responsible for the activation of different downstream signaling pathways. Created with BioRender.

Once the response to the external stimuli has been effected, the catalytic capability of Gα permits the hydrolysis of GTP to GDP, thus allowing the regeneration of the "resting" G-protein form (Gαβγ). However, Gα catalyzed GTP → GDP hydrolysis is slow and can be often accelerated by Regulators of G-protein Signaling (RGS proteins). On the other hand, signal turnoff in GPCRs is achieved by a two-step mechanism: receptor phosphorylation by GPCR kinases (GRKs)

followed by arrestin binding.[22,23] However, GPCRs are not simple ligand-dependent on/off switches; a proportion of these receptors also activate G protein signaling in the absence of a ligand, giving rise to a basal activity that depends on the receptor type and the biological system studied. This highlights the existence of an equilibrium between active and inactive receptor conformations in their resting state.

1.2.2 Deactivation of GPCRs by GRKs and Arrestins

As it has been previously mentioned, GPCR signaling mediated by G proteins is often terminated by phosphorylation of the active receptor by GRKs, followed by binding of arrestin proteins. There are only seven GRKs (GRK1-7) responsible for the phosphorylation of over 800 GPCRs, which implies that these kinases display low phosphorylation site selectivity. In fact, it has been described that G protein kinases specifically phosphorylate active receptors, while other protein kinases enable selective phosphorylation upon sequence recognition.[24] This is attributed to a particular mechanism of GRK function; these kinases get activated by physical contact with active receptors. Upon activation, GRKs can phosphorylate any Serine or Threonine accessible residues.[25,26] Phosphorylation of GPCRs such as rhodopsin or β_2-AR cause a reduction in the signaling via G protein (Figure 6).[27,28] However, signal transduction is not fully stopped until arrestins are recruited (Figure 6). Arrestins, which are a small family of proteins, contribute to GPCR desensitization via two different pathways. On one hand, they form interactions with both, the phosphorylated parts of the receptor and the inter-helical cavity where G proteins bind. In consequence, recruitment of arrestin proteins precludes G protein binding and enhances receptor desensitization.[29,30] On the other hand, these proteins can also promote receptor internalization via coated pits, which further reduces cell responsiveness.[29] In addition, it has been described that receptor-bound arrestins can also trigger signal transduction processes, such as the activation of pro-proliferative MAP kinases ERK1/2 (Figure 6).[31] However, it seems that activation of these pathways is not G protein independent. [32]

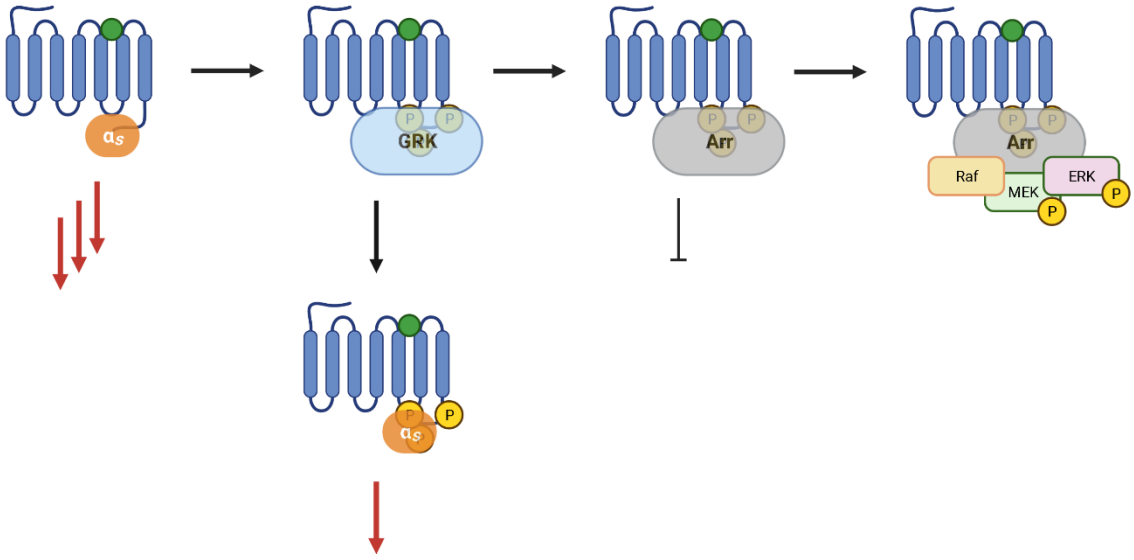

Figure 6. GPCR signaling and the role of GRKs and arrestins. Agonist-activated GPCR can bind a GRK that phosphorylates the receptor, thus reducing G protein mediated signal transduction processes. If the phosphorylated receptor recruits an arrestin protein, the G protein signaling is completely blocked. Finally, the arrestin-GPCR complex can also trigger the activation of different signaling cascades. Adapted from Gurevich (2019). Created with BioRender.

1.2.3 GPCR Pharmacology

The role of GPCRs in signaling transduction processes is generally regulated by ligands, either endogenous (naturally produced by the organism) or exogenous (external substance or drug uptaken by the organism). Ligands, which are highly heterogeneous molecules, can induce a variety of responses in their target receptors. The property that gives a molecule the capability of changing a receptor to produce a cellular response is termed **efficacy**, which is directly related to the maximal effect that a molecule can trigger (E_{max}). Another important pharmacological parameter to consider in GPCR pharmacology is the **affinity**, that describes the strength of the binding interaction between the ligand and its target receptor. Finally, the **potency** of a molecule is determined by the ligand concentration required to trigger maximal receptor response. This parameter depends on compound affinity and number of available receptors. At this point it is also worth noting that the receptor expression levels in the studied system also has an important effect on the detected response for a particular ligand. In fact, it has been described that the same ligand can induce opposing responses in systems with high and low target receptor levels respectively. A general classification divides ligands in two groups (orthosteric and allosteric) according to the topology of their binding site. The different types of ligands within the mentioned groups and their prototypical responses in functional assays will be described in following sections.

Orthosteric ligands

Orthosteric ligands interact with the same binding site as the endogenous agonist. This binding site is known as the orthosteric pocket, which is highly conserved among the families and subtypes of GPCRs. In consequence, development of selective orthosteric ligands to target GPCRs has proven very challenging and still remains as one of the biggest issues in GPCR drug discovery.[33] GPCR orthosteric ligands can be classified into three categories: agonists (activate the receptor), antagonists (compete with the agonist for the orthosteric binding site and have a neutral effect) and inverse agonists (suppress receptor constitutive activity).

Agonists

Ligands that induce an activation of the receptor upon binding are known as agonists. These ligands stabilize the active conformation of their target GPCR and trigger signal transduction processes via G protein activation, as previously described. [34]

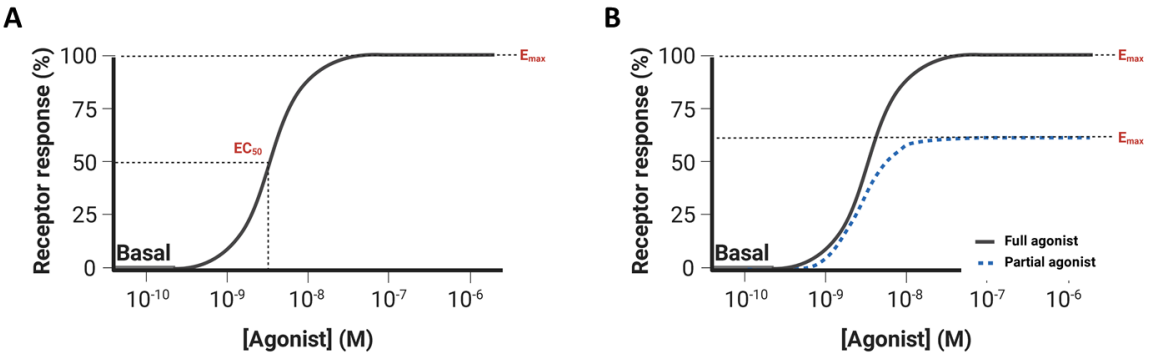

Figure 7. Different pharmacological profiles of agonism. Dose-response of a full agonist (A) and of a partial agonist (B). Adapted from Kenakin (2014). Created with BioRender.

Pharmacological characterization of agonists through functional assays is usually achieved by performing dose-response curves of the studied ligand (Figure 7). From these assays, two pharmacological parameters can be estimated: **EC_{50}** and **E_{max}**. The concentration of agonist required to induce a 50% activation of the receptor is named EC_{50}, which is related to the potency of the agonists. Ligands with lower EC_{50} values present better efficiency, considering that lower concentrations of the compound are required to trigger 50% of receptor activation. The maximal receptor response induced by an agonist defines the E_{max}; this parameter is a good indicator of compound efficacy.[34]

According to their efficacy, agonists can be classified in two groups:

- **Full agonists**: upon binding, these ligands induce maximal receptor activation (Figure 7A).

- **Partial agonists**: these ligands bind to the receptor but induce only partial activation, even at maximal receptor occupancy. This indicates that partial agonists have lower efficacies compared to full agonists and, for this reason, they present lower E_{max} values (Figure 7B).

Antagonists

Ligands that inhibit receptor activation are referred to as antagonists. Orthosteric antagonists bind to the orthosteric site, thus preventing agonist-receptor interactions due to steric effects. Therefore, interactions between agonists and orthosteric antagonists are in general competitive and binding of one molecule over the other depends on the relative affinities and concentrations of the two ligands. [22,35]

Importantly, the kinetics of the agonist-antagonist-receptor system are very important and can define two types of antagonism: **surmountable or insurmountable**. Surmountable antagonists show relatively fast re-equilibration periods (time required for the three system components to reach an equilibrium). Therefore, if pharmacological characterization is performed with adequate equilibration timings, pure competitive antagonism should be detected. On the other hand, insurmountable antagonists have very slow unbinding rates which hamper the equilibration process. In consequence, receptor inhibition is pseudo-irreversible and noncompetitive antagonism will be observed, where the maximal response can be reduced.[35]

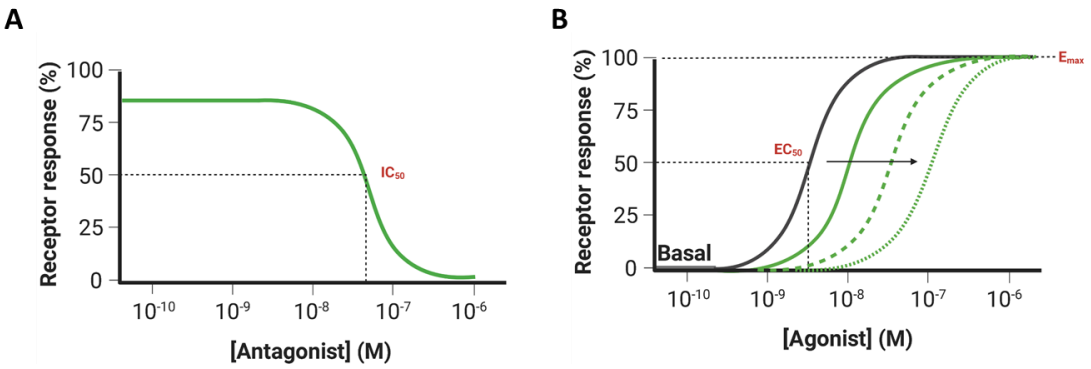

Figure 8. Different pharmacological profiles of antagonism. (A) Dose-response of the antagonist with a constant concentration of agonist. (B) Dose response curves of agonist with different fixed concentrations of antagonist. Adapted from Kenakin (2014). Created with BioRender.

In order to pharmacologically determine the properties of antagonists there are two classical types of functional assay that can be performed:

A) **Antagonist dose-response curve of the antagonist with a constant concentration of agonist** (Figure 8A): Generally, the agonist concentration added is selected to induce an 80% of receptor activation, thus ensuring a good assay window preventing receptor saturation. Additionally, this type of experiment allows an estimation of the concentration of antagonist that reduces receptor activity by 50%, a parameter named IC_{50} that measures the inhibitory potency of the molecule.

B) **Agonist dose-response curves of the agonist with constant concentrations of antagonist** (Figure 8B): In a purely competitive antagonist, increasing concentrations of the ligand should produce equipotent displacements of the curves to the right, reducing the receptor sensitivity towards the agonist. Nevertheless, this type of assays also allows to detect additional effects on the E_{max}, that can be attributed to noncompetitive processes or insufficient equilibration times.

Interestingly, when an antagonist has higher affinity for the receptor in an active state, it will be detected as a partial agonist in an efficiently coupled receptor system. This highlights the complexity of ligand-induced responses in GPCRs and how variable their pharmacological characterization can be.[35]

Additionally, some antagonists have been included in a specific sub-group due to a particular feature in their antagonistic properties: **Inverse agonists** display higher affinity for the inactive state of the receptor. These types of ligands can only be identified in constitutively active receptor systems, where the basal activity is increased due to the spontaneous formation of active receptor states. Their preference for the receptor inactive state alters the GPCR active-inactive equilibrium, leading to a reduction in the basal state or constitutive activity of the system. However, these ligands will behave as competitive antagonists in quiescent receptor systems, where the basal activity is not elevated (Figure 9).[35]

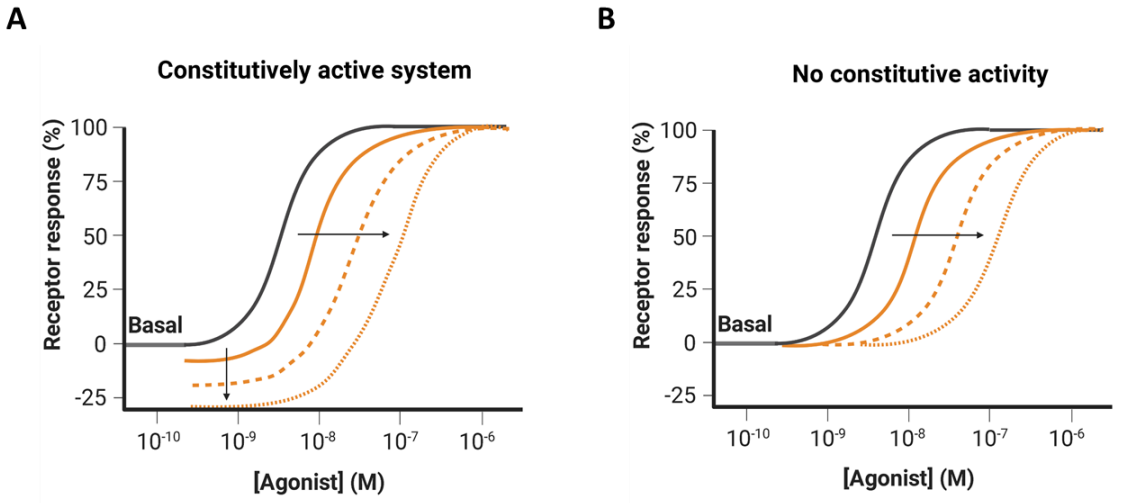

Figure 9. Different pharmacological profiles of inverse agonists. Dose-response curves of an agonist with or without the addition of an inverse agonist. Different effects are observed for the same inverse agonist in a constitutively active system (A) and a system with no constitutive activity (B). Adapted from Kenakin (2014). Created with BioRender.

Allosteric ligands

Allosteric ligands bind to an allosteric binding site, which is topologically different from the orthosteric binding pocket. Upon binding, an allosteric modulator induces a conformational change in the shape of the receptor, which can modify the affinity or efficacy of orthosteric ligands, both in positive and negative directions. In addition, these ligands can also increase (agonism) or decrease (inverse agonism) receptor signaling independently from orthosteric molecules (Figure 10).[36] An additional feature of allosteric modulators is that their effects are saturable; maximal modulation is reached when the allosteric pocket is fully occupied.[37] Moreover, allosteric ligands tend to modulate the activity of receptors with higher selectivity; this is because allosteric binding pockets are less conserved among the different receptor families and subtypes.[33] Other differences between the properties of orthosteric and allosteric ligands are summarized in Table 4.

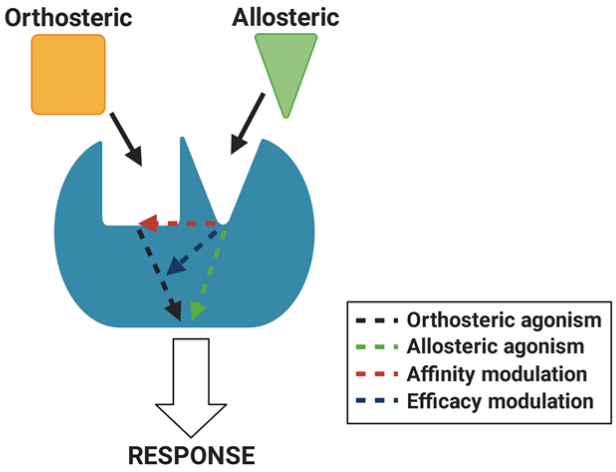

Figure 10. Orthosteric and allosteric modulation. Allosteric ligands bind to the receptor via an alternative pocket and induce a conformational change in the target receptor. This can affect the affinity (red) or the efficacy (blue) of the orthosteric ligands. In addition, some allosteric modulators can mediate signaling responses on their own (green). Adapted from Conn *et al.* (2009). Created with BioRender.

Table 4. Differences in the pharmacological properties of orthosteric antagonism and negative allosteric modulators.[38]

Orthosteric	Allosteric
Orthosteric antagonists block all agonists with the same potency.	Allosteric antagonists may block different agonists with different potencies.
At high concentrations, antagonists block receptor signalling to basal levels.	Receptor signalling can be reduced but not blocked to basal levels
Low receptor selectivity	Higher receptor selectivity

Generally, we can define five phenotypic profiles for allosteric modulation. These emerge from various combinations of effects on affinity, efficacy and direct agonism.

Negative allosteric modulators (NAMs)

NAMs are molecules that reduce the affinity and/or efficacy of orthosteric agonists. When allosteric ligands cause a reduction in the agonistic affinity, dose-response curves of the agonists are shifted to the right, and their maximal response is not modified (Figure 11A). Therefore, higher concentrations of allosteric ligand cause an increase in the agonistic EC_{50}. On the other hand, if the modulation only affects the efficacy of the orthosteric ligand, increasing the concentrations of the NAM reduce the maximal response of the agonist (E_{max}) (Figure 11A). If allosteric modulation affects both parameters, increasing concentrations of the allosteric ligand cause modifications on both, E_{max} and EC_{50}. [38]

Additionally, there is a specific group of NAMs that also display intrinsic agonism:

- **NAM-agonists:** these compounds increase the basal activity of the system by stabilizing an active receptor conformation on their own. As NAMs they can also modulate the E_{max} and EC_{50} of orthosteric agonists (Figure 11B).

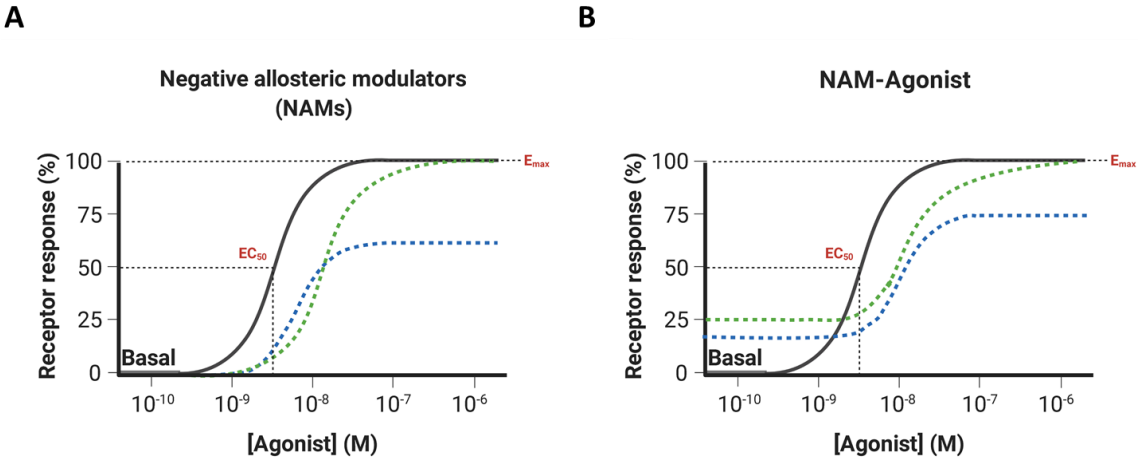

Figure 11. Negative allosteric modulators phenotypic profiles. (A) NAMs reduce the sensitivity of the receptor to the agonist; they can affect their affinity (green dashed line) or their efficacy (blue dashed line). (B) NAM agonists present intrinsic agonism, which causes an increase in the basal activity levels. Adapted from Kenakin (2014). Created with BioRender.

Positive allosteric modulators (PAMs)

This group of allosteric ligands induce positive effects on the affinity and/or efficacy of agonists. PAM modulation in the affinity of an agonist is observed as a shift in its dose-response curve to the left. Therefore, PAMs cause a decrease in the measured EC_{50} of the agonist. When positive modulation affects the efficacy, increases in the maximal response of the agonist are observed with increasing concentrations of PAM ligand (Figure 12).[38]

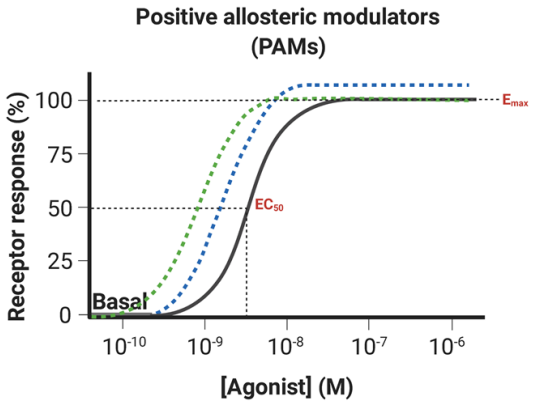

Figure 12. Positive allosteric modulators phenotype. PAMs increase the sensitivity of the receptor towards an agonist. They can increase the affinity (green dashed line) or the efficacy (blue dashed line) of an agonist. Adapted from Kenakin (2014). Created with BioRender.

There are two additional types of PAMs that display intrinsic positive or negative effects:

- **PAM-agonists:** These ligands are PAMs that can also induce an agonistic response independently from orthosteric ligands. This causes an increase in the basal activity of the system (Figure 13A).

- **PAM-antagonists:** PAM-antagonists increase the affinity of the agonist while decreasing its efficacy. Thus, PAM-antagonists reduce EC_{50} values and decrease the maximal response achieved by agonist activation (Figure 13B).

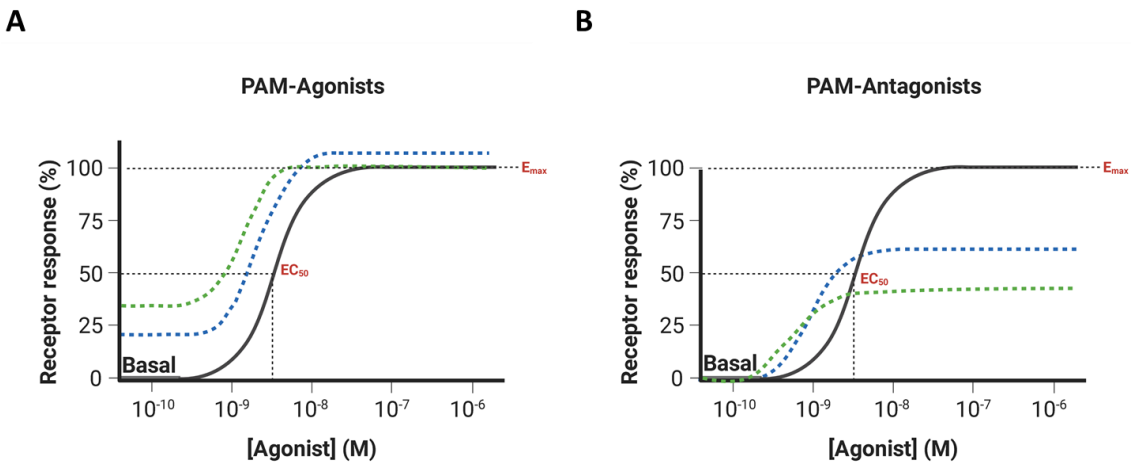

Figure 13. Phenotypic profiles of PAM-Agonists and PAM-Antagonists. (A) PAM-agonists increase basal levels of receptor activity as they can induce agonistic response. (B) PAM-antagonists increase the affinity of the agonist towards the receptor but also prevents the induction of agonistic response as a consequence of ligand binding. Adapted from Kenakin (2014). Created with BioRender.

Biased ligands

Historically, ligands were classified according to the topology of their binding site and/or depending on the nature of their receptor-induced functional response. However, recent studies have demonstrated that some GPCR ligands (orthosteric and allosteric) constitute a novel and functionally distinct group: **biased ligands**. Even though the mechanisms underlying ligand bias

are not well understood yet, it has been demonstrated that these molecules stabilize the target receptor in a unique conformation.[39] This causes activation of a particular effector (either G-protein or β-arrestin), which leads to signal transduction via a specific signaling pathway (Figure 14). Therefore, ligand bias can be described as the capability of a compound to selectively engage or inhibit a specific signaling pathway, leading to a different functional outcome compared to balanced ligands.[39,40]

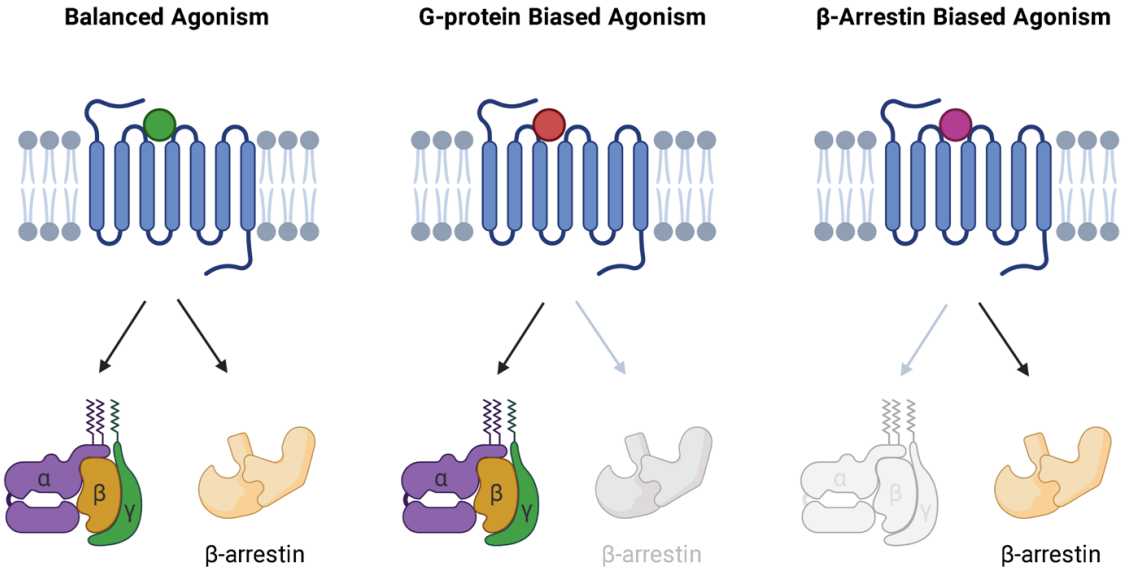

Figure 14. Types of agonism according to the preferential activation of the different signaling effector pathways. Balanced agonism leads to activation of the different signaling pathways with no preference. In contrast, G-protein biased agonists trigger signal transduction processes through activation of G proteins, and β-arrestin biased agonists induce β-arrestin activation preferentially. Created with BioRender.

In the last decade, many biased ligands have been identified or developed for around 30 different GPCRs (within class A, class B and class C).[41–43] This novel type of molecules has contributed to gain a better understanding of GPCR signaling and has opened new avenues for the development of improved drugs targeting GPCRs. The therapeutic potential of biased ligands relies on the higher selectivity offered by the ligands towards a particular signaling pathway, thus providing molecules with higher efficiency and reduced side effects. In this line, several biased ligands have reached the late stages of clinical development; additionally, some currently approved drugs have shown biased GPCR modulation.[40,44]

1.3 Beta-adrenoceptors

1.3.1 Overview, classification and localization

Adrenergic receptors (AR) belong to the aminergic receptor subfamily within the rhodopsin like family (or class A GPCRs) of G protein-coupled receptors. This group of receptors are classified into three major types (α_1, α_2, and β) which are further divided into three subtypes each (Table 5). Adrenoceptors are endogenously activated by catecholamines, such as adrenaline or noradrenaline, and regulate a variety of physiological functions including heart rate, lung function and a variety of metabolic and CNS functions. The crucial role exerted by these receptors in maintaining the homeostasis of important physiological functions has signaled

them as classic pharmacological targets. Interestingly, signaling transduction processes are mediated through different G proteins in each of the three subtypes. α_1-Adrenoceptors interact with G_q upon activation and activate the phospholipase C – phosphatidylinositol-4,5-biphosphate – inositol triphosphate signaling pathway. On the contrary, α_2 receptors activate the inhibitory G protein (G_i); this causes inhibition of adenylyl cyclase (AC) which results in a reduced production of cAMP. Finally, β-adrenoceptors mainly bind to the stimulatory G protein (G_s) and increase the levels of cAMP through the activation of AC.[45,46]

Among adrenoceptors, beta-adrenoceptors are the most reviewed and studied type. This can be due to their importance in the regulation of cardiac function, among others.[47] β-AR are divided in three subtypes, β_1-, β_2- and β_3-AR. Both β_1- and β_2-AR induce cAMP production from ATP through G_s coupling. However, their biological effects are fairly different, mostly due to their different organic localization. For instance, β_1-adrenoceptors, that regulate the cardiac output, are mainly located in the heart and cerebral cortex. In contrast, β_2-AR are prevalent in the respiratory airways and cerebellum, and control smooth muscle relaxation processes.[45,48] β_3-AR are majorly located in the adipose tissue and control metabolic processes such as the regulation of lipolysis and thermogenesis.[49] This receptor subtype is also found in the urinary bladder, where upon activation triggers relaxation of the bladder smooth tissue. In fact, β_3-AR agonism is being investigated for the treatment of overactive bladder. Even though the presence of each receptor subtype is more predominant in specific organs, their expression can be found in other tissues. Additionally, co-expression of different subtypes is a common phenomenon.[50]

Table 5. Classification of adrenoceptors and definition of their main physiological functions.[46,51,52]

Type	Subtype	G-protein coupling	Physiological functions
α_1	α_{1A}	G_q	Smooth muscle constriction in different tissues and organs (bronchioles, blood vessels, ureter etc.). Vasoconstriction is triggered in the skin, gastrointestinal system, kidney and brain.
	α_{1B}	G_q	
	α_{1D}	G_q	
α_2	α_{2A}	G_i	Regulation of presynaptic neurotransmitter release from adrenergic neurons and sympathetic nerves in the CNS. Regulation of translation.
	α_{2B}	G_i	
	α_{2C}	G_i	
β	β_1	G_s	Increases the cardiac output by increasing heart rate and cardiac muscle contractility.
	β_2	G_s	Smooth muscle relaxation in different tissues and organs (bronchi, GI tract and skeletal muscle). Increases perfusion and vasodilation.
	β_3	G_s /G_i	Increase of lipolysis in the adipose tissue. Thermogenesis regulation in the skeletal muscle. Relaxation of the bladder.

1.3.2 Activation and intracellular signaling

Upon agonist binding, GPCRs experience a global conformational change that trigger the activation of G proteins and different downstream signaling pathways. The molecular mechanisms and structural changes induced by agonists that lead to signal transduction in GPCRs have been extensively studied. In fact, a recent study identified a common activation pathway for class A GPCRs; this preserved mechanism was proposed after careful analysis of the structural changes detected between active and inactive conformations of several rhodopsin-like receptors, including β_2-AR. [53]

The conserved activation pathway, identified from structural analyses, links the ligand-binding pocket and the G protein-coupling regions through 34 residue pairs, which are highly conserved among class A GPCRs. Similar residue rearrangements connect different and well-known motifs (such as CWxP, PIF and the Na+ pocket), from the extracellular to the intracellular sides. These rearrangements enable the transition of GPCRs from an inactive to an active conformation; movements in the transmembrane helices are observed, which result in inter-helical contact modifications. In particular, binding of different agonists converges to trigger an outward movement of the cytoplasmic end of TM6, which eliminates TM3-TM6 contacts and repacks TM5-TM6. Additionally, an inward movement of TM7 towards TM3 is observed, which creates new TM3-TM7 contacts. Overall, the final disposition of the helices in the GPCR active conformation creates an intracellular crevice for G protein coupling (Figure 15A).[54–56]

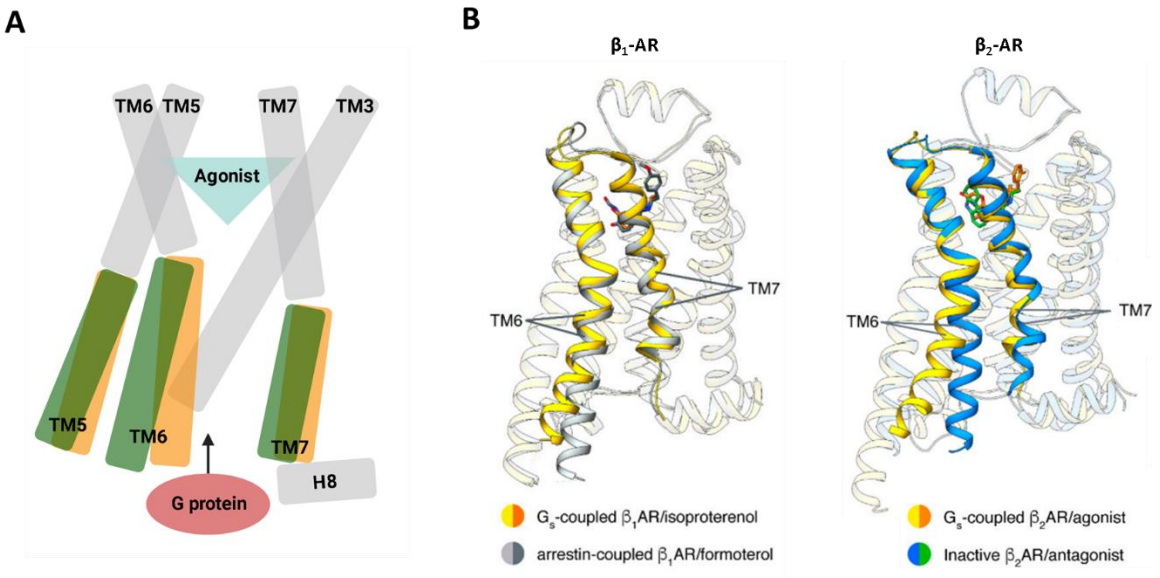

Figure 15. Common activation mechanism of class A GPCRs. (A) Common structural changes described between inactive (orange) and active (green) conformations of class A GPCRs. Adapted from Zhou (2019). Created with BioRender. (B) Superposed structures of the active and inactive conformations of β_1AR (PDB IDs: 7JJO[57] and 6TKO[58] respectively) and β_2AR (PDB IDs: 3SN6[59] and 2RH1[60] respectively). Adapted from Wu (2021).

Therefore, the molecular mechanisms that lead to an active receptor conformation are highly conserved among class A GPCRs. In fact, the pronounced outward movement of TM6 is observed in the active structures reported for both β_1- and β_2-AR, in consistency with the common activation mechanism described (Figure 15B). Nevertheless, it is worth noting that despite the

described similarities, each receptor presents a unique ligand-receptor activation pathway. Moreover, the signaling transduction pathways that get activated upon agonist binding can be notably different even within different receptor subtypes.

Both β_1- and β_2-adrenoceptors preferentially interact with Gαs upon agonist binding. Active Gs exchanges GDP for GTP, dissociates from the βγ dimer and activates adenylyl cyclase (AC). These processes cause an increase of intracellular cAMP, that activates protein kinase A (PKA). Active PKA triggers the phosphorylation of a variety of important target proteins such as L-type calcium channels.[52] Upon activation, β_3-AR can also interact with the stimulatory G protein and induce signal transduction via a similar pathway to the one described for β_1- and β_2-adrenoceptors. However, β_3-AR can also trigger Gi activation, which can either block AC or activate the endothelial NO synthase (eNOS). Active eNOs produces nitric oxide (NO) and consequently activates the enzyme guanylate cyclase, which transforms GTP into cGMP. An increase in the intracellular concentration of cGMP subsequently activates protein kinase G (PKG), that phosphorylates several target proteins. B_2-AR have also been described to interact with Gi but fewer examples of signaling through this effector are reported in the literature for this receptor subtype (Figure 16).[52,61,62]

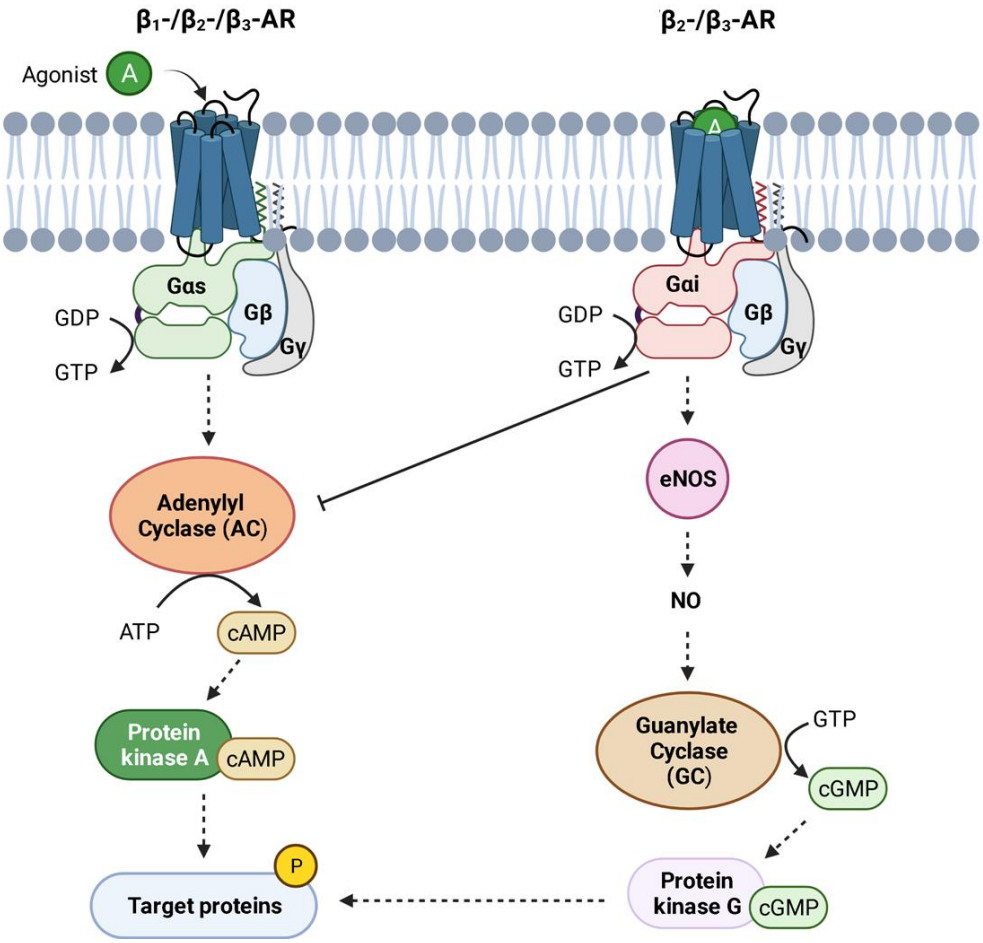

Figure 16. Signaling transduction processes in β-adrenoceptors. Upon agonist binding, the three subtypes of beta-adrenoceptors (β_1-, β_2-, and β_3-AR activate the stimulatory G protein (Gαs), which consequently increases cAMP levels and activates PKA. In addition, both β_2- and β_3-AR can activate the inhibitory G protein (Gαi). Activation of Gαi can reduce cAMP levels or activate the endothelial NO synthase, which produces nitric oxide and activates PKG. Created with BioRender.

Thus, the distinct physiological functions attributed to the different subtypes of beta-adrenoceptors can be attributed to a combination of at least two factors: the interaction with different effectors upon activation and a different localization in the organism.

Additionally, activation of G protein independent signaling pathways has also been described for beta-adrenoceptors, which increases the complexity of the mechanisms involved in receptor function.[63]

1.3.3 Therapeutic potential of beta-adrenoceptors

The role of β-AR in the regulation of important physiological and physiopathological processes has appointed this group of GPCRs as classic therapeutic targets. Development of molecules that modulate the activity of these receptors in a positive or negative direction has enabled the treatment of a wide variety of pathologies and physical conditions.

For instance, **β-AR agonists** are considered the golden standard treatment for respiratory diseases such as asthma and chronic obstructive pulmonary disease (COPD). Agonistic activation of β_2-AR, that are predominantly found in the airway smooth tissue, results in smooth muscle relaxation. In consequence, bronchodilation is achieved, which prevents the appearance of respiratory difficulties induced by airway narrowing.[64–66] The first β_2-AR agonists discovered, displayed an action span of 4-6 h.[67] In order to increase the effectiveness of the asthma and COPD treatments, long-acting β_2-agonists (LABAs) were developed with action durations ranging from 12 to 24 hours.[68]

The use of **β_3-AR agonists** as therapeutic agents has been studied in a variety of diseases. Due to the role of β_3-AR in the regulation of lipolysis and thermogenesis, β_3-AR agonists have been extensively studied as a potential treatment for diabetes and obesity.[69,70] Additionally, an increase on the activity of β_3-AR has shown to improve the overactive bladder-related symptoms.[71–73]

On the other hand, the use of **β-AR antagonists** to treat cardiac conditions such as hypertension and heart failure is well stablished.[74] Both β_1- and β_2-AR are expressed in cardiomyocytes and work synergically to regulate myocardial contractility; however, several studies described that β_1-AR have more clinical significance in cardiac development and function, compared to β_2-AR.[75,76] Catecholamine-triggered β-AR signaling is essential for the correct functioning of a normal heart. However, abnormally high levels of catecholamines have been detected in heart failure patients, which causes a reduction in the expression of β-AR. The benefits of beta-blockers in the treatment of heart failure are attributed to the reduction of the detrimental outcomes of sustained β_1-AR signaling.[77] Interestingly, some β-AR also antagonize α_1-AR, which results in vasodilation a biological effect that can benefit some patients.[78] However, the poor selectivity of beta-blockers, specially between cardiac β_1-AR and respiratory β_2-AR, constitutes a problem for the treatment of patients with both, cardiac and respiratory conditions.[79] Therefore, an appropriate selection of the beta blocker is essential for the correct management of patients with COPD and cardiac pathologies.

1.3.4 Ligands targeting β-AR: molecular structure, function and selectivity

The endogenous ligands of beta-adrenoceptors are epinephrine (**1**) and norepinephrine (**2**), also known as adrenaline and noradrenaline, respectively. These two ligands are catecholamines, with a catechol moiety (highlighted in yellow, Figure 17) and an amine group (highlighted in blue, Figure 17) connected to the aromatic ring (highlighted in purple, Figure 17) through a two-carbon bridge. Additionally, both compounds display a secondary alcohol in the benzylic position; the ethanolamine moiety is a distinctive feature of adrenergic ligands, considering that other catecholamines targeting aminergic receptors do not have it, such as dopamine (**3**) (Figure 17A).

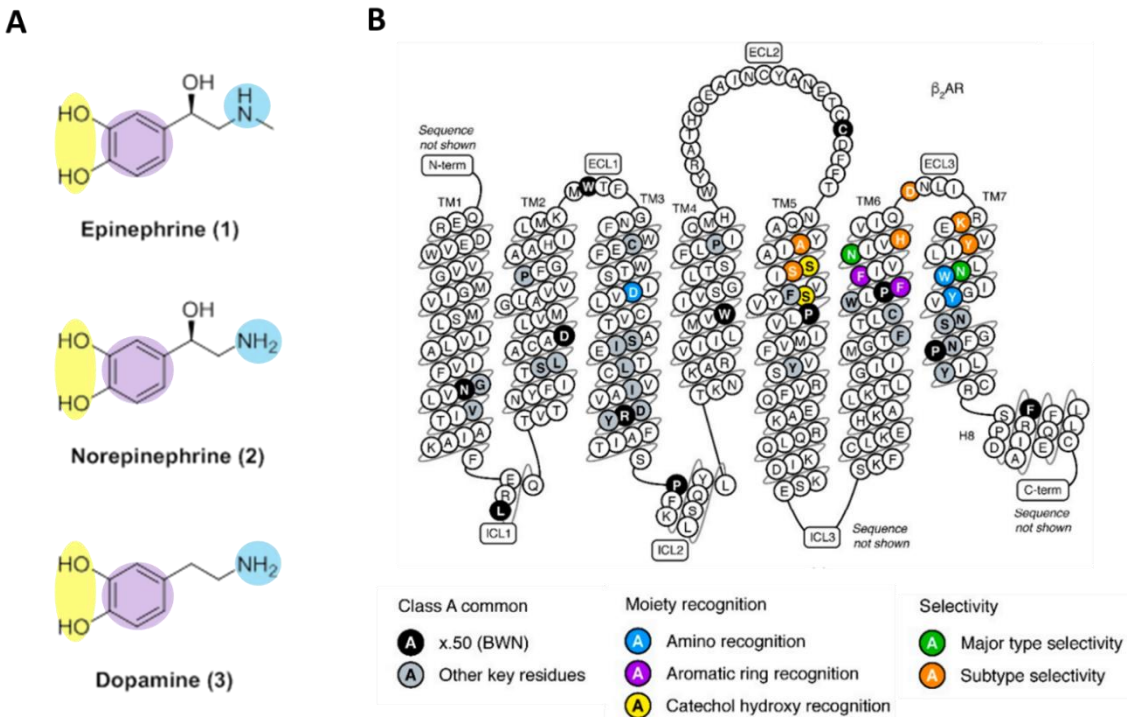

Figure 17. Ligand recognition mechanisms in beta-adrenoceptors. (A) Chemical structures of catecholamine neurotransmitters. Relevant moieties for ligand-receptor interaction are highlighted in yellow (catechol), purple (aromatic moiety) and blue (amine). (B) Key residues for ligand recognition and selectivity among the different adrenoceptor types are colored on a snake plot of β_2-AR. The color code for amino acids involved in ligand moiety recognition is consistent with the colors used to highlight the catecholamine moieties in panel A. Adapted from Wu (2021). Created with BioRender.

The binding mode of the two endogenous ligands is very similar (depicted in Figures 17B and 18). The aromatic ring forms π-π interactions with two phenylalanine residues highlighted in purple, which are conserved among the different adrenoceptor subtypes. Amine recognition is facilitated through H-bond interactions with an aspartate residue (D3.32) present in all adrenoceptors. Additionally, the catechol moiety is identified by two serine groups in TM5 (yellow colored) that are present in all adrenergic and dopaminergic receptors but are not conserved in other aminergic receptors. However, the presence of the two serine residues (S5.42 and S5.46) conserved in both adrenergic and dopaminergic receptors difficults the specific ligand-receptor recognition of catecholamines between these two types of GPCRs. For this reason, dopamine has been identified as a modulator for adrenoceptors[80,81] and adrenaline and noradrenaline stimulate some dopamine receptor subtypes.[82]

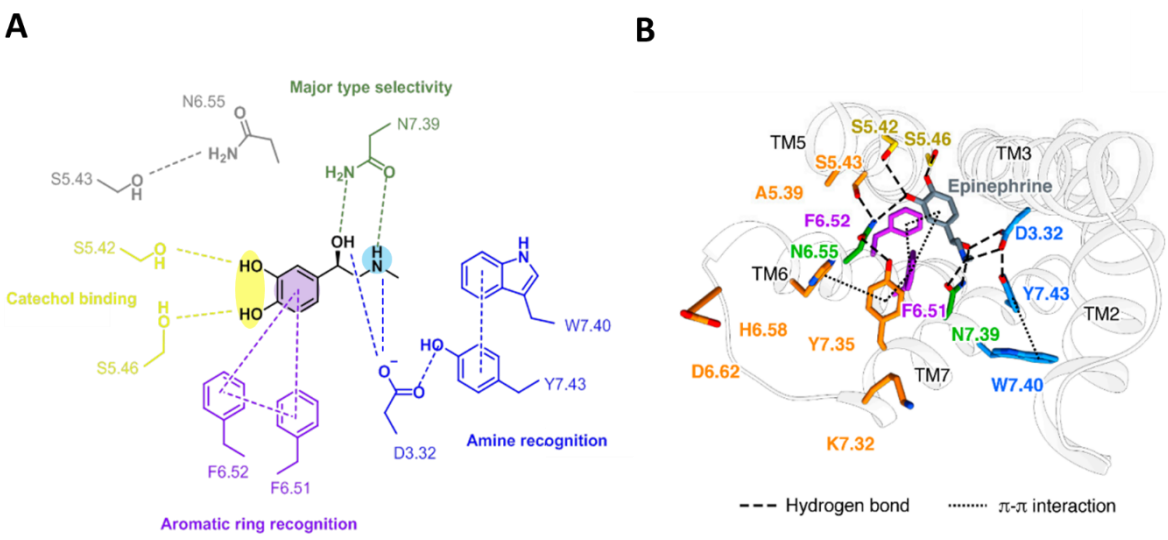

Figure 18. Key interactions between the endogenous ligand epinephrine and the binding pocket in β_2-adrenoceptors. (A) Schematic 2D representation of the interactions between epinephrine and the residues within the binding pocket. (B) 3D representation of the interactions and the binding mode of epinephrine in β_2-AR (PDB ID: 4LDO[83]). Residues interacting with the catechol moiety are colored in yellow; amino acids that interact with the phenyl ring are purple and residues responsible for the amine recognition are depicted in blue. Additionally, key amino acids associated with adrenergic selectivity are highlighted in green. Adapted from Wu (2021).

Interestingly, ligands targeting β-AR retain an ethanolamine moiety to form dual hydrogen bonds with N7.39, highlighted in green (Figure 18). In order to interact with the asparagine residue in β-AR, amines must be primary or secondary. Tertiary substitution of the amine in the ethanolamine moiety does not enable H-bond formation with N7.29, which highly reduces the binding affinities of the molecules towards β-AR.[84] This residue is substituted by a phenylalanine (F7.39) in α-AR, and binding of agonists and antagonists to these receptors relies on the formation of π-π interactions with this residue. Therefore, asparagine N7.39 is the residue responsible for β-AR ligand selectivity in the orthosteric pocket.[85]

Non-selective agonists and antagonists targeting β-AR

A common scaffold is found repeatedly in the molecular structure of agonists targeting beta-adrenoceptors. This substructure, also present in the endogenous ligands, is constituted by a phenyl ring linked to an ethanolamine backbone (highlighted in green, Figure 19). The importance of conserving this common scaffold in agonism, and the interactions that these moieties form with the binding pocket of β-AR have been previously described. In fact, the ionic/H-bond interactions established between the ethanolamine backbone and residues D3.32 and N7.39 of the binding pocket is found in all ligands, not only agonists.[86] In addition, some agonists maintain the catechol moiety present in the chemical structure of endogenous ligands. Phenol groups in the aromatic ring allow the formation of an H-bond with serine residue S5.46, located in TM5; this interaction has been identified as essential for the agonistic activity of ligands, as it triggers the movement of TM5 towards TM3/6, and away from TM7. As a consequence of this helical movement, the intracellular pocket is expanded, which is an important part of the receptor activation mechanism.[87] However, the catechol substructure can be modified by introducing other H-bond donor/acceptor substituents in the aromatic ring that also form polar interactions with TM5. For instance, cimaterol (**6**) is a non-selective agonist that

presents an aniline and a cyano- group in substitution of the catechol moiety. Finally, substituents at the amine position are very diverse, and admit the incorporation of large and sterically demanding moieties (see dobutamine (**5**), Figure 19).

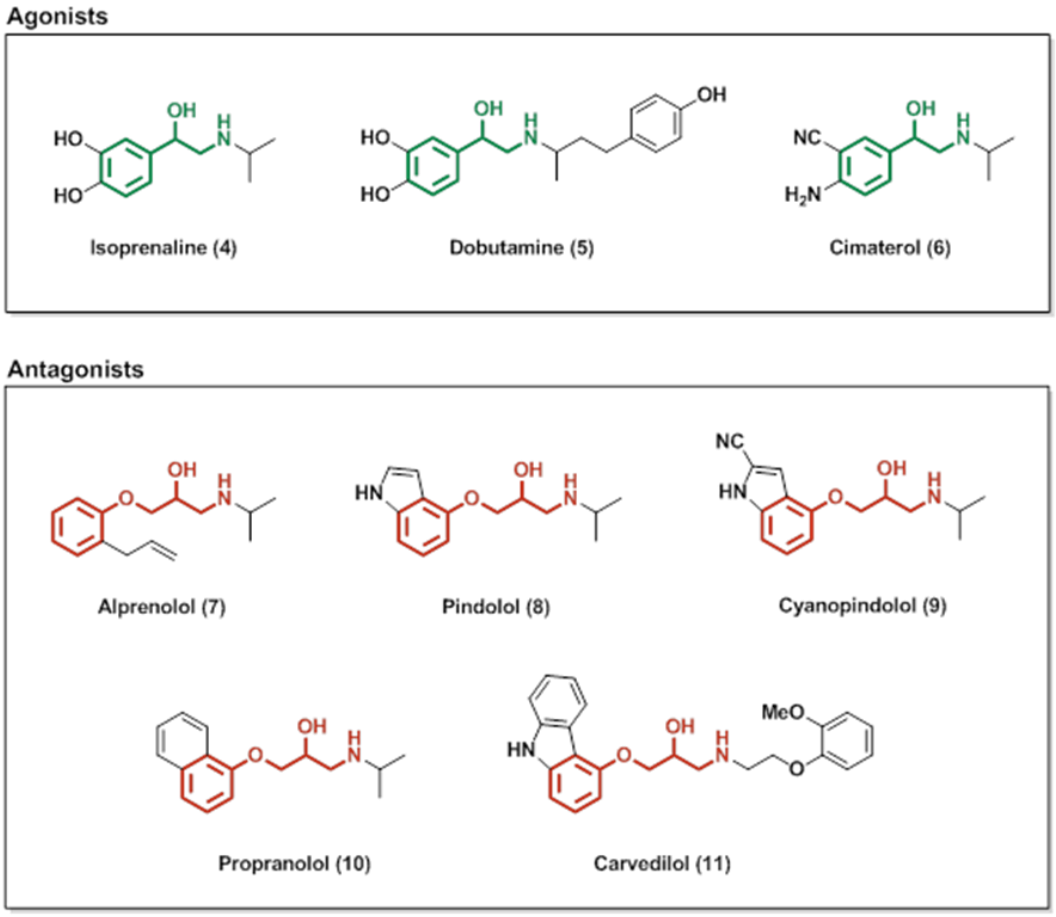

Figure 19. Molecular structures of non-selective β-adrenoceptor agonists and antagonists. The moiety repetitively found in all agonists is highlighted in green and the conserved scaffold in most antagonists is colored in red.

On the other hand, most antagonists also share a common scaffold, with the ethanolamine backbone connected to the phenyl ring through an oxymethylene bridge. The oxymethylene linker is a particularity on the molecular structure of antagonists and is only found in the structure of partial agonists. Introducing these two additional atoms creates specific interactions with TM5 that favor stabilization of the inactive receptor form. Another important difference in the scaffold of antagonists is that the phenyl ring is less polar and is often fused with other aromatic groups (Figure 19). This produces compounds with bulky hydrophobic moieties, which form stabilizing hydrophobic interactions with residues in TM5 and TM6 (Figure 20). In contrast to β-AR agonists, antagonists targeting beta-adrenoceptors very rarely form polar interactions with TM5. Thus, an analysis of the protein-ligand fingerprint interactions in different crystal structures for β-AR has identified that polar interactions with TM5 are necessary to maintain the active state of these receptors. Contrarily, stabilization of the inactive state is achieved when ligands form hydrophobic interactions with TM5 and 6. These interactions prevent the described helical movements that lead to expansion of the intracellular pocket, where G proteins bind.[86,87] Finally, as described for agonists, amine substitution in the ethanolamine backbone admits variation, even if many reported ligands display an isopropyl group.

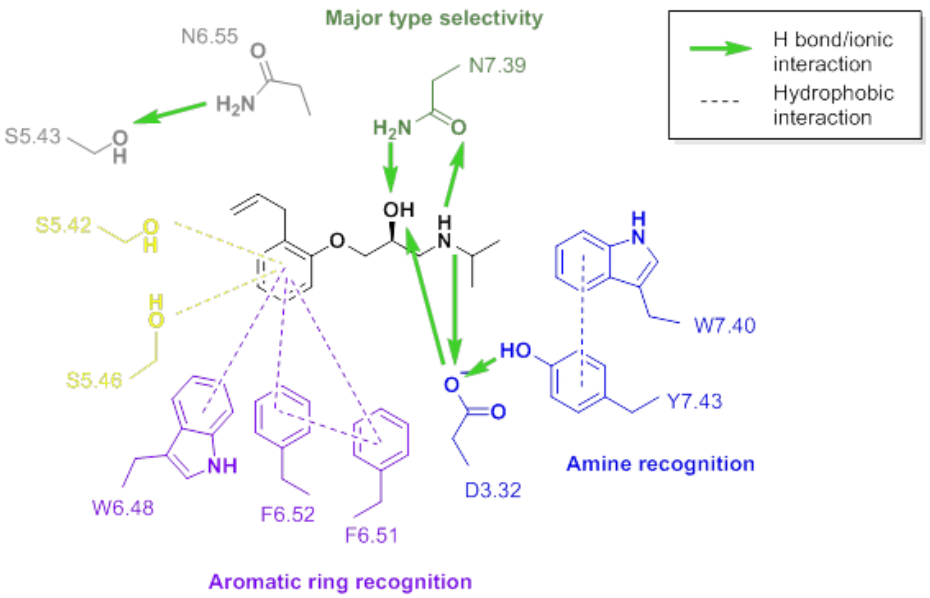

Figure 20. Schematic binding mode of the non-selective antagonist alprenolol to β_2-adrenoceptors. H-bonds or ionic interactions are represented through green arrows and hydrophobic interactions are depicted as dashed lines. Color code for the different residues is maintained as described in Figure 16. Adapted from Chan (2016).

Achieving β_1-/ β_2- ligand selectivity

Development of ligands that selectively target one of the beta-adrenoceptor subtypes is a challenging task as a consequence of the high homology observed between their full-length sequences (51-57%). Moreover, and to increase the difficulty of selective targeting of β-AR, residues in the binding pocket are highly conserved within beta-adrenoceptors, with homology levels ranging from 57% (between β_2- and β_3-AR) to 70% (between β_1- and β_2-AR).[87] Nevertheless, several selective ligands targeting beta-adrenoceptors (agonists and antagonists) have been described due to their therapeutic interest. For instance, the therapeutic potential of β_2-AR agonists for the treatment of respiratory diseases has led to the development of a number of β_2- selective agonists (Figure 21). These ligands maintain the scaffold common in all agonists (green colored), which enable the formation of interactions with key residues within the binding pocket responsible for ligand binding. In addition, most of the ligands present aromatic substituents that can form ionic or H-bond interactions with TM5, previously described to be essential for receptor activation.[86] Interestingly, many of the selective agonists targeting β_2-AR display a *tert*-butyl amine substitution (highlighted in orange); this suggests that introducing this bulky substituent favor selectivity of agonists towards the beta 2 subtype. In contrast, salmeterol (**15**) presents a very large and particularly long amine substituent, which is markedly different from the *tert*-butyl substituent displayed in other selective agonists (Figure 21). The observed selectivity for this ligand is attributed to the interaction of this long molecule with amino acid residues at the end of the binding pocket, which are different between beta 1 and beta 2 subtypes.[88] Finally, due to the lack of therapeutic interest for the development of selective agonists targeting β_1-AR, very few molecules with this pharmacological profile have been reported in the literature.

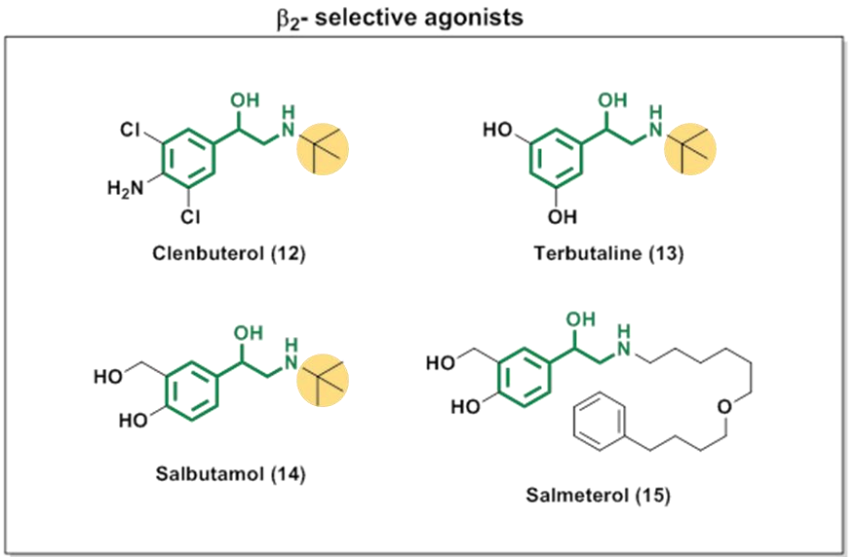

Figure 21. Chemical structures of β_2- selective agonists. The moiety that is repetitively found in all agonists is highlighted in green and the common *tert*-butyl amine substitution is highlighted in yellow.

On the other hand, the main role of β_1-AR in the modulation of the cardiac output has risen interest on beta 1 selective antagonists, as they are expected to provide "cardio-selective" beta-blockers. In consequence several antagonists targeting selectively β_1-AR have been reported in the literature (Figure 22). These ligands share the scaffold common in all antagonists and very often present an isopropyl amine substituent. Interestingly, most β_1-AR antagonists display a *para*- aromatic substitution pattern, which indicates that this has a relevant impact on the selectivity of antagonists towards beta 1 adrenoceptors (highlighted in green, Figure 22). However, the nature of this substituent is variable and admits the introduction of long and short moieties (Figure 22). Finally, few β_2- selective antagonists have been reported due to the lack of therapeutic interest of these ligands.

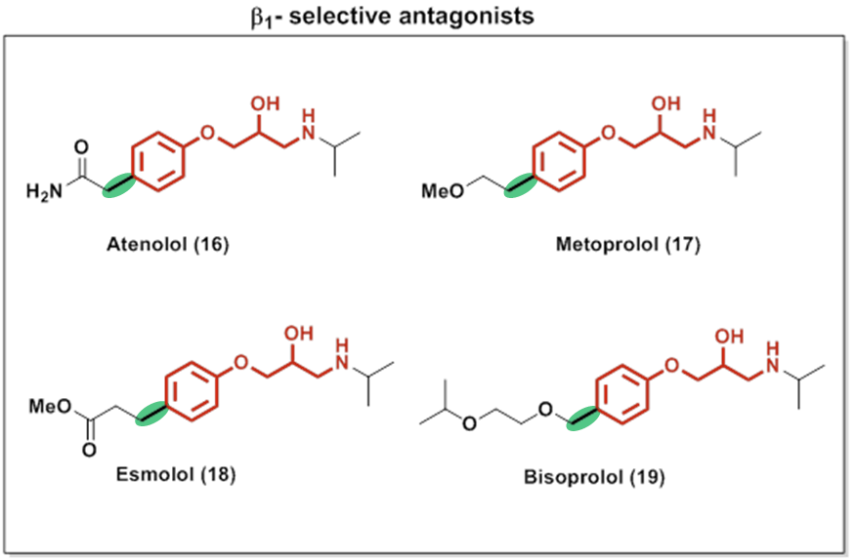

Figure 22. Molecular structures of β_1- selective antagonists. The common scaffold found in all antagonists is colored in red and the aromatic *para*-substitution characteristic of β_1- selective antagonists is highlighted in green.

Allosteric modulation of β-adrenoceptors

Achieving allosteric modulation of GPCRs has been of great interest in drug discovery due to the improved selectivity of these type of ligands. The fact that the allosteric binding pocket is topologically different from the highly conserved orthosteric binding site has facilitated the development of drugs with better pharmacological profiles. In addition, allosteric modulators affect the activity of the receptor in the presence of the endogenous ligand, which also constitutes a benefit for therapeutic applications.

Allosteric modulation of beta adrenoceptors and the binding mode of allosteric ligands have been widely studied for the beta 2 subtype. Different allosteric modulators, PAMs and NAMs, have been developed (Figure 23B) and their binding pockets identified by X-Ray crystallography. Figure 23A shows a schematic representation of the different allosteric binding sites described for β_2-AR. PAM and NAM ligands can bind to the groove in the lipidic interface formed by helices TM3, TM4 and TM5. However, their binding sites are located at different heights of the groove, thus allowing for the formation of different interactions that stabilize the receptor in different states.[87] For instance, Cmpd-6FA (**20**) was identified as a PAM that binds close to the cytoplasmic end (highlighted in orange) and stabilizes the active state of the receptor through interactions with TM3 and TM4.[89] The NAM AS408 (**21**) binds closer to the center of the receptor (colored in dark green) and interacts with TM3 and TM5, stabilizing the inactive conformation of β_2-AR.[90] On the other hand, cmpd-15PA (**22**) was identified as a negative allosteric modulator that binds to the cytoplasmic surface of β_2-AR (highlighted in blue). This ligand was found to stabilize the inactive state of the receptor and hampers the binding of the G protein to the receptor.[91]

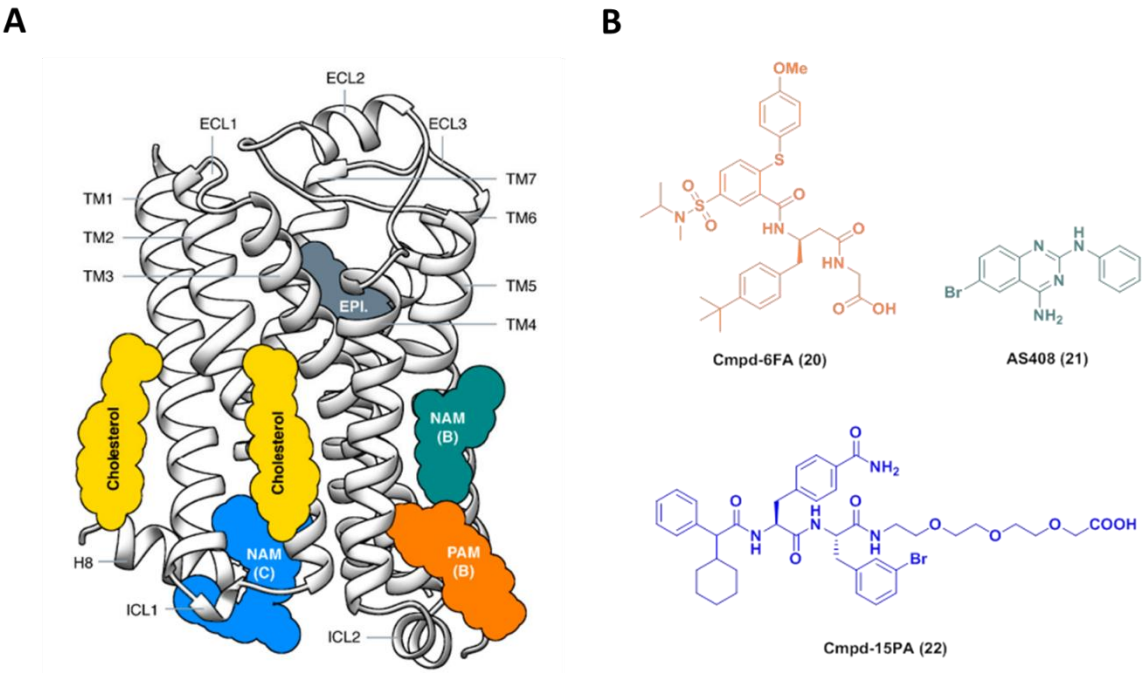

Figure 23. Allosteric modulation of beta-adrenoceptors. (A) Allosteric binding sites for β_2-AR are depicted in a schematic representation of the tridimensional structure of β_2-AR. Cholesterol binding sites are colored in yellow and the orthosteric binding site in represented in grey (EPI.). (B) Chemical structures of beta-adrenoceptor allosteric modulators. Ligands are highlighted according to the color assigned to their allosteric binding pocket. Adapted from Wu (2021).

It is worth noting that the chemical structures of the described allosteric modulators are very diverse, and do not share the common scaffold depicted previously for orthosteric ligands. Additionally, allosteric binding pockets are less conserved, and may lead to compounds with subtype selectivity. In fact, even if high sequence homology is observed between β_1- and β_2- AR, the mentioned allosteric ligands present higher selectivity towards the modulation of β_2-AR compared to β_1-AR.[87,92]

2 Structural studies in GPCRs

The determination of many GPCR structures in the last 20 years has been essential to enlighten the signaling mechanisms of this superfamily of receptors and the binding mode of orthosteric and allosteric ligands. Understanding the binding mode of GPCR ligands from a structural point of view has assisted the design of novel molecules in drug development programs (structure-based drug design approaches); structural information of the receptors has provided a rationale that identifies which chemical moieties are likely to establish key interactions with the binding pocket. In addition, analysis and comparison of structural information from different receptor subtypes has also identified possible strategies for the development of ligands with higher selectivity.[93]

Classically, GPCR structures have been determined by X-Ray crystallography, both in active and inactive conformations. Protein crystals are generally obtained from ligand-bound proteins, that present a stabilized conformation. The 3D disposition of the receptor is extracted from the diffraction patterns obtained from protein crystals after being shot with X-Rays. On the other hand, the structure of small proteins in solution can also be determined by Nuclear Magnetic Resonance (NMR) analysis.

Nevertheless, crystallizing GPCRs entails diverse challenges; firstly, it requires heterologous production of large quantities of recombinant protein. Once the expression system has been optimized, these receptors must be extracted from the membrane in a functional form using detergents, where they show reduced stability. In addition, one of the major problems in GPCR X-Ray crystallography is attributed to the intrinsic dynamism and fluidity of the transmembrane receptors; the flexible nature of GPCRs difficults the formation of crystal contacts, which prevents the formation of protein crystals or provides crystals that are not appropriate due to their small size or poor diffraction.

However, GPCR X-Ray crystallography has suffered a dramatic advance in the recent years due to the development of technologies and techniques, such as protein engineering, that improve the main problems of protein instability and heterogeneity.[94,95] Moreover, optimal systems for efficient protein expression and improved purification techniques have also facilitated an increase in the number of solved GPCR crystal structures. Additionally, novel approaches and techniques have been developed in crystallography, such as Lipidic Cubic Phase (LCP) crystallization and serial femtosecond crystallography (SFX)[96], which have also contributed enormously to the advances in structural biology. Finally, the development of a completely different technique, electron cryo-microscopy (cryo-EM)[97], is revolutionizing the field of structural biology. This innovative methodology is providing solutions for many of the limitations

attributed to classic X-Ray crystallography. Moreover, NMR studies have become increasingly popular for the study of protein structure and dynamics. Nonetheless, these two techniques will not be reviewed in this section as they are not particularly relevant for the work conducted in the present thesis.

2.1 Molecular biology approaches to facilitate GPCR crystallography

As previously stated, one of the main limitations of GPCR crystallography relies on the inherent flexibility of this large family of receptors. In general, GPCR crystals are only obtained when the protein is bound to a ligand, which stabilizes the receptor in a particular conformation and reduces flexibility and instability of the receptor in detergent. Receptor stabilization is detected through an increase in the receptor's melting temperature (Tm), which is the temperature at which the receptor denaturizes. For this reason, ligands that stabilize the receptor are known as thermostabilizing; this term is also used to describe stabilizing modifications in the protein sequence. The most stable form of the receptor is in its inactive state. In consequence, the majority of GPCR crystal structures have been resolved in the presence of an antagonist or an inverse agonist that stabilize the receptor in an inactive conformation. However, ligand-induced stabilization is not sufficient to enable protein crystallization in GPCRs. Therefore, several molecular biology approaches have been developed to produce proteins with a stabilized conformation that can form well-ordered crystals (Figure 24).[98,99]

2.1.1 Mutagenesis and conformational stabilization

The use of **site-directed mutagenesis** has been an approach used to remove post-translational modification sites, to enhance receptor expression and, also to stabilize the receptor in a particular conformation. The first receptor to be stabilized in the inactive conformation through the introduction of six point mutations was the turkey β_1-AR receptor.[100] Two different strategies can be used to introduce thermostabilizing mutations in a receptor: alanine scanning mutagenesis or directed evolution for high expression and stability.[101]

- **Alanine screening mutagenesis:** this approach is the most stablished technique in the generation of stabilized GPCRs for structural studies. It consists in the generation of series of mutants where a single amino acid has been substituted by an alanine residue. The obtained mutants are then tested individually to evaluate detergent stability. Stabilizing mutations identified in the first screening are then combined in different ways, clone by clone, and generally confer mutants with higher stability. The most stable construct obtained after series of mutation combination can then be used for the desired applications, such as crystallography.[102]

- **Directed evolution for high expression and stability:** this approach allows to screen for mutations that increase receptor expression and/or mutations that increase the receptor stability in detergent. Direct evolution requires the generation of a DNA library encoding millions of mutants of the target protein through random mutagenesis. Competent *Escherichia coli* (*E. coli*) are then transformed with the genetic library, and a population of cells is obtained, where each expresses a single GPCR mutant of the library. The bacterial population is then treated with a fluorescent ligand that binds to functional receptor, and

cells with the highest fluorescence levels are selected due to their higher expression of the target receptor. Fluorescent cells are selected via fluorescence-activated cell sorting (FACS) and constitute an evolved population, which can be cycled through further rounds of mutagenesis and selection until the desired level of expression is achieved. Subsequently, individuals from this optimal population can be isolated and tested to assess their thermal stability. The mutant that shows highest thermal stability is finally selected, its genetic identity determined and used for the desired applications. This approach presents as a main advantage that it enables the screening of a wider number of mutations in a very short timeframe.[103]

In addition to the introduction of point mutations that increase the thermal stability of the receptor in detergent, it is very common to truncate and/or delete flexible loops or flexible regions to reduce the intrinsic dynamism of GPCRs. For instance, many of the GPCR crystal structures have **truncations** in the N-terminus.[104]

Finally, obtention of crystal structures of active GPCRs proved more challenging, as this conformation shows lower stability. As previously described, mutagenesis can be applied to produce constitutively active receptors, where the active conformation is stabilized and can crystallize. A more physiological approach to produce a stabilized GPCR in an active conformation is to couple it with a native signaling partner (G-proteins or arrestins). However, the interactions that build the active complex are very sensitive and thus, difficult to crystallize. In consequence, alternative approaches have been developed, such as the use of **crystallization chaperones** to form stable active complexes and/or to trap the receptor in a specific conformation.

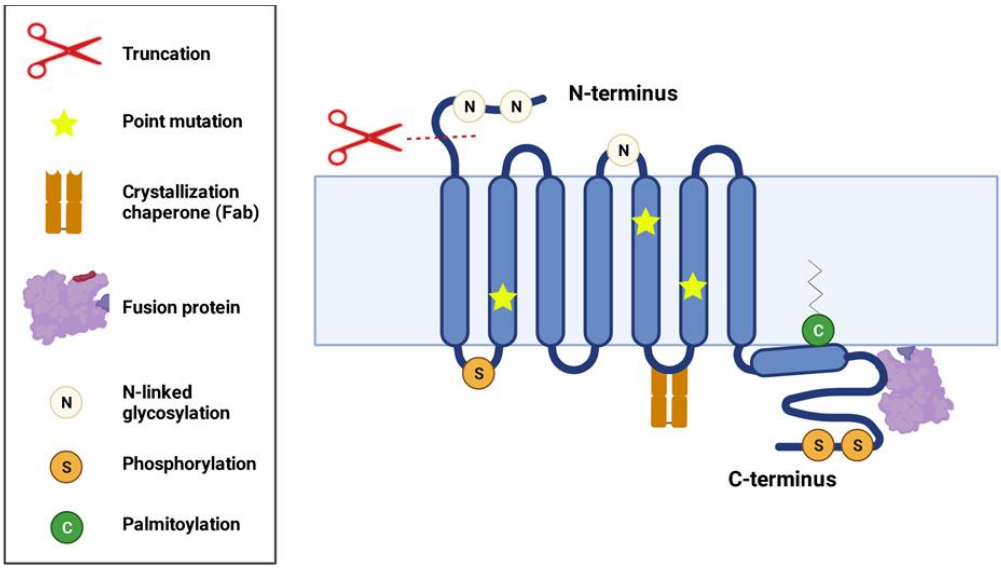

Figure 24. Schematic representation of protein engineering approaches for GPCR crystallography. All the distinct modifications available to reduce GPCR flexibility and/or stabilize a particular receptor conformation are schematically represented. Created with BioRender.

Monoclonal antibody fragments (Fabs) have been used in the crystallization of several active GPCRs, including β_2-AR.[105] Fabs bind to a specific epitope of the target protein and create an extended hydrophobic area that facilitates crystal contacts; moreover, they usually bind to an epitope present in the flexible ICL3 and contribute to reduce the flexibility of the receptor.

Another established type of crystallization chaperones are nanobodies, which can mimic G proteins and stabilize the active conformation of the receptor.[106] Active structures of β_2-AR and M2 muscarinic acetylcholine receptor were solved using nanobodies.[107,108] It is worth noting that the use of crystallization chaperones has also allowed crystallization of GPCRs in an inactive conformation.

2.1.2 Chimeric constructs

One of the most successful approaches used in protein engineering is the creation of chimeric constructs in which the GPCRs are genetically **fused to a soluble protein**. Soluble proteins are generally added in replacement of an intracellular loop (commonly ICL3 or ICL2) or as a tag in the N-terminus and favor the formation of crystal contacts.[109,110] The most commonly used fusion proteins are the T4 Lysozyme (T4L)[58] and a thermostabilized apocytochrome (b_{562}RIL).[111] However, it has to be noted that introducing these large modifications in the studied receptor can perturb the disposition of the structural component, which has raised concerns about the reliability and accuracy of this approach. [98]

2.1.3 Heterogeneity from post-translational modifications

The selection of an expressing system has important effects on the characteristics of the produced protein. This occurs because of the maturation and folding pathways that follow protein biosynthesis, where a number of post-translational modifications (PTMs) are introduced. There are a wide number of PTMs, which differ in the different expressing organisms. It is known that they exert important roles in cell signaling processes. Nevertheless, the high heterogeneity of PTMs in the proteins produced by a single expressing system and the fact that some of the modifications also introduce flexibility in the receptor constitutes an additional difficulty in GPCR crystallography. For this reason, some PTMs are removed during the protein purification process, prior to crystallization. The most commonly removed PTMs for crystallization purposes, either by mutagenesis or by chemical inhibition of the responsible enzymes, are glycosylation, phosphorylation and palmitoylation.[98,100]

2.2 GPCR expression: limitations and optimal systems

In order to produce the protein crystals required for X-Ray crystallography, high amounts of the protein of interest have to be produced. This also constituted a major problem in the early days of GPCR crystallography, considering that the majority of these receptors present low expression in endogenous systems. In order to produce sufficient amounts of the target receptor, several recombinant protein hosts were tested, including *E. coli*, yeast, mammalian cells and insect cells. Due to the low relevance of yeast and bacterial cells as protein expressing systems in the present thesis, they will not be reviewed in this section. In addition, several approaches can be used to evaluate and quantify receptor expression levels. Ligand-binding assays using a fluorescent ligand are extensively used to assess protein expression. Surface plasmon resonance can also be used to perform this type of assays in the absence of a fluorescent ligand for the target receptor.[112] An alternative approach that simplifies the analysis of protein expression consists on the introduction of fluorescent fusion tags, such as Green Fluorescent Protein (GFP), in the protein sequence. Fluorescent tags allow for a simple and direct measure of protein expression in whole cells.[113]

2.2.1 Mammalian cells

Mammalian cells have been commonly used as an expressing system in GPCR crystallography. Overexpression in this type of cells provides good amounts of functional protein, which constitutes its main advantage. To express the target receptor in mammalian cells, the gene that encodes for the protein of interest has to be inserted into the host expressing system. This process, generally named **transfection**, can be conducted through viral methods (known as transduction) or non-viral methods. There are several non-viral transfection methods but the most common are chemically based. In these methods, chemicals are used to form a complex with plasmid DNA that allow its insertion into cells. In addition, there are two approaches for protein expression in mammalian cells: **transient and stable expression** (Figure 25).[114]

- **Transient expression:** the gene of interest does not integrate into the genome and thus, it will not be transferred to daughter cells. Therefore, transiently transfected cells only express the protein of interest for a short amount of time. Transient expressing systems present high heterogeneity, are difficult to scale up and are associated with higher costs. For this reason, this approach is generally used during the initial screening processes.

- **Stable expression:** the gene of interest gets integrated into the genome and thus, it will be transferred to daughter cells. In consequence, these cells will continuously express the receptor of interest. In order to obtain a stably expressing cell line, the plasmid that contains the protein gene also incorporates an antibiotic resistance gene. Cells that have integrated the DNA will survive to selection with antibiotic. Additionally, stable cell lines can be polyclonal or monoclonal. In monoclonal cell lines, where all the cells are identical, protein production is less heterogeneous. The main drawback for this approach is that the process for the generation of stable cell lines is long and tedious.[115]

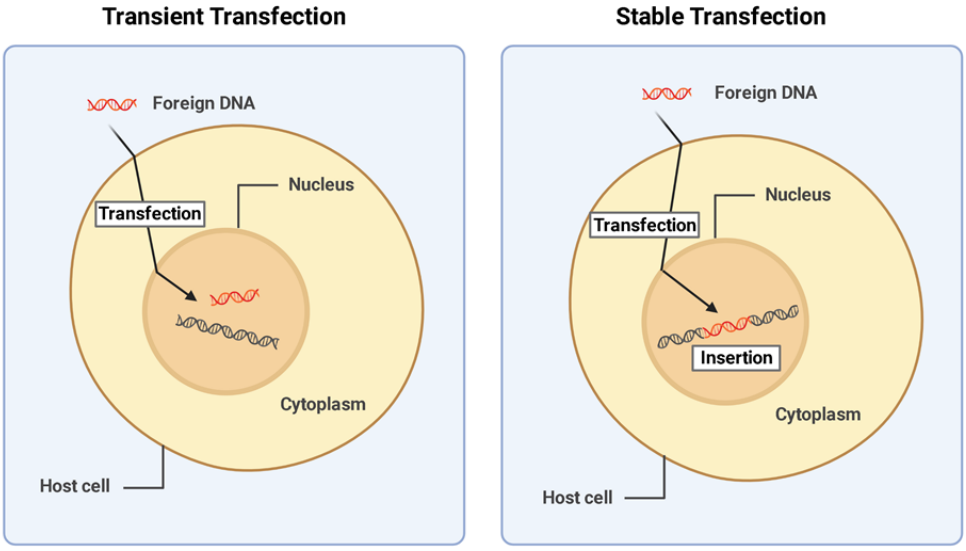

Figure 25. Different types of cellular transfection. Left panel illustrates that, in transient transfections, the gene of interest is not inserted within the cellular genome. Right panel shows insertion of the gene of interest into the cellular genome, that upon selection produces a stable cell line. Created with BioRender.

In addition, protein expression can be constitutive or inducible, depending on the promoter that has been selected. For instance, if protein expression leads to cellular toxicity, it will be

necessary to use an inducible plasmid. High levels of GPCR expression have been obtained in tetracycline-inducible expression systems in mammalian cells. Nevertheless, the use of these cells to obtain crystal structures is barely described.[116]

2.2.2 Insect cells

Insect cells constitute the main expression system used in GPCR crystallographic studies. In fact, most of the membrane receptors that have been crystalized were produced in insect cells. There are different types of insect cells used for protein production in structural studies; protein expression can differ significantly among the distinct cell lines, and a cell line screening is recommended to select the optimal system for the expression of the target GPCR. Among the available cell lines, *Spodoptera frugiperda Sf9* cells are extensively used. Receptor expression in this type of cells is based on infection with a lytic baculovirus that incorporated the GPCR gene. Baculovirus-mediated expression in insect cells occurs in the late state of cellular infection by the virus, where cells highly express the GPCR receptor. There are two main approaches that enable the preparation of the baculovirus containing the GPCR gene. The extensively used bac-to-bac system (Invitrogen) is based on the site-specific transposition of the gene of interest from a donor plasmid into the parent baculovirus shuttle present in DH10Bac *E.Coli* (Figure 26).[117] An expression bacmid is formed in bacterial cells that have been successfully transformed, and insertion of the gene of interest disrupts the lacZ sequence. This allows the detection of bacterial colonies with recombinant bacmid via the blue/white selection process. Recombinant bacmid is then isolated and used to transfect insect cells (*Sf9* and *Sf21*), that produce the baculovirus containing the gene of interest (named V0). Recombinant virus (V0) is subsequently amplified in successive rounds of infections and finally used to produce the protein of interest through infection of high amounts of insect cells. [116]

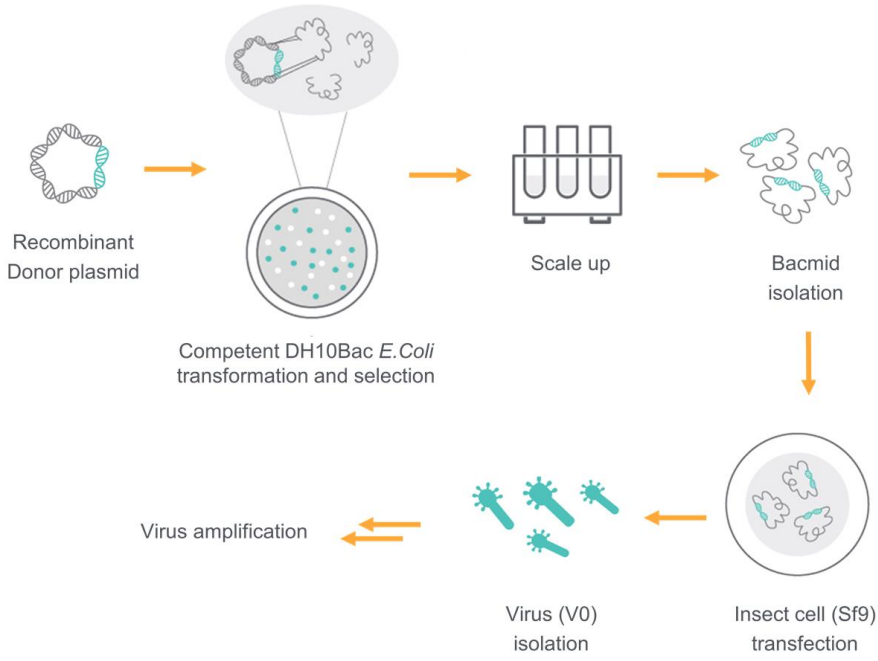

Figure 26. Schematic description of baculovirus production via the Bac-to-Bac system (Invitrogen). The produced baculovirus contains the gene of interest and can infect insect cells, which then express the protein of interest. Created with BioRender.

This procedure, as expression in mammalian cells, can be very time consuming and expensive. Additionally, one of the main drawbacks of the using insect cells to produce high amounts of GPCRs is the presence of a higher levels of misfolded protein (non-functional) compared to the proportion described in mammalian cells. Nevertheless, this system is very well established in structural biology and has enabled the production of crystal structures for a wide variety of GPCRs.[118–121]

2.3 Protein purification

In order to perform structural studies, GPCRs have to be extracted from the biological membranes, purified and treated with the appropriate enzymes to eliminate protein tags or post-translational modifications. Figure 27 depicts a schematic flowchart summarizing the general steps to produce purified protein for crystallization purposes once it has been expressed in cells.

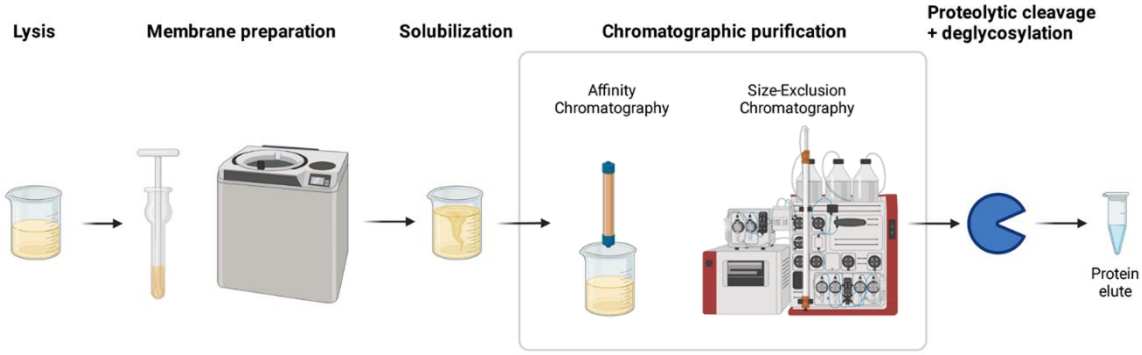

Figure 27. Flowchart of the general steps in protein purification processes for crystallographic studies. Created with BioRender.

In the present sub-section, the different steps listed in the flowchart (Figure 27), as well as the variety of options within each part of the process, will be described.

2.3.1 Cellular disruption

Firstly, cells must be disrupted, prior to the extraction of the receptor from the membranes. Both insect and mammalian cells are relatively easy to break open. Cellular membranes explode due to the osmotic pressure when treated with a hypotonic buffer. Following the lysis, it is very common to perform a membrane preparation, where most cytoplasmic proteins are removed by performing washing cycles with high and low salt buffers. During this step, it is very important to use protease inhibitors to prevent the proteolytic cleavage digestion of the target GPCR.[116]

2.3.2 Solubilization

After cellular disruption, the membrane protein has to be solubilized in detergent. Detergents are amphiphilic molecules, chemically constituted by a polar head and a hydrophobic tail. At high concentrations, detergents aggregate to form water-soluble micelles. The concentration at which micelles start to form is known as Critical Micelle Concentration (CMC). In micelles, hydrophilic heads are exposed at the surface while hydrophobic tails are buried in its interior. This type of detergent aggregates, have many interesting properties and can be used to extract

GPCRs from the membranes. At high concentrations, micelles can break the membranes and form mixed micelles containing membrane proteins and lipids. The resulting protein-detergent complex can be imagined as a belt of detergent molecules where the membrane protein is embedded, co-solubilized with membrane lipids that assist receptor stability.[116] There are many detergents that can be used in crystallographic studies, and a screening is usually recommended to select the optimal one. However, DDM (concentrations: 0.5-1%) and DM (concentrations: 1.5-2%[122]) are extensively used in the literature for the solubilization of non-rhodopsin GPCRs. Moreover, adding a cholesterol derivative (CHS) to the solubilization mixture has proven to further stabilize some GPCRs in the detergent solutions.[123] Finally and considering that GPCR stability is reduced at the high detergent concentrations used for solubilization, a gradual concentration decrease is usually applied in the following purification steps.

2.3.3 Chromatographic purification

After the solubilization step, the protein of interest must be thoroughly purified in order to remove non-desired components from the solubilization mixture. Usually, a protein purification protocol contains one or more chromatographic steps, that enable the removal of non-desired molecules according to their different properties (size, charge, etc.). Nevertheless, the most common chromatographic methods for protein production in crystallography are **affinity chromatography** and **size exclusion chromatography**.

Affinity Chromatography (AC)

This technique takes advantage of the highly specific binding interactions between two molecules. These interactions, which are generally reversible, are used for purification by immobilizing an affinity ligand into a matrix (stationary phase) while the target protein is in the mobile phase. The mixture that has to be purified is applied to the stationary phase where only target protein will bind. Washing the stationary phase will remove all non-bound molecules, and only bound protein will remain in the resin. Finally, the protein of interest is eluted from the column through the application of a high outcompeting ligand concentration (Figure 28). [124]

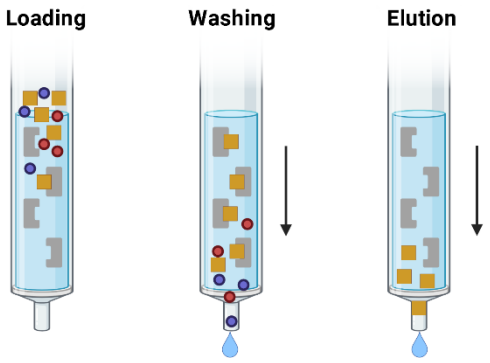

Figure 28. Basis of affinity chromatography (AC). The protein mixture is loaded to the resin, which only binds the target protein. Non-bound proteins are then washed away, and finally purified protein is eluted from the resin. Created with BioRender.

There are many types of biological interactions that can be exploited in order to purify the protein of interest by affinity chromatography (AC). However, in protein purification for crystallographic studies, proteins have been genetically modified and present affinity tags in

order to assist their purification by AC. Different tags that can be introduced in recombinant proteins; some of the most commonly used affinity tags and their characteristics are summarized in Table 6. Selecting the optimal tags and affinity ligands to purify the protein of interest requires knowing the nature of the receptor and the interactions it can form.[116,125]

Table 6. Characteristics of affinity tags.[124]

Tag	Size (aa)	Matrix	Elution	Properties
His-tag	6-10	Ni^{2+}-NTA	Imidazole, low pH	Binding to immobilized metals in native or denaturing conditions
FLAG	8	mAb-Matrix	EDTA, Flag peptide	Specific binding to FLAG monoclonal antibodies. Calcium dependent
Strep tag	8	Strep-Sepharose	Desthiobiotin	High specificity and affinity towards the protein streptavidin
Glutathione S-Transferase (GST)	201	GST-Sepharose	Reduced Glutathione	GST-Ab affinity

Size-Exclusion Chromatography (SEC)

This chromatographic method separates the components of a mixture according to their size (Figure 29A). The SEC resin is composed by a porous matrix of stable spherical particles that minimally adsorb biomolecules. Molecules larger than the pores of the matrix do not interact with it and are eluted together, directly from the column in the so-called void peak. Molecules that interact with the porous matrix are separated and eluted in order of decreasing size. The smaller the molecule, the longer it is retained in the matrix (Figure 29B).

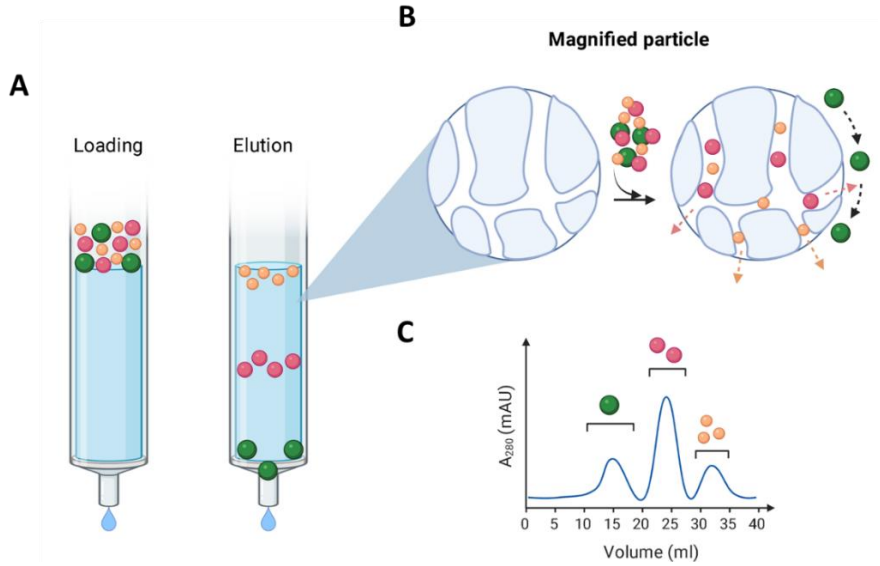

Figure 29. Basis of size-exclusion chromatography (SEC). (A) Schematic description of SEC purification; loaded molecules are separated according to their size in decreasing order. (B) Zoom of the porous matrix that forms the SEC resin; smaller molecules get retained in the porous particles for longer times and are eluted later. (C) SEC results appear as an elution chromatogram; absorbance is represented in front of eluted volume. Created with BioRender.

Results from SEC are generally represented as an elution chromatogram, where absorbance and/or fluorescence are represented for the increasing elution volumes (Figure 29C). This purification method is often considered a polishing step, and is generally performed at the end, after proteolytic cleavage and deglycosylation processes.[116]

2.3.4 Proteolytic cleavage

Affinity tags are extremely useful for protein purification. However, these tags are highly flexible and can prevent crystallization. In addition, the highly flexible N-terminus and C-terminus might be necessary for functional expression, thus precluding the truncation of these domains in certain cases. Therefore, as part of the purification procedures for crystallographic studies, these flexible parts can be removed by proteolytic cleavage.[126] There are many different proteases that can be used; however, TEV and HRV 3C are highly specific and widely used.[127] In fact, their use has been described for the proteolytic cleavage of affinity tags, fusion partners[128] and N-terminus domains in many GPCR constructs[105,129].

2.3.5 Deglycosylation

As it has been previously described, N-linked glycosylation of membrane proteins can be essential for the proper folding and function of the receptor. Nevertheless, their intrinsic flexibility and heterogeneity can hamper the formation of crystals. For this reason, glycosylation sites that are not relevant for GPCR folding are usually removed by mutagenesis or truncation in the protein engineered construct. Otherwise, GPCRs produced in insect cells are generally deglycosylated at the end of the purification by peptide N-glucosidase F (PNGase F), an amidase that removes this type of PTMs from asparagine residues.[116]

2.3.6 Purity analysis

The last step of every purification protocol is the purity analysis of the isolated protein, which is generally performed by polyacrylamide gel electrophoresis (SDS-PAGE). This electrophoretic technique enables protein separation according to their size only, as sodium dodecyl sulphate (SDS) is used to remove structural and charge effects. SDS is a detergent that denaturizes proteins and homogenizes their negative charge. Therefore, when proteins migrate through the polyacrylamide matrix, smaller proteins move faster towards the positively charged end.[116]

2.3.7 Protein characterization

Prior to crystallization, the recombinant protein has to be characterized to determine its thermal stability in the apo state, but it is especially important to assess ligand-induced thermostabilization effects. This is particularly relevant considering that, so far, most GPCRs have to be crystallized bound to a ligand that stabilizes the receptor in a specific conformation. For this reason, selecting an adequate ligand is crucial. Thermal shift assays (TSA) are commonly used for this purpose in the structural biology field, as they detect changes in protein stability through changes in the thermal denaturization temperature. At increasing temperatures, proteins start to unfold until they are denaturized (completely unfold). TSA assays measure protein unfolding through the addition of a ligand that fluoresces upon protein binding. More molecules of ligand can bind to the protein when it is denaturized, and thus increasing fluorescence values are obtained at higher temperatures (Figure 30A). Different ligands can be

used in TSA, which establish different types of binding interactions with the analyzed protein. For instance, *N*-[4-(7-diethylamino-4-methyl-3-coumarinyl)phenyl]maleimide (CPM) is a compound that only fluoresces after reacting with a nucleophile, such as cysteine side chains of proteins. Fluorescence values are represented as a function of the temperature and a melting curve is obtained. The melting temperature (Tm) is the temperature at which 50% of the protein is denaturized (Figure 30A). Addition of a ligand that stabilizes the protein upon binding triggers a shift in the melting curve and an increase in the melting temperature (Figure 30B).[130]

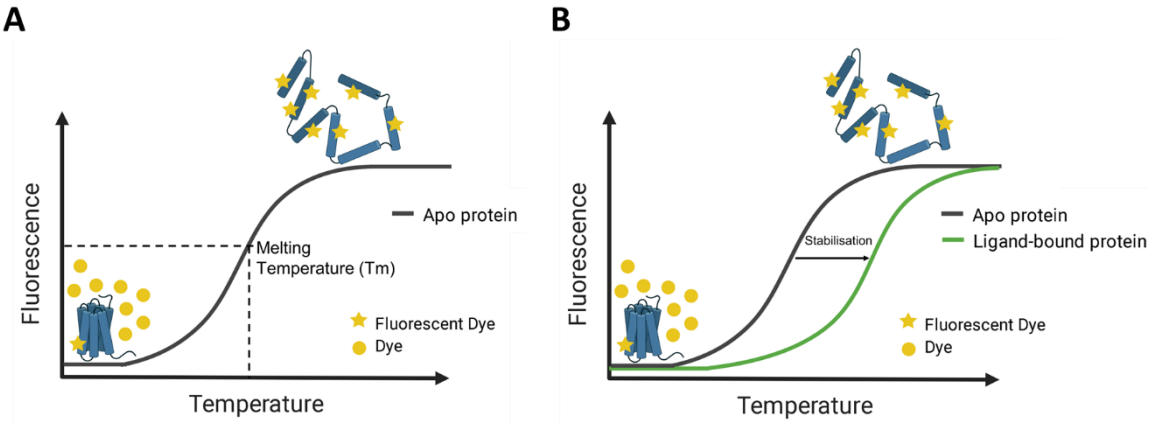

Figure 30. Results from Thermal Shift Assays (TSA). (A) At increasing temperatures, protein unfolds and fluorescence increases. The inflection point of the curve corresponds to the melting temperature (Tm) (B) Addition of a thermostabilizing ligand shifts the melting curve and increases the Tm, as higher temperatures are required to denaturize the studied protein. Created with BioRender.

2.4 GPCR crystallization

Once the protein has been appropriately purified and characterized, it has to be crystallized. The formation of protein crystals requires, among other things, high protein densities (10-60 mg/mL). Consequently, the purified protein has to be concentrated, which is generally achieved using protein concentrators.

Different crystallization techniques can be employed; however, the majority of GPCR crystal structures have been obtained using lipidic cubic phase (LCP) crystallization. In this approach the receptor is crystallized in a lipidic bilayer, which mimics cellular membranes and improves receptor stability. This water/lipid method uses the solubilized protein as the aqueous phase, that is then mixed with a monoacylglycerol (MAG) to create a 3D-lipid bilayer that incorporates the membrane proteins. The resulting phase from the protein/lipid mixture highly depends on the ratio of the two mixed components as well as the temperature (Figure 31). For this reason, to obtain the LCP mesophase for crystallization it is very important to strictly control these factors.[131] The LCP phase is a bicontinuous lipidic bilayer with isolated water channels, which provides a native-like environment where the membrane protein is reconstituted.

Once the protein-containing LCP phase has been formed, crystallization trials are set up to determine the optimal crystallization conditions. There are different approaches that can be used to set up crystallization trials. A very common method is the use of glass or plastic sandwiches. In this approach, LCP droplets are added to each of the 96-wells of a crystallization

plate. On top of the LCP drop, precipitant solutions are then dispensed, which are different in each of the wells to allow screening of the best crystallization conditions. Finally, a glass/plastic coverslip is used to seal the crystallization plate forming a sandwich, that has to be kept at a stable temperature for several days to allow crystal growth. However, crystals obtained by LCP crystallization tend to be small and highly sensitive to radiation damage, which has difficulted the collection of high-resolution data through classical X-Ray crystallography. Nevertheless, this challenge has been addressed with the recent development of X-Ray free electron lasers (XFELs). XFELs can generate ultrafast pulses of X-Rays that enable high quality data collection from microcrystals before radiation damage appears.[98]

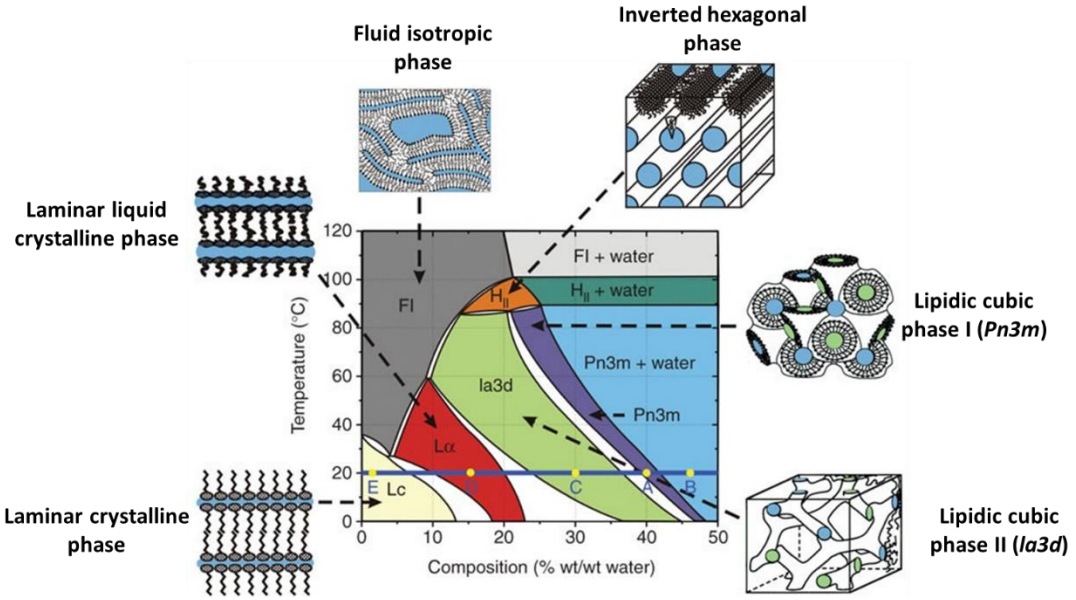

Figure 31. Phase diagram of the monoolein/water system. The different mesophases that can be obtained from different component ratios at different temperatures have been represented. Blue colored areas indicate water disposition in the 3D lipidic structures. Adapted from Caffrey (2015).

2.5 X-ray crystallography and structure determination

In the previous sections we have outlined the different methods to produce and purify stabilized GPCRs, as well as the best options to grow crystals for X-Ray crystallography. In this section the basis of X-Ray crystallography and how it allows structural determination will be revised.

Briefly, X-ray crystallography is based in the principle that a crystalline sample will diffract a beam of X-rays into different directions creating a specific diffraction pattern that is monitored. An analysis of the angles and intensities of the diffracted beams, leads to the creation of a tridimensional picture of electron density distribution. Using this electron density map, the crystallographer builds a 3D model that optimally fits the protein atoms to the detected electron densities (Figure 32). The main limitation of classical X-ray crystallography is that it requires big crystals with good diffraction for high-quality data collection. This is due to the radiation damage induced by the application of multiple X-ray beams to a single crystal positioned with different orientations, which is necessary to collect 3D electron density maps. If crystals are too small the high levels of crystal damage caused by X-rays preclude the collection of good quality data.

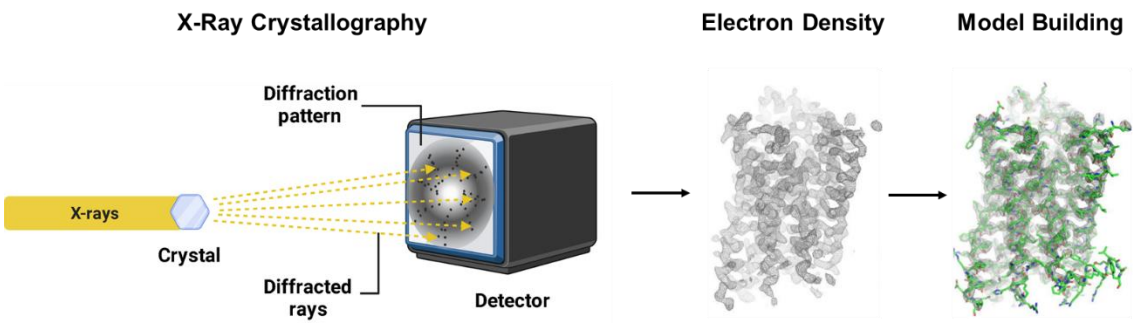

Figure 32. Steps for structural determination of proteins by X-Ray crystallography. Firstly, the protein crystal is shot with X-rays. Radiation that impacts the crystal gets diffracted forming a particular pattern that gets monitored by a detector. Using computational methods, an electron density map can be extracted from the diffraction pattern. Finally, a model that appropriately fits with the electron density map is built, providing a solved crystal structure. Created with BioRender.

Crystallization of membrane proteins frequently yields small, weakly diffracting crystals, which are not suitable for classic synchrotron X-ray crystallography. In this context, serial X-ray crystallography was developed, which combines diffraction data from many microcrystals, instead of using only one, or several big crystals. In **serial Femtosecond Crystallography** (SFX), a continuous stream containing crystals of a variety of sizes is jetted into de XFEL beam. This allows to collect a dataset that contains hundreds of thousands of diffraction patterns. Posterior analysis of the data obtained from many different crystals in all possible orientations allows to generate a 3D model of the studied receptor. Structural results obtained from SFX for a number of GPCRs are in good agreement with data obtained from conventional X-ray crystallography, which has validated this novel methodology. The main problem with this approach is the scarcity of XFEL sources. Recent advances have allowed the development of **Serial Microsecond Crystallography** (SMX), in which microcrystals are jetted into the synchrotron X-ray beam. In both techniques, experiments can be conducted at room temperature, contrarily to the low temperatures required in conventional X-ray crystallography.[98]

Moreover, these novel techniques have evolved to a variation called **time-resolved serial X-ray crystallography**, which allows the study of protein dynamics on a timescale from femtoseconds to milliseconds. Time-resolved serial X-ray crystallography uses an optical pump laser synchronized with X-ray pulses, generated either by a synchrotron or a free-electron laser (FEL), to obtain X-ray diffraction snapshots from photoactivated states of proteins.[132] Single-crystal X-ray diffraction images with partial reflections are collected from a set of randomly oriented crystals. An increasing time delay between the pump laser and the probing X-ray pulse allows recording of sequential stages following the initial activation. Collection of enough X-ray snapshots with different time delays enables the assembly of complete molecular movies of protein dynamics.[133–137] The potential of XFELs on time-resolved crystallographic studies has been demonstrated in intrinsically light-responsive proteins, where the laser source triggers the process under study.[138] Time-resolved X-ray crystallography is only a few years old but considering past successes, it might become a game changer with respect to our understanding of protein dynamics.

3 Photo-control of biological systems

3.1 Light-technologies: an overview

As described in previous sections, GPCRs are a large family of receptors involved in many important physiological functions. These membrane proteins respond to external stimuli and trigger signaling transduction via different effectors. Even though research efforts have facilitated evidence for the mechanisms and function of this large family of proteins, their intricated and complex behavior still present many unanswered questions. In addition, GPCRs are classical drug targets, with up to a third of the currently approved drugs modulating their activity.[139] Nevertheless, clinical candidates, and even approved drugs targeting GPCRs display several limitations that hamper their pharmacological use. For instance, the main problems with most molecules are the low selectivity, sub-optimal pharmacokinetic properties and low efficacies. Many of these obstacles arise from the lack of knowledge on receptor function and its role in the pathology to be treated. Additionally, GPCR pharmacology has classically been tackled from a mono-dimensional approach, which might be inefficient taking into account the complexity of the signaling pathways that can be involved in a particular disease.

In order to overcome the described limitations, research has put the focus on the development of novel molecular tools that allow the dynamic control of GPCR activity. Achieving a fine and precise control of the receptor opens up many research and therapeutic applications, which might contribute to unravel the complex mechanisms underlying GPCR signaling. In this context, the development of molecules and techniques that are regulated with light have increasingly gained popularity in the study of GPCRs. Light constitutes a powerful tool to study biological systems, as it can be applied with spatial and temporal precision, and it has low or negligible toxicity in the visible range. Three different light-technologies to control biological function have been developed: Optogenetics, Photopharmacology and Optogenetics pharmacology.

Briefly, optogenetics transforms light-insensitive proteins into light-responsive proteins by genetic manipulation methods. Particularly, light-sensitive proteins, such as opsins, are combined with the studied receptor, which renders it light-sensitive. This methodology has been widely used in the last decade, revolutionizing experimental neurobiology and physiology.[140,141] However, the need for genetic manipulation clearly limits the therapeutic applicability of this successful technique. On the other hand, photopharmacology uses light-sensitive molecules that enable the modulation of target receptors with light. In this approach, endogenous receptors are converted into light-sensitive proteins by using carefully designed photochromic ligands, which can be freely-diffusible or tethered to the native protein.[142–145] Finally, optogenetics pharmacology (also known as tethered pharmacology) generally uses genetically modified proteins that allow the formation of a covalent bond with a photochromic ligand. In this approach, the photoswitchable tethered ligand (PTL) reacts and forms a covalent bond with a cysteine residue introduced by mutagenesis near the binding site. Consequently, the light-sensitive ligand gets irreversibly tethered to the target protein, which enables an efficient receptor control with light. However, its therapeutic applicability is also limited, as described for optogenetics.[146] Several examples of tethered pharmacology in GPCRs have been described in the literature,[147–150] highlighting the potential of these reversible light-sensitive tools.

3.2 Photopharmacology

Therefore, photopharmacology offers a clear advantage compared to the other two light-technologies, as it does not require genetic modification and can be applied to wild type organisms. In addition, photopharmacology requires the development of a small molecule with light sensitive properties, which can be validated and approved through standard drug development procedures. Consequently, this is the only light-sensitive approach that has true therapeutic potential, which makes it very appealing. Ideally, a photopharmacological drug would be administered to the patient in an inactive form and get distributed throughout the organism normally, via ADME (absorption, distribution, metabolism and excretion) processes. Once the molecule has reached the area of interest, light would be applied with spatio-temporal precision, according to the medical needs. Light application would trigger a conformational change in the photochromic ligand, rendering it bioactive. The active molecule could then bind to the target receptor and exert the desired biological effect in a precise and localized manner (Figure 33). This would give access to drugs with reduced side effects and higher efficiency. Nevertheless, no light-sensitive molecules that have reached the clinical state yet. Of note, the use of light as a tool in clinical applications has proved to be extremely useful in other approaches such as Photodynamic Therapy (PDT). This technique, that uses photosensitizer chemical substances to induce light-triggered cellular death, has been clinically used for the treatment of various skin conditions and different types of cancer.[151]

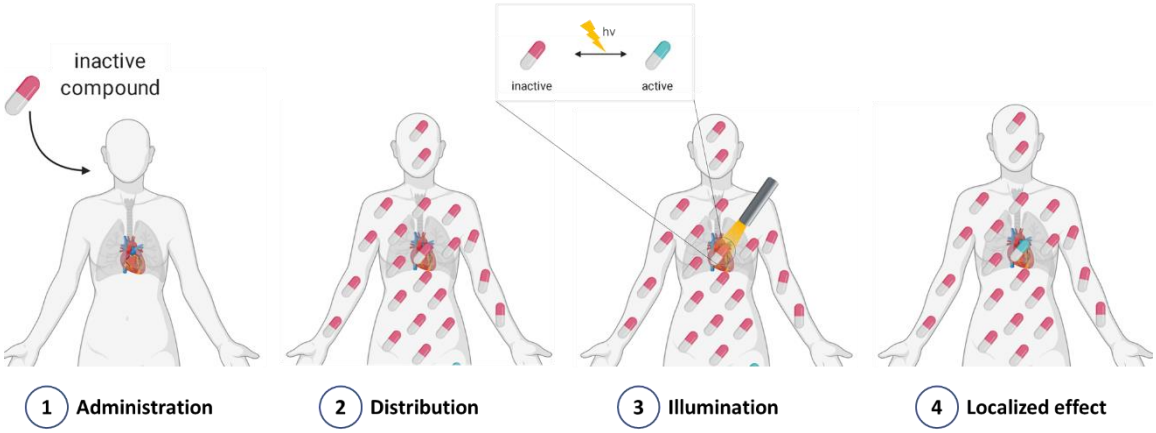

Figure 33. Therapeutic potential of photopharmacology. Ideally, the photochromic ligand would be precisely activated in the area of interest through light application. Created with BioRender.

Photopharmacology has been widely applied for research purposes, including the study of GPCRs. Many photochromic ligands have been described in the literature allowing the optical control of a wide variety of GPCRs. These studies have provided valuable information on the mechanisms of receptor function and activation, the importance of receptor localization in its function and the relevance of the temporal dimension, among others. Moreover, many of the developed ligands have also been used for the optical control of physiological functions in living animals.[152]

Mainly, two different chemical strategies have been used in photopharmacology to design diffusible molecules that allow spatiotemporal localization of the drug action. The first approach, named compound caging, produces molecules that can be activated in a non-reversible manner

through the application of light. The second strategy provides molecules that can be reversibly interconverted between two states, which display different pharmacological properties.

3.2.1 Irreversible strategies: caged ligands

The caging strategy is an approach that produces irreversible light-sensitive compounds. This technique allows the transformation of biologically active molecules into inactive compounds through the attachment of a photolabile protecting group (PPG) to their chemical structure. Photoprotecting groups can be irreversibly cleaved upon illumination, thus locally releasing the drug that subsequently acts following conventional pharmacology patterns (Figure 34). The fact that illumination allows a controlled release of an approved drug or a fully validated ligand, can improve its efficacy and reduce possible side effects. Therefore, caged compounds can constitute a useful tool to study biological systems, as it enables a local and controlled release of active molecules with light. However, the activity of caged compounds is not reversible, which limits the temporal regulation of the bioactive molecule once released.[153,154]

One of the advantages of the caging strategy is that it usually requires a simple molecular design, that includes the selection of an appropriate PPG and its optimal emplacement. In order to select a PPG for biological studies there are several considerations that must be taken into account. Firstly, the addition of the PPG should render the active compound inactive in the studied biological system. Moreover, the photolytic release of the bioactive compound should be relatively fast and occur at non-hazardous wavelengths with good uncaging yields. Finally, the subproducts obtained from the photolytic reaction should be inert in the studied system to avoid undesired interferences.[155]

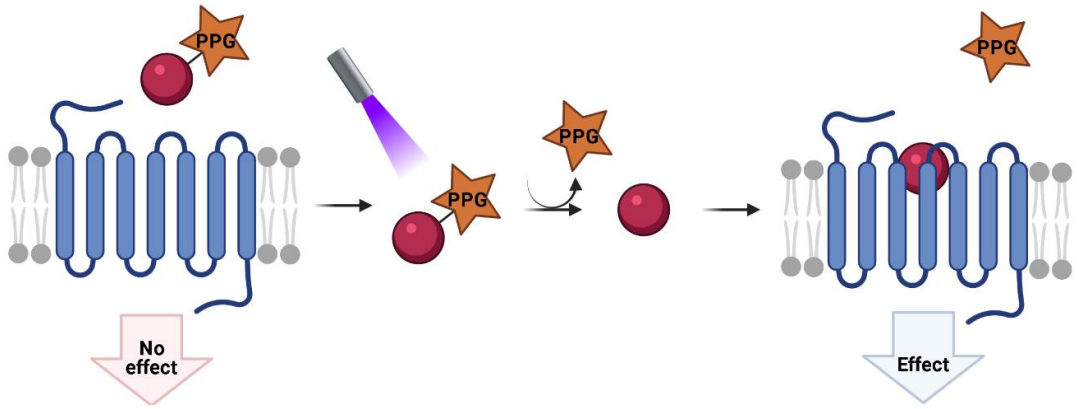

Figure 34. Schematic representation of the uncaging strategy. Initially, the caged ligand is inactive due to covalent attachment of a photoprotecting group. Illumination releases the bioactive molecule, which can bind to the target receptor and exert the desired biological effect. Created with BioRender.

Photoprotecting groups

One of the most important steps for a successful application of the caging strategy is the selection of an appropriate photocleavable protecting group. Since the development of this approach in the late seventies, many photoactivatable molecules and systems have been developed for different applications with improved photolytic properties.

Several parameters are usually evaluated to define the properties of PPG: the maximum absorbance wavelength (λ_{max}), the quantum yield of uncaging (ϕ_u) and the molar absorption coefficient (ε). λ_{max} is the wavelength at which the molecule will absorb a maximal number of photons, thus constituting the optimal wavelength for chromophore excitation and uncaging. On the other hand, the quantum yield is a measure of the uncaging efficiency, and the molar absorption coefficient measures the molecular absorption ability for a particular wavelength.

Moreover, it is worth noticing that uncaging is triggered by excitation of the chromophore present in the photocleavable protecting group. Chromophore excitation in some of the PPG can occur via two different pathways. In general, the cleavable moiety is excited after absorbing one photon of the appropriate energy. This process, known as one photon excitation (OPE), can be very efficient but has limited spatial localization (Figure 35). On the other hand, molecules can be excited to S_1 through the absorption of two consecutive photons in a non-linear process. Two photon absorption (TPA) involves a short-lived virtual state that corresponds to approximately half the energy of the final excited state (S_1). Uncaging via TPA requires low energy photons (IR area) and allows for high spatial localization (Figure 35). Nevertheless, this process has very low efficiency and requires the application of high photonic intensities, such as laser beams, thus limiting the application of TPA for uncaging processes.[156,157]

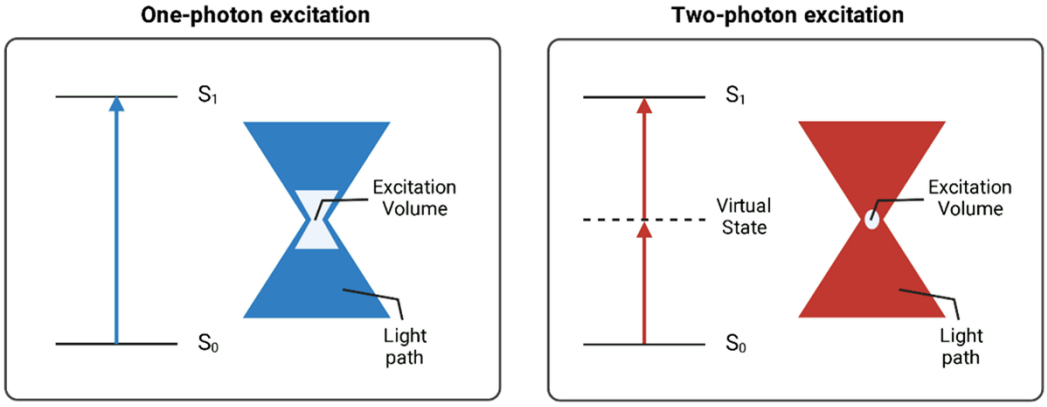

Figure 35. One-photon vs two-photon excitation of chromophores. Left panel shows the main properties of one-photon excitation (OPE), where the excited state S_1 is achieved after absorption of one photon of the appropriate wavelength. Right panel shows the properties of two-photon excitation (TPE), that requires consecutive absorption of two low energy photons. The excitation volume is much lower in TPE, thus allowing for a highly localized excitation of the target chromophore. Created with BioRender.

Finally, caging moieties can be either organic or metal-containing. However, this section will only review the most common organic photoreleasing groups: *o*-nitrobenzyl and coumarin PPG. In addition, the recent development of red-shifted organic photocleavable groups will also be briefly revised.

O-Nitrobenzyls

O-Nitrobenzyls (*o*NB) constitute a family of caging moieties that have been widely used for many applications since their discovery in the sixties. These photocleavable groups have a well-stablished synthetic procedure and can be efficiently uncaged through the application of UV light, thus becoming a first line option for the caging strategy. Nonetheless, the photolytic

reaction of *o*NB photocages requires the application highly energetic wavelengths, which can be cytotoxic. In consequence, synthetic efforts have been applied for the development of *o*NB that can be cleaved with visible light. Caging groups showing considerable bathochromic shifts have been reported, such as **24**, with maximum absorptions reaching the high UV region. However, limited examples of visible light cleavable *o*NB have been described in the literature. Figure 36 depicts the chemical structures of the most commonly used *o*NB groups. Additionally, *o*-nitrobenzyl protecting groups can also be photolyzed through a two-photon absorption process, which allows the use of near-IR wavelengths.[158]

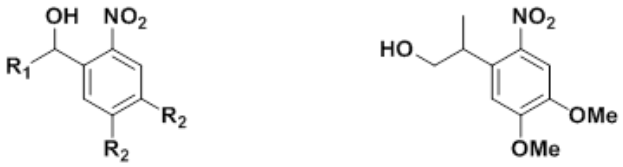

23a: R_1 = H R_2 = H (NB-OH)
23b: R_1 = COOH R_2 = H (CNB-OH)
23c: R_1 = Me R_2 = H (NPE-OH)
23d: R_1 = H R_2 = OMe (DMNB-OH)
23e: R_1 = Me R_2 = OMe (DMNPE-OH)

24

Figure 36. Chemical structures of some of the most commonly used *o*-nitrobenzyl PPG.

The photorelease mechanism of this family of cages is well established (Scheme 1). Excitation of the ground state of ***o*NB** is followed by intramolecular hydrogen removal from the nitro group, yielding an aci-nitro intermediate (**26**), that exists in equilibrium between two differently protonated forms (**26 a,b**). Irreversible cyclization of intermediate **26** leads to benzisoxazoline (**27**). Subsequent ring-opening produces intermediate (**28**) that is then hydrolyzed to release the leaving group (LG), forming an *o*-nitrosobenzaldehyde byproduct (**29**).[159,160]

Scheme 1. Proposed photolytic mechanism of *o*-nitrobenzyl PPG.

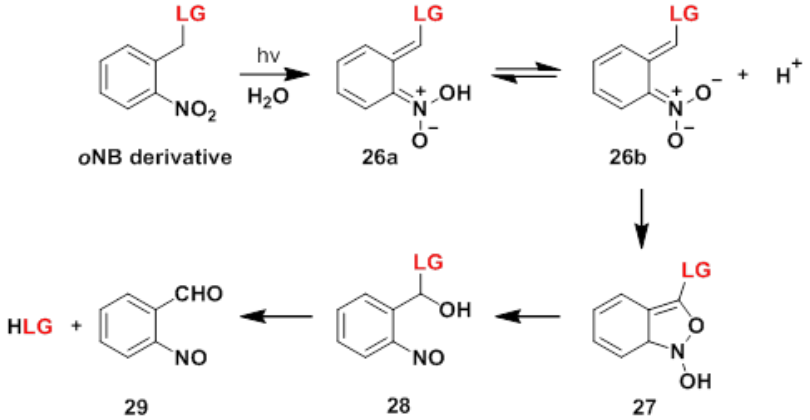

O-Nitrobenzyl groups have been used to photorelease many functional groups, including amines, carboxylic acids, thiols and alcohol. In addition, many photoactivatable molecules targeting GPCRs have been developed through the attachment of *o*NB to a known bioactive molecule, some of which are summarized in Table 7.

Table 7. Caged ligands targeting GPCRs.

GPCR class	GPCR target	Name	Chemical structure	Uncaging λ (nm)	Pharmacological activity
A	α_1-AR	Caged phenylephine	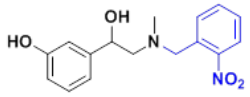 29	355	Agonist
A	AR	Caged norepinephrine	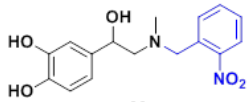 30	355	Agonist
A	β-AR	Caged isoprenaline	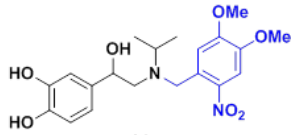 31	355	Agonist
A	D_2/D_3	MG307	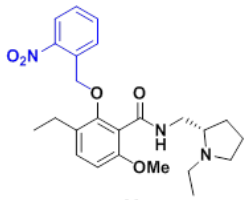 32	365	Antagonist
A	μ	Caged Dynorphin A	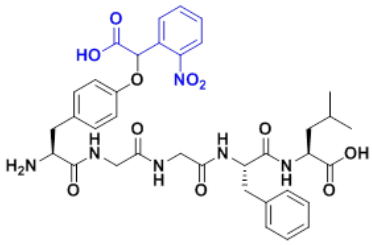 33	355	Agonist
C	GABA	Caged GABA	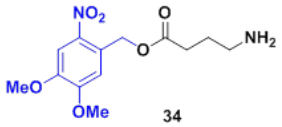 34	308	Agonist
C	mGlu	Caged Glutamate	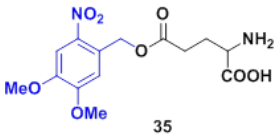 35	308	Agonist

There are many *o*NB caged ligands targeting class A GPCRs. For instance, caged derivatives of three adrenoceptor agonists (**29-31**) were described by Muralidharan and colaborators.[161] On another study, a caged analogue of dechloroeticlopride (**32**), a D_2/D_3 antagonist, was developed and used for the photolytic control of the target receptors *in vitro.* [162] Modulation μ-opioid

receptors with light was also achieved using a peptidic caged compound (**33**), which enabled the local and controlled release of the active neuropeptide opioid.[163]

In addition, there are also caged ligands that allow the irreversible control of class C GPCRs with the application of light. For instance, a research study reported the development of several caged neurotransmitters, such as GABA (**34**) or glutamate (**35**), through the introduction of an *o*-nitrobenzyl protecting group. The resulting ligands were efficiently photolyzed upon the application of UV light, releasing the active neurotransmitters.[164]

Therefore, despite the short wavelengths required for the photolytic reaction to occur, *o*-nitrobenzyl protecting groups have proved to be very useful for the study of a diversity of biological systems with spatiotemporal precision. Results obtained from research studies conducted with the described ligands have provided valuable information on GPCR signaling and function. This further confirms the potential of these photoactivatable molecular tools on research applications.[165]

Coumarins

Another group of popular photoprotecting groups is constituted by coumarins, a secondary metabolite found in many plants. The use of (coumarin-4-yl)methyl protecting groups to produce photoactivatable compounds is well-established and extended. The most common coumarin-based PPG are depicted in Figure 37. However, the maximum absorption of most of these molecular scaffolds is still in the UV range, which can constitute a limitation as previously stated. From the initial coumarin scaffold (MCM, **36**), which displayed very low λ_{max}, different modifications were explored to improve the photochemical properties of the chromophore. A significant increase in the absorption maximum was achieved when the methoxy in the 7-position was substituted by a diethylamine (DEACM, **37**), yielding a moiety with λ_{max} reaching the visible range. On the other hand, the introduction of an additional methoxy in the 6-position (DMCM, **38**) caused a moderate increase on the maximum absorption of the PPG. Among the coumarin moieties with substitutions in the 6- and 7-positions, important improvements were obtained with the 6-bromo-7-hydroxy analogues (Bhc, **39**), that displayed λ_{max} in the near UV range.[166]

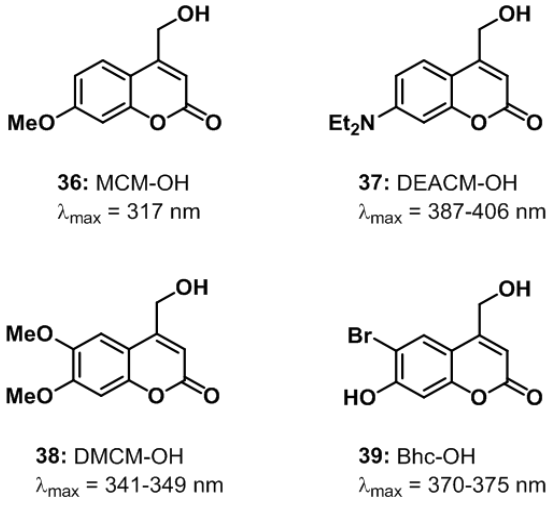

Figure 37. Chemical structures of some of the most commonly used (coumarin-4-yl)methyl PPG.

The mechanisms underlying the photolytic release of (coumarin-4-yl)methyl caged compounds have been well studied, and the proposed steps leading to the cleavage of C-O bonds are depicted in Scheme 2. Upon illumination, the chromophore of **40** is excited to the lowest excited state (**I-1**), from which heterolytic bond cleavage occurs. In consequence, the leaving group and a positively charged coumarin are released (**I-2**); The intermediate coumarin-4-yl cation is finally trapped by the solvent to provide **41** (Scheme 2).[167]

Scheme 2. Proposed photolytic mechanism of coumarin-4-yl PPG linked to an alcohol group.

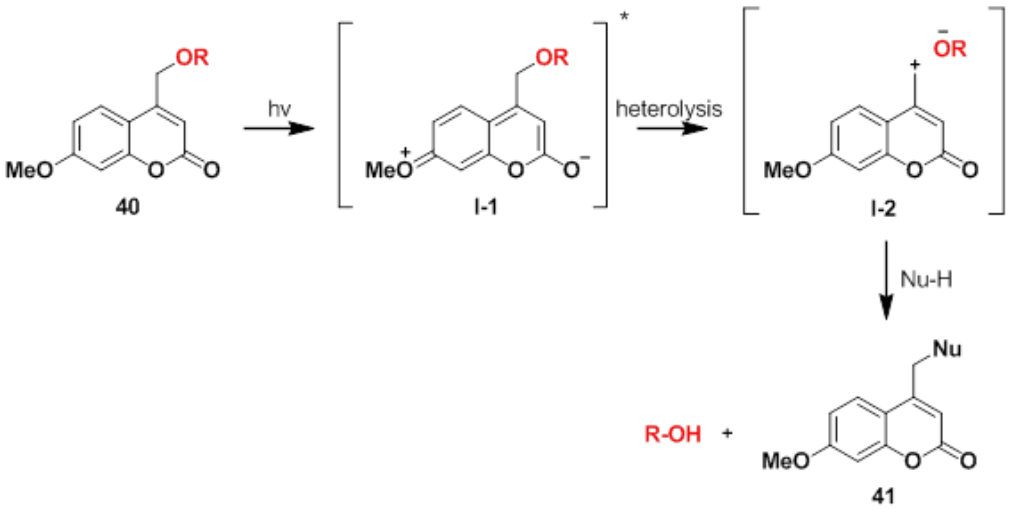

On the other hand, a single example of the photolytic release of a C-N bond has been reported in the literature. The mechanism proposed for this particular example differs from the one proposed for the photoheterolytic cleavage of C-O bonds. In this case, a radical mechanism was proposed (Scheme 3). Light excites the coumarin chromophore of **42** to produce intermediate (**I-3**)**.** An electron transfer between the amine and the coumarin groups of **I-3** occurs, yielding intermediate **I-4.** followed by the cleavage of the C–N bond. As a result, an aminyl radical and a resonance-stabilized coumarin radical are produced (**I-5**), both of which can be trapped by hydrogen-atom donors to produce **43**.[168]

Scheme 3. Proposed photolytic mechanism of coumarin-4-yl PPG directly linked to an amine.

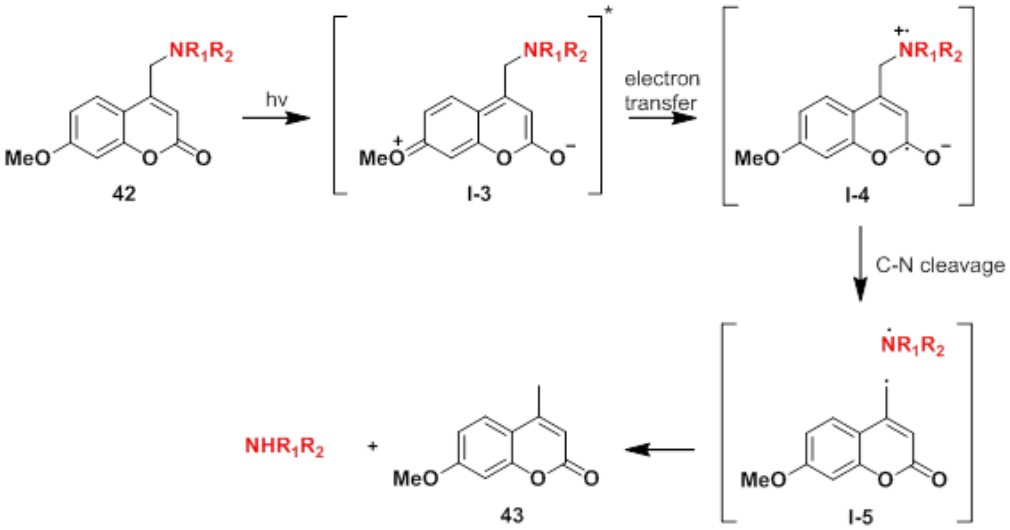

Due to their early discovery, coumarin PPG have been extensively studied and used for the generation of photocaged ligands to control biological systems with spatiotemporal precision. In fact, several coumarin-based photoactivatable compounds targeting GPCRs have been reported in the literature. For instance, two neurotransmitters, glutamate and GABA, were rendered light-sensitive through the addition of a coumarin analogue. Photoactivation of the two caged compounds was proven successful in neurons and brain slices. [169]

The interesting properties shown by coumarin-4-yl chromophores have raised interest on the development of moieties with lower energy absorption. Introducing electron-donating groups (EDG) or extending the π-conjugation in the coumarin substructure has shifted the photolytic wavelengths towards the blue, and even green, ranges of the visible spectrum. Nonetheless, most of these red-shifted scaffolds have not been used for the spatiotemporal control of biological systems but as fluorophores for imaging techniques. Coumarins can also be excited via two-photon absorption (TPA), which allows the photolysis of the caged analogues with NIR light.[166]

Towards red-shifted PPG

As previously stated, using visible light to trigger the photolytic release of bioactive molecules is appealing due to its negligible toxicity and better tissue penetration compared to UV light. In fact, near-IR light (650-900 nm) has been identified as optimal for biological applications, as it has the best tissue penetration profile. At lower wavelengths of the visible spectrum, endogenous chromophores present in the target tissues absorb most of the photons, thus reducing light penetration. For this reason, recent research efforts in this field are focusing on the development of photocages operating at visible light wavelengths (Figure 38). [159,166]

Classical PPG, such as *o*-nitrobenzyl groups, have been successfully used on many biological applications. Nevertheless, the requirement of highly energetic light for their photolytic uncaging constitutes a limitation, as UV light has been identified as cytotoxic and presents low tissue penetration. Several coumarin-based PPG have been described in the literature, with decaging wavelengths reaching the blue range of the visible spectrum. Despite the non-toxic nature of blue light, it still presents very poor tissue penetrability, which difficults the use of coumarin photocages in physiological or therapeutic applications. The recent development of coumarin-4-yl chromophores with extended π-conjugation has allowed substantial bathochromic shifts of λ_{max}, reaching the green and red areas of the visible spectrum. However, the use of these moieties in biological applications is not well explored yet.[159,166]

On the other hand, the use of imaging fluorophores, such as BODIPY derivatives and cyanines, has been extended to the development of red-shifted PPG. Boron dipyrromethene (BODIPY) derivatives have been used to produce several caged compounds with uncaging wavelengths in the green and red regions of the visible spectrum. Nevertheless, the use of this compounds has solely been tested in cellular assays, and their applicability in physiological systems still remains to be seen. Finally, cyanines are valuable fluorophores with an absorption maximum in the near-IR as a consequence of their highly conjugated chemical structure. There are not many reported examples on the use of cyanines as PPG; however, the known examples have already shown their good applicability *in vivo*. [166]

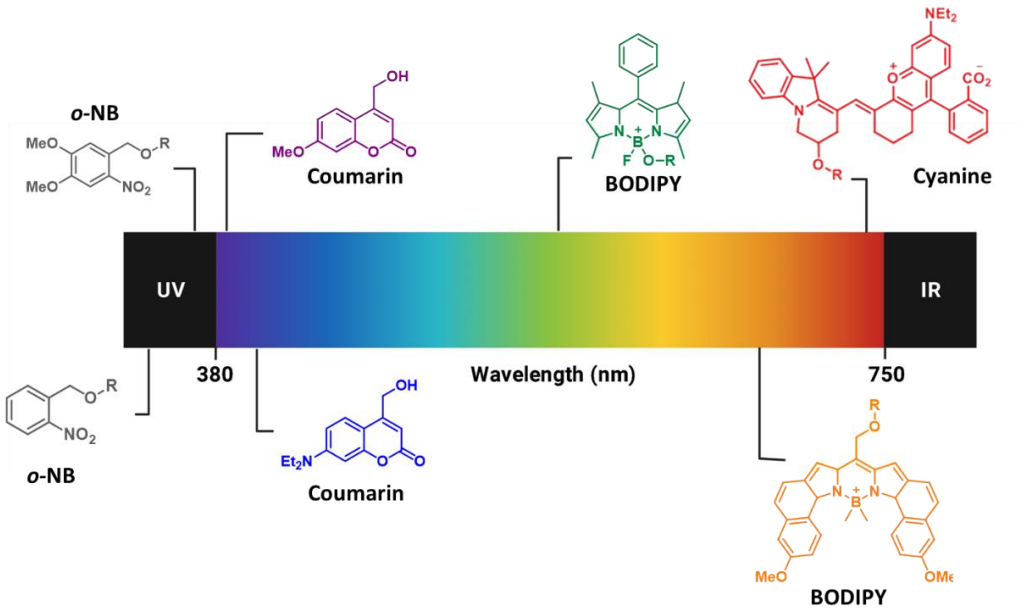

Figure 38. PPG and their maximum absorbance wavelengths. Advances in photoprotecting groups are leading to the development of red-shifted chromophores. Created with BioRender.

3.2.2 Reversible strategies: photochromic ligands (PCLs)

The development of reversible light-sensitive molecules to control the activity of target receptors can be achieved by introducing a photochromic moiety within a drug structure.[170] This strategy affords compounds that can exist in two distinct states, which can be reversibly interconverted by light illumination. In consequence, light application induces changes in the polarity, geometry, and end-to-end distance of the photochromic molecule. These light-regulated changes in the molecule can be designed to alter its functional properties as a ligand (e.g., agonist/ antagonist character) or the accessibility to its binding site within the receptor (affinity) (Figure 39). Therefore, photoswitchable ligands constitute valuable molecular tools that allow a fine control of receptor activation state by modulating the light power or the wavelength used. The use of these molecules has allowed the study of many biological systems from a different perspective, as it permits receptor modulation in two dimensions, space and time. [171,172]

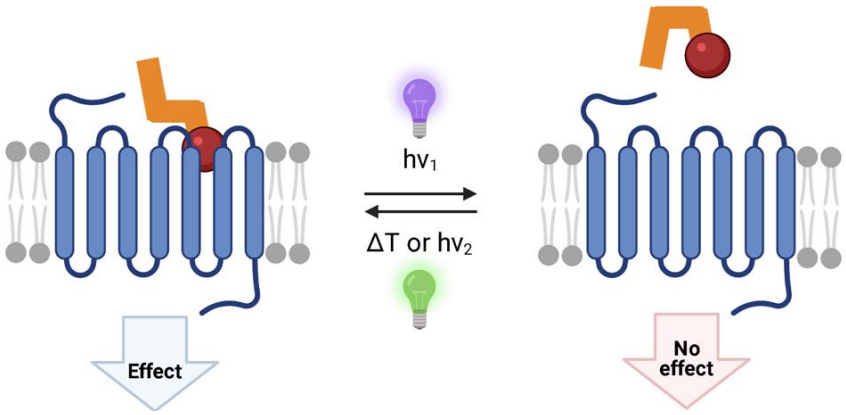

Figure 39. Schematic representation of reversible photopharmacology. Initially, the PCL is bound to the receptor and is exerting an effect over its activation state. Light application (hv_1) triggers excitation of the PCL, which now cannot bind to the target protein. The initial state can be recovered either by thermal relaxation, or through the application of light (hv_2). Created with BioRender.

Due to the growing interest generated by photoswitchable ligands, a variety of photochromic moieties has been developed, which can be classified in two groups depending on their isomerization mechanism (Figure 40). Moieties that can be interconverted between *cis* and *trans* isomers upon light illumination (azobenzenes, stilbenes and hemithioindigos) and moieties that are photoconverted between open and closed forms (spiropyrans, diarylethenes and thiophenefulgides). In order to select the appropriate synthetic photoswitch for the design of a PCL, there are several important properties that have to be considered:

a) Good chemical stability and non-toxicity of the compound before and after illumination.

b) Appropriate ADME (absorption, distribution, metabolism and excretion) properties.

c) Optimal photophysical properties; high absorbance, preferably in the visible range, and efficient photoisomerization.

d) Large geometrical changes upon isomerization.[171]

Azobenzenes fulfill most of the described criteria and have great synthetic accessibility. For this reason, these photoswitches are the most commonly used light-sensitive scaffold for the design of synthetic photochromic ligands.[165]

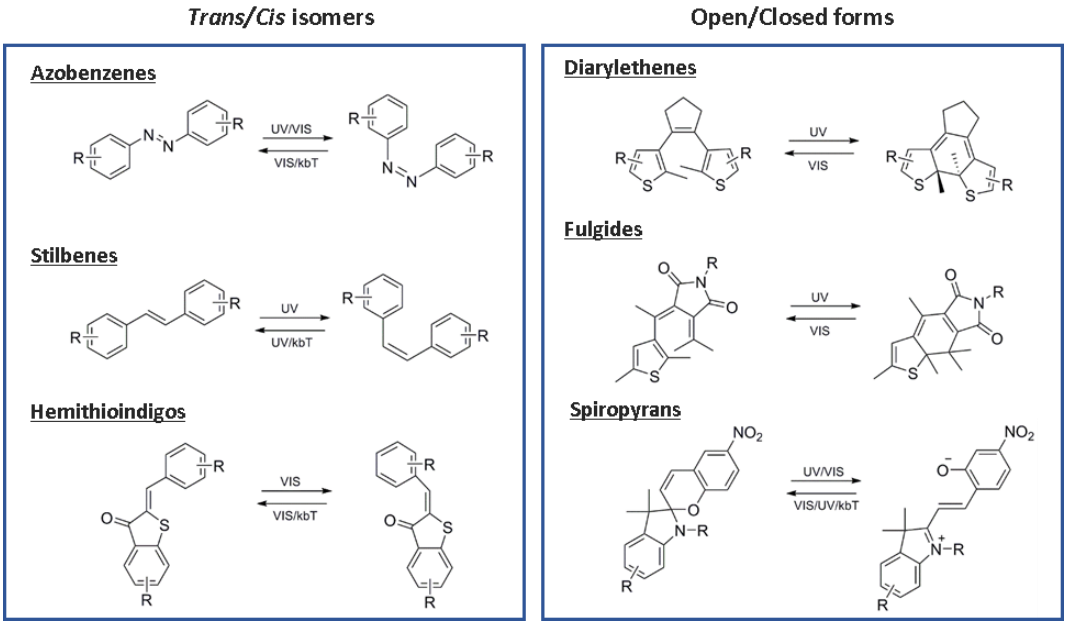

Figure 40. Chemical structures of the main photochromic moieties used in photopharmacology. Left panel shows moieties that exist in *trans* and *cis* isomeric forms, where *trans* isomers are drawn on the left and *cis* isomer are drawn on the right. Right panel shows the photoswitches that are photoconverted between open and closed forms. Adapted from Ricart-Ortega *et al.* (2019).

Azobenzenes

The structure of an azobenzene (AB) is constituted by two phenyl rings linked through an N=N bond, known as the azo-bond or azo-bridge (Figure 41). As previously described, azobenzenes can exist in two different isomeric forms: *trans*- and *cis*-. The *trans* isomer has a planar geometry, with a dihedral angle of 180°. As a consequence of its planarity, π-electrons are delocalized over

the aromatic rings and the azo-bond, thus stabilizing this isomeric state. On the other hand, the *cis* isomer has a bent geometry, with its phenyl rings twisted 55° out of the plane, thus resulting in a shorter structure. Its twisted geometry causes a rupture in the π-electron delocalization, thus increasing the energy of this isomer. For this reason, in most cases the photoswitchable group exists in the *trans* configuration under dark conditions, which is the thermodynamically stable isomer, and can be excited to the *cis* with the application of an appropriate wavelength.[173]

One of the interesting features of ABs is that light introduces great changes in geometry, thus rendering compounds with very different physical and chemical properties (Figure 41A). These large variations between the two photoisomers, also introduce notable changes on the NMR and absorbance spectra of the compounds. Therefore, interconversion of the PCL between the two configurations can be followed and quantified using these two methods. In addition, changes in the retention times can also be observed when samples containing a mixture of *trans,* and *cis* isomers are analyzed by HPLC. Therefore, this method can also be used to quantify photoisomeric ratios after illumination. However, it has to be considered that the longer times required for this analytic technique limit its use in the quantification of fast relaxing compounds.

The absorption spectra of the *trans* unsubstituted azobenzene displays two main bands: a strong transition near 320-350 nm (π-π*), and a weak transition between 400-450 nm (n-π*), which is forbidden by symmetry. Upon illumination, the *cis* isomer presents a stronger n-π* band at the same area and two bands at 250 and 280 nm, corresponding to the π-π* transition (Figure 41B). Therefore, absorbance spectra of the two configurations of an AB are significantly different, but also present a certain degree of overlapping. Careful evaluation of the absorbance spectra of the two photoisomers is essential to select the optimal wavelengths to trigger photoisomerization in both directions. [174]

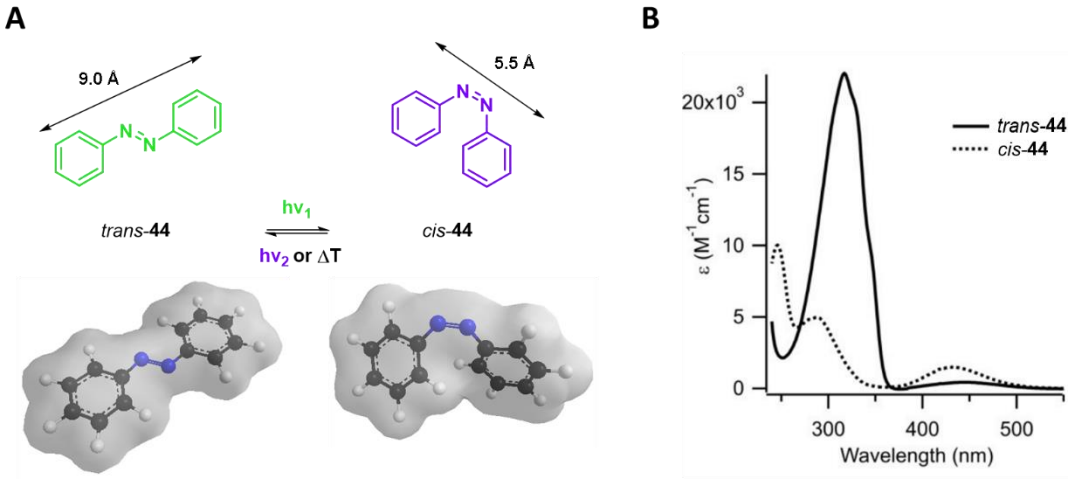

Figure 41. Photoisomerization of unsubstituted azobenzene 44. (A) 2D and 3D chemical structures of the two photoisomers of **44**. (B) Superposed UV-Vis spectra of the *trans* and *cis* isomers of **44**. Adapted from Baroncini (2019).

Maximal excitation to the *cis* isomer is achieved upon illumination with the appropriate wavelength, where maximum absorbance difference is observed between the *trans* and *cis* isomers (generally the π-π* transition). After light application, the system reaches a so-called photostationary state (PSS), where the azobenzene is found in a kinetic equilibrium as long as

the compound is illuminated. In the PSS the isomeric ratio remains temporally constant in time as a result from equal interconversion rates between the *cis* and *trans* isomers. The isomeric rations obtained in the photostationary state highly depend on illumination conditions (wavelength) and on the studied system (concentration, solvent, pH, temperature, etc.). Concentrations of the isomers at a particular PSS are generally determined by ^{1}H NMR spectroscopy. [174]

Back-isomerization to the thermally stable *trans* configuration is expected to occur spontaneously by thermal relaxation processes. While excitation to the *cis* isomer is very fast, thermal relaxation rates highly depend on the chemical and electronic properties of the system, that can range from nanoseconds to days, or even years. Isomerization to the thermostable configuration can also be triggered by light, which can, in some cases, accelerate the thermal process. The optimal wavelength to induce this transition generally corresponds to that of the n-π* band, at which the *cis* configuration maximally absorbs, and the *trans* isomer has very low absorption.[174] However, one of the main limitations found in most azobenzenes arises from the overlapping in the absorbance spectra of the two photoisomers. This hampers the quantitative photoconversion between the two states, and isomeric mixtures are generally obtained after illumination with the optimal wavelengths.

The mechanism of azobenzene isomerization has been very controversial and two pathways are extensively considered viable (Figure 42); however, up to four different mechanisms have been proposed as possible, all of which differ on bonding movements and resulting changes in the C-N=N-C dihedral angle. The rotational pathway proposes the rupture of the N=N double bond to allow free rotation about the N–N bond. On the other hand, in the inversion mechanism involves a semi-linear and hybridized transition state where one N=N–C angle increases to 180° while the C–N=N–C dihedral angle remains fixed at 0°. Nevertheless, combination of different mechanisms is generally required to explain the experimental data.[175]

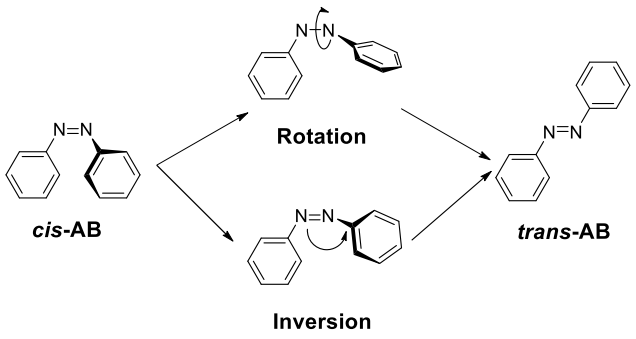

Figure 42. Rotation and inversion mechanisms for the *trans*→*cis* isomerization of azobenzene 44. Adapted from Baroncini (2019).

Substituted azobenzenes

The presence of substituents in the phenyl rings of ABs can induce great variations on the absorbance spectra of the compounds, and consequently on their photochemical properties. The accessible functionalization of azobenzenes has allowed the synthesis of many azobenzene derivatives. Subsequent evaluation of the substituent-induced photophysical changes has provided a rationale for straightforward design of AB derivatives with predictable absorbance

and kinetic properties. This is highly convenient, as chemical engineering allows fine-tuning modulation of azobenzene light-dependent properties to match the requirements of the different research applications. Historically, functionalized azobenzenes have been classified in three categories according to their spectroscopic properties (Table 8).[176]

Table 8. Classification of substituted AB according to their spectroscopic properties.

Name	Chemical structure	Type of substituents	π-π* λ (nm)	Thermal relaxation
Azobenzene (AB)	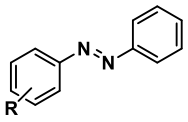 **R**: alkyl, aryl, halide, keto, carboxylic acid, ester, amide, nitrile, nitro, 3-amino, 3-alkoxy	EWG or mild EDG	310-340	Slow; $t_{1/2}$: days-hours
Aminoazobenzene (aAB)	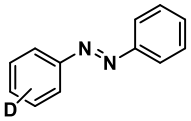 **D**: 2- or 4-amino, 2-or 4-hydroxy, 2-or 4-alkoxy	Strong EDG	340-440	Moderate to fast; $t_{1/2}$: hours-seconds
Pseudostilbene (pSB)	Protonated-azobenzenes (pAB) 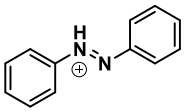	EDG can be introduced	400-600	Fast
	Push-pull azobenzenes (ppAB) 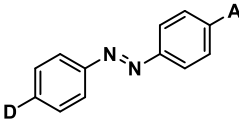 **A**: nitro, carboxylic acid **D**: amino, alkoxy	EDG and EWG in opposing positions	440-460	Fast; $t_{1/2}$: minutes-milliseconds

Azobenzene derivatives (AB) include plain azobenzenes or substituted azobenzenes that incorporate electron withdrawing groups (EWG) or mild electron donating groups (EDG) (Table 8). This family of photoswitches present the typical spectroscopic features of unsubstituted azobenzenes, with two well-separated bands corresponding to the π-π* (intense) and the n-π* (weak) transitions. Thermal relaxation of the *cis* isomer is generally slow; however, the relaxation rate can be noticeably increased with the addition of strong EWG in the *para* positions.

Azobenzenes functionalized with one or more amino, methoxy or hydroxy substituents in the 2 or 4 positions are classified as aminoazobenzenes (aABs). Introducing electron donating groups (EDG) in the phenyl rings induces a bathochromic shift of the π-π* transition, which overlaps or partially overlaps with the n-π* transition. Azobenzenes with *N*-amide, *N*-carbamate or urea substituents in the *para* positions can also be included in the aAB family, as these compounds also present a moderately red-shifted π-π* band. The presence of EDG in the azobenzene moiety increases the electron density in the π* orbital, thus decreasing the thermal isomerization energetic barrier. Consequently, thermal relaxation in aABs occur faster than in ABs.[177,178]

Additionally, when the azobenzene incorporates a phenol or aniline substituent, the half-life of the *cis* isomer is even shorter due to the existence of an azo-hydrazone tautomeric equilibrium (Figure 43). Finally, thermal relaxation of aABs highly depend on solvent polarity.[174]

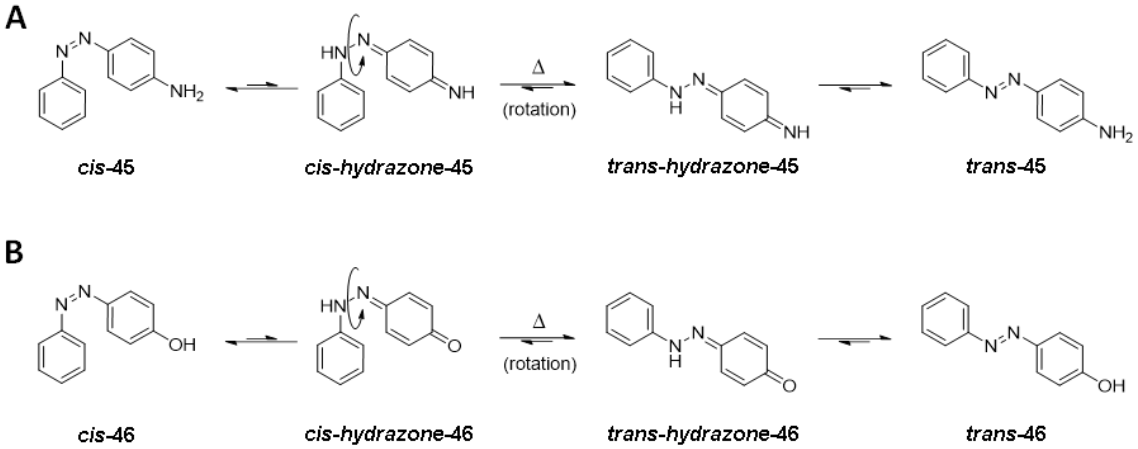

Figure 43. Back-isomerization mechanisms for aABs containing aniline or phenol substituents. Thermal relaxation of *cis*-aABs containing aniline (A) or phenol (B) substituents occurs via an *a*zo-hydrazone tautomeric equilibrium.

The third class of azobenzene derivatives is represented by pseudo-stilbenes (pSB), which can be divided in two classes respectively: protonated-azobenzenes (pAB) and push-pull azobenzenes (ppAB). Push-pull azobenzenes have a characteristic substitution, with an electron donor group on one phenyl ring and an electron acceptor group on the other. ppABs are spectroscopically characterized by a significant bathochromic shift of the π-π* band, which completely overlaps with the n-π* transition. In addition, these compounds show extremely fast thermal back-isomerization processes, ranging from seconds to milliseconds. This can constitute a clear advantage for certain applications, as this type of compounds can be controlled using only one wavelength that triggers excitation of the compounds to their *cis* isomer; the moment light application is stopped, the *cis* isomer immediately relaxes back to its *trans* isomeric form, thus providing a tool that allows for very rapid modulation of the target receptor with light. However, the short half-life of *cis* isomer in ppABs can also introduce a limitation for some applications that require longer relaxation times.[179]

Recent chemical efforts have allowed the development of a new type of azobenzenes, which are red-shifted but have longer thermal back-isomerization processes. This new family, named tetra-*o*-substituted azobenzenes (to*o*AB), presents the four *ortho* positions substituted with EDG (i.e. methoxy groups) or halides (i.e. fluorines).[180,181]

To sum up, azobenzenes constitute versatile light-sensitive moieties that can be used for the development of photochromic ligands to reversibly control protein function with light. As previously stated, this substructure is synthetically accessible, and its functionalization is well-described. Moreover, the introduction of substituents allows to finely tune the photophysical properties of the compound in a predictable manner. Different families of ABs have been described, with different spectroscopic and kinetic properties. Therefore, there is a wide range of photophysical properties within the library of azobenzene-based scaffolds. Thus, one can

almost always find an azobenzene scaffold with photochemical properties matching the requirements for a specific application of interest.

PCLs to reversibly control GPCRs with light

Photochromic ligands have found a wide variety of research applications, including the development of innovative light-sensitive materials or their use in imaging techniques. However, one of the most attractive possibilities offered by PCLs is the optical control of biological systems in a reversible manner. This approach provides mechanisms to regulate physiological systems in a more natural manner compared to conventional pharmacology, as targets can be activated with light in a precise location and deactivated once its function has been effected.

Nowadays, optical control of many different targets has been achieved with photoswitchable ligands; however, PCLs modulating the GPCR superfamily of proteins have been frequently reported in a variety of biological systems, including living animals. Today, the GPCR photopharmacological toolbox contains a variety of pharmacological and chemical strategies, such as ligands with opposing pharmacological properties (agonists/antagonists) depending on the applied light,[182,183] photoswitchable dualsteric ligands,[184] light regulated ligands based on dithienylethenes and fulgides, etc. In addition, all classes of GPCRs have been targeted with PCLs, which have been extensively reviewed elsewhere.[165] Table 9 summarizes the characteristics of three PCLs, each targeting a different class of GPCR.

Table 9. Classification of substituted AB according to their spectroscopic properties.[183,185,186]

GPCR class	GPCR target	Compound name	Chemical structure	Active isomer	Compound activity
A	CXCR3	VUF16216	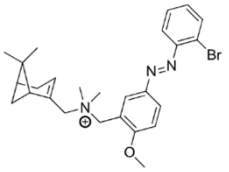 **46**	*trans* *cis*	Antagonist Agonist
B	GLP1-1R	LirAzo	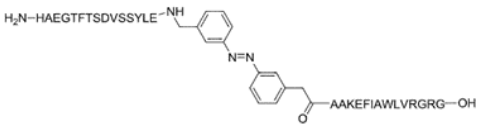 **47**	*trans*	Agonist
C	mGlu5	Alloswitch-1	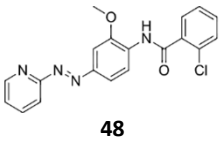 **48**	*trans*	NAM

Many class A GPCRs have been optically regulated using PCLs, including muscarinic, dopamine, histamine and μ-opioids, among others.[165] Interestingly, a recent publication reported the development of VUF16216, a photoswitchable ligand targeting chemokine receptor CXCR3 based on the biaryl scaffold of CXCR3 ligands. This compound was described as a dualsteric ligand, as it antagonizes the receptor under dark conditions and behaves as an agonist upon UV

light (360 nm) application. The light-dependent properties of this compound were studied in radiolabeling binding experiments, functional and electrophysiology assays.[183]

On the other hand, GLP-1R is the only receptor from class B that has been optically modulated. LirAzo, a photoswitchable ligand was obtained through the introduction of an azobenzene moiety to the GLP-1 analogue Liraglutide, which is an approved drug.[186]

Finally, many class C GPCRs have also been successfully targeted through the use of PCLs. In a very interesting example, Alloswitch-1 was described as a *trans*-on negative allosteric modulator of $mGlu_5$. The NAM activity of the compound was efficiently regulated with the application of UV light in a variety of physiological systems, including living zebrafish and tadpoles.[185]

Overall, the given examples provide good evidence on the potential of PCLs in research and clinical applications. For this reason, the development of photoswitches to regulate GPCRs with light is an emerging field that may open new avenues for the treatment of many diseases with unmet needs with classical pharmacology.[145,152]

3.2.3 Reversible strategies: tethered ligands

Light-sensitive tethered ligands are constituted by photochromic compounds covalently attached to the target protein through a bioconjugation reaction. In this strategy, the light-activatable molecules cannot diffuse away, and this allows a fast, reproducible and spatially acute protein modulation with the application of light. Therefore, this type of photochromic ligands can be reversibly interconverted between their two photoisomeric states, allowing activation and deactivation of proteins within milliseconds. [148,149]

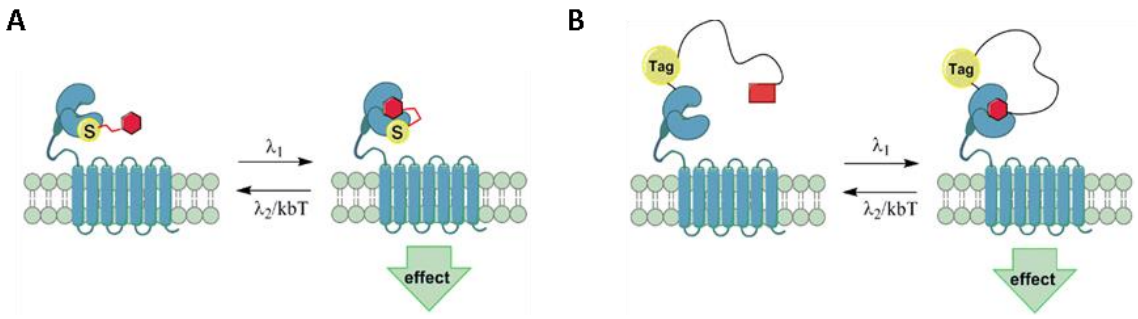

Figure 44. Common strategies on tethered pharmacology. (A) Photoswitchable tethered ligands (PTLs); (B) Photoswitchable orthogonal remotely tethered ligands (PORTLs) (D). Adapted from Ricart-Ortega et al. (2019).

Photoswitchable tethered molecules can be classified depending on the attachment site and the length of the tether moiety (Figure 44):

- **Photoswitchable tethered ligands (PTLs):** these small chemical compounds are composed by a photoswitch and a covalent attachment with a cysteine residue that is in the proximity of the binding site (Figure 44A). [148]

- **Photoswitchable orthogonal remotely tethered ligands (PORTLs):** PORTLs are large bioconjugation motifs constituted by a reactive moiety that is connected to a light-sensitive ligand through a long, water-soluble and flexible polyethylene glycol (PEG)

linker (Figure 44B). The reactive scaffold is anchored far from the ligand binding pocket to a self-labelling tag (SNAP-tag[187], CLIP-tag[188] or HALO-tag[189]). These tags are chemically stable in aqueous solution and each reaction tag is biorthogonal. [148]

The two tethered strategies described herein have been applied to modulate the activation state of a variety of GPCRs from classes A and C[147,190–192], demonstrating good modulation of the target receptor and higher selectivity.

Finally, there are other strategies that allow covalent tethering in unmodified receptors, such as Photoswitchable Affinity Labels (PALs). However, these approaches have not yet been applied to G-Protein Coupled Receptors and will not be further reviewed in this section.

3.2.4 Advantages, considerations, and future perspectives

The use of light-dependent ligands offers a unique possibility for the regulation of GPCRs in their native environments with high spatiotemporal precision. This has provided valuable tools for mechanistic studies of GPCR function and activation, allowing to better understand the complex processes involved in signaling transduction. Moreover, the use of photopharmacology has allowed to discern the role of GPCRs in important physiological functions; these studies have been performed in a variety of organisms, from cells to living animals.

In addition to the value of photopharmacology in research applications, this innovative technique holds enormous therapeutic potential. In an ideal future scenario, photoswitchable ligands will allow the control and regulation of pathologic pathways in a precise manner, leading to more efficient and safe treatments. In particular, the optimal ligand for clinical uses should be inactive in dark conditions and activatable with light (*cis*-on). However, most photoswitchable ligands reported in the literature show an opposing light-dependency (*trans*-on), as they are pharmacologically active in dark conditions and can be switched off through the application of light. Consequently, one of the current challenges in the field of photopharmacology is development of molecules with increased therapeutic value and *cis*-on light-dependent behaviors.[193] On the other hand, the evolution of photopharmacology will be especially stringed to the advances in the fields of photonics and optical engineering. Design and production of better optical devices will be essential to solve unmet needs for some research applications and to translate the developed tools for a precise use in the clinics.[193]

Finally, there are some important considerations that should be taken into account for the pharmacological characterization of photocontrolled ligands in the future. As previously stated, ligands targeting GPCR can present biased signaling, activating preferentially specific pathways in the signaling cascade. For this reason, this property should be further investigated when characterizing a light-dependent ligand, by performing different types of functional assays. Moreover, the activity of allosteric photoswitches should be assayed with different orthosteric ligands, as it has been described that different behaviors can be obtained (probe dependence). Finally, it is advisable to evaluate the pharmacology of the studied photoswitch against target receptors from different species, as it can assist in the identification of important differences between the GPCR variants.[193]

References

1. Fredriksson, R., Lagerström, M. C., Lundin, L.-G. & Schiöth, H. B. The G-Protein-Coupled Receptors in the Human Genome Form Five Main Families. Phylogenetic Analysis, Paralogon Groups, and Fingerprints. *Molecular Pharmacology* **63**, 1256–1272 (2003).

2. Bockaert, J. Molecular tinkering of G protein-coupled receptors: an evolutionary success. *The EMBO Journal* **18**, 1723–1729 (1999).

3. Hauser, A. S., Attwood, M. M., Rask-Andersen, M., Schiöth, H. B. & Gloriam, D. E. Trends in GPCR drug discovery: new agents, targets and indications. *Nature Reviews Drug Discovery* **16**, 829–842 (2017).

4. Sriram, K. & Insel, P. A. G Protein-Coupled Receptors as Targets for Approved Drugs: How Many Targets and How Many Drugs? *Molecular Pharmacology* **93**, 251–258 (2018).

5. Kolakowski, L. F. GCRDb: a G-protein-coupled receptor database. *Receptors & channels* **2**, 1–7 (1994).

6. Attwood, T. K. & Findlay, J. B. C. Fingerprinting G-protein-coupled receptors. *"Protein Engineering, Design and Selection"* **7**, 195–203 (1994).

7. Shonberg, J., Kling, R. C., Gmeiner, P. & Löber, S. GPCR crystal structures: Medicinal chemistry in the pocket. *Bioorganic & Medicinal Chemistry* **23**, 3880–3906 (2015).

8. Sierra, S., Toneatti, R. & González-Maeso, J. Class A GPCR oligomerization. in *GPCRs* 121–140 (Elsevier, 2020). doi:10.1016/B978-0-12-816228-6.00008-8.

9. Zhou, Q. *et al.* Common activation mechanism of class A GPCRs. *eLife* **8**, (2019).

10. Rosenbaum, D. M., Rasmussen, S. G. F. & Kobilka, B. K. The structure and function of G-protein-coupled receptors. *Nature* **459**, 356–363 (2009).

11. Alexander, S. P. H. *et al.* THE CONCISE GUIDE TO PHARMACOLOGY 2019/20: G protein-coupled receptors. *British Journal of Pharmacology* **176**, (2019).

12. Bortolato, A. *et al.* Structure of Class B GPCRs: new horizons for drug discovery. *British Journal of Pharmacology* **171**, 3132–3145 (2014).

13. de Graaf, C. *et al.* Extending the Structural View of Class B GPCRs. *Trends in Biochemical Sciences* **42**, 946–960 (2017).

14. Rondard, P., Goudet, C., Kniazeff, J., Pin, J.-P. & Prézeau, L. The complexity of their activation mechanism opens new possibilities for the modulation of mGlu and GABAB class C G protein-coupled receptors. *Neuropharmacology* **60**, 82–92 (2011).

15. Pin, J.-P. *et al.* Allosteric functioning of dimeric class C G-protein-coupled receptors. *FEBS Journal* **272**, 2947–2955 (2005).

16. Kniazeff, J., Prézeau, L., Rondard, P., Pin, J.-P. & Goudet, C. Dimers and beyond: The functional puzzles of class C GPCRs. *Pharmacology & Therapeutics* **130**, 9–25 (2011).

17. Dijksterhuis, J. P., Petersen, J. & Schulte, G. WNT/Frizzled signalling: receptor-ligand selectivity with focus on FZD-G protein signalling and its physiological relevance: IUPHAR Review 3. *British Journal of Pharmacology* **171**, 1195–1209 (2014).

18. G protein-coupled receptors. IUPHAR/BPS Guide to Pharmacology.

19. Janda, C. Y., Waghray, D., Levin, A. M., Thomas, C. & Garcia, K. C. Structural Basis of Wnt Recognition by Frizzled. *Science* **337**, 59–64 (2012).

20. Simundza, J. & Cowin, P. Adhesion G-Protein-Coupled Receptors: Elusive Hybrids Come of Age. *Cell Communication & Adhesion* **20**, 213–225 (2013).

21. Hamann, J. *et al.* International Union of Basic and Clinical Pharmacology. XCIV. Adhesion G Protein–Coupled Receptors. *Pharmacological Reviews* **67**, 338–367 (2015).

22. Weis, W. I. & Kobilka, B. K. The Molecular Basis of G Protein–Coupled Receptor Activation. *Annual Review of Biochemistry* **87**, 897–919 (2018).

23. Hilger, D., Masureel, M. & Kobilka, B. K. Structure and dynamics of GPCR signaling complexes. *Nature Structural & Molecular Biology* **25**, 4–12 (2018).

24. Gurevich, V. v. & Gurevich, E. v. GPCR Signaling Regulation: The Role of GRKs and Arrestins. *Frontiers in Pharmacology* **10**, (2019).

25. Palczewski, K., Buczyłko, J., Kaplan, M. W., Polans, A. S. & Crabb, J. W. Mechanism of rhodopsin kinase activation. *The Journal of biological chemistry* **266**, 12949–55 (1991).

26. Chen, C. Y., Dion, S. B., Kim, C. M. & Benovic, J. L. Beta-adrenergic receptor kinase. Agonist-dependent receptor binding promotes kinase activation. *The Journal of biological chemistry* **268**, 7825–31 (1993).

27. Sibley, D. R., Strasser, R. H., Benovic, J. L., Daniel, K. & Lefkowitz, R. J. Phosphorylation/dephosphorylation of the beta-adrenergic receptor regulates its functional coupling to adenylate cyclase and subcellular distribution. *Proceedings of the National Academy of Sciences* **83**, 9408–9412 (1986).

28. Arshavsky, V. Yu., Dizhoor, A. M., Shestakova, I. K. & Philippov, P. P. The effect of rhodopsin phosphorylation on the light-dependent activation of phosphodiesterase from bovine rod outer segments. *FEBS Letters* **181**, 264–266 (1985).

29. Gurevich, V. v., Pals-Rylaarsdam, R., Benovic, J. L., Hosey, M. M. & Onorato, J. J. Agonist-Receptor-Arrestin, an Alternative Ternary Complex with High Agonist Affinity. *Journal of Biological Chemistry* **272**, 28849–28852 (1997).

30. Wilden, U. Duration and Amplitude of the Light-Induced cGMP Hydrolysis in Vertebrate Photoreceptors Are Regulated by Multiple Phosphorylation of Rhodopsin and by Arrestin Binding. *Biochemistry* **34**, 1446–1454 (1995).

31. Luttrell, L. M. *et al.* β-Arrestin-Dependent Formation of β_2 Adrenergic Receptor-Src Protein Kinase Complexes. *Science* **283**, 655–661 (1999).

32. Grundmann, M. *et al.* Lack of beta-arrestin signaling in the absence of active G proteins. *Nature Communications* **9**, 341 (2018).

33. Jakubík, J., Randáková, A., El-Fakahany, E. E. & Doležal, V. Analysis of equilibrium binding of an orthosteric tracer and two allosteric modulators. *PLOS ONE* **14**, e0214255 (2019).

34. Kenakin, T. P. Agonists. in *A Pharmacology Primer* (Elsevier, 2014). doi:10.1016/B978-0-12-407663-1.00005-3.

35. Kenakin, T. P. Orthosteric Drug Antagonism. in *A Pharmacology Primer* (Elsevier, 2014). doi:10.1016/B978-0-12-407663-1.00006-5.

36. Jeffrey Conn, P., Christopoulos, A. & Lindsley, C. W. Allosteric modulators of GPCRs: a novel approach for the treatment of CNS disorders. *Nature Reviews Drug Discovery* **8**, 41–54 (2009).

37. Gregory, K. J. & Conn, P. J. Molecular Insights into Metabotropic Glutamate Receptor Allosteric Modulation. *Molecular Pharmacology* **88**, 188–202 (2015).

38. Kenakin, T. P. Allosteric Modulation. in *A Pharmacology Primer* (Elsevier, 2014). doi:10.1016/B978-0-12-407663-1.00007-7.

39. Rankovic, Z., Brust, T. F. & Bohn, L. M. Biased agonism: An emerging paradigm in GPCR drug discovery. *Bioorganic & medicinal chemistry letters* **26**, (2016).

40. Tan, L., Yan, W., McCorvy, J. D. & Cheng, J. Biased Ligands of G Protein-Coupled Receptors (GPCRs): Structure–Functional Selectivity Relationships (SFSRs) and Therapeutic Potential. *Journal of Medicinal Chemistry* **61**, 9841–9878 (2018).

41. Correll, C. C. & McKittrick, B. A. Biased Ligand Modulation of Seven Transmembrane Receptors (7TMRs): Functional Implications for Drug Discovery. *Journal of Medicinal Chemistry* **57**, 6887–6896 (2014).

42. Violin, J. D., Crombie, A. L., Soergel, D. G. & Lark, M. W. Biased ligands at G-protein-coupled receptors: promise and progress. *Trends in Pharmacological Sciences* **35**, 308–316 (2014).

43. Shonberg, J. *et al.* Biased Agonism at G Protein-Coupled Receptors: The Promise and the Challenges-A Medicinal Chemistry Perspective. *Medicinal Research Reviews* **34**, 1286–1330 (2014).

44. Rominger, D. H., Cowan, C. L., Gowen-MacDonald, W. & Violin, J. D. Biased ligands: pathway validation for novel GPCR therapeutics. *Current Opinion in Pharmacology* **16**, 108–115 (2014).

45. Ahles, A. & Engelhardt, S. Polymorphic Variants of Adrenoceptors: Pharmacology, Physiology, and Role in Disease. *Pharmacological Reviews* **66**, 598–637 (2014).

46. Altosaar, K. *et al.* Adrenoceptors (version 2019.4) in the IUPHAR/BPS Guide to Pharmacology Database. *IUPHAR/BPS Guide to Pharmacology CITE* **2019**, (2019).

47. Stapleton, M. P. Sir James Black and propranolol. The role of the basic sciences in the history of cardiovascular pharmacology. *Texas Heart Institute journal* **24**, 336–42 (1997).

48. Wachter, S. B. & Gilbert, E. M. Beta-Adrenergic Receptors, from Their Discovery and Characterization through Their Manipulation to Beneficial Clinical Application. *Cardiology* **122**, 104–112 (2012).

49. Skeberdis, V. A. Structure and function of beta3-adrenergic receptors. *Medicina (Kaunas, Lithuania)* **40**, (2004).

50. Cotecchia, S., Stanasila, L. & Diviani, D. Protein-Protein Interactions at the Adrenergic Receptors. *Current Drug Targets* **13**, 15–27 (2012).

51. ELLIOTT, J. Alpha-adrenoceptors in equine digital veins: Evidence for the presence of both alpha $_1$ and alpha $_2$ -receptors mediating vasoconstriction. *Journal of Veterinary Pharmacology and Therapeutics* **20**, 308–317 (1997).

52. Velmurugan, B. K., Baskaran, R. & Huang, C.-Y. Detailed insight on β-adrenoceptors as therapeutic targets. *Biomedicine & Pharmacotherapy* **117**, 109039 (2019).

53. Zhou, Q. *et al.* Common activation mechanism of class A GPCRs. *eLife* **8**, (2019).

54. Rasmussen, S. G. F. *et al.* Crystal structure of the β2 adrenergic receptor–Gs protein complex. *Nature* **477**, 549–555 (2011).

55. Nygaard, R., Frimurer, T. M., Holst, B., Rosenkilde, M. M. & Schwartz, T. W. Ligand binding and micro-switches in 7TM receptor structures. *Trends in Pharmacological Sciences* **30**, 249–259 (2009).

56. Venkatakrishnan, A. J. *et al.* Diverse activation pathways in class A GPCRs converge near the G-protein-coupling region. *Nature* **536**, 484–487 (2016).

57. Rasmussen, S. G. F. *et al.* Crystal structure of the β2 adrenergic receptor–Gs protein complex. *Nature* **477**, 549–555 (2011).

58. Cherezov, V. *et al.* High-Resolution Crystal Structure of an Engineered Human β $_2$ -Adrenergic G Protein–Coupled Receptor. *Science* **318**, 1258–1265 (2007).

59. Su, M. *et al.* Structural Basis of the Activation of Heterotrimeric Gs-Protein by Isoproterenol-Bound β1-Adrenergic Receptor. *Molecular Cell* **80**, 59-71.e4 (2020).

60. Lee, Y. *et al.* Molecular basis of β-arrestin coupling to formoterol-bound β1-adrenoceptor. *Nature* **583**, 862–866 (2020).

61. Balligand, J.-L. Cardiac beta3-adrenergic receptors in the clinical arena: the end of the beginning. *European Journal of Heart Failure* **19**, 576–578 (2017).

62. Takimoto, E. Cyclic GMP-Dependent Signaling in Cardiac Myocytes. *Circulation Journal* **76**, 1819–1825 (2012).

63. Patel, C. B., Noor, N. & Rockman, H. A. Functional Selectivity in Adrenergic and Angiotensin Signaling Systems. *Molecular Pharmacology* **78**, 983–992 (2010).

64. Cazzola, M., Calzetta, L. & Matera, M. G. β2-adrenoceptor agonists: current and future direction. *British Journal of Pharmacology* **163**, 4–17 (2011).

65. Tashkin, D. P. & Fabbri, L. M. Long-acting beta-agonists in the management of chronic obstructive pulmonary disease: current and future agents. *Respiratory Research* **11**, 149 (2010).

66. Barisione, G., Baroffio, M., Crimi, E. & Brusasco, V. Beta-Adrenergic Agonists. *Pharmaceuticals* **3**, 1016–1044 (2010).

67. CHEN, K. K. & SCHMIDT, C. F. The action and clinical use of ephedrine, an alkaloid isolated from the Chinese drug ma huang; historical document. *Annals of allergy* **17**,.

68. Cazzola, M., Page, C. P., Rogliani, P. & Matera, M. G. β_2-Agonist Therapy in Lung Disease. *American Journal of Respiratory and Critical Care Medicine* **187**, 690–696 (2013).

69. Cypess, A. M. *et al.* Activation of Human Brown Adipose Tissue by a β3-Adrenergic Receptor Agonist. *Cell Metabolism* **21**, 33–38 (2015).

70. de Souza, C. & Burkey, B. Beta3 -Adrenoceptor Agonists as Anti-diabetic and Anti-obesity Drugs in Humans. *Current Pharmaceutical Design* **7**, 1433–1449 (2001).

71. Bragg, R., Hebel, D., Vouri, S. M. & Pitlick, J. M. Mirabegron: A Beta-3 Agonist for Overactive Bladder. *The Consultant Pharmacist* **29**, 823–837 (2014).

72. Andersson, K.-E., Martin, N. & Nitti, V. Selective β_3-Adrenoceptor Agonists for the Treatment of Overactive Bladder. *Journal of Urology* **190**, 1173–1180 (2013).

73. Igawa, Y., Aizawa, N. & Homma, Y. Beta3-Adrenoceptor Agonists: Possible Role in the Treatment of Overactive Bladder. *Korean Journal of Urology* **51**, 811 (2010).

74. Madamanchi, A. Beta-adrenergic receptor signaling in cardiac function and heart failure. *McGill journal of medicine : MJM : an international forum for the advancement of medical sciences by students* **10**, 99–104 (2007).

75. Rohrer, D. K. *et al.* Targeted disruption of the mouse beta1-adrenergic receptor gene: developmental and cardiovascular effects. *Proceedings of the National Academy of Sciences* **93**, 7375–7380 (1996).

76. Chruscinski, A. J. *et al.* Targeted Disruption of the β2 Adrenergic Receptor Gene. *Journal of Biological Chemistry* **274**, 16694–16700 (1999).

77. Lohse, M. J., Engelhardt, S. & Eschenhagen, T. What Is the Role of β-Adrenergic Signaling in Heart Failure? *Circulation Research* **93**, 896–906 (2003).

78. Wachter, S. B. & Gilbert, E. M. Beta-Adrenergic Receptors, from Their Discovery and Characterization through Their Manipulation to Beneficial Clinical Application. *Cardiology* **122**, 104–112 (2012).

79. Baker, J. G. & Wilcox, R. G. β-Blockers, heart disease and COPD: current controversies and uncertainties. *Thorax* **72**, 271–276 (2017).

80. Baker, J. G. The selectivity of β-adrenoceptor agonists at human β1-, β2- and β3-adrenoceptors. *British Journal of Pharmacology* **160**, 1048–1061 (2010).

81. Butini, S. *et al.* Polypharmacology of dopamine receptor ligands. *Progress in Neurobiology* **142**, 68–103 (2016).

82. Lanau, F., Zenner, M.-T., Civelli, O. & Hartman, D. S. Epinephrine and Norepinephrine Act as Potent Agonists at the Recombinant Human Dopamine D4 Receptor. *Journal of Neurochemistry* **68**, 804–812 (2002).

83. Ring, A. M. *et al.* Adrenaline-activated structure of β2-adrenoceptor stabilized by an engineered nanobody. *Nature* **502**, 575–579 (2013).

84. Peng, Y. *et al.* 5-HT2C Receptor Structures Reveal the Structural Basis of GPCR Polypharmacology. *Cell* **172**, 719-730.e14 (2018).

85. Ruffolo, R. R., Spradlin, T. A., Pollock, G. D., Waddell, J. E. & Murphy, P. J. Alpha and beta adrenergic effects of the stereoisomers of dobutamine. *The Journal of pharmacology and experimental therapeutics* **219**, 447–52 (1981).

86. Chan, H. C. S., Filipek, S. & Yuan, S. The Principles of Ligand Specificity on beta-2-adrenergic receptor. *Scientific Reports* **6**, 34736 (2016).

87. Wu, Y., Zeng, L. & Zhao, S. Ligands of Adrenergic Receptors: A Structural Point of View. *Biomolecules* **11**, 936 (2021).

88. Masureel, M. *et al.* Structural insights into binding specificity, efficacy and bias of a β2AR partial agonist. *Nature Chemical Biology* **14**, 1059–1066 (2018).

89. Liu, X. *et al.* Mechanism of β_2 AR regulation by an intracellular positive allosteric modulator. *Science* **364**, 1283–1287 (2019).

90. Liu, X. *et al.* An allosteric modulator binds to a conformational hub in the β2 adrenergic receptor. *Nature Chemical Biology* **16**, 749–755 (2020).

91. Ahn, S. *et al.* Allosteric "beta-blocker" isolated from a DNA-encoded small molecule library. *Proceedings of the National Academy of Sciences* **114**, 1708–1713 (2017).

92. Shoichet, B. K. & Kobilka, B. K. Structure-based drug screening for G-protein-coupled receptors. *Trends in Pharmacological Sciences* **33**, 268–272 (2012).

93. Grisshammer, R. New approaches towards the understanding of integral membrane proteins: A structural perspective on G protein-coupled receptors. *Protein Science* **26**, 1493–1504 (2017).

94. Thal, D. M. *et al.* Recent advances in the determination of G protein-coupled receptor structures. *Current Opinion in Structural Biology* **51**, 28–34 (2018).

95. Grisshammer, R. The quest for high-resolution G protein-coupled receptor–G protein structures. *Proceedings of the National Academy of Sciences* **117**, 6971–6973 (2020).

96. Liu, W. *et al.* Serial Femtosecond Crystallography of G Protein–Coupled Receptors. *Science* **342**, 1521–1524 (2013).

97. Vinothkumar, K. R. & Henderson, R. Single particle electron cryomicroscopy: trends, issues and future perspective. *Quarterly Reviews of Biophysics* **49**, e13 (2016).

98. Piscitelli, C. L., Kean, J., de Graaf, C. & Deupi, X. A Molecular Pharmacologist's Guide to G Protein–Coupled Receptor Crystallography. *Molecular Pharmacology* **88**, 536–551 (2015).

99. Ghosh, E., Kumari, P., Jaiman, D. & Shukla, A. K. Methodological advances: the unsung heroes of the GPCR structural revolution. *Nature Reviews Molecular Cell Biology* **16**, 69–81 (2015).

100. Warne, T. *et al.* Structure of a β1-adrenergic G-protein-coupled receptor. *Nature* **454**, 486–491 (2008).

101. Heydenreich, F. M., Vuckovic, Z., Matkovic, M. & Veprintsev, D. B. Stabilization of G protein-coupled receptors by point mutations. *Frontiers in Pharmacology* **6**, (2015).

102. Scott, D. J., Kummer, L., Tremmel, D. & Plückthun, A. Stabilizing membrane proteins through protein engineering. *Current Opinion in Chemical Biology* **17**, 427–435 (2013).

103. Waltenspühl, Y., Ehrenmann, J., Klenk, C. & Plückthun, A. Engineering of Challenging G Protein-Coupled Receptors for Structure Determination and Biophysical Studies. *Molecules* **26**, 1465 (2021).

104. Tate, C. G. & Schertler, G. F. Engineering G protein-coupled receptors to facilitate their structure determination. *Current Opinion in Structural Biology* **19**, 386–395 (2009).

105. Rasmussen, S. G. F. *et al.* Crystal structure of the human β2 adrenergic G-protein-coupled receptor. *Nature* **450**, 383–387 (2007).

106. Steyaert, J. & Kobilka, B. K. Nanobody stabilization of G protein-coupled receptor conformational states. *Current Opinion in Structural Biology* **21**, 567–572 (2011).

107. Rasmussen, S. G. F. *et al.* Structure of a nanobody-stabilized active state of the β2 adrenoceptor. *Nature* **469**, 175–180 (2011).

108. Kruse, A. C. *et al.* Activation and allosteric modulation of a muscarinic acetylcholine receptor. *Nature* **504**, 101–106 (2013).

109. Wang, C. *et al.* Structure of the human smoothened receptor bound to an antitumour agent. *Nature* **497**, 338–343 (2013).

110. Fenalti, G. *et al.* Structural basis for bifunctional peptide recognition at human δ-opioid receptor. *Nature Structural & Molecular Biology* **22**, 265–268 (2015).

111. Chun, E. *et al.* Fusion Partner Toolchest for the Stabilization and Crystallization of G Protein-Coupled Receptors. *Structure* **20**, 967–976 (2012).

112. Fang, Y. Ligand–receptor interaction platforms and their applications for drug discovery. *Expert Opinion on Drug Discovery* **7**, 969–988 (2012).

113. Drew, D., Lerch, M., Kunji, E., Slotboom, D.-J. & de Gier, J.-W. Optimization of membrane protein overexpression and purification using GFP fusions. *Nature Methods* **3**, 303–313 (2006).

114. Andréll, J. & Tate, C. G. Overexpression of membrane proteins in mammalian cells for structural studies. *Molecular Membrane Biology* **30**, 52–63 (2013).

115. Chaudhary, S., Pak, J. E., Gruswitz, F., Sharma, V. & Stroud, R. M. Overexpressing human membrane proteins in stably transfected and clonal human embryonic kidney 293S cells. *Nature Protocols* **7**, 453–466 (2012).

116. MiliÄ‡, D. & Veprintsev, D. B. Large-scale production and protein engineering of G protein-coupled receptors for structural studies. *Frontiers in Pharmacology* **6**, (2015).

117. Luckow, V. A., Lee, S. C., Barry, G. F. & Olins, P. O. Efficient generation of infectious recombinant baculoviruses by site-specific transposon-mediated insertion of foreign genes into a baculovirus genome propagated in Escherichia coli. *Journal of Virology* **67**, 4566–4579 (1993).

118. Doré, A. S. *et al.* Structure of class C GPCR metabotropic glutamate receptor 5 transmembrane domain. *Nature* **511**, 557–562 (2014).

119. Jaakola, V.-P. *et al.* The 2.6 Angstrom Crystal Structure of a Human A_{2A} Adenosine Receptor Bound to an Antagonist. *Science* **322**, 1211–1217 (2008).

120. White, J. F. *et al.* Structure of the agonist-bound neurotensin receptor. *Nature* **490**, 508–513 (2012).

121. Warne, T., Chirnside, J. & Schertler, G. F. X. Expression and purification of truncated, non-glycosylated turkey beta-adrenergic receptors for crystallization. *Biochimica et Biophysica Acta (BBA) - Biomembranes* **1610**, 133–140 (2003).

122. Warne, T., Serrano-Vega, M. J., Tate, C. G. & Schertler, G. F. X. Development and crystallization of a minimal thermostabilised G protein-coupled receptor. *Protein Expression and Purification* **65**, 204–213 (2009).

123. Weiß, H. M. & Grisshammer, R. Purification and characterization of the human adenosine A_{2a} receptor functionally expressed in *Escherichia coli*. *European Journal of Biochemistry* **269**, 82–92 (2002).

124. Urh, M., Simpson, D. & Zhao, K. Chapter 26 Affinity Chromatography. in *Methods in enzymology* vol. 463 417–438 (2009).

125. Urh, M., Simpson, D. & Zhao, K. Chapter 26 Affinity Chromatography. in *Methods in enzymology* vol. 463 417–438 (2009).

126. Waugh, D. S. An overview of enzymatic reagents for the removal of affinity tags. *Protein Expression and Purification* **80**, 283–293 (2011).

127. Vergis, J. M. & Wiener, M. C. The variable detergent sensitivity of proteases that are utilized for recombinant protein affinity tag removal. *Protein Expression and Purification* **78**, 139–142 (2011).

128. Shimamura, T. *et al.* Structure of the human histamine H1 receptor complex with doxepin. *Nature* **475**, 65–70 (2011).

129. Granier, S. *et al.* Structure of the δ-opioid receptor bound to naltrindole. *Nature* **485**, 400–404 (2012).

130. Elgert, C., Rühle, A., Sandner, P. & Behrends, S. Thermal shift assay: Strengths and weaknesses of the method to investigate the ligand-induced thermostabilization of soluble guanylyl cyclase. *Journal of Pharmaceutical and Biomedical Analysis* **181**, 113065 (2020).

131. Caffrey, M. & Cherezov, V. Crystallizing membrane proteins using lipidic mesophases. *Nature Protocols* **4**, 706–731 (2009).

132. Neutze, R. & Moffat, K. Time-resolved structural studies at synchrotrons and X-ray free electron lasers: opportunities and challenges. *Current Opinion in Structural Biology* **22**, 651–659 (2012).

133. Barends, T. R. M. *et al.* Direct observation of ultrafast collective motions in CO myoglobin upon ligand dissociation. *Science* **350**, 445–450 (2015).

134. Pande, K. *et al.* Femtosecond structural dynamics drives the trans/cis isomerization in photoactive yellow protein. *Science* **352**, 725–729 (2016).

135. Tenboer, J. *et al.* Time-resolved serial crystallography captures high-resolution intermediates of photoactive yellow protein. *Science* **346**, 1242–1246 (2014).

136. Young, I. D. *et al.* Structure of photosystem II and substrate binding at room temperature. *Nature* **540**, 453–457 (2016).

137. Kupitz, C. *et al.* Serial time-resolved crystallography of photosystem II using a femtosecond X-ray laser. *Nature* **513**, 261–265 (2014).

138. Nango, E. *et al.* A three-dimensional movie of structural changes in bacteriorhodopsin. *Science* **354**, 1552–1557 (2016).

139. Hauser, A. S., Attwood, M. M., Rask-Andersen, M., Schiöth, H. B. & Gloriam, D. E. Trends in GPCR drug discovery: new agents, targets and indications. *Nature Reviews Drug Discovery* **16**, 829–842 (2017).

140. Deisseroth, K. Optogenetics: 10 years of microbial opsins in neuroscience. *Nature Neuroscience* **18**, 1213–1225 (2015).

141. Weitzman, M. & Hahn, K. M. Optogenetic approaches to cell migration and beyond. *Current Opinion in Cell Biology* **30**, 112–120 (2014).

142. Gorostiza, P. & Isacoff, E. Y. Optical Switches for Remote and Noninvasive Control of Cell Signaling. *Science* **322**, 395–399 (2008).

143. Velema, W. A., Szymanski, W. & Feringa, B. L. Photopharmacology: Beyond Proof of Principle. *Journal of the American Chemical Society* **136**, 2178–2191 (2014).

144. Broichhagen, J., Frank, J. A. & Trauner, D. A Roadmap to Success in Photopharmacology. *Accounts of Chemical Research* **48**, 1947–1960 (2015).

145. Lerch, M. M., Hansen, M. J., van Dam, G. M., Szymanski, W. & Feringa, B. L. Emerging Targets in Photopharmacology. *Angewandte Chemie International Edition* **55**, 10978–10999 (2016).

146. Leippe, P., Koehler Leman, J. & Trauner, D. Specificity and Speed: Tethered Photopharmacology. *Biochemistry* **56**, 5214–5220 (2017).

147. Donthamsetti, P. C. *et al.* Optical Control of Dopamine Receptors Using a Photoswitchable Tethered Inverse Agonist. *Journal of the American Chemical Society* **139**, 18522–18535 (2017).

148. Leippe, P., Koehler Leman, J. & Trauner, D. Specificity and Speed: Tethered Photopharmacology. *Biochemistry* **56**, 5214–5220 (2017).

149. Kramer, R. H., Mourot, A. & Adesnik, H. Optogenetic pharmacology for control of native neuronal signaling proteins. *Nature Neuroscience* **16**, 816–823 (2013).

150. Xu, X. *et al.* Binding pathway determines norepinephrine selectivity for the human β1AR over β2AR. *Cell Research* **31**, 569–579 (2021).

151. Dougherty, T. J. *et al.* Photodynamic Therapy. *JNCI Journal of the National Cancer Institute* **90**, 889–905 (1998).

152. Hüll, K., Morstein, J. & Trauner, D. *In Vivo* Photopharmacology. *Chemical Reviews* **118**, 10710–10747 (2018).

153. Adams, S. R. & Tsien, R. Y. Controlling Cell Chemistry with Caged Compounds. *Annual Review of Physiology* **55**, 755–784 (1993).

154. Ellis-Davies, G. C. R. Caged compounds: photorelease technology for control of cellular chemistry and physiology. *Nature Methods* **4**, 619–628 (2007).

155. Maurice Goeldner & Richard Givens. Dynamic Studies in Biology: Phototriggers, Photoswitches and Caged Biomolecules. (2006).

156. Bort, G., Gallavardin, T., Ogden, D. & Dalko, P. I. From One-Photon to Two-Photon Probes: "Caged" Compounds, Actuators, and Photoswitches. *Angewandte Chemie International Edition* **52**, 4526–4537 (2013).

157. Klausen, M. & Blanchard-Desce, M. Two-photon uncaging of bioactive compounds: Starter guide to an efficient IR light switch. *Journal of Photochemistry and Photobiology C: Photochemistry Reviews* **48**, 100423 (2021).

158. Pelliccioli, A. P. & Wirz, J. Photoremovable protecting groups: reaction mechanisms and applications. *Photochemical & Photobiological Sciences* **1**, 441–458 (2002).

159. Weinstain, R., Slanina, T., Kand, D. & Klán, P. Visible-to-NIR-Light Activated Release: From Small Molecules to Nanomaterials. *Chemical Reviews* **120**, 13135–13272 (2020).

160. Corrie, J. E. T., Barth, A., Munasinghe, V. R. N., Trentham, D. R. & Hutter, M. C. Photolytic Cleavage of 1-(2-Nitrophenyl)ethyl Ethers Involves Two Parallel Pathways and Product Release Is Rate-Limited by Decomposition of a Common Hemiacetal Intermediate. *Journal of the American Chemical Society* **125**, 8546–8554 (2003).

161. Muralidharan, S. & Nerbonne, J. M. Photolabile "caged" adrenergic receptor agonists and related model compounds. *Journal of Photochemistry and Photobiology B: Biology* **27**, 123–137 (1995).

162. Gienger, M., Hübner, H., Löber, S., König, B. & Gmeiner, P. Structure-based development of caged dopamine D2/D3 receptor antagonists. *Scientific Reports* **10**, 829 (2020).

163. Banghart, M. R. & Sabatini, B. L. Photoactivatable Neuropeptides for Spatiotemporally Precise Delivery of Opioids in Neural Tissue. *Neuron* **73**, 249–259 (2012).

164. Wilcox, M. *et al.* Synthesis of photolabile precursors of amino acid neurotransmitters. *The Journal of Organic Chemistry* **55**, 1585–1589 (1990).

165. Ricart-Ortega, M., Font, J. & Llebaria, A. GPCR photopharmacology. *Molecular and Cellular Endocrinology* **488**, 36–51 (2019).

166. Josa-Culleré, L. & Llebaria, A. In the Search for Photocages Cleavable with Visible Light: An Overview of Recent Advances and Chemical Strategies. *ChemPhotoChem* **5**, 296–314 (2021).

167. Schmidt, R., Geissler, D., Hagen, V. & Bendig, J. Mechanism of Photocleavage of (Coumarin-4-yl)methyl Esters. *The Journal of Physical Chemistry A* **111**, 5768–5774 (2007).

168. Schoenleber, R. O. & Giese, B. Photochemical Release of Amines by C,N-Bond Cleavage. *Synlett* 0501–0504 (2003) doi:10.1055/s-2003-37507.

169. Amatrudo, J. M. *et al.* Wavelength-Selective One- and Two-Photon Uncaging of GABA. *ACS Chemical Neuroscience* **5**, 64–70 (2014).

170. Morstein, J., Awale, M., Reymond, J.-L. & Trauner, D. Mapping the Azolog Space Enables the Optical Control of New Biological Targets. *ACS Central Science* **5**, 607–618 (2019).

171. Szymański, W., Beierle, J. M., Kistemaker, H. A. v., Velema, W. A. & Feringa, B. L. Reversible Photocontrol of Biological Systems by the Incorporation of Molecular Photoswitches. *Chemical Reviews* **113**, 6114–6178 (2013).

172. Hoorens, M. W. H. & Szymanski, W. Reversible, Spatial and Temporal Control over Protein Activity Using Light. *Trends in Biochemical Sciences* **43**, 567–575 (2018).

173. Beharry, A. A. & Woolley, G. A. Azobenzene photoswitches for biomolecules. *Chemical Society Reviews* **40**, 4422 (2011).

174. Bandara, H. M. D. & Burdette, S. C. Photoisomerization in different classes of azobenzene. *Chem. Soc. Rev.* **41**, 1809–1825 (2012).

175. Fujino, T., Arzhantsev, S. Yu. & Tahara, T. Femtosecond Time-Resolved Fluorescence Study of Photoisomerization of *trans* -Azobenzene. *The Journal of Physical Chemistry A* **105**, 8123–8129 (2001).

176. H. Rau. Photochemistry and Photophysics (Ed: J. F. Rabek). in 119 (1990).

177. Sadovski, O., Beharry, A. A., Zhang, F. & Woolley, G. A. Spectral Tuning of Azobenzene Photoswitches for Biological Applications. *Angewandte Chemie International Edition* **48**, 1484–1486 (2009).

178. Pozhidaeva, N., Cormier, M.-E., Chaudhari, A. & Woolley, G. A. Reversible Photocontrol of Peptide Helix Content: Adjusting Thermal Stability of the Cis State. *Bioconjugate Chemistry* **15**, 1297–1303 (2004).

179. Aleotti, F. *et al.* Spectral Tuning and Photoisomerization Efficiency in Push–Pull Azobenzenes: Designing Principles. *The Journal of Physical Chemistry A* **124**, 9513–9523 (2020).

180. Leistner, A. *et al.* Fluorinated Azobenzenes Switchable with Red Light. *Chemistry – A European Journal* **27**, 8094–8099 (2021).

181. Knie, C. *et al. ortho* -Fluoroazobenzenes: Visible Light Switches with Very Long-Lived *Z* Isomers. *Chemistry - A European Journal* **20**, 16492–16501 (2014).

182. Bahamonde, M. I. *et al.* Photomodulation of G Protein-Coupled Adenosine Receptors by a Novel Light-Switchable Ligand. *Bioconjugate Chemistry* **25**, 1847–1854 (2014).

183. Gómez-Santacana, X. *et al.* Photoswitching the Efficacy of a Small-Molecule Ligand for a Peptidergic GPCR: from Antagonism to Agonism. *Angewandte Chemie International Edition* **57**, 11608–11612 (2018).

184. Agnetta, L. *et al.* A Photoswitchable Dualsteric Ligand Controlling Receptor Efficacy. *Angewandte Chemie International Edition* **56**, 7282–7287 (2017).

185. Pittolo, S. *et al.* An allosteric modulator to control endogenous G protein-coupled receptors with light. *Nature Chemical Biology* **10**, 813–815 (2014).

186. Broichhagen, J. *et al.* Optical Control of Insulin Secretion Using an Incretin Switch. *Angewandte Chemie International Edition* **54**, 15565–15569 (2015).

187. Keppler, A. *et al.* A general method for the covalent labeling of fusion proteins with small molecules in vivo. *Nature Biotechnology* (2003) doi:10.1038/nbt765.

188. Gautier, A. *et al.* An Engineered Protein Tag for Multiprotein Labeling in Living Cells. *Chemistry and Biology* (2008) doi:10.1016/j.chembiol.2008.01.007.

189. Los, G. V. *et al.* HaloTag: A novel protein labeling technology for cell imaging and protein analysis. *ACS Chemical Biology* (2008) doi:10.1021/cb800025k.

190. Levitz, J. *et al.* Optical control of metabotropic glutamate receptors. *Nature Neuroscience* **16**, 507–516 (2013).

191. Izquierdo-Serra, M. *et al.* Optical control of endogenous receptors and cellular excitability using targeted covalent photoswitches. *Nature Communications* **7**, 12221 (2016).

192. Broichhagen, J. *et al.* Orthogonal Optical Control of a G Protein-Coupled Receptor with a SNAP-Tethered Photochromic Ligand. *ACS Central Science* **1**, 383–393 (2015).

193. Berizzi, A. E. & Goudet, C. Strategies and considerations of G-protein-coupled receptor photopharmacology. in 143–172 (2020). doi:10.1016/bs.apha.2019.12.001.

OBJECTIVES

Photopharmacology is an emerging field of research based on the usage of light-regulated molecules to allow reversible spatiotemporal control of target proteins or receptors. Therefore, this approach transforms light-insensitive proteins into light-sensitive proteins without the need of genetic manipulation. In the past years, several photocontrollable molecules have been reported, showing their ability to modulate the activation state of several G-protein coupled receptors (GPCRs). Using these innovative molecular tools, unprecedented research has been performed, which has enabled to better understand the complex roles and mechanisms of GPCR pharmacology. Additionally, several studies have evidenced the performance of this chemical approach to dynamically manage physiological conditions in a variety of biological systems through the application of light. These, and other recent studies, highlight the enormous potential of photopharmacology for the study of GPCR roles in physiological processes and the future development of improved therapeutics.

Beta-adrenoceptors (β-AR) are prototypical GPCRs, which have been widely studied due to their relevance in the regulation of important physiological roles, such as the cardiac output or smooth tissue relaxation in many areas of the body. Consequently, many approved drugs, both agonists and antagonists, are described to target these membrane proteins. Nevertheless, and despite the evident research and therapeutic potential of β-AR, the capabilities offered by the emerging field of photopharmacology have never been applied to the modulation of these GPCRs. In this context, the ***main objective*** of the present thesis is:

To design and synthesize photocontrollable (reversible and irreversible) molecules that enable modulation of the activation state of beta-adrenoceptors through the application of external light *in vitro* and *in vivo*.

Taking into account the main objective, the Ph.D. thesis was conducted according to the following ***specific objectives***:

I. To conceive and produce caged analogues of beta-adrenoceptor ligands that allow to irreversibly modulate targeted receptors through the application of light *in vitro* and *in vivo.* The molecular design of a caged antagonist, its photochemical characterization, and its light-dependent pharmacology in three different physiological systems are described in **Chapter 1**.

II. To develop the first photoswitchable ligands targeting beta-adrenoceptors to reversibly modulate their activation state with light. The design of the first series of azobenzene-based ligands, their photochemical characterization, and *in vitro* photopharmacology towards β_1-AR and β_2-AR are summarized in **Chapter 2**.

III. To devise the first β_1-AR selective photochromic ligands to optically modulate the beta-adrenergic drive in living animals. Design, photochemistry, *in vitro*, and *in vivo* assays performed for β_1-AR selective ABs are reported in **Chapter 2**.

IV. To enlarge the toolbox of azobenzene-based ligands targeting beta-adrenoceptors through the development of "red-shifted" photoswitches, which allow the reversible control of β-AR using the less toxic and more penetrant visible light. Two new series of azobenzene-based compounds that can be photoisomerized with blue and green light are described in **Chapter 3**.

V. To employ the developed molecular tools to perform structural studies of beta-adrenoceptors. Results from these studies can provide insight into the molecular determinants underlying the different functional activities described between the two photoisomers of a photochromic ligand. Expression, purification, and crystallization trials of β_1-AR and β_2-AR recombinant proteins bound to a photoswitchable ligand are summarized in **Chapter 4**.

RESULTS & DISCUSSION

Results & Discussion contents

Chapter 1. Caged ligands targeting β-AR: an irreversible approach to optically control physiological systems

Abstract

The aim of this chapter was to develop irreversible light-sensitive ligands targeting β-adrenoceptors. Using these photoactivatable ligands to modulate the activity of β-AR with spatiotemporal precision, we intended to provide an innovative tool to better understand the complex role of beta-adrenoceptors in physiological processes. Light-sensitive protecting groups were introduced in the chemical structure of well-known β-adrenoceptor ligands, both agonists and antagonists. The obtained caged ligands were then photochemically characterized, to ensure the light-triggered release of active molecules. Finally, one of the developed caged compounds was used to explore the light dependent modulation of the studied receptor in physiological systems, which included native cardiac tissues and living zebrafish larvae.

A paper related to this chapter has been submitted:

- Anna Duran-Corbera, Joan Font, Melissa Faria, Eva Prats, Marta Consegal, Juanlo Catena, Lourdes Muñoz, Demetrio Raldúa, Antonio Rodríguez-Sinovas, Amadeu Llebaria and Xavier Rovira. "*Caged-carvedilol as a new tool for visible-light photopharmacology of β-adrenoceptors in native tissues*"

1.1 Caged antagonists

1.1.1 Design and synthesis

Photochromic ligands can be designed following two approaches: photoswitching and photocaging. In the caging strategy, a described bioactive ligand is covalently bound to a PPG, which renders it inactive. Application of a particular wavelength triggers the release of the active molecule, which then is able to exert the desired biological effects. Photolytic release of the bioactive ligand is irreversible, which prevents subsequent deactivation of the compound. However, due to the simplicity of their chemical design, caged compounds have been extensively used in photopharmacology.[1–3] In addition, the release of a known compound, such as an approved drug, ensures a safe modulation of the physiological system after light application. For this reason, selecting an appropriate ligand to apply the caging strategy to, constitutes the first step on the design process.

Nowadays there are a number of synthetic ligands reported as β-adrenoceptor antagonists. Many of these molecules are approved drugs embedded within the category of beta-blockers, which are widely used for the treatment of various diseases, including cardiac conditions. For our study, we wanted to use a non-selective beta-blocker, which allowed to study the role of beta-adrenoceptors in a variety of physiological systems. Among the possible ligands, carvedilol (**11**) arose as an interesting option considering that it mainly targets beta

adrenoceptors in a non-selective manner, and it has also been described as an alpha-1 adrenergic receptor (α_1-AR) antagonist.[4] It is the modulation of α_1-AR what confers this drug with particular hypotensive effects. Furthermore, it has been recently demonstrated that carvedilol possesses a unique mechanism of action since it can stimulate β-arrestin signaling and promote receptor internalization while blocking Gs protein activation, a property named biased agonism.[5] Special efficacy for the treatment of heart failure has been attributed to these particular features, conferring carvedilol additional therapeutic potential which is worth exploring. Indeed, new applications based on the interesting pharmacological profile of carvedilol are emerging, such as enhancement of skeletal muscle contractility.[6] Altogether, makes carvedilol a specially interesting drug for physiological and pharmacological research, and it was consequently considered an appropriate ligand for the application of the caging strategy.

Once we had selected the active molecule for our studies, it was necessary to design the caged compound. Firstly, the optimal emplacement for the photocleavable moiety had to be defined, which is key for the success of the caging strategy. In order to assist this process, computational studies depicting the binding mode of carvedilol to our target receptor (β-AR) were performed (Figure 44A). From these studies, the ethanolamine backbone was identified as the ideal area to introduce the caging group, considering that it has two reactive groups responsible for key binding interactions (Figure 44A).[7] A careful evaluation of the two possible caging positions highlighted the secondary amine as our best option, both for its increased reactivity and its location within the binding pocket. This amine is strongly interacting with key residues Asp121$^{3.32}$ and Asn329$^{7.39}$,[8] and has no space to allow the introduction of a sterically demanding substituent. As a result, it was expected that introducing a cage moiety in this position would induce repulsive interactions leading to a loss in affinity and functional activity (Figure 44B).

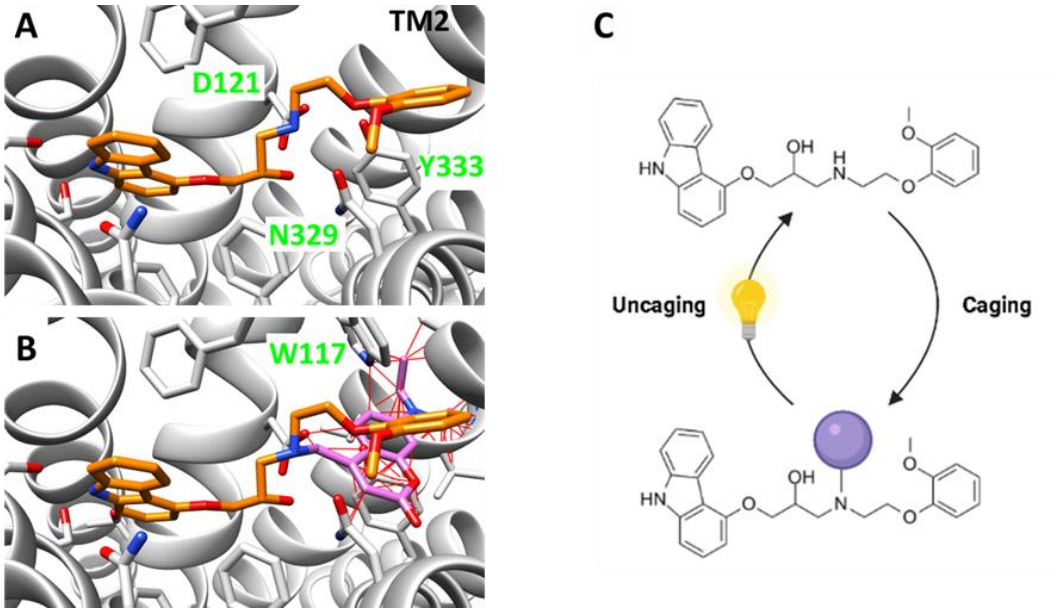

Figure 44. Design strategy of caged-carvedilol. Binding mode of carvedilol (A) and placement of caged-carvedilol (B) in the crystal structure of β_1-AR (PDB id: 4AMJ).[8] Carvedilol is colored in orange, coumarinyl group is colored in pink and clashes with residues of the receptor are represented by red lines. (C) General strategy to produce an irreversible light-sensitive β-AR antagonist.

Following the determination of the caging position, an appropriate photocleavable moiety had to be selected. A variety of PPG have been developed in the last decades, where photochemical and physicochemical properties of the caging groups have been improved.[9] Nevertheless, *o*-nitrobenzyl and coumarin groups are classical PPG, very well characterized and extensively used in biological systems.[9–11] Among these two conservative options, [7-(diethylamino)coumarin-4-yl]methyl (DEACM) was chosen as a PPG due to its higher λ_{max}, which decages within the visible range. Additionally, *o*-nitrobenzyl cages are photolyzed very easily when exposed to daylight, which makes the synthetic experimental part very challenging.

Chemical synthesis of the caged beta-blocker (**54**) was achieved by direct *N*-alkylation of carvedilol (**11**) with Br-DEACM (**53**) in the presence of triethylamine (Scheme 4). This constitutes a rare approach to introduce the PPG, considering that protection of an amine group is usually achieved through a carbamate linker. However, the possible intramolecular reaction between the carbamate and the alcohol groups, prompted us to attempt the direct alkylation of the PPG to the secondary amine. Racemic carvedilol was used as a starting material for the synthesis as this approved beta-blocker is administered as a racemate.

Scheme 4. Synthesis of caged-carvedilol (C-C, 54).

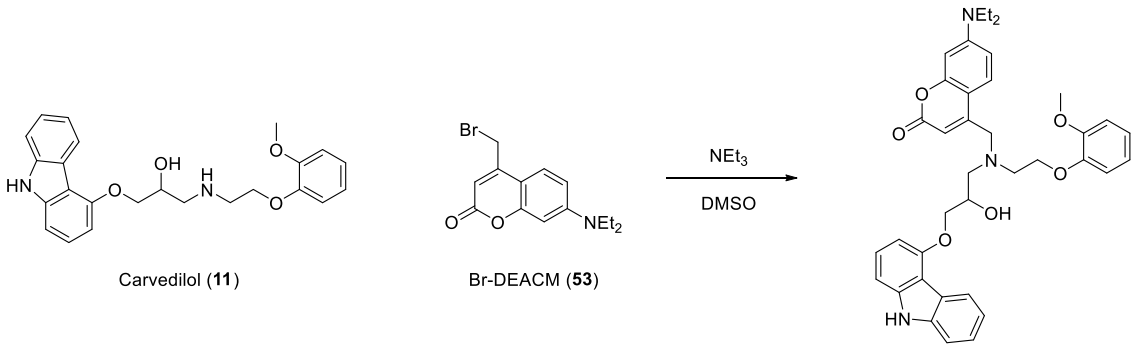

On the other hand, Br-DEACM (**53**) was synthesised through a well-described three step synthesis (Scheme 5).[12,13] Firstly, commercially acquired 7-diethylamino-4-methylcoumarin (**50**) was oxidized to **51** using SeO_2. The obtained aldehyde was then reduced to the respective alcohol (**52**) in good yield (85 %) using $NaBH_4$. Finally, the alcohol in **52** was substituted by a bromine using methanesulfonyl chloride and LiBr to yield Br-DEACM (**53**).

Scheme 5. Synthesis of Br-DEACM (53).[a]

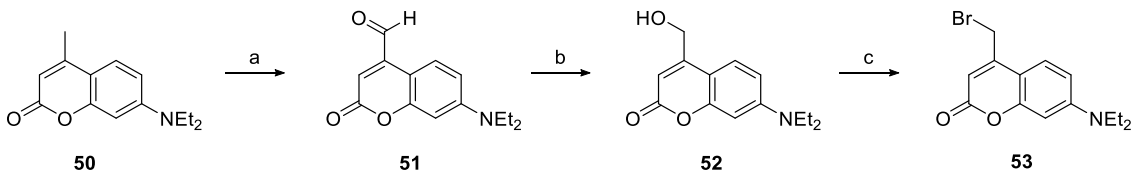

[a] Reagents and conditions: (a) SeO_2, xylene, Ar atmosphere, reflux, 5 days, 96%; (b) $NaBH_4$, MeOH, 0ºC, 12 h, 85%; (c) $MeSO_2Cl$, NEt_3, dichloromethane (DCM), 0 °C, 2 h. LiBr, THF, 2h, 26%.

1.1.2 Photochemistry and *in vitro* photopharmacology

Following the synthesis of the caged analogue of carvedilol we performed the photochemical characterization of the developed compound. However, caged compounds usually present poor solubility due to its highly lipophilic composition. For this reason, we previously performed solubility assays.

Aqueous solutions of the caged ligand at 1 mM concentration showed visible precipitation. Therefore, two diluted solutions of **54** were prepared at 100 µM and 10 µM concentrations (10 % and 1 % DMSO in H_2O respectively). From the same working solution, series of aliquots were taken and analyzed by HPLC-MS over the course of 1 h. HPLC-MS area analysis provided a qualitative assessment on the evolution of solution concentration over time (Figure 45). Results showed that HPLC-MS areas of the 100 µM solution were exponentially decreasing during the first hour, which suggested that precipitation was occurring even if it could not be visually detected. On the other hand, the diluted solution (10 µM) showed stable HPLC-MS areas over time, indicating that this is the optimal concentration to work with this compound to avoid precipitation issues.

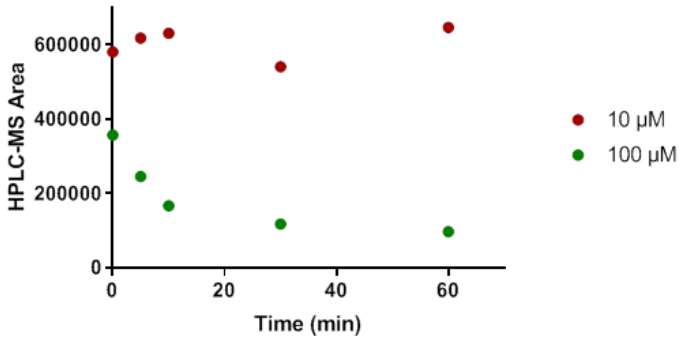

Figure 45. Evaluation of the solubility of the caged ligand 54. HPLC-MS areas of the 100 µM aqueous solution of **54** (10 % DMSO) are represented in green and the areas of the 10 µM aqueous solution of **54** (1 % DMSO) are represented in dark red.

Following the solubility studies and prior to the performance of uncaging experiments we also assessed the stability of carvedilol to illumination (Figure 46). For these experiments we prepared a 10 µM aqueous solution of carvedilol (1 % DMSO). Aliquots from the same working solution were illuminated for different times up to 3 minutes (CoolLED light system) and analyzed by HPLC-MS. Coumarin DEACM photoprotecting groups are usually photolyzed at 405 nm, which was the wavelength used in these experiments. In addition, we also evaluated the impact of applying different light intensities (50 % and 25 %) to the stability of the bioactive compound.

Results showed that carvedilol is chemically stable to illumination with 405 nm light at the two applied intensities, considering that the HPLC-MS areas were unaffected by the application of light for different times (Figure 46); Variations detected between the different samples can be attributed to the intrinsic variability of the HPLC-MS instrument. Therefore, the caged compound can be illuminated for up to 3 minutes using 405 nm light with no light-induced degradation of released carvedilol.

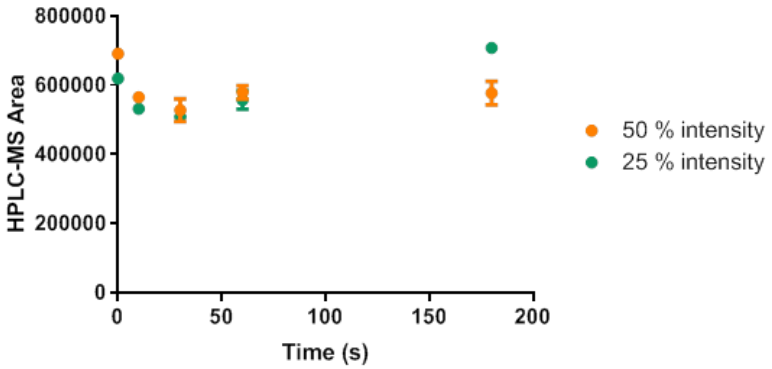

Figure 46. Evaluation of the stability of carvedilol (11) to illumination (405 nm). HPLC-MS areas of the solutions illuminated using the CoolLED light system set at 50 % intensity are represented in orange and areas of the solutions illuminated at 25 % intensity are represented in green. Data shows the mean ± S.E.M of two experiments performed in duplicate.

At this point, with all preliminary considerations successfully explored, we started the photochemical characterization of caged-carvedilol (**54**). Firstly, UV-Vis spectroscopy experiments were performed in order to identify the optimal wavelength to trigger compound uncaging. Figure 47A shows that the absorbance spectrum of caged-carvedilol results from the combination of the main absorption peaks of its two components (carvedilol and Br-DEACM). The introduction of a coumarinyl group is responsible for the appearance of a new maximal absorption band between 395-410 nm. This transition, which is not present in the absorbance spectrum of carvedilol, can be used to trigger the photolytic cleavage of the caging group. Illumination of the caged compound **54** using 405 nm light resulted in a noticeable decrease in the absorption at λ_{max}, which indicated a partial loss of the coumarin group.

On the other hand, quantification of uncaging was performed by HPLC-MS. The photolytic reaction is expected to occur through the cleavage of the C-N bond, releasing carvedilol and coumarinylmethyl alcohol. Samples were illuminated for different times up to 8 min and analyzed by HPLC-MS. HPLC-MS areas of carvedilol and its caged analogue were transformed into concentrations using previously prepared calibration curves. From these experiments it was evidenced that the uncaging efficiency of the developed compound is rather low. Only 12 % of the caged molecule was deprotected to yield carvedilol after 3 min of illumination at 405 nm (Figure 47B).

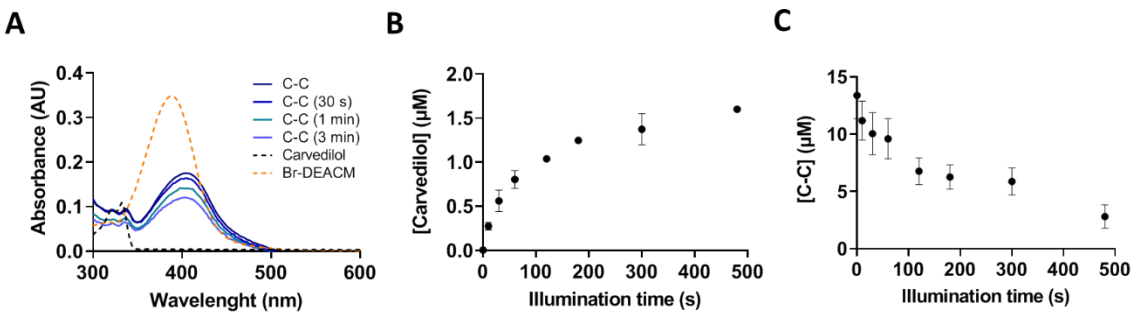

Figure 47. Photochemical characterization of caged-carvedilol (54). (A) UV-Vis spectra of carvedilol (**11**), Br-DEACM (**53**) and caged-carvedilol (**54**). (B) HPLC-MS quantification of released carvedilol after illumination of the caged compound with visible light (405 nm). (C) HPLC-MS quantification of **54** after illumination with visible light (405 nm). Data are shown as the mean ± SEM of three independent experiments.

This slower photolytic reaction, in comparison to other caged molecules, can be attributed to the linkage of the PPG through direct alkylation, which renders a relatively stable photocage. Indeed, it is known that carbamate linkers of amino groups facilitate the deprotection reaction and enable fast and efficient photocleavage.[14] However, for our purposes, working with a compound with lower photolytic reactivity facilitates purification and handling in biological assays, thus allowing for a precise administration of highly potent molecules, such as carvedilol which counts with sub-nanomolar binding affinities for β-AR.

We identified that uncaging reached a saturation level after 3 minutes of light application, with very little changes detected in the amounts of released carvedilol after 5- or 8-min illuminations. Nevertheless, even though longer illumination times did not result in higher carvedilol concentrations, the amount of caged carvedilol **54** kept decreasing (Figure 47B and C, Table 10), which suggested that an undesired reaction was occurring with the application of light. In order to further understand this unexpected event, we evaluated the molecular structure of the caged compound and proposed an alternative photolytic cleavage of **54** (Scheme 6).

Table 10. Uncaging quantification by HPLC-MS.

	Illumination time (s)							
	0	**10**	**30**	**60**	**120**	**180**	**300**	**480**
[Carvedilol] (μM)	0.006 ± 0.002	0.28 ± 0.04	0.56 ± 0.12	0.81 ± 0.10	1.0 ± 0.03	1.2 ± 0.02	1.4 ± 0.18	1.6 ± 0.02
[C-C (54)] (μM)	13.4 ± 2.0	11.2 ± 1.7	10.0 ± 1.8	9.6 ± 1.7	6.8 ± 1.2	6.2 ± 1.0	5.9 ± 1.2	2.8 ± 1.0

The application of light is known to trigger excitation of the coumarin-4-yl chromophore to an intermediate excited state. From this transient state, the C-N bond that links carvedilol to the coumarin-4-yl protecting group is expected to suffer heterolytic cleavage, thus releasing carvedilol (**11**) and DEACM-OH (**52**). However, we postulated that the excited state of compound **54** could also experience another heterolytic cleavage, where the C-N bond within the ethanolamine backbone of carvedilol could be broken, releasing a stable secondary amine (**55**). For this reason, we re-analyzed the HPLC-MS samples from our uncaging experiments and qualitatively detected the increasing presence of the secondary amine (**55**) with longer illuminations. This was a good indicative that undesired C-N cleavage upon the ethanolamine backbone of caged-carvedilol was occurring, as well as the expected uncaging reaction (Scheme 6).

Despite the difficulties arising from the light-triggered cleavage of C-C (**54**) through an undesired side reaction, we identified appropriate illumination conditions that allowed an acceptable photolytic release of carvedilol (**11**). Illumination of samples for 3 min at 405 nm (CoolLED system, 10 % intensity) induced the release of approximately 12 % carvedilol, while 62 % of caged compound still remained in solution. This constituted the best ratio obtained for carvedilol uncaging, with minimal compound degradation. Additionally, releasing low amounts

of carvedilol was not a problem considering the high affinity and efficacy of the beta-blocker. Therefore, we decided to further explore the possible biological applications of the developed molecular tool.

Scheme 6. Photolytic reactions of caged-carvedilol (54).

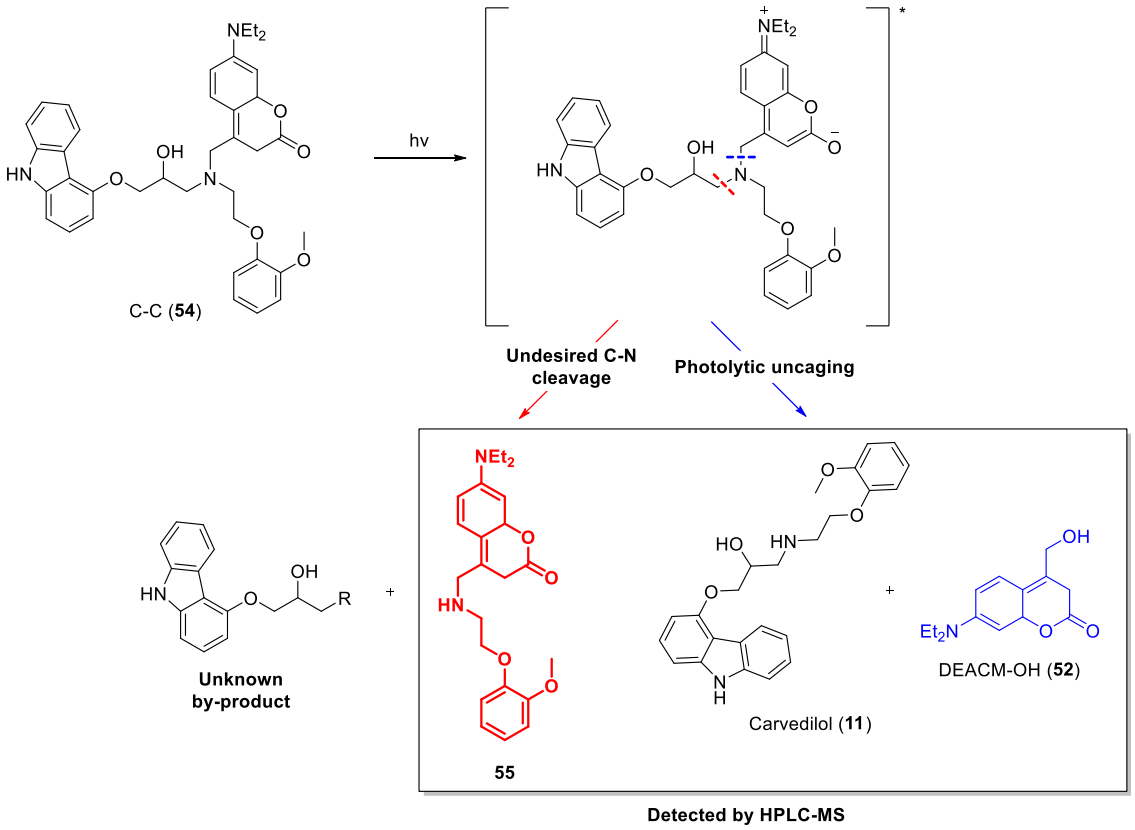

Firstly, *in vitro* experiments were performed in order to assess the potential of caged compound **54** to irreversibly control the activity of β-AR with light. For this reason, we developed a cellular system that would allow evaluation of the β-AR activation state in a simple and reproducible manner. β-AR are primarily coupled to the Gs protein, which upon activation causes an increase of the intracellular concentration of cAMP through the regulation of adenylate cyclase.[15] Consequently, the biological activity of the caged antagonist was evaluated through its ability to block the increase of intracellular cAMP induced by the addition of an agonist. An assay suitable to be employed under different illumination conditions was developed, using a genetically encoded Epac CFP-YPF fluorescence resonance energy transfer (FRET) sensor that allowed to dynamically monitor intracellular concentrations of cAMP.[16] Briefly, a HEK293 cell line, which endogenously expresses β_2-AR, was transfected with the cAMP sensor and a single clone was selected to establish a stable cell line. These cells, which homogeneously express the target receptor and the cAMP sensor, were used to evaluate ligand light-dependent activities. Complete characterization of the stable cell line, described in Materials & Methods (section 3.1), was performed prior to the characterization of light-sensitive molecules.

Light-dependent release of carvedilol was examined by antagonizing the activating effect of a β-AR agonist, cimaterol (**6**). Results showed that the introduction of the caging moiety to carvedilol completely abolished its functional activity at the tested concentrations (Figure 48). Additionally, application of light to caged-carvedilol (C-C) triggered the appearance of antagonistic activity over the cimaterol activated receptors. For instance, 100 nM samples subjected to 10 s illumination already reduced the activation state of β_2-AR by 55 %. Longer illuminations resulted in higher inhibition of the system, with 90 % of receptor function inhibition achieved when cells were treated with 100 nM caged-carvedilol illuminated for 3 min at 405 nm (Figure 48B). Therefore, these results mark the potential of the developed compound to regulate the activation state of β-AR with light in an irreversible manner.

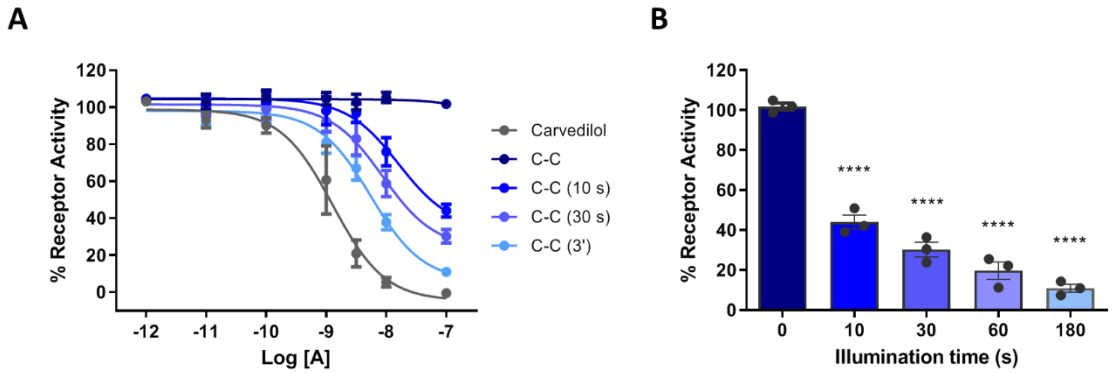

Figure 48. Photopharmacological characterization of caged-carvedilol. (A) Dose-response curves of carvedilol and its caged analogue **54** under different pre-illumination conditions treated with a constant concentration of agonist cimaterol (3 nM). (B) % Receptor Activity of a 100 nM solution of caged carvedilol **54** after illumination with blue light (405 nm) for different times. Data are shown as the mean ± SEM of three independent experiments. Statistical differences are denoted for adjusted p-values as follows: ****p < 0.0001.

1.1.3 Light-activated caged-carvedilol in cardiac function

Carvedilol is a non-selective beta-blocker, highly used for the treatment of a diverse number of cardiac conditions. For this reason, photolytic effects of caged-carvedilol (C-C) upon cardiac function were assessed. In a first series of experiments, perfused mice hearts or Langendorff hearts were used.[17] These assays were performed by the group of Dr. Antonio Rodríguez from the Vall d'Hebron Research Institute (VHIR).

In the Langendorff preparation, hearts are removed from mice and perfused in a reverse mode via the aorta (retrograde perfusion). Usually, a nutrient rich and oxygenated solution is used to perfuse the heart. Through this approach, nutrients and oxygen are continuously feeding the cardiac muscle, which can continue beating for hours outside of the animal body.[17] Therefore, this *ex-vivo* technique constituted a good physiological model to evaluate the light-dependent modulation of the cardiac frequency exerted by the caged beta-blocker without the complications involved with *in vivo* experimentation.

Cardiac effects of the light-sensitive antagonist were evaluated by the ability of the compound to reduce the increased cardiac frequency of a heart treated with an agonist. However, prior to experiments with the caged molecule, a dose-response curve of the bioactive molecule carvedilol was performed in the studied biological system (Figure 49). With this assay we

intended to determine the concentration of carvedilol required to significantly decrease the cardiac frequency and extrapolate it to a working concentration of its caged analogue. The obtained IC_{50} of carvedilol in perfused hearts was 2.5 µM. Therefore, and considering that we can maximally release 12 % of carvedilol after 3 min illumination, we used 25 µM of caged **54** for the rest of experiments.

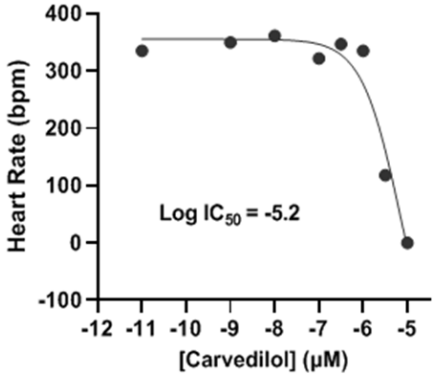

Figure 49. Dose-Response curve of the beta-blocker carvedilol in perfused mice hearts. Data are shown as the mean ± SEM of three independent experiments.

Control hearts were treated with the agonist isoprenaline (100 nM, for 10 min), which induced a significant increase in heart rate. A peak of about 160% of baseline values was observed after 3-4 min of starting agonist perfusion. This increment in the cardiac frequency was maintained for the entire duration of isoprenaline infusion. A progressive decline in the measurements was only observed after washing the agonist out. The increase in heart rate induced by isoprenaline was not modified when perfused hearts were simultaneously treated with 25 µM of C-C. In contrast, when the same experiment was performed with 25 µM of illuminated C-C no increment in the cardiac frequency was detected. This indicated that upon light application, free carvedilol had been released and was consequently blocking the effects of isoprenaline in perfused hearts (Figure 50).

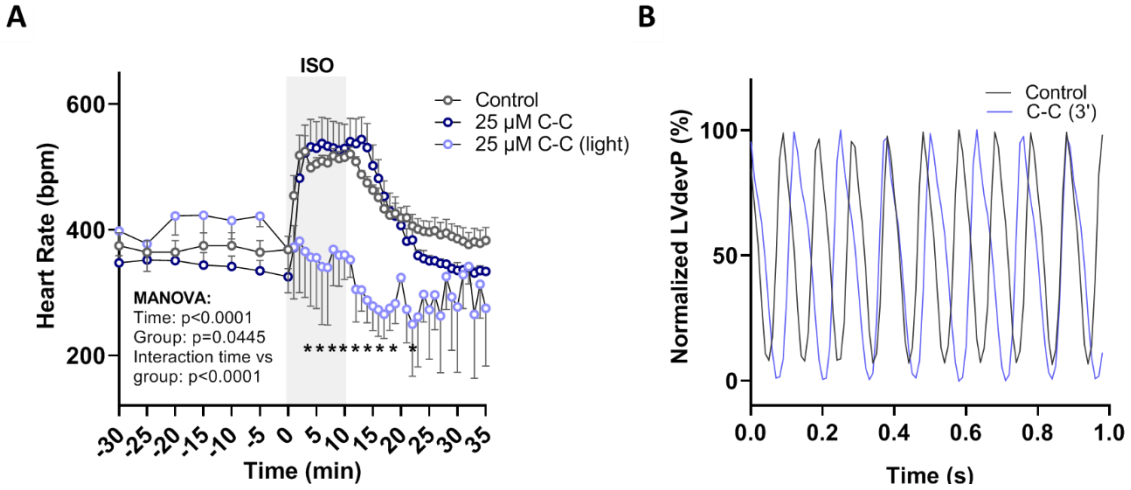

Figure 50. Evaluation of the light-dependent cardiac effects of C-C in Langendorff hearts. (A) Heart rate monitorization in isolated mice hearts treated with isoprenaline in the absence or presence of caged or uncaged (after 2x2.5 min illumination at 405 nm) carvedilol (n = 3-5). (B) Normalized left ventricular developed pressure (LvdevP) of mice perfused hearts treated with isoprenaline and isoprenaline + 25 µM C-C illuminated for 2x2.5 min. Data are shown as the mean ± SEM of three independent experiments. Statistical differences are denoted for adjusted p-values as follows: *p < 0.05.

In order to extrapolate the promising results obtained *ex-vivo*, the potential of the developed compound as a light-sensitive beta-blocker was also evaluated in an *in vivo* model. Zebrafish larvae of 7 days postfertilization (dpf) were used for this purpose considering that the subjects are transparent, which enabled non-invasive heart monitorization.

Exposures to the different treatment conditions were conducted for 1 h and the cardiac rhythm of the larvae was monitored using a microscope equipped with a camera. The obtained results were in good agreement with the cardiac effects observed in perfused hearts. No significant effects were measured in the cardiac frequency of animals treated with 25 µM C-C. In contrast, subjects exposed to the caged compound illuminated for only 30 s already presented a significantly reduced cardiac rhythm; furthermore, larvae illuminated for 3 min reduced the heart rate by 40 %. A comparable effect was observed when larvae were treated with 10 µM carvedilol, corroborating that the cardiac effects observed after illumination are related to the photolytic release of the beta-blocker (Figure 51). This activity is readily observable by visual inspection and when plotting the heartbeat (Figure 51B). Indeed, a delay in frequency becomes evident upon the addition of illuminated caged-carvedilol in comparison to control animals, similar to what it is observed in perfused mice hearts (Figure 50B). Therefore, we have successfully developed a diffusible caged antagonist targeting β-AR, that enables a selective control of cardiac function through the application of light in two distinct physiological models.

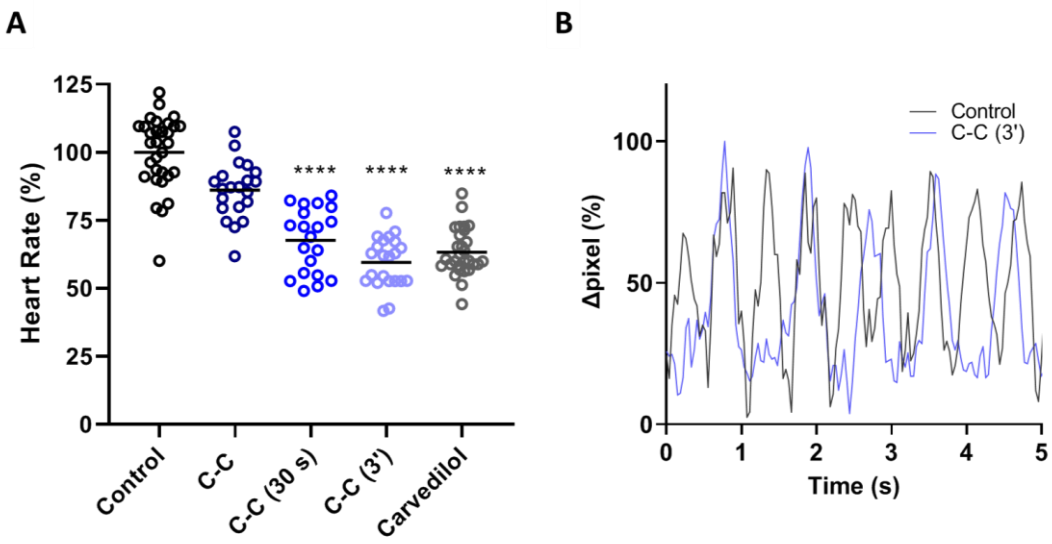

Figure 51. Evaluation of light-dependent cardiac effects of C-C in living zebrafish larvae (7 dpf). (A) Normalized heart rate of different experimental groups of zebrafish larvae (n = 20-31). (B) Representation of the cardiac profile extracted from the recorded videos using MATLAB. Data are shown as the mean ± SEM of three independent experiments. Statistical differences are denoted for adjusted p-values as follows: ****p < 0.0001.

Cardiac modulation with the application of light was firstly achieved by means of optogenetics.[18–22] The use of this innovative technique provided a valuable tool for the investigation of cardiac physiology and pointed to possible therapeutic applications based on the precise control of the heart rhythm using light. However, this approach requires genetic manipulation, which limits its clinical prospects. More recently, light-dependent cardiac modulation of rats and frog tadpoles was reported using a photoswitchable agonist targeting

muscarinic receptors.[23] However, photocardiac control through the modulation of the adrenergic pathway had never been reported. Therefore, the developed caged-carvedilol enlarges the photopharmacological toolbox to study the complex mechanisms of cardiac function. Additionally, the proof of concept of this study, in which a photolytic release of an approved drug is demonstrated, highlights the potential of this approach for future therapeutic applications.

1.1.4 *In vivo* modulation of animal behavior

Finally, it is well described that the activation of β-AR is related to the "fight or flight" response. A recent study reports that blocking the adrenergic signaling pathway significantly reduces the escape response of zebrafish embryos to external visual stimuli.[24] Similarly, here we evaluated the modulation of the vibrational-evoked startle response exerted by the developed caged compound under different illumination conditions using zebrafish larvae. Behavioral assays were established with the advice and technical support of Dr. Demetrio Raldúa, Dr. Melissa Faria and Dr. Eva Prats (IDAEA-CSIC).

In these experiments, animals were exposed to different treatments (carvedilol, C-C and C-C illuminated for 30 s and 3 min) during 1 h under dark conditions. Following the exposure, animals were left to acclimate for 10 min and then monitorization of zebrafish behavior was conducted. Initially, following the acclimation period, the basal locomotor activity (BLA) of the different groups of zebrafish was recorded. Then, the studied groups were subjected to 50 consecutive vibrational stimuli which assessed two behavioral parameters, vibrational-evoked startle response and its habituation after repetitive stimuli.[25]

Results showed no significant differences in BLA between the treatment groups, suggesting that blocking the adrenergic pathway does not have effects on the mobility of zebrafish larvae (Figure 52).

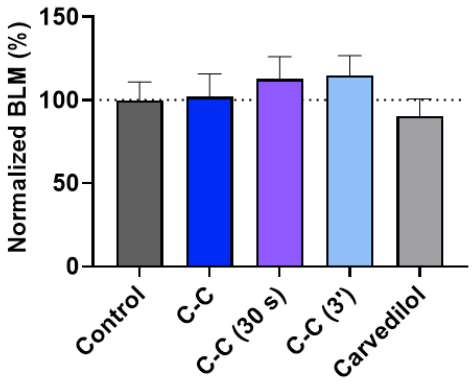

Figure 52. Normalized Basal Locomotor Activity of zebrafish larvae from different experimental groups. Control (n = 47), Carvedilol 10 µM (n = 36), Caged-Carvedilol (C-C) 25 µM (n = 27) and C-C 25 µM illuminated with 405 nm light for 30s (n = 25) or 3 min (n = 27). To determine the BLM, larvae movement was recorded for 10 min after a 10 min period of acclimatation. Data are shown as the mean ± SEM. Tukey's multiple comparison test did not show statistical difference between the different experimental groups.

On the other hand, a significant reduction of the startle response to the first tapping stimulus was observed only when larvae had been exposed to carvedilol or C-C illuminated for 3 min.

Both treatments reduced the escape response of zebrafish larvae similarly, by approximately 35 % (Figure 53A). This, according to the reported literature, indicated that in both zebrafish groups the adrenergic drive had been blocked.[24] Additionally, habituation of the vibrational-evoked escape response was significantly delayed (AUC above the control) by carvedilol and C-C illuminated for 3 minutes (Figure 53B). These results demonstrate that groups treated with carvedilol have an altered non-associative learning process, as the larvae maintained a higher escape response through the 50 consecutive vibrational stimuli. Therefore, we have successfully achieved a light-dependent control of zebrafish behavior using the developed caged.

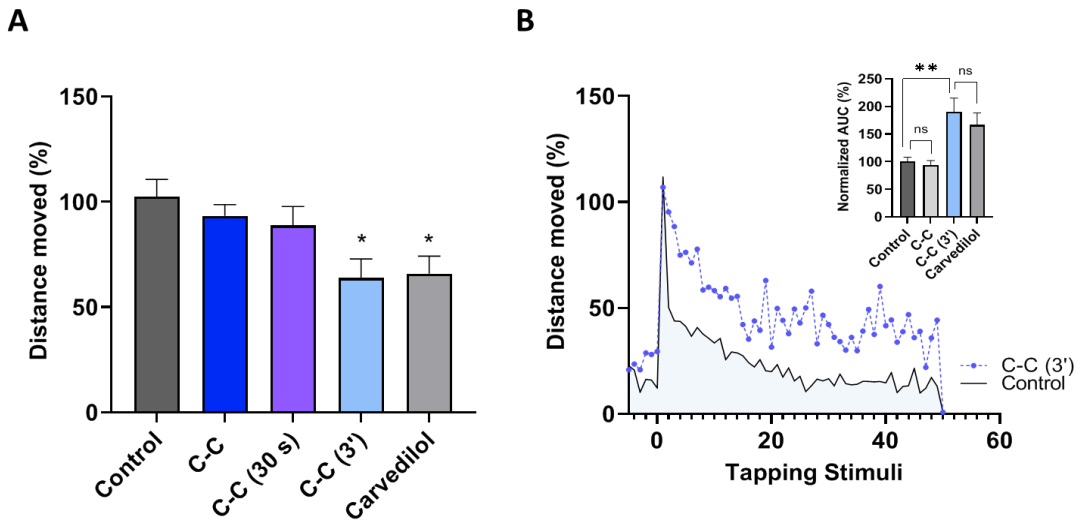

Figure 53. Zebrafish larvae escape response and their habituation behavior. (A) Normalized distance moved (mean ± SEM) during the startle response of the zebrafish larvae (7 dpf) treated with 1% DMSO, 10 µM carvedilol and 25 µM C-C, either in the dark or after 30 s and 3 min illuminations (405 nm); startle response was measured immediately after the application of the first tapping stimulus (n = 26-44). (B) Habituation profile of zebrafish larvae treated with 1% DMSO or 25 µM C-C illuminated for 3 min (405 nm). The profile is represented as the decrease in the normalized distance moved by the animals across 50 tapping stimuli delivered with 1 s intervals. AUCs (mean ± SEM) of the two groups and of 10 µM carvedilol and 25 µM C-C in the dark are represented as an inset to the plot (n = 21-46). Statistical differences are denoted for adjusted p-values as follows: *p < 0.05 and **p < 0.01.

The complex mechanisms underlying the effects observed on stimuli habituation are not completely understood and can be a consequence of multiple factors as numerous receptors and neural circuits can be involved in this process.[26,27] For instance, it has been described that modulation of the cholinergic and serotonergic pathways can affect this simple form of non-associative learning.[27] Interestingly, interactions of carvedilol with the muscarinic receptor M2 and the serotonin receptor 5-HT_{2A} have been reported in the literature.[28,29]. In addition, other aminergic systems, such as dopamine D2 receptors have also been involved in behavioral plasticity and habituation.[26] Interestingly, D2 and β_1-AR have been found to co-localize in prefrontal cortical cells affecting each other functional properties upon activation.[30] Overall, the significant effects of carvedilol and uncaged C-C observed in the habituation behavior of zebrafish larvae could be due to the modulation of these or other pathways. However, given the wide distribution of β-AR in the brain[31] it can be difficult to map the neural circuits involved. In this context, caged-carvedilol could represent an interesting research tool to explore the involvement of β-AR in this and other animal behaviors, thus providing a better understanding on their important role in the central nervous system.

1.2 Caged agonists

1.2.1 Design and synthesis

Following the successful development of a caged antagonist targeting beta-adrenoceptors, we decided to apply a similar strategy to develop a caged agonist. Once again, the first step of the design process consisted of the selection of a known ligand suitable for the caging approach.

As previously described with beta-blockers, there is also a large number of molecules reported as β-AR agonists. Additionally, many of these compounds are approved drugs for the treatment of several conditions, including respiratory diseases such as asthma.[32] After an initial evaluation of the possible options, we considered two options: isoprenaline (**4**) and cimaterol (**6**) (Figure 54).

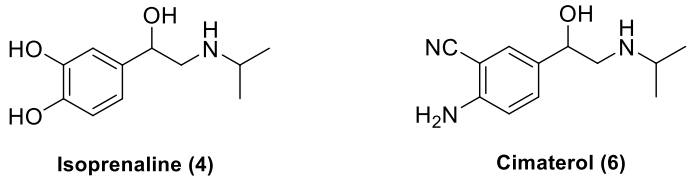

Figure 54. Chemical structure of two non-selective β-AR agonists.

Isoprenaline was our initial option as it is an approved drug widely used in both research and clinical applications. However, there were some red flags we wanted to evaluate before continuing to the design of the caged analogue. For instance, the chemical structure of isoprenaline presents several reactive groups, such as the two phenols of the catechol moiety and the secondary amine on the ethanolamine backbone. This would constitute a problem if we wanted to regioselectively introduce the photo protecting group, as we could expect multiple mono-, di-, and tri-substituted by-products resulting from alkylation of the phenols and the secondary amine. Therefore, additional synthetic complexity or purification efforts would have to be taken in order to isolate a mono-substituted caged compound. On the other hand, isoprenaline is a catecholamine, which could also introduce a chemical stability issue. The catechol moiety (**56**) can be easily oxidized to highly reactive *o*-quinones (**57**) in protic media (Figure 55).[33] As a consequence, it had to be evaluated if the compound is stable to light application.

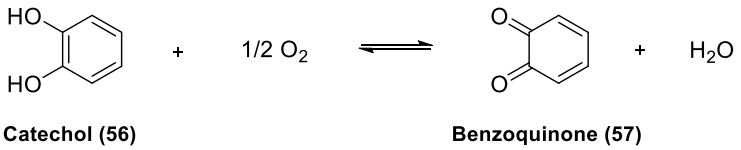

Figure 55. Oxidation of a catechol moiety to a quinone.

For these reasons, we also considered cimaterol as a possibility, an agonist increasingly used in β-AR research applications. This compound has an aniline group that could be potentially alkylated with our caging group. However, it is expected that the secondary amine will be more reactive than the aniline group, facilitating a regioselective alkylation. On the other hand, the molecular structure of the compound does not appear to have any substructures susceptible to be degraded or reactive upon light application.

Therefore, to select an appropriate ligand, we evaluated the stability of the two compounds to light application (Figure 56). Aqueous samples of the compounds (0.5 mg/mL, 1% DMSO) were illuminated for different times at 405 nm for up to 2 hours. Qualitative analysis was performed by HPLC-MS in an equivalent manner to the experiments performed with carvedilol (Materials & Methods, section 2.2).

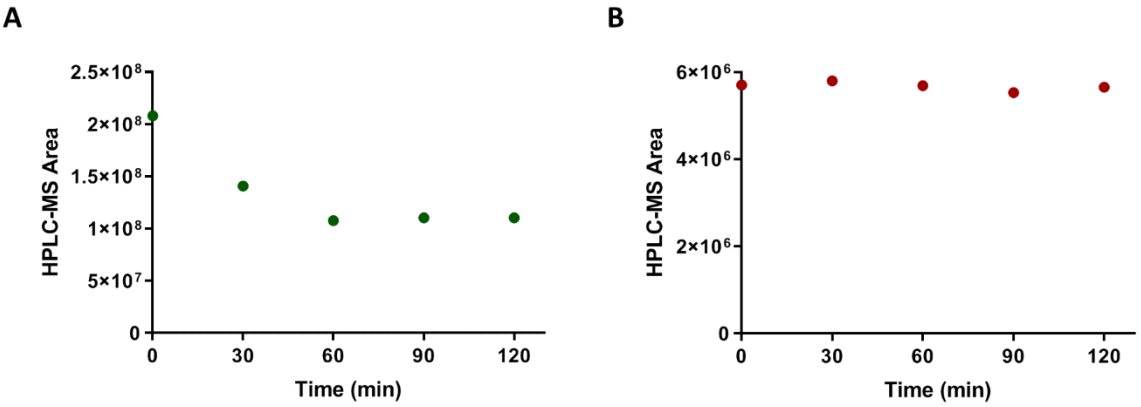

Figure 56. Evaluation of the stability of isoprenaline (A) and cimaterol (B) to illumination (405 nm). HPLC-MS areas of the solutions illuminated with the CoolLED (set at 10% intensity) are represented.

Results showed that, as we predicted, isoprenaline gets degraded with time. Interestingly, a continuous decrease in the HPLC-MS areas was observed during the first hour followed by a stabilization of the HPLC-MS areas in the second hour, which suggested that the oxidation process had reached an equilibrium (Figure 56A). On the contrary, cimaterol showed good stability to light application, with homogeneous HPLC-MS area values over the course of two-hour illuminations (Figure 56B). As a consequence, cimaterol was selected as the optimal ligand to apply the caging strategy to.

In order to design the caged molecule, we followed an analogous strategy to the one used with the caged antagonist, which provided successful results. Therefore, our design was based on the introduction of a coumarin photo protecting group (PPG) to the secondary amine of the ethanolamine backbone. This substitution was expected to hamper the key interactions of the ethanolamine substructure with the binding pocket of β-AR, providing an inactive caged agonist.

In this case, the agonist cimaterol was not obtained commercially; it was synthesized following a reported route (Scheme 7).[34,35] Firstly, bromination of acetophenone (**58**) was achieved through an electrophilic aromatic substitution with *N*-bromosuccinimide (NBS). Both aromatic substituents on **58** directed the aromatic halogenation to the 3-position and compound **59** was obtained in good yield (96%). Then, the aromatic bromine of **59** was substituted by cyanide using CuCN and compound **60** was isolated (80% yield). The α-carbon of the ketone was then brominated using $CuBr_2$, which yielded **61**. The alpha bromination reaction proceeded with good yield (88%). Finally, a one-pot reaction was performed to produce the agonist cimaterol (**11**) in low yield (16%). The bromine in the alpha carbon was firstly substituted by isopropylamine and the ketone was then sequentially reduced to the secondary alcohol using $NaBH_4$, which yielded agonist **11**.

Scheme 7. Synthesis of the beta-adrenoceptor agonist cimaterol.[a]

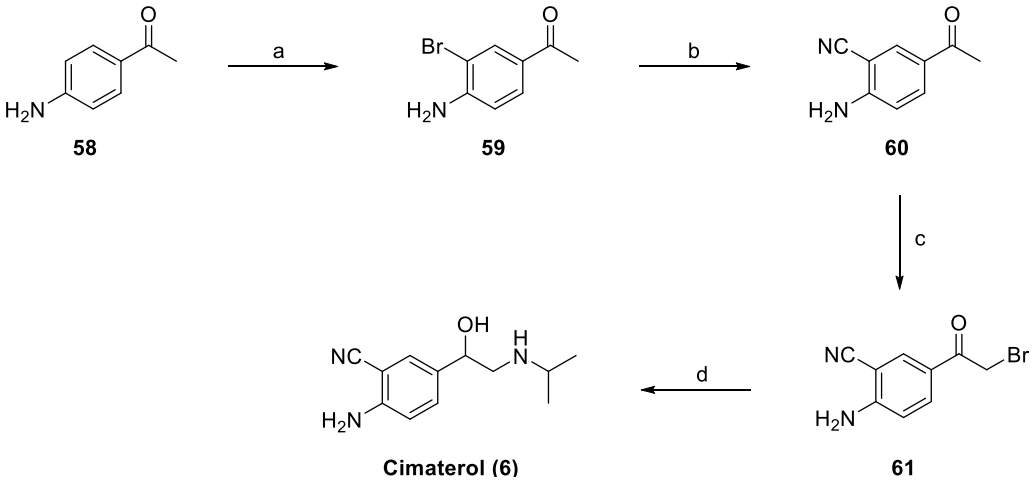

[a] Reagents and conditions: (a) NBS, acetonitrile, 0ºC to r.t, 12 h, 96%; (b) CuCN, DMF, Ar atmosphere, 160ºC, 6 h, 80%; (c) $CuBr_2$, 1:1 $CHCl_3$:EtOAc, N_2 atmosphere, 70°C, 2 h, 88%; (d) (I) Isopropylamine, EtOH, N_2 atmosphere, 0ºC to 60ºC, 2h; (II) $NaBH_4$, 0ºC to r.t, 4h, 16%.

Once cimaterol (**62**) had been synthesized, its caged version was produced by direct alkylation of the secondary amine with Br-DEACM (**53**) in DMSO with triethylamine. As described for carvedilol, the PPG could not be introduced in the form of a carbamate due to the possible intramolecular reaction occurring between the carbonyl group of the carbamate and the secondary alcohol of cimaterol.

Scheme 8. Synthesis of a caged analogue of cimaterol.

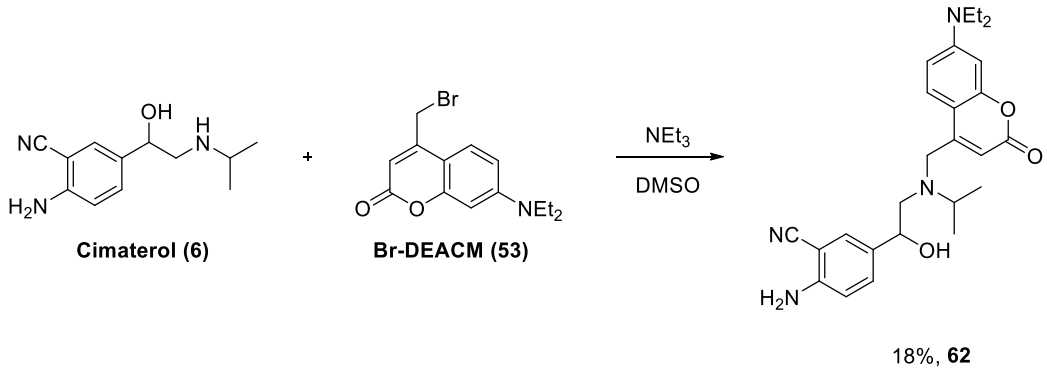

1.2.2 Photochemistry

Once the caged analogue of cimaterol (**11**) had been synthesized, we had to characterize its photolytic properties to establish the appropriate illumination conditions to release β-AR agonist cimaterol. As a consequence of the photolytic reaction occurring in the C-N bond, DEACM-OH (**52**) is expected to be released as a by-product (Scheme 9).

Firstly, UV-Vis experiments were performed to evaluate the optimal wavelength to trigger uncaging of **62** (Figure 57A). Similarly to what we observed with the caged antagonist, introducing a coumarin-4-yl group to cimaterol causes the appearance of a new maximal absorption band between 395-410 nm. Therefore, 405 nm was again selected as the appropriate wavelength to trigger the release of the active compound cimaterol.

Scheme 9. Photolytic reaction of caged-cimaterol (62).

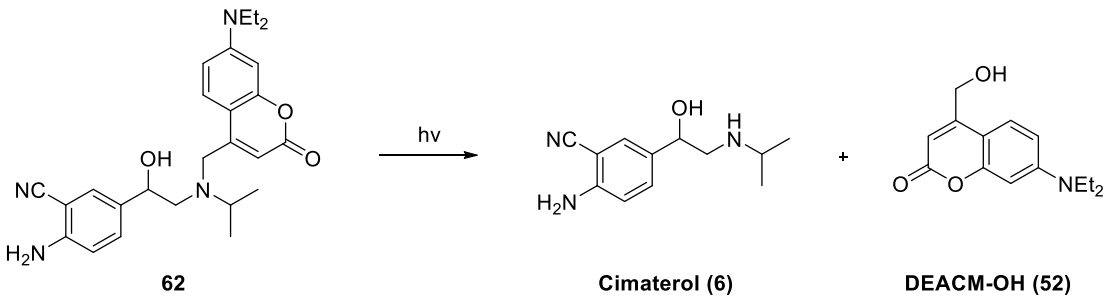

62 Cimaterol (6) DEACM-OH (52)

Quantification of the uncaging of caged-cimaterol (**62**) was performed by HPLC analysis. Samples of **62** (100 µM, 1% DMSO in PBS) were illuminated for different times at 405 nm (CoolLED set at 10% intensity) for up to 10 minutes. Illuminated solutions were then analyzed by HPLC and the areas corresponding to cimaterol were transformed into concentrations using a calibration curve of the agonist previously prepared. Results from these experiments showed that approximately 10% of cimaterol had been released upon illumination (Figure 57B), which was in good agreement with the maximal uncaging achieved with caged-carvedilol (**54**). In this case, the concentration of released cimaterol reached its maximum (10 µM) after 3 min of illumination at 405 nm and was thereafter maintained even if light was applied for longer times.

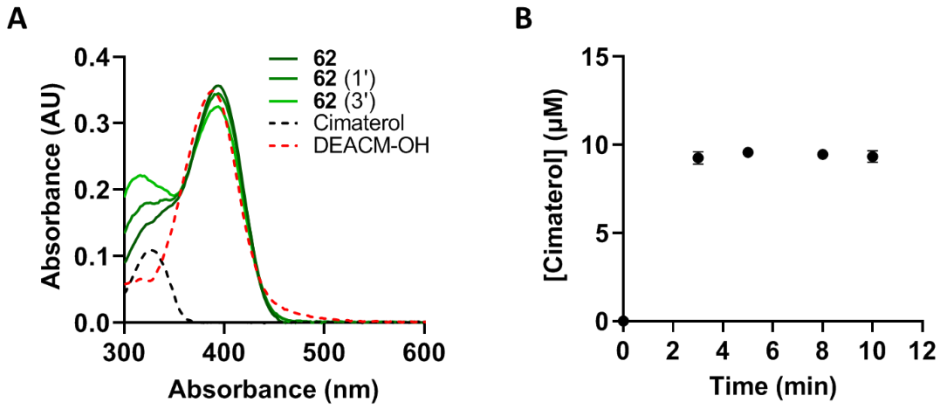

Figure 57. Photochemical characterization of caged-cimaterol (62). (A) UV-Vis spectra of cimaterol, Br-DEACM and caged-cimaterol (**62**). (B) HPLC quantification of released cimaterol after illumination of a 100 µM solution of caged compound (**62**) with visible light (405 nm). Data are shown as the mean ± SEM of two independent experiments.

However, careful evaluation of the HPLC profile of the illuminated samples (absorbance was followed at 385 nm) highlighted unexpected light-triggered processes (Figure 58). After 3 minutes of light application (405 nm), HPLC showed no remaining caged compound (**62**) (r.t. = 4.16 min), which was surprising considering that only 10% of cimaterol had been released. The chromatogram showed two main peaks, one of which corresponded to the uncaging by-product DEACM-OH (**52**) (r.t. = 4.47 min). Nevertheless, the major peak (r.t. = 3.41 min) obtained after the photolysis of caged-cimaterol (**62**) corresponded to an unknown by-product.

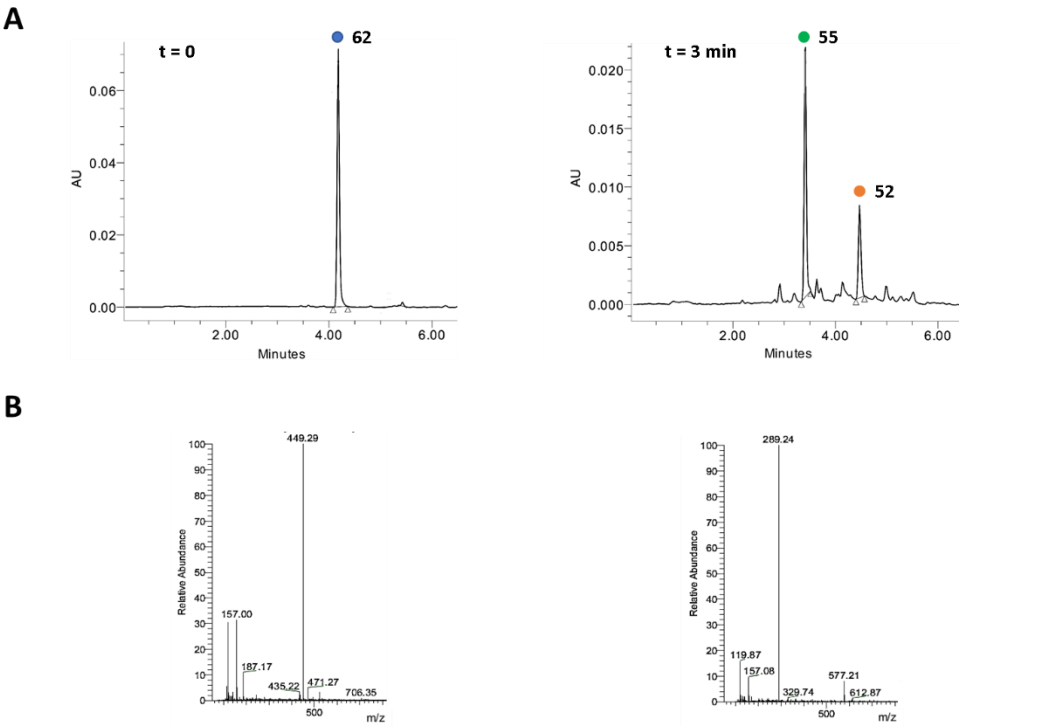

Figure 58. Uncaging characterization of caged-cimaterol (62). (A) HPLC chromatograms of caged-cimaterol **62** before and after illumination with 405 nm light; absorbance was detected at 385 nm. (B) MS spectra for the major peaks of caged-cimaterol (**62**) samples before and after illumination (405 nm) analyzed by HPLC-MS.

In order to further understand the light-triggered photolysis of caged-cimaterol, samples illuminated for 3 min were analyzed by HPLC-MS (Figure 58B). The main peak of the illuminated sample presented an *m/z* $[M+H]^+$ of 289. This mass was consistent with the molecular weight of the coumarin by-product (**55**), that results from the C-N cleavage of the ethanolamine backbone of cimaterol. Therefore, it was identified that the developed caged derivative (**62**) was undergoing undesired heterolytic cleavage due to the application of light, in an analogous manner to the process described for caged-carvedilol (**54**) (Scheme 10).

However, undesired lysis of the compound triggered by light occurred in a faster manner for the caged agonist compared to C-C (**54**), as no caged compound was remaining after 3 min illuminations at 405 nm. This suggested that direct linkage of the molecular fingerprint to the aromatic substructure of cimaterol was favoring the unwanted photolytic reaction. Nevertheless, the mechanisms underlying this alternative cleavage of the caged compounds are not well-understood and were not further explored.

Scheme 10. Undesired photolytic reaction of caged-cimaterol (62).

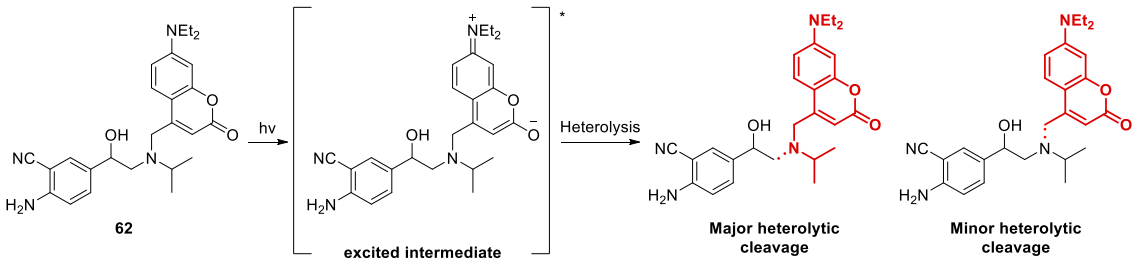

Additional uncaging experiments were performed using different wavelengths to assess if the alternative photolytic reaction could be prevented from occurring. Samples containing 100 µM of **62** (1% DMSO in PBS) were illuminated for 5 minutes using 4 different wavelengths: 380 nm, 455 nm, 500 nm and 535 nm (CoolLED light system, 10% intensity).

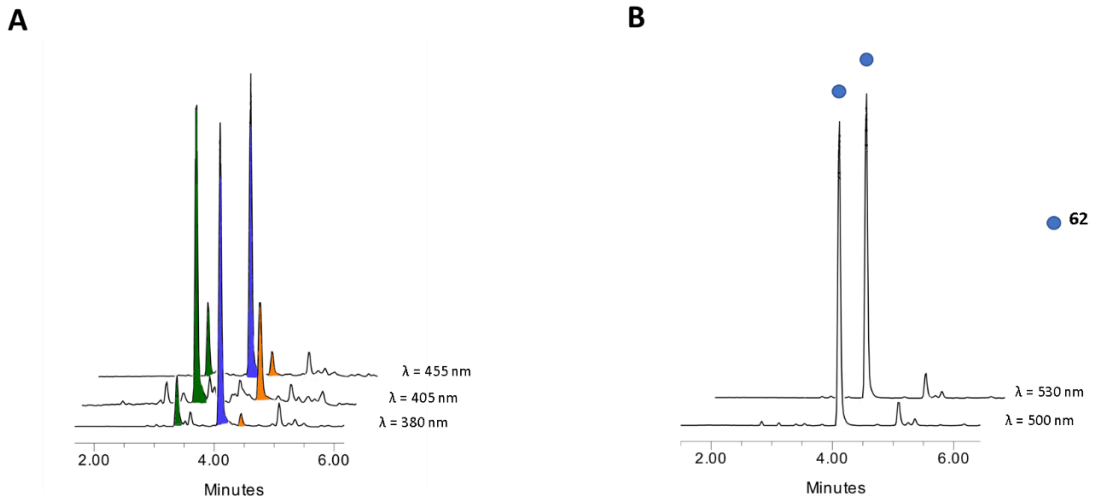

Figure 59. Optimization of the uncaging reaction of caged-cimaterol. (A) HPLC chromatograms of caged-cimaterol **62** after 5 min illuminations with the CoolLED source at 380 nm, 405 nm and 455 nm. Peaks of the secondary amine (**55**) are highlighted in green, peaks corresponding to the caged ligand (**62**) are colored in blue and peaks corresponding to the uncaging coumarin by-product (**52**) are highlighted in orange. (B) HPLC chromatograms of caged-cimaterol **62** after 5 min illuminations with the CoolLED source at 500 nm and 535 nm. Intensity was set at 10% for all wavelengths tested.

These results highlighted that illuminating samples using lower energy wavelengths (500 nm and 535 nm) did not trigger any photolytic reaction, as one main peak corresponding to caged-cimaterol (**62**) was detected by HPLC (Figure 59B). This was consistent with the lack of absorption of the caged compound at the mentioned wavelengths. On the other hand, it was observed that the best wavelength to trigger photolytic cleavage of **62**, both desired and undesired, was 405 nm. When samples were illuminated at 380 nm and 455 nm most of the caged compound remained intact and very low amounts of the uncaging by-product were detected (Figure 59A). In both cases, the alternative heterolytic C-N cleavage was favored when compared to the uncaging reaction, as the peak for the resulting by-product **55** was more intense than the peak corresponding to DEACM-OH (**52**). Consequently, no appropriate illumination conditions were identified to trigger the uncaging of caged compound **62**. Taking into account that 90% of the compound is photolyzed in an undesired manner, the developed caged molecule is not suitable for biological applications.

Due to the fact that caged agonists have already been described in the literature[36], it was decided to discontinue the development of this part of the project. However, there are two strategies that could possibly amend the encountered problem. The first approach would consist on the introduction of a labile photo-protecting group, such as an *o*-nitrobenzene, to the secondary amine of the molecular fingerprint. By doing this, the uncaging reaction would be favored, and the cleavage of the ethanolamine backbone of the compounds potentially minimized. The second approximation would consider the modification of the caging position to the aromatic area, which would ensure the correct photolytic release of the bioactive molecule. However, this approach would probably entail higher synthetic complexity.

1.3 Conclusions

In the present chapter, we have described the development of the first diffusible caged antagonist targeting β-AR. Carvedilol (**11**), a non-selective beta-blocker, was the chosen ligand for the application of the caging strategy. A coumarin-4-yl protecting group (DEACM) was introduced to the secondary amine of carvedilol by direct alkylation. Release of the active compound was achieved by the application of light in the visible range (405 nm), which was essential in order to avoid phototoxicity. However, the uncaging reaction was rather inefficient, considering that only 12% of the beta-blocker was released in the optimal illumination conditions. Additionally, HPLC and HPLC-MS uncaging experiments identified that an alternative and undesired photolytic reaction was occurring as well as the light-triggered release of carvedilol. However, illumination conditions were optimized, and the possibilities offered by the caged compound were evaluated in different biological systems.

Firstly, light-dependent properties of caged-carvedilol **54** were assessed *in vitro*. Cellular assays showed that the caged analogue of carvedilol does not inhibit β_2-AR at the tested concentrations. Light application triggered an increase of the inhibitory potency, with longer illumination times resulting in higher inhibition of the target receptor. Following the cell-based assays, the caged compound was used to evaluate the regulation of the cardiac frequency in two physiological models. Perfused mice hearts were used in a first series of experiments. Caged-carvedilol (**54**) was only able to reduce the cardiac frequency of perfused mice hearts if it had been exposed to light, indicating that carvedilol had been released and was modulating the activation state of β-AR. As a consequence of the promising results obtained *ex-vivo*, the compound was tested *in vivo*. Zebrafish larvae (7 dpf) showed a significantly reduced heart rate when they were exposed to illuminated caged compound (**54**), which was consistent with results obtained *ex-vivo*. Finally, behavioral experiments were also conducted using zebrafish larvae (7 dpf). The startle response of the larvae to a vibrational stimulus was only reduced in the experimental group that had been exposed to caged-carvedilol illuminated for 3 minutes. Additionally, this particular experimental group also presented a significantly delayed habituation to a repetitive vibrational stimulus, which suggested that released carvedilol is modulating its target receptors located in the brain. Thus, we have provided a proof of concept for an irreversible light-dependent modulation of the adrenergic drive. The obtained results highlight the potential of caged compounds in clinical or research applications that require spatiotemporal precision.

On the other hand, we attempted to develop a caged agonist following an analogue strategy. Cimaterol (**6**), a non-selective β-AR agonist, was protected using the same coumarin PPG (DEACM). However, the application of visible light (405 nm) triggered an undesired photolytic cleavage of 90% of the caged compound (**62**). The unexpected heterolytic cleavage of the C-N bond within the ethanolamine backbone of cimaterol was also described for C-C (**54**); however, this process in the caged antagonist occurred in a slower manner and with lower frequency compared to caged-cimaterol (**62**). Despite the efforts invested in the optimization of illumination conditions to favor uncaging of **62**, undesired heterolysis of the compound was always major. For this reason, the development of a caged agonist was finally discontinued.

Chapter 2. Development of the first photoswitchable ligands to reversibly control β-AR function with light

Abstract

In the first chapter of the present thesis, a caged analogue of the beta-blocker carvedilol was developed. This caged compound allowed light-dependent modulation of β-AR in a variety of physiological systems, including living animals. However, the photolytic release of the bioactive molecule has an irreversible nature, and no compound deactivation is possible after the application of light. This can constitute a limitation if the activation state of the target receptor requires fine-tune modulation in the temporal dimension. **In this chapter, we report the first photoswitchable compounds targeting β-AR, which allow a reversible modulation of the studied receptors with light**. Firstly, a series of azobenzene based ligands were designed, synthesized and photochemically characterized. Then, the light-dependent pharmacological properties of the ligands were evaluated *in vitro* for both receptor subtypes, β_1-AR and β_2-AR. The pharmacological results obtained for the first series of photochromic ligands allowed to design two additional azobenzenes with the aim of selectively modulating β_1-AR. Both ligands, based on a *para*-substituted azobenzene (*p*-AB) scaffold, were synthesized, photochemically characterized and assayed *in vitro*. The excellent β_1-AR selectivity profile exhibited by the two *p*-AB was further investigated *in vivo*. As a result, light-dependent cardiac modulation was achieved in zebrafish larvae, highlighting the enormous potential of the developed *p*-AB as tools for research and clinical applications

A paper related to this chapter has been published and an additional manuscript is in preparation:

- Anna Duran-Corbera, Juanlo Catena, Marta Otero-Viñas, Amadeu Llebaria and Xavier Rovira, "*Photoswitchable Antagonists for a Precise Spatiotemporal Control of β_2-Adrenoceptors*", Journal of Medicinal Chemistry, **2020**, 63, 15, 8458-8470, https://doi.org/10.1021/acs.jmedchem.0c00831.
- Anna Duran-Corbera, Juanlo Catena, Amadeu Llebaria and Xavier Rovira, "*Selective modulation of β_1-adrenoceptors using photoswitchable ligands*", manuscript in preparation.

2.1 First series of photoswitchable compounds targeting β-adrenoceptors

2.1.1 Design and synthesis of Photoazolols 1-3

As described in the introduction, the development of photoswitchable ligands to optically control GPCRs can be achieved through the addition of a photochromic moiety to the chemical structure of a known ligand. Following this strategy, the design of photoswitchable compounds targeting β-adrenoceptors was based on the molecular scaffold commonly found in β-adrenoceptor antagonists (Figure 60). Noticeably, these molecules are constituted by an

aromatic ring connected to an ethanolamine backbone through an oxymethylene bridge. It is well described that the ethanolamine moiety plays an essential role on the ligand-protein interaction, considering that it forms H-bond interactions with key residues on the binding pocket.[37] Additionally, compounds incorporating the oxymethylene bridge on their structure have been signaled as β-adrenoceptor antagonists.[38] Therefore, the relevance of the oxyaminoalcohol substructure in ligand function highlights it as the so-called molecular fingerprint of β-adrenoceptor antagonists.[37] On the other hand, the hydrophobic moiety admits certain variations as it can integrate multiple aromatic fused rings or heteroaromatic substructures (e.g. carbazole and indole). Consequently, we identified the hydrophobic core as suitable for the azologization strategy.[39] We proposed three different molecules, where the naphthalene of propranolol and the tricyclic carbazol moiety of carazolol are substituted for an azobenzene. The designed azobenzenes are structural isomers, where the only difference relies on the aromatic substitution pattern of the oxyaminoalcohol with respect to the N=N double bond (Figure 60).

Importantly, the vast majority of ligands targeting β-AR are chiral. In fact, different pharmacological behavior has been distinguished for the enantiomers, with better β-AR pharmacological properties always observed for the (*S*)-eutomers.[40] Therefore, and according to the structure of potent ligands, we aimed to synthesize the (*S*)-enantiomers of the designed azobenzenes. Finally, all azobenzene compounds were designed with a *p*-acetamido substituent, which was introduced with the objective to obtain photochromic ligands with appropriate photochemical properties.

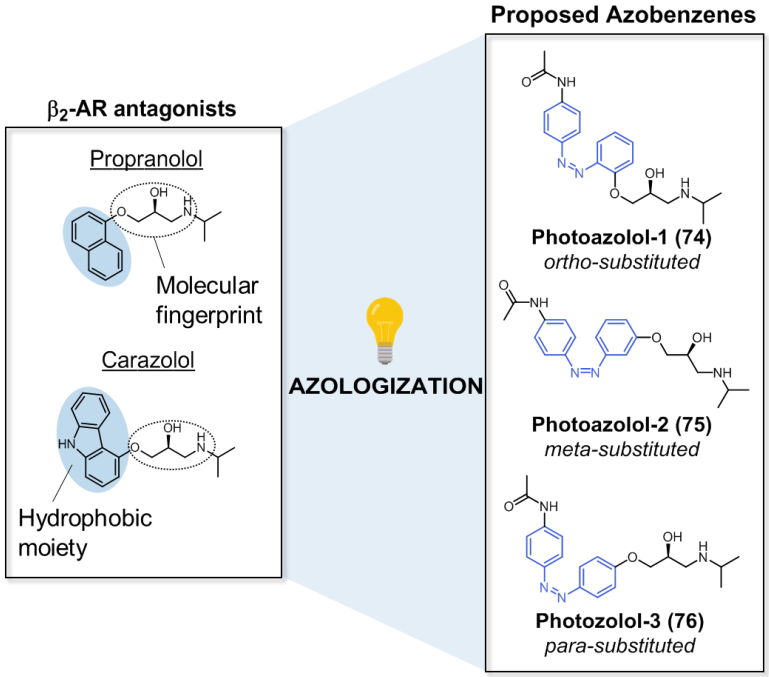

Figure 60. Design of photoswitchable azobenzene β-AR antagonists Photoazolols (PZLs). Left panel, prototypical beta-adrenoceptor antagonists. Right panel, designed photoisomerizable molecules following the azologization strategy. Reproduced from Duran-Corbera *et al.* (2020).

The synthetic routes developed to produce photo-controlled β-AR antagonists are depicted in Scheme 11. All three routes share an analogous intermediate, which is a phenolic azobenzene (**67**, **68** and **72**). Direct diazotization of the *p*-acetamidoaniline (**66**) followed by reaction with

phenol yielded phenylazophenolic intermediate **68**. Nevertheless, synthesis of acetamido intermediates **67** and **72** was conducted via the typical Mills reaction involving condensation of appropriate anilines and aromatic nitroso compounds. This alternative procedure was explored after the attempted diazotization of the respective aminophenols proved unsuccessful. Thus, *ortho*-phenolic azobenzene **72** was obtained by oxidation of the *p*-acetamidoaniline (**66**) to the corresponding nitroso compound (**71**), followed by Mills condensation with 2-aminophenol. On the other hand, it is worth noting that to produce *m*-phenolic azobenzene **67** a methoxy protected intermediate **65** had to be synthesized. Condensation of the nitroso acetamide with 3-aminophenol proceeded with very low yields. In consequence, 3-methoxyaniline (**63**) was oxidized to its nitroso derivative (**64**) and reacted with the *p*-acetamidoaniline (**66**) to yield azobenzene **65**. Subsequent *O*-demethylation of **65** using BBr_3 led to the desired azobenzene intermediate **67** in good yield.

Scheme 11. Synthesis of Photoazolol-1–3.[a]

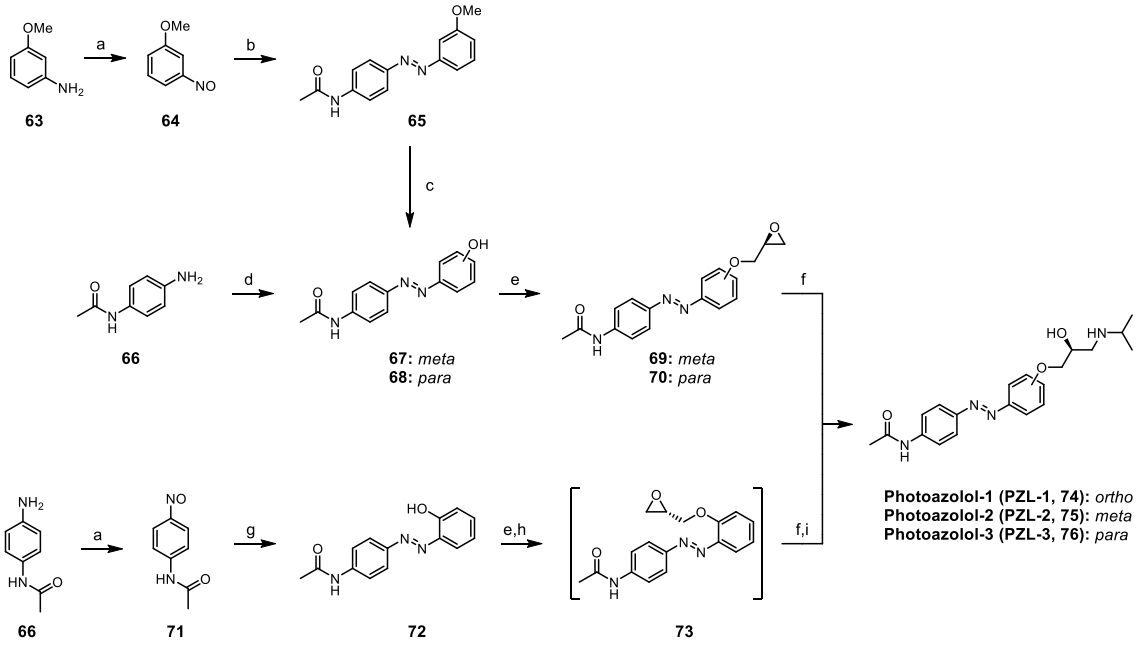

[a] Reagents and conditions: (a) Oxone, H_2O/DCM 1:1, r.t, 2h; (b) *p*-Acetamidoaniline, AcOH, r.t, 24-48h, 25-41%; (c) BBr_3, DCM, 0ºC to r.t, 24h, 95%; (d) (I) $NaNO_2$, aq HCl, 0ºC, 5 min; (II) Phenol, aq NaOH, 0ºC, 30 min 63%; (e) (*R*)-Epichlorohydrin, K_2CO_3, butanone, reflux, 24-48h, 59%-quantitative; (f) i-$PrNH_2$, 2-12h, r.t or MW, 29-56%; (g) 2-Aminophenol, AcOH, r.t, 24-48h, 16-21%(h) (2*S*)-Glycidyltosylate, K_2CO_3, DMF, r.t, 12h; (i) i-$PrNH_2$, 90ºC, 48h, 33%.

Once the key intermediates were synthesized, the following steps required the use of enantioselective reactions to afford the (*S*)-enantiomers of **PZL-1–3**. To obtain the proposed light-regulated β-AR antagonists, we initially followed a commonly reported route for the synthesis of β_2-AR antagonists.[41] The phenolic azobenzenes were alkylated by direct reaction with (*R*)-epichlorohydrin (**69**, **70** and **73**). This reaction, using either acetone or butanone as a solvent, proceeds with inversion of configuration to yield the (*S*)-oxiranes.[41] The obtained epoxides were finally opened by nucleophilic attack of isopropylamine. This route provided azobenzenes **PZL-2** and -**3** with good enantiomeric purity. In contrast, the *ortho*-substituted product was found to be partially racemized. The exact reasons for this behavior in the *o*-diazenylphenol **72** remain unknown. In order to overcome this difficulty, a different enantioselective route reported for the production of (2*S*)-propranolol was explored.[42] This

new approach consists in a one-pot reaction of phenol **72** using (2*S*)-glycidyltosylate and isopropylamine as main reagents. Regioselective displacement of the tosylate moiety by phenol under mild basic conditions afforded epoxyether intermediate **73** that was not isolated. Epoxide opening was thereafter effected by refluxing the reaction mixture with isopropylamine to give **PZL-1** with good enantiomeric purity.

2.1.2 Photochemical characterization of Photoazolols 1-3

Following the synthesis of the desired compounds, the photochemical properties of **PZL-1–3** (**74-76**) were evaluated. To be able to effectively control β-AR with light, it is an essential requisite to find specific light parameters to interconvert *trans* and *cis* azobenzenes in both directions in a relatively fast manner and with high isomeric conversion rates. Firstly, UV-Vis spectra of the three compounds were recorded in dark and after illumination with different wavelengths for 3 minutes (Figure 61B-C). The absorption spectra of the studied compounds in the dark corresponded to the *trans* isomeric form, which presented a strong band near 360 nm, characteristic for the azobenzene π-π* transition. Considering that the π-π* transition is bathochromically shifted in the *cis* isomer, the height of this band can be used to qualitatively assess the amount of *trans* isomer in each photostationary state (PSS).

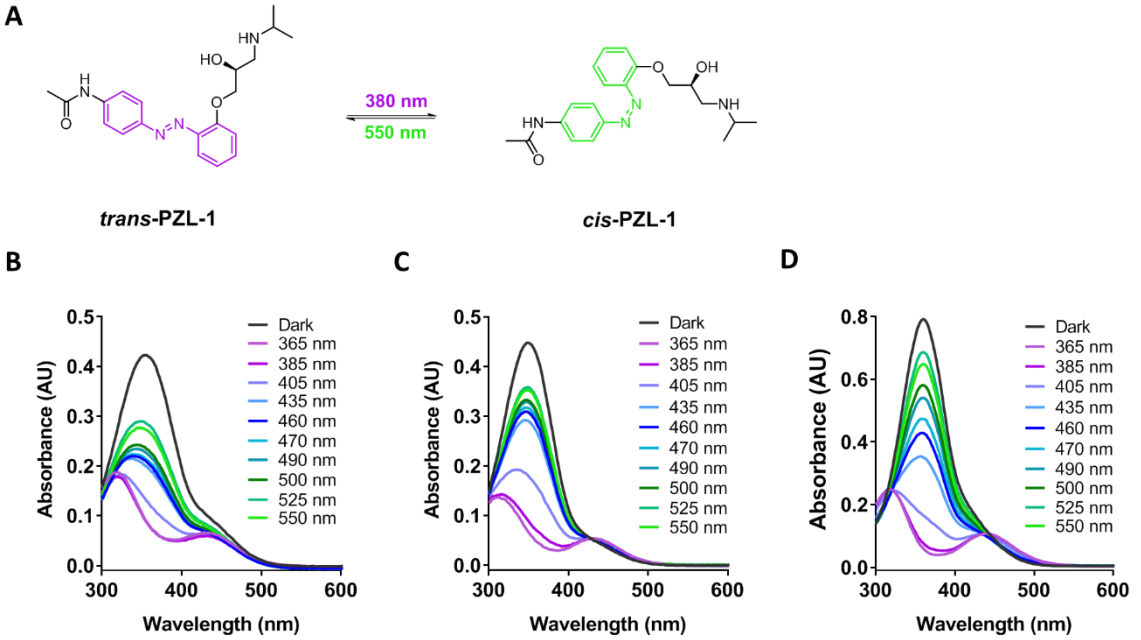

Figure 61. UV-Vis absorption spectra of PZLs. (A) 2D chemical structures of the photoisomers of **PZL-1**. UV-Vis absorption spectra of a 50 µM solution of **PZL-1** (B), **PZL-2** (C) **and PZL-**3 (D) in Epac buffer (0.5% DMSO) under different light conditions. Samples were illuminated continuously for 3 minutes for each studied wavelength using the CoolLED light source set at 50% intensity.

General tendencies can be observed for the three azobenzenes. Suitable isomerization from the thermostable *trans* to the *cis* configuration occurs when applying near ultraviolet light (365/380 nm). Compounds can also be back-isomerized to their thermally stable isomer using green-yellow light (525/550 nm) (Figure 61). Despite the photochemical similarities between the three structural isomers, evident differences can also be observed. For instance, back-isomerization occurs with lower efficiency for **Photoazolol-1** (**74**) and **-2** (**75**), where the absorbance height of the π-π* transition at PSS_{525} is notably lower compared to their dark

spectrum. This can be explained through the shape of the *trans* isomer UV-Vis spectrum. As previously mentioned, this family of compounds presents a strong π-π* band at 360 nm under dark conditions but also shows a shoulder n-π* band around 440 nm (Figure 61). The n-π* transition is generally forbidden by symmetry in *trans* azobenzenes, which frequently leads to spectra with very weak n-π*absorption bands. Therefore, the presence of this slightly prominent n-π* band in the UV-Vis spectra of **PZLs** *trans* isomers suggests that this transition is not completely forbidden for these compounds, but especially for the *ortho*-substituted azobenzene (**74**). This, results in a non-negligible absorption of *trans* isomers at higher wavelengths and can be considered a particular feature on the UV-Vis spectra of the described azobenzenes. In any case, this absorption hinders a more efficient light-triggered transition from *cis* towards the more thermodynamically stable *trans* isomer.

Thermal relaxation of the metastable *cis* isomers to their thermodynamic isomers was also assessed at 25 ºC. Aqueous samples of the compounds (50 µM, 0.5% DMSO) were illuminated for 3 min at 380 nm (CoolLED light source, 50% intensity), and absorbance was periodically measured until absorbance values were stabilized. For all three compounds, thermal relaxation in aqueous media was found to be relatively slow, considering that all measured half-life times at 25ºC were longer than 1h (Figure 62A-C). Nevertheless, thermal relaxation of **PZL-1** (**74**) was noticeably faster compared to the other two compounds (Figure 62A). Taking into account that the substituents in the three compounds are identical, the difference in the half-life time of **74** can be attributed to the position of the molecular fingerprint with respect to the N=N bond. It is possible that the bulky ortho- substitution in **PZL-1** causes the appearance of steric interactions in the *cis* isomeric form, which favor a faster relaxation to a disposition with reduced steric hindrance. Additionally, photoisomerization in all compounds was found to be stable and reversible over the application multiple light cycles (Figure 62D-F).

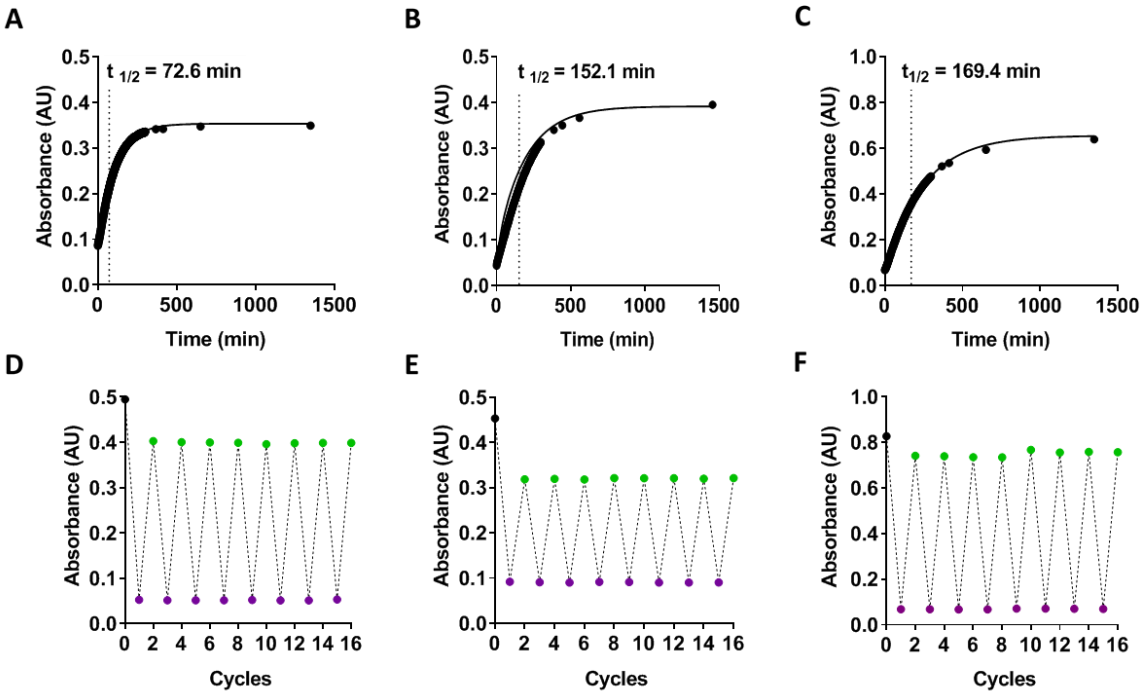

Figure 62. Thermal relaxation and stability cycles of PZLs Half-lifetime estimation of *cis*-**PZL-1** (A), *cis*-**PZL-2** (B) and *cis*-**PZL-3** (C) at 25ºC after continuous illumination at 380 nm for 3 minutes; absorbance was measured at 364 nm for all compounds. Multiple *cis*/*trans* isomerization cycles (380/550 nm) of **PZL-1** (D), **PZL-2** (E) and **PZL-3** (F); good reversibility confirms the stability of the photoswitches over 45 minutes of light application.

Finally, in the last series of UV-Vis spectroscopic experiments performed, the rates of the isomeric transitions triggered by light application were evaluated (Figure 63). Absorbance was continuously measured during the experiments, and light (365/525 nm) was applied to trigger isomerization of the photochromic ligands for at least two cycles.

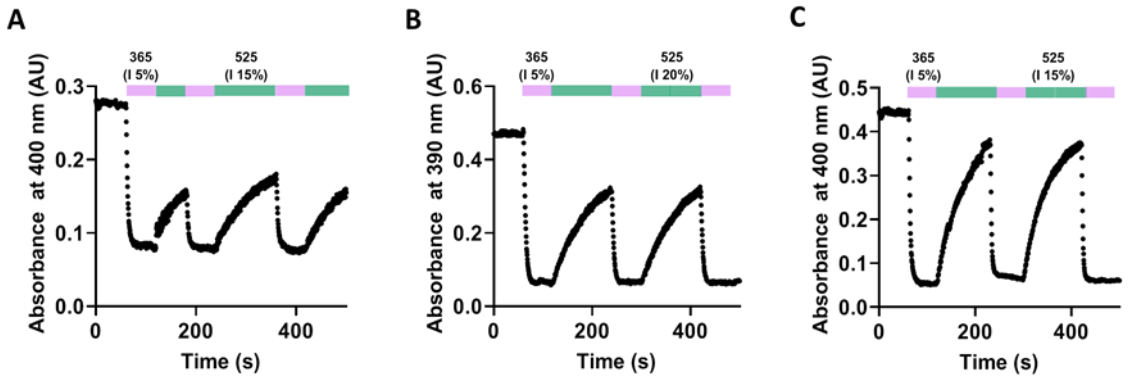

Figure 63. Continuous *cis/trans* isomerization cycles. Multiple *cis*/*trans* isomerization cycles (365/525 nm) of **PZL-1** (A), **PZL-2** (B) and **PZL-3** (C) were performed. Absorbance was measured continuously with the Thermo Fisher Evolution 350 spectrophotometer, even during the application of light. Light was applied from top using the CoolLED system, set at the intensities depicted in the figure.

Interestingly, these experiments showed that for all compounds, excitation of the ligands to the *cis* isomer always occurred faster than back-isomerization to the thermodynamic isomer (Figure 63). Half-times for the transitions (τ) were also estimated in order to quantitatively assess isomerization rate differences (Table 11). While excitation to the *cis*-azobenzene occurred with a τ of 2-3 seconds, back-isomerization required 33 to 60 seconds. This can be attributed to the different absorption efficiency existing between the two isomers. *Trans* compounds present high absorptivity at the wavelength used to trigger excitation, which causes efficient absorption of the delivered photons. Contrarily, c*is*-isomers present low absorptivity at the wavelengths used to induce relaxation to the *trans* azobenzene. For this reason, it is expected that a higher number of photons will be required to reach the PSS, resulting in longer transition times.

Table 11. Kinetics of light-driven isomerization of Photoazolols-1-3[a]

Compound	$\tau_{trans \rightarrow cis}$[a] (s)	$\tau_{cis \rightarrow trans}$[a] (s)
PZL-1 (74)	2.4	60.7
PZL-2 (75)	3.0	51.4
PZL-3 (76)	2.2	33.4

[a] Determined at 50 µM in aqueous buffer + 0.5 % DMSO, 25 ºC.

Finally, determination of the photoisomeric ratios of the ligands at the PSS can be crucial to correctly understand the light-dependent pharmacological outcomes of a ligand. For this reason, photoisomeric ratios of the three ligands were determined by ^{1}H-NMR spectroscopy. Chemical shifts of the *trans* and *cis* configurations are different, which allowed the relative

quantification of the two isomers. Ideally, these assays should be performed in analogous conditions to the biological assay conditions. Nevertheless, this technique has limited sensitivity and requires the use of deuterated solvents to avoid interference signals.

Therefore, NMR assays were performed using 100 µM solutions of compounds in deuterium oxide (D_2O), the most similar conditions to *in vitro* assays allowed by the employed technique. ^{1}H-NMR spectra were measured in the dark and after 3 min illuminations with the optimal photoisomerization wavelengths (380/550 nm) (Figure 64). All experiments were performed at 12ºC to reduce thermal relaxation and ensure a robust quantification of photoisomeric ratios.

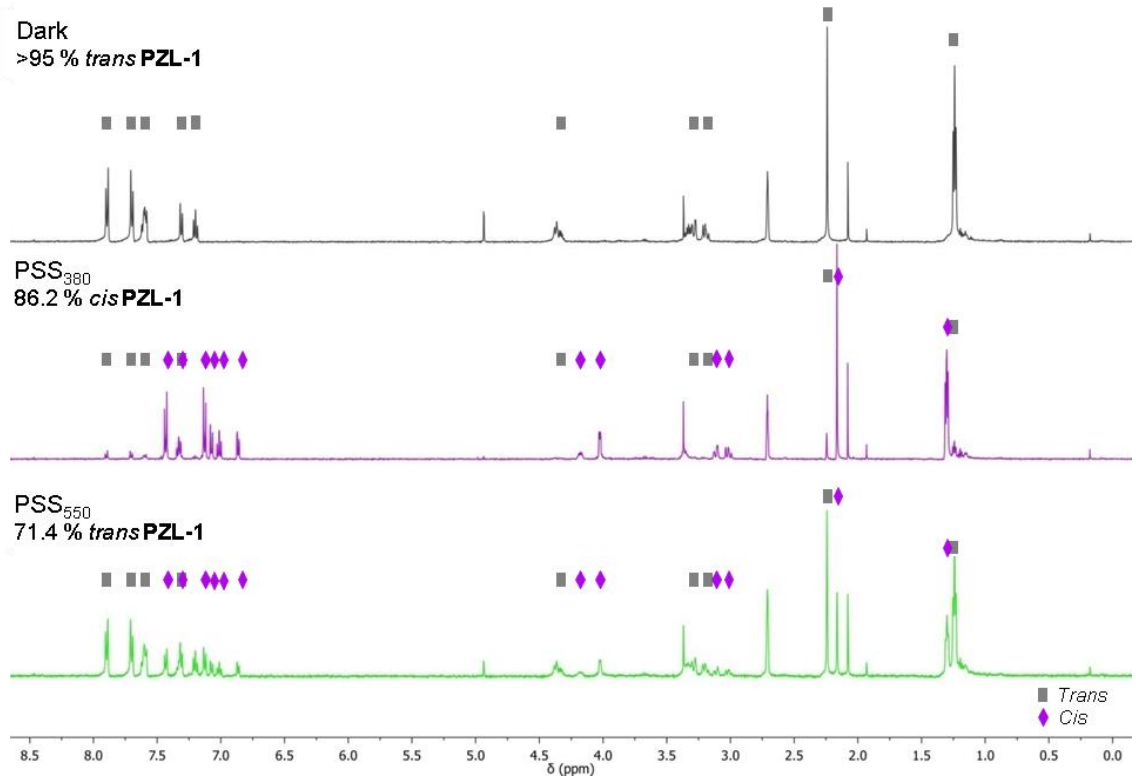

Figure 64. ^{1}H NMR studies of the photostationary states of Photoazolol-1. A sample containing 0.1 mM **PZL-1** in D_2O was analyzed in dark conditions and after illumination with 380 nm and 550 nm light. Grey squares illustrate the NMR signals corresponding to the trans isomer and the violet diamonds represent the *cis* signals.

Figure 64 highlights that at the different PSS, the photochromic ligand is temporally in equilibrium existing in determined proportions of the two isomeric forms. Additionally, quantification of the photoisomeric ratios for all three compounds was performed using the methyl signal of the acetamide group, considering that this is the only singlet signal and allows a more robust signal integration (Figure 65).

Importantly, conversion ratios from *trans* to *cis* isomers are higher than 86% for compounds **74-76**. Particularly, the *para*-substituted azobenzene (**76**) showed a very good isomerization ratio after illumination with 380 nm, with 94% of the ligand converted to the *cis* isomer. Nevertheless, back-isomerization occurs with lower efficiency, especially for **Photoazolol-1** and **-2**, with conversions ranging from 71 to 77 %, as qualitatively predicted from UV-Vis spectroscopy experiments.

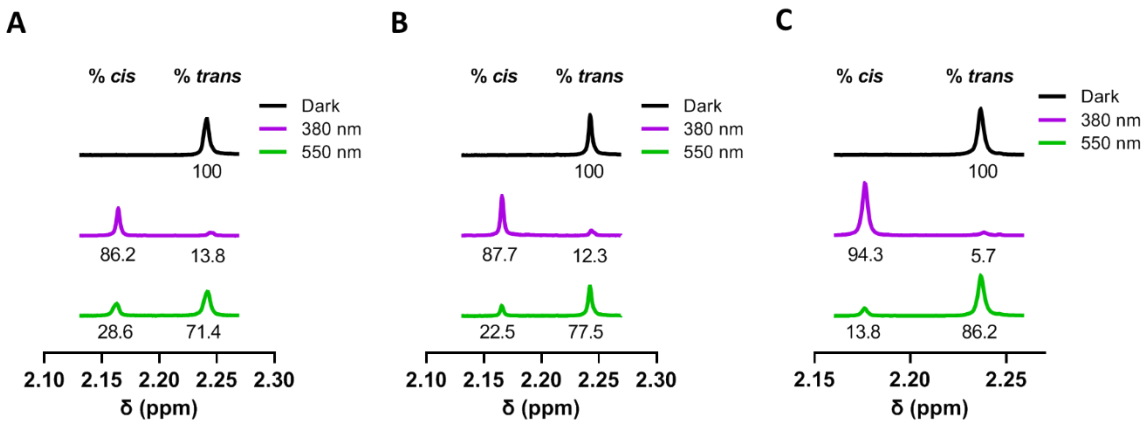

Figure 65. Photostationary state (PSS) quantification by ^{1}H-NMR. Proportions of *cis* and *trans* isomers of **PLZ-1** (A), **PZL-2** (B) and **PZL-3** (C) at PSS_{380} and PSS_{550} were determined by ^{1}H NMR. Samples were continuously illuminated using 380nm and 550 nm light.

Results from the complete photochemical characterization of the obtained azobenzenes are summarized in Table 12.

Table 12. Photochemical properties of Photoazolols-1-3[a]

Compound	λ_{trans}[a] (nm)	λ_{cis}[a] (nm)	$t_{½}$[a] (min)	PSS_{380}[b] (%*cis*)	PSS_{550}[b] (% *trans*)
PZL-1 (74)	356	428	72.6	86.2	71.4
PZL-2 (75)	350	430	152.1	87.7	77.5
PZL-3 (76)	360	440	169.4	94.3	86.2

[a] Determined at 50 µM in aqueous buffer + 0.5 % DMSO, 25 ºC. [b] PSS state areas were determined at 12 ºC by ^{1}H-NMR after illumination (380/550 nm) of a 100 µM sample in D_2O.

2.1.3 Photoswitchable modulation of β_2-adrenoceptors

Assay development to evaluate photoswitchable ligands

Following the photochemical characterization of the first series of photochromic ligands, the pharmacological properties of the compounds under different illumination conditions were evaluated. *In vitro* assays were performed using the cellular system established to assay the caged compound in Chapter 1.

As previously stated, HEK293 H188-M1 cells homogeneously express the target receptor and a FRET biosensor, which enable quantification of the secondary messenger cAMP. The activity of the photochromic compounds was evaluated as their ability to block the receptors activated by β-AR agonist cimaterol. Experiments performed in the dark provided good dose-response curves for the tested compounds in their *trans* form. Nevertheless, the continuous application of light for 45 min damaged the cAMP biosensor, and consequently abolished the detection of

cAMP changes. In consequence, the assay methodology to assess the pharmacological properties of *cis* isomers had to be optimized.

Initially, black 96-well plates with transparent bottom were used to perform the cell-based assays. After 45 min of continuous illumination (Teleopto light source), it was evident that the temperature of the dark plates had substantially increased. Thus, possible denaturation of the cAMP biosensor and cellular death were attributed to a combination of radiation-induced and heat-induced damage. For this reason, transparent plates were tested in order to address sensor degradation associated to an increase in the temperature of the system. Using transparent plates, the described photobleaching effect was noticeably reduced, and no significant differences were observed between the measured potencies for the agonist cimaterol in the dark or after illumination (Figure 66). Consequently, all experiments were thereafter conducted in transparent 96-well plates and light was continuously applied over the course of 45 min to ensure the photochromic ligand had reached the PSS and equilibrium in the biological system.

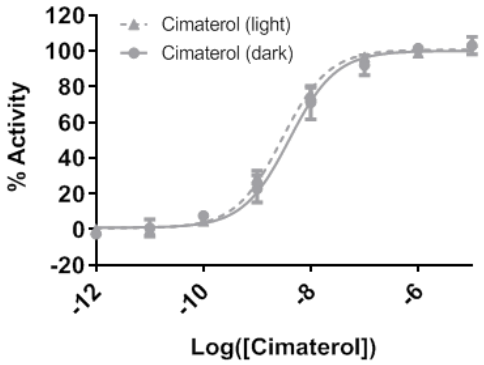

Figure 66. Dose-response curves of cimaterol under dark or light (380 nm) conditions. Data are shown as the mean ± SEM of four to six independent experiments performed in duplicate.

Photopharmacological characterization of PZLs *in vitro*

We firstly evaluated the activity of the developed molecules under different light conditions. Dose-response curves were performed for **PZLs 1-3** supplemented with 3 nM cimaterol in dark conditions and under continuous illumination with violet light (Figure 67). Cimaterol was selected as a β-AR agonist for the assays considering that it is a potent ligand and has proved to be stable in aqueous solution, even after 2h of continuous illumination with near ultraviolet light (see Chapter 1).[43]

Remarkably, our results show that both **PZL-1** (**74**) and **PZL-2** (**75**) are potent β_2-AR antagonists with nanomolar activity (Table 13). On the other hand, their structural isomer **PZL-3 (76)** showed negligible antagonism and no light-dependency (Figure 67C). Strikingly, the light-dependent properties of the two active azobenzenes presented an opposite behavior. While the most thermodynamically stable configuration of **PZL-1** was found to be more potent (*trans*-on compound), *cis*-**PZL-2** demonstrated a significantly higher inhibition compared to its *trans* form (*cis*-on compound). Indeed, **PZL-2** was found to be approximately 3.4 times more active upon illumination than in the dark. The light-induced shift in activity was noticeably higher for **PZL-1**, with 18-fold shift of the inhibitory potency measured for the compound in dark conditions.

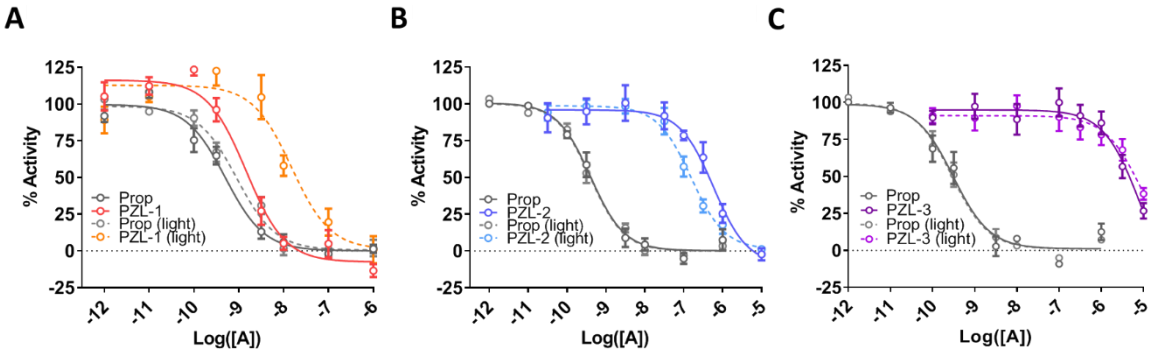

Figure 67. Light-dependent β_2-AR inhibition of PZLs 1-3. Dose-response curves of **PZL-1** (A), **PZL-2** (B) and **PZL-3** (C) with a constant concentration of the agonist cimaterol (3 nM) in the dark and under constant violet light (380 nm). Data are shown as the mean ± SEM of four independent experiments in duplicate.

Table 13. Pharmacological Data of photoswitchable β_2-AR antagonists and propranolol.

	DARK		LIGHT			
Cmpd	**IC_{50} (nM)**	**SEM**	**IC_{50} (nM)**	**SEM**	**PPS[a]**	**SEM**
PZL-1	0.87**	0.27	15.74	0.55	17.99	3.81
PZL-2	593.88****	35.73	160.64	32.20	0.28	0.05
PZL-3	11297.95	0.09	14256.07	0.4	1.83	1.91
Propranolol	0.55	0.13	0.48	0.11	0.97	0.21

[a] PPS refers to Photoinduced Potency Shift which is the relation between the measured IC_{50} in light and dark conditions respectively. Statistical differences from light IC_{50} values are denoted for adjusted p values as follows: **p<0.01 and ****p<0.0001.

Finally, we aimed to corroborate that the measured antagonism for the two active azobenzenes was directly linked to β_2-AR. To do so, we performed analogous experiments on cells treated with forskolin, which induces an increase on cAMP concentration by activating adenylate cyclase instead of β_2-AR. In these experiments, no significant decrease of cAMP levels was observed for **PZL-1** or **PZL-2** (Figure 68), which demonstrates that the described antagonism is specific to the activation of β_2-AR by cimaterol.

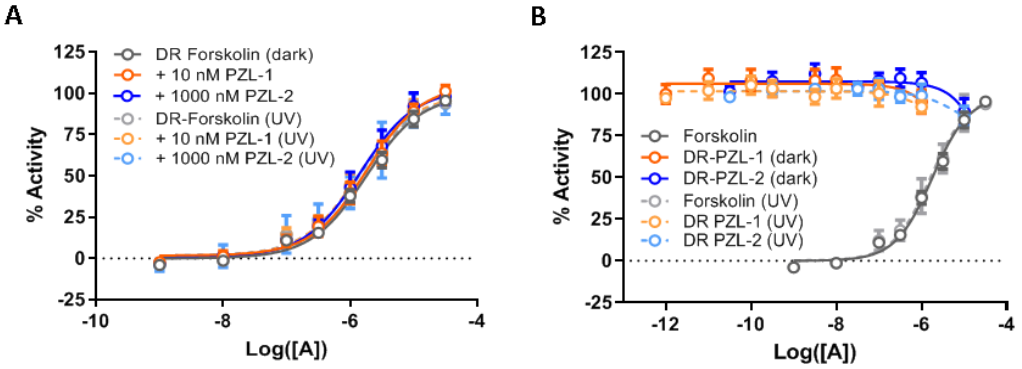

Figure 68. Validation of the selective effect of PLZ-1 and PLZ-2 over β_2-AR. (A) DR curves of forskolin with constant concentrations of **PLZ-1** and **PLZ-2** (10 nM and 1000 nM respectively) in the dark (continuous lines) or under 380nm light illumination (discontinuous lines). (B) DR curves of **PZL-1** and **PZL-2** with 10 µM forskolin in dark and 380 nm light conditions. Data are shown as the mean ± SEM of three independent experiments in duplicate.

To better characterize the light-dependent pharmacology of **PZL-1** and **PZL-2**, dose-response curves of the agonist cimaterol were measured in the presence of different concentrations of antagonist, both in dark and light conditions (Figures 69, 70). Results confirm a competitive antagonism for both compounds and a light-triggered modulation of their potency. In particular, the addition of 10 nM **PZL-1** displaces 37-fold the dose-response curve of cimaterol to the right when cells are kept in the dark, whereas EC_{50} variation is not significantly different to the control without **PZL-1** when the cells are illuminated, thus validating the *trans*-on activity of this compound (Figure 69A and 70A).

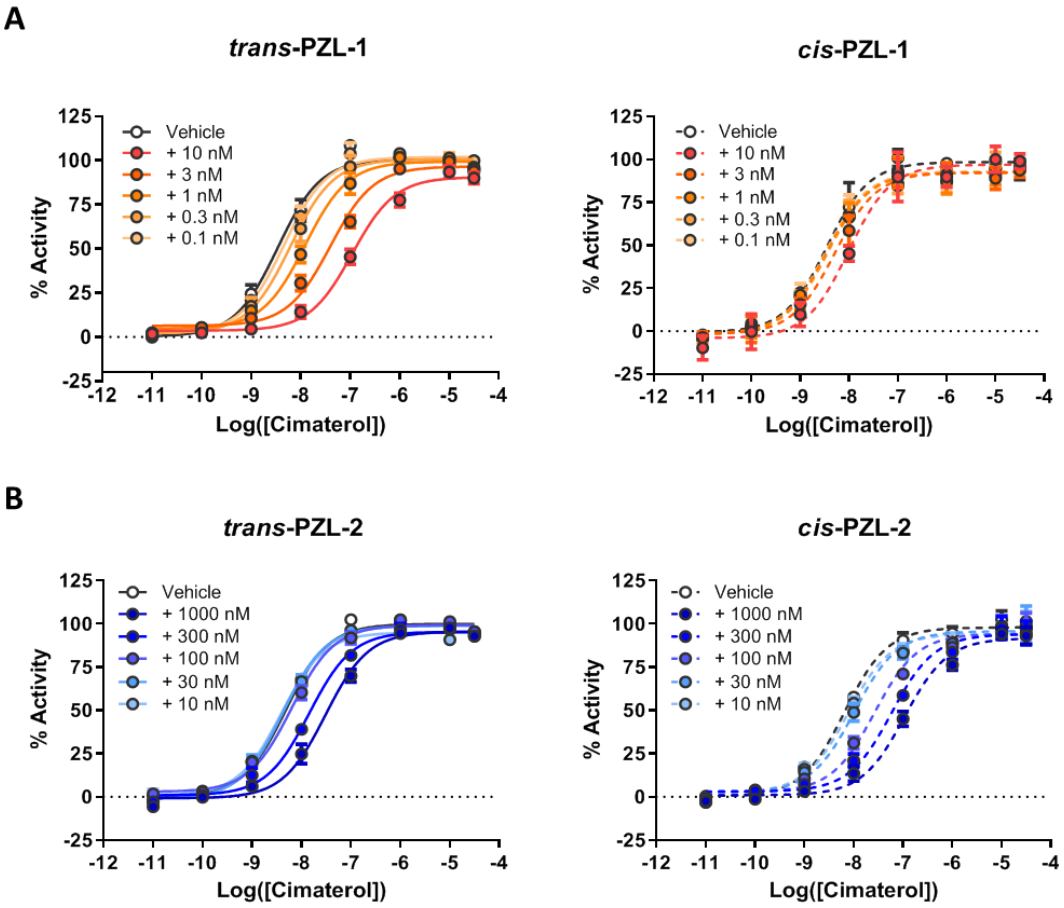

Figure 69. Antagonistic activity of PLZ-1 (74) and PZL-2 (75). Dose-response curves of cimaterol with different concentrations of **PZL-1** (A) and **PZL-2** (B) under dark conditions or after 380 nm light illumination. Each data point represents the mean and SEM of four experiments performed in duplicate.

On the other hand, the addition of 1 µM **PZL-2** shifts 20-fold the dose-response curve of cimaterol when cells are illuminated with violet light, whereas the curve displacement is significantly lower when cells are kept in the dark. This further confirms the *cis*-on activity of **PZL-2**. For both compounds, a progressive increase on the concentration of the assayed compound produces equipotent displacements of the agonist curve and an increase of the agonist EC_{50} (Figure 69B and 70B). Additionally, these experiments show no saturation of the inhibitory effect and no significant decrease of the maximal efficacy or basal activity, which is again consistent with a competitive antagonist pharmacological activity.

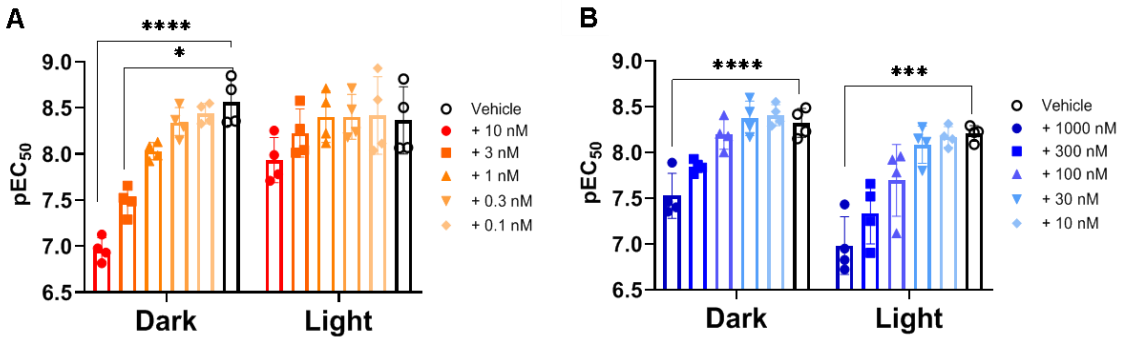

Figure 70. Representation of the pEC_{50} values for **PZL-1** (A) and **PZL-2** (B) obtained on the different replicates on Figure 69. Each data point represents the mean and SEM of four experiments performed in duplicate. Statistical differences from light pEC_{50} values are denoted for adjusted p values as follows: *p<0.05, ***p<0.001 and ****p<0.0001.

The development of compounds with opposing light-dependent pharmacology is of great interest since it provides a toolbox of molecules that enable the control of β_2-AR upon illumination in different manners. Thus, **PZL-1**, blocking β_2-AR activity in the dark and allowing the receptor to be activated upon illumination, might be useful for certain research applications that require spatiotemporal activation of specific receptors while the rest remain inactive. In contrast, molecules like **PZL-2**, inactive in the dark and blocking β_2-AR upon illumination, allow a strict inactivation of a subset of receptors during a specific time while the rest remain under physiological conditions, which opens the door to precise medical applications without side effects in other tissues and organs.

Dynamic and reversible photocontrol of β_2-AR.

Probably the most interesting and biologically unexplored capacity of photoisomerizable drugs acting on GPCRs is their ability to modulate receptor activity over time using light as an externally operated regulatory control element of biological activity. For this to happen, it is necessary that the differential pharmacological effect of *cis* and *trans* states can be reverted and dynamically governed by means of light. At this point, we addressed whether **PZL-1** and **PZL-2** were able control the β_2-AR activation state with temporal precision.

Firstly, we evaluated temporal evolution of receptor activity after treatment with the two active azobenzenes in dark and light conditions. To address this question, cells were incubated for 45 minutes with cimaterol and **PZL-1** or **PZL-2** in the dark and under violet illumination. After the incubation period, the activity of β_2-AR was continuously monitored in the dark for 30 min (Figure 71). As expected, experiments where **PZL-1** and **PZL-2** were kept in dark conditions showed a steady evolution of receptor activity over time. This indicates that both *trans* isomers have reached an equilibrium after 45 min incubation. However, results after light application highlighted a remarkably different behavior for the two azobenzenes. At time zero, **PZL-1** shows a significantly higher inhibition of the receptor in dark conditions, consistent with the reduced activity measured for the *cis* isomer (Figure 67A and 69A). Continuous tracking of receptor functional activity for 30 min demonstrated that *cis*-**PZL-1** was spontaneously isomerizing to its thermodynamically stable *trans* isomer, as the antagonism was gradually restored overtime. At the end of measurements, both illuminated and dark experiments showed similar levels of receptor activity. This suggests that **PZL-1** completely back-isomerized

in the course of 30 minutes in the cell assay system, which is much faster than the measured relaxation time for the compound in in a 0.5% DMSO buffer solution (Figure 62A). The increased thermal relaxation rate of *cis*-**PZL-1** in these experiments evidences a distinct photochemical behavior of the compound when it is enclosed in a more physiological environment. On the other hand, **PZL-2** was more efficient antagonizing the activity of cimaterol under violet illumination, which is aligned with its described *cis*-on behavior (Figure 67B and 69B). Interestingly, the antagonism observed for *cis*-**PZL-2** immediately after UV light application was maintained for at least 30 min post-illumination. This suggests that the interaction with the receptor stabilizes **PZL-2** in its *cis* isomer and leads to slower kinetics of the thermal spontaneous relaxation to *trans*-**PZL-2** (Figure 71B).

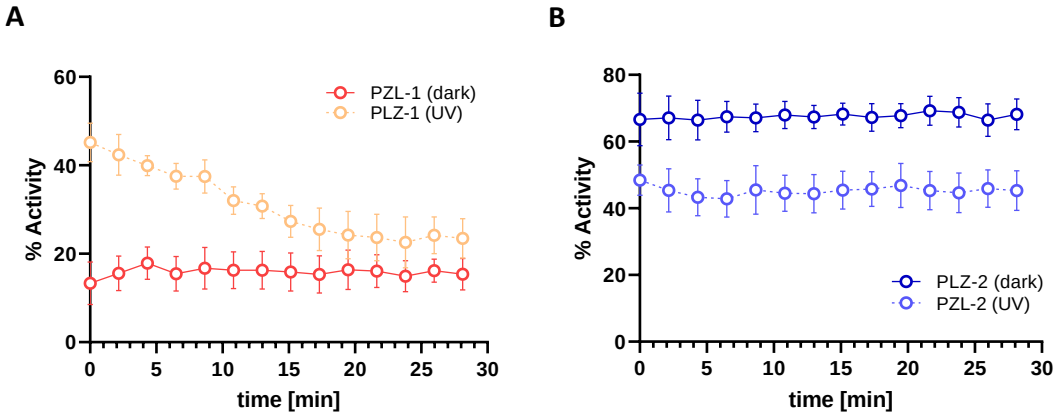

Figure 71. Temporal evolution of receptor activation in cells treated with PZL-1 and PZL-2 in the dark and under illumination. *In vitro* intracellular cAMP was continuously monitored in the dark for 30 min after a 45 min pre-incubation with the azobenzenes in the dark or under 380 nm light illumination. (A) Cells treated with 10 nM **PZL-1** and 10 nM of the agonist cimaterol. (B) Cells treated with 1µM **PZL-2** and 100 nM of the agonist cimaterol. Each data point represents the mean and SEM of three experiments performed in duplicate.

From the previous experiments a question arises concerning the light-triggered reversibility of **PZL-1** and **PZL-2**, considering whether light is able to destabilize the ligand-receptor interaction once the active isomer is bound to β_2-AR. To address the temporal control of β_2-AR with light, in a subsequent series of experiments we aimed to assess the capacity of **PZL-1** and **PZL-2** to dynamically modulate the receptor activation state using cycles of violet and green light (Figure 72). Interestingly, we found that receptor function could be efficiently controlled in a reversible manner by the photoswitchable antagonists reported here through the application of intercalated light cycles at 380 nm and 550 nm. This β_2-AR reversible control *in vitro* was observed for at least 3 consecutive cycles. In particular, for the *trans*-on **PZL-1**, close to a complete inhibition of the agonist was measured when it was co-added with cimaterol in the dark (Figure 72). This inhibitory effect largely diminished when violet light was applied and could be restored upon the application of green light. The *cis*-on antagonist **PZL-2** showed a decrease of almost 30% on receptor activation when violet light was applied (Figure 72). This significant effect was completely reversed upon illumination with green light and this on/off cycle could be efficiently repeated several times with the same result. The described light-dependent effects were not observed when both azobenzenes were assayed in dark conditions, where the ligand activity remained stable throughout the course of the experiment.

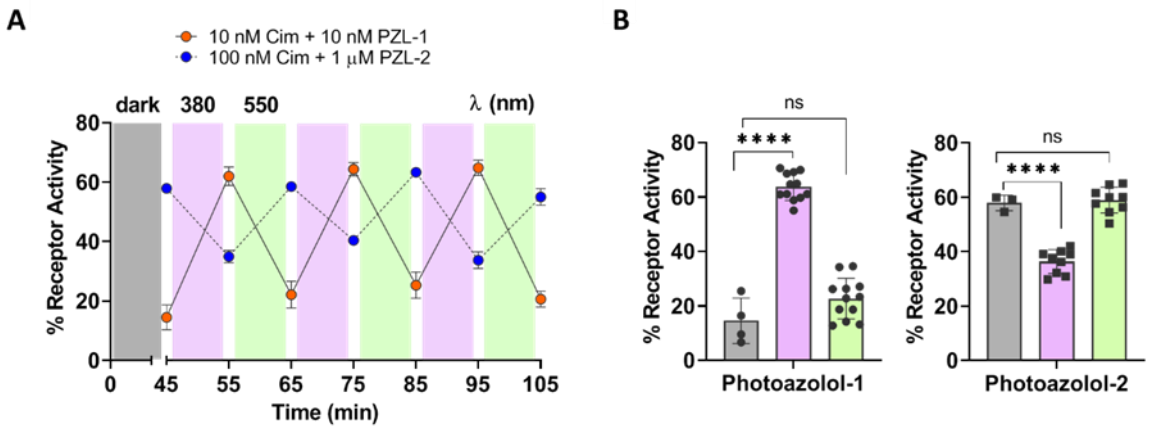

Figure 72. Real-time optical control of β_2-AR. (A) Time course quantification of intracellular cAMP challenged with the β-AR agonist cimaterol in the presence of **PZL-1**(orange dots) and **PZL-2** (blue dots). Purple and green boxes correspond to 10 min illumination breaks using 380 nm and 550 nm lights respectively. (B) Receptor activity values measured for the different light conditions. Data are shown as the mean ± SEM of three to four independent experiments. Statistical differences are denoted for adjusted p values as follows: ****p<0.0001. Figure adapted from Duran-Corbera *et al.* (2020).

These experiments demonstrate the potential and versatility of the developed photopharmacological tools to control the activity of β_2-AR, not only in space but also in time. Indeed, one of the main differences between reversible photoswitches and other drug delivery methods is that the activity of reversible ligands can be pulsed with several ON/OFF cycles. Therefore, the use of molecular photoswitches to reversibly control specific receptors may be used to resemble the dynamic control exerted in physiological regulatory processes. This particularity can also be extremely useful to uncover the role of a particular protein in a biological process[44] or to adapt a therapeutic treatment to a right time window and rhythm. Interestingly, the adaptation of a FRET-biosensor to a photopharmacology assay has proven very useful to measure the functional activity of photoswitchable compounds in an end point mode, but it has also permitted to monitor the evolution of ligand and light effects in the temporal dimension in a very simple manner. This has provided additional information on the interactions established between the ligand in both isomeric forms and the receptor. Moreover, this novel approach in photopharmacology has also enabled an assessment on the dynamic control of receptor activity through light cycles, which is essential for further research applications with **PZL-1** and **-2.**

Binding modes of active photoisomers

To gain insight in the molecular interactions leading to the light-dependent effects of photoswitchable β_2-AR antagonists, a computational study was performed (Dr. Xavier Rovira, IQAC-CSIC). We examined the binding mode of the described photoisomerizable molecules presented in this work using the crystal structure of human β_2-AR in complex with carazolol (PDB code: 2RH1).[45] This structure was chosen for the following reasons: first, it corresponds to the human β_2-AR, the same that was used in pharmacological assays; second, carazolol was used in the rational drug design of the azobenzene-based molecules investigated; and third, this crystal structure displays the highest resolution among all available β_2-AR structures.

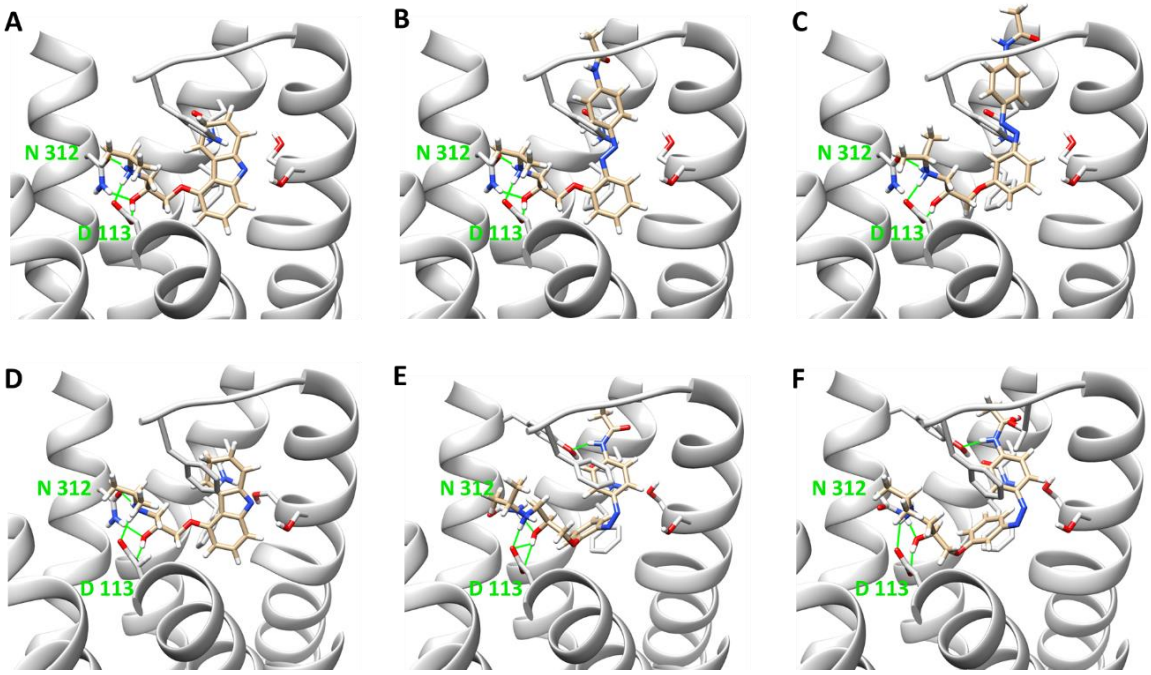

Figure 73. Binding mode of the two photoisomers of PZL-1 and PZL-2 in the crystal structure of human β_2-AR in complex with carazolol (PDB code 2RH1). Docking of carazolol in the empty receptor serves as a validation of the procedure by rigid docking (A) and by induced fit (D). Binding mode of *trans*-**PZL-1** (B) and *trans*-**PZL-2** (C) within the orthosteric binding site of β_2-AR determined by rigid docking. Binding mode of *cis*-**PZL-1** (E) and *cis*-**PZL-2** (F) within the orthosteric binding site of β_2-AR determined by induced fit. Two amino acid positions (Asp113$^{3.32}$ and Asn312$^{7.39}$) are highlighted due to their importance in the binding of β_2-AR antagonists through a network of hydrogen bonds (represented by green lines).

Both, conventional rigid docking and induced fit protocols were used to introduce the small molecule in the pocket. Due to the planar geometry of the tricyclic carbazol moiety of carazolol, it was required the introduction of some flexibility in the receptor to allocate larger structures such as the *cis* azobenzene. These procedures were previously validated by re-introducing carazolol in the empty pocket of the receptor with a very similar binding mode in comparison to the crystal structure (Figure 73A and D). Calculations performed with **Photoazolol-3** did not retrieve any positive result neither by rigid docking nor by the induced fit protocol, which is in accordance with the lack or very low activity measured for this compound in pharmacological assays (Figure 67C). For **PZL-1** and **PZL-2**, several poses were obtained for both *cis* and *trans* isomers. One of the most important molecular determinants for the affinity and activity of β_2AR competitive antagonists is the formation of a hydrogen bond network with the amino acids Asp113$^{3.32}$and Asn312$^{7.39}$ (Figure 73). In our calculations these interactions are conserved for all active photoisomers except for *trans*-**PZL-2**, which lacks one hydrogen bond with Asn312$^{7.39}$ (Figure 73C). This may suggest that during the dynamics of the receptor the mentioned hydrogen bond is not as stable as when the molecule is in its *cis* form, in which this interaction is consistently found. This molecular feature may account for the light-triggered activity increase observed in pharmacological assays for this ligand. Regarding **PZL-1**, both *trans*-**PZL-1** and *cis*-**PZL-1** configurations are forming the hydrogen bond network (Figure 73E and F). However, in *trans*-**PZL-1** these interactions are completely aligned with those found in the crystal structure of carazolol, whereas *cis*-**PZL-1** requires repositioning of several amino acids and the central part of the ligand. Interestingly,

the *cis*-**PZL-1** interaction with the receptor is found to be very similar to that of *cis*-**PZL-2** (Figure 73F), which is around 100-fold less potent than that of *trans*-**PZL-1**. These data suggest that both, *cis*-**PZL-1** and cis-**PZL-2**, may have very similar binding modes and thereafter present similar functional activities. Another remarkable difference found for the *cis*- binding of both molecules is the parallel offset aromatic interaction of the azobenzene ring with F290$^{6.52}$. This particular interaction is found to be T-shaped for carazolol, *trans*-**PZL-1** and the majority of β_2-AR antagonists crystallized so far. Moreover, an additional hydrogen bond is formed between the two *cis* molecules and the hydroxyl group of Y308$^{7.35}$ residue in the upper part of the pocket, which may compensate the loss of affinity in other regions (Figure 73E and F). Altogether, these data provide a molecular rationale aligned with the measured activities for the novel β_2-AR photoantagonists. Indeed, the sub nanomolar activity of the *trans*-**PZL-1** would suggest a very similar interaction pattern with the receptor compared to the co-crystalized carazolol. On the other hand, *cis* isomers of both active azobenzenes interact with a noticeably different binding mode which decreases their activity but also provides an original new mode of interaction with the receptor. The novel binding mode comprises valuable knowledge that will facilitate the future design of new *cis*-on β_2-AR photoswitches. Further studies will be necessary to shed light over these novel interactions and to apply the highlighted concepts to the development of improved *cis*-on compounds.

2.1.4 Photoswitchable modulation of β_1-adrenoceptors

Assay development

With the promising photopharmacological results obtained for **PZLs 1-3** in β_2-AR, we then aimed to study their behavior towards the β_1-AR subtype.

In our initial approach, we used a cellular system that did not endogenously express any of the β-adrenoceptor subtypes. For this reason, we commercially acquired CHO cells that stably expressed human β_1-AR (ES-033-CV, Perkin Elmer), as this cell type does not naturally express β-AR. In order to detect the activation state of the studied receptors, a double stable cell line that expressed the cAMP Epac biosensor and the target receptor was generated. Nevertheless, as a consequence of the high expression levels of β_1-AR, the FRET response monitored was saturated in the assay conditions and no ligand activity could be detected. To overcome the encountered limitation, we used the CHO β_1-AR cells with a different detection system, the cAMP Gs Dynamic HTRF kit (Cisbio). However, the high amounts of cAMP produced by the cells also saturated the measured signal and hampered the detection of variations in functional activity.

For this reason, we decided to use a different cellular system that allowed modulation of receptor expression levels. HEK-293 ^{i}SNAP β_1AR cells, which express β_1AR upon induction with doxycycline, were kindly obtained from Dr. Karen Martinez (University of Copenhagen). Initial assays to test control compounds were performed with cells transiently transfected with the Epac biosensor and after cellular induction with 1 µg/mL doxycycline for 24 h. Results showed that the agonistic dose-response curve presented a smaller assay window than the inhibition dose-response obtained for the β_1AR selective inhibitor CGP 12177 (Figure 74A). In fact, the FRET ratio of the basal activity of untreated cells was found to be significantly higher than the basal activity of cells treated with a β_1AR selective inhibitor (Figure 74B). This behavior can be a

consequence of a variety of events, such as receptor internalization or a high basal activity of the cellular system.

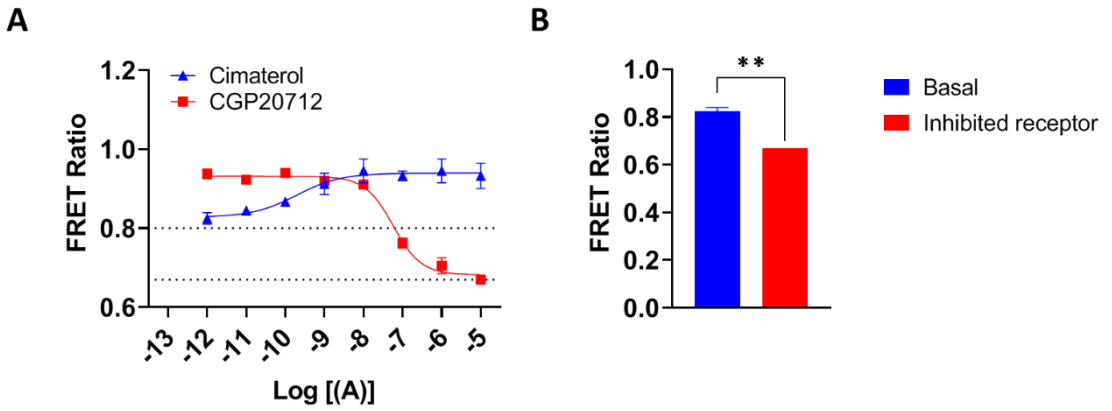

Figure 74. β_1-AR functional assays performed in HEK291 iSNAP β_1-AR cells transiently transfected with an Epac biosensor. (A) Dose-response curves of the agonist cimaterol and the β_1-AR selective antagonist CGP20712 in the presence of a constant concentration (3 nM) of cimaterol. (B) FRET ratios of the basal activity of untreated cells and of cells treated with CGP20712. Data are shown as the mean ± S.E.M of two independent experiments performed in duplicate. Statistical differences from FRET ratio values are denoted for adjusted p values as follows: **p<0.01.

To perform the assays depicted in Figure 74 we were using an analogous protocol to the one developed for β_2-AR, where Epac buffer was supplemented with IBMX, which is a phosphodiesterase inhibitor and favors cAMP accumulation. IBMX is frequently used in pharmacology to improve the assay window, considering that it amplifies signals induced by changes in the receptor activation state. However, if the biological system used already presents high levels of cAMP, the addition of IBMX would increase the detected basal activity reducing the assay window as observed in Figure 74.

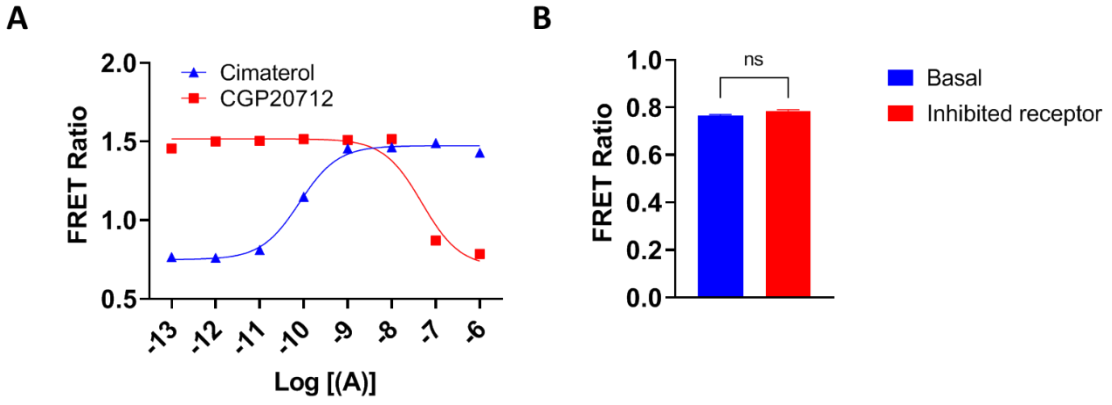

Figure 75. β_1-AR functional assays performed in HEK291 iSNAP β_1-AR cells transiently transfected with an Epac biosensor in the absence of IBMX. (A) Dose-response curves of the agonist cimaterol and the β_1-AR selective antagonist CGP20712 in the presence of a constant concentration (3 nM) of cimaterol. (B) FRET ratios of the basal activity of untreated cells and of cells treated with CGP20712. Data are shown as the mean ± S.E.M of two independent experiments performed in duplicate.

Consequently, an assay using both agonist and antagonist controls was performed with no addition of IBMX (Figure 75). Results confirmed that the addition of IBMX was responsible for the high basal activity detected in cimaterol dose-responses. When no IBMX was added to the

cellular system, no differences were observed in the basal activities of untreated and treated cells (Figure 75B).

Finally, in order to obtain more reproducible results, a double stable polyclonal cell line was generated, where the FRET biosensor was stably transfected to HEK-293 ^{i}SNAP β_1AR cells. Using these cells, receptor expression tests were performed in an effort to avoid high overexpression of β_1-AR, which can alter the measured pharmacological results of the compounds (Figure 76).

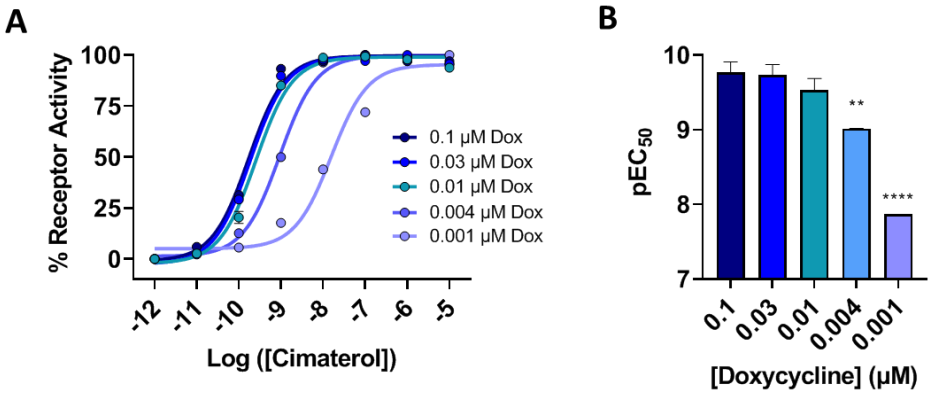

Figure 76. Optimization of β_1-AR expression levels in HEK293 iSNAP β_1-AR cells stably transfected with an Epac cAMP biosensor. (A) Dose-response curves of cimaterol in cells induced with different levels of doxycycline (0.1-0.001 µM) for 24h. (B) pEC50 values from the cimaterol dose-response curves depicted in graph A. Data are shown as the mean ± SEM of two independent experiments in duplicate. Statistical differences from pEC_{50} values obtained after 0.1 µM doxycycline induction are denoted for adjusted p values as follows: **p<0.01 and **p<0.0001.

Results showed that similar cimaterol dose-response curves were obtained when cells were induced for 24 h using doxycycline concentrations ranging between 0.1-0.01 µM (Figure 76A). pEC_{50} values obtained for cimaterol at the three highest induction conditions tested were not significantly different (Figure 76B). Moreover, pEC_{50} values oscillated around 9.7, which is consistent with the pEC_{50} obtained for cimaterol against β_1AR. On the other hand, when inducing cells with lower doxycycline concentrations (0.004-0.001 µM) cimaterol dose-response curves were increasingly shifted to higher concentrations. This indicated that upon cellular induction using 0.004-0.001 µM doxycycline, β_1AR expression was too low and the detected functional activity was influenced by the endogenous presence of β_2AR (Figure 76A). In fact, functional results obtained for cimaterol when cells were treated with 0.001 µM doxycycline can be solely attributed to β_2AR response, as the pEC_{50} is approximately 8, which is consistent with the reported values for the tested agonist towards β_2AR (Figure 76B).

Therefore, we identified that optimal levels of receptor expression can be achieved after 24h of cellular induction using 0.01µM doxycycline. At these conditions, β_1AR expression levels in the used cells have been maximally reduced without compromising the rigorous detection of β_1AR functional activity. This optimization process was conducted in an effort to obtain a cellular system that emulates the endogenous receptor levels in natural biological systems. In consequence, the best induction conditions established in this section were thereafter used to perform all β_1AR functional assays for the characterization of all photochromic ligands developed during the present thesis.

Photopharmacological characterization of PZLs in cultured cells

Once the appropriate biological system to evaluate functional activity of β_1-AR had been established, the photopharmacological behavior of the **Photoazolols** (**74-76**) was studied. Dose-response curves of the compounds were performed in the dark and after illumination with UV light (380 nm) (Figure 77).

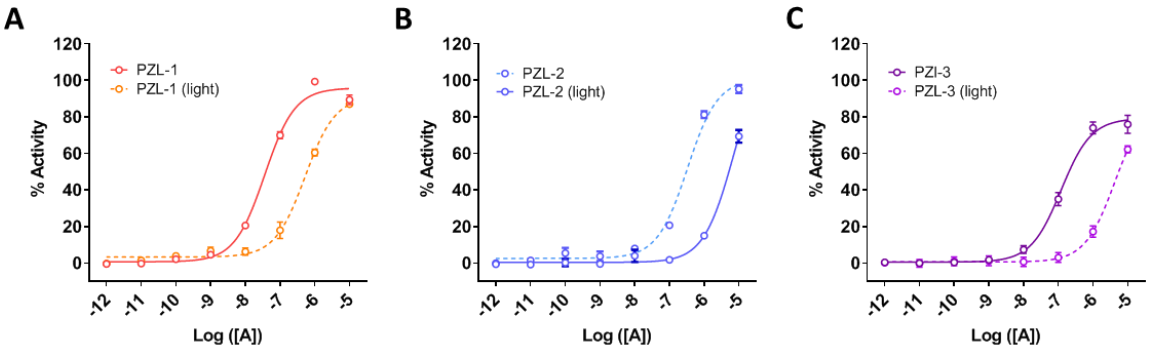

Figure 77. Light-dependent β_1-AR inhibition of PZLs 1-3. Dose-response curves of **PZL-1** (A), **PZL-2** (B) and **PZL-3** (C) in the dark and under constant violet light (380 nm). Data are shown as the mean ± SEM of four to five independent experiments in duplicate.

Results showed that all three compounds trigger an activation of the receptor in at least one of their isomeric forms. For instance, **PZL-1** (**74**) appeared as a *trans*-on agonist with an EC_{50} of 36 nM in dark conditions. Light triggered a significant decrease (13-fold) in the agonistic dose-response curve (Table 14). Additionally, we performed an analysis to evaluate the selectivity of the compound, the relation between the activities of β_1-AR and β_2-AR showed that the two isomers show approximately 20-fold selectivity towards the β_2-AR subtype (Table 15).

Table 14. Pharmacological Data of photoswitchable β_1-AR antagonists and propranolol.

	DARK		LIGHT			
Cmpd	**EC_{50} (nM)**	**SEM**	**EC_{50} (nM)**	**SEM**	**PPS[a]**	**SEM**
PZL-1	36.56****	4.21	497.74	93.40	13.09	3.13
PZL-2	-	-	328.10	39.30	-	-
PZL-3	120.50****	12.46	4581.41	1026.81	37.67	9.55

[a] PPS refers to Photoinduced Potency Shift which is the relation between the measured EC_{50} in light and dark conditions respectively. Statistical differences from light EC_{50} values are denoted for adjusted p values as follows: ****p<0.0001.

On the other hand, *meta*-substituted azobenzene **75** (**PZL-2**) showed negligible activity in dark conditions, with an EC_{50} in the micromolar range. The application of light increased the agonistic activity of the ligand by a factor of 22. Thus, this compound presented a *cis*-on behavior, with a good photoinduced shift that enabled receptor activation from 15% to 81% using 1 µM of **PZL-2** (Table 14). However, it only showed selectivity (12-fold) towards β_2-AR in its *trans* isomeric form (Table 15). Interestingly, the photopharmacological behavior of both

compounds is very similar to the results obtained with the β_2-AR subtype; nevertheless, it seems that they activate the receptor instead of blocking it.

Finally, **PZL-3** (**76**) showed partial activation of the receptor in the dark, with an EC_{50} of 120 nM. The application of UV light caused a 37-fold decrease in the measured EC_{50}, which indicated that the compound is a *trans*-on photochromic ligand. These results constituted a very exciting turnout, considering that this compound constitutes the first β_1-AR selective photoswitchable ligand. In fact, the selectivity ratio showed that **PZL-3** (**76**) is almost 94-fold more selective towards β_1-AR than β_2-AR (Table 15). The molecular mechanisms related to the β_1-AR selectivity obtained with the *para*-substituted azobenzene will be further explored in the next section.

Table 15. Selectivity ratios of PZLs 1-3.[a]

	DARK		LIGHT	
Cmpd	**β_1 vs β_2**		**β_1 vs β_2**	
PZL-1		21.2		17.2
PZL-2		12.3		2.04
PZL-3	93.8		3.1	

[a] A ratio of 1 implies no receptor selectivity for a receptor subtype over another. The column side where the ratio is located identifies towards which receptor subtype the compound displays higher selectivity.

Additionally, it is worth noting that both **PZL-1** and **PZL-2** were detected as full agonists while **PZL-3** behaved a partial agonist, with an 80% of maximal activation. However, it is very likely that all three compounds are partial agonists that are detected as full or partial agonists due to the biological system employed. This idea arises from the fact that β_1-AR was overexpressed in the cells upon induction, even if low levels of doxycycline were added. In consequence, even if only a part of the receptors gets activated by the ligand, high amounts of the monitored secondary messenger cAMP will be produced, which can lead to a saturation of the detected signal. Moreover, the cAMP FRET biosensor is also overexpressed in these cells, which provides a cellular system that is highly sensitive to cAMP changes. Consequently, the developed biological system might be amplifying the agonistic response induced by the ligands, which could be concealing their behavior as partial agonists; this hypothesis will also be explored in the following section.

Finally, we evaluated if the ligands enabled a dynamic modulation of β_1-AR with the application of intercalated light cycles in cultured cells. For these experiments, a fixed concentration of the photochromic ligand was incubated with the cells in dark conditions for 1h and the activity was measured. Following system equilibration, 10 min light cycles (380/550 nm) were applied, and the activation state of the receptor was immediately measured after illumination (Figure 78).

Results showed that all **PZLs** enable a dynamic control of β_1-AR through the application of light cycles. **PZL-1**, which behaves as a *trans*-on agonist, shows 58% of receptor activation in the

dark. This agonistic effect largely diminished upon application of violet light and could be restored when cells were illuminated with green light. The *cis*-on agonist **PZL-2** showed almost negligible agonism in the dark. Application of violet light triggered an increase in the activity of β_1-AR up to 86%, which was then partially reduced to 50% through illumination at 550 nm. Finally, the β_1-AR selective partial agonist **PZL-3** showed an initial activation state of 70%. The agonistic effect of the compound was almost completely abolished upon illumination with violet light and could be completely restored after the application of green light. Therefore, the developed **PZLs** also enable the reversible and dynamic modulation of β_1-AR (Figure 78).

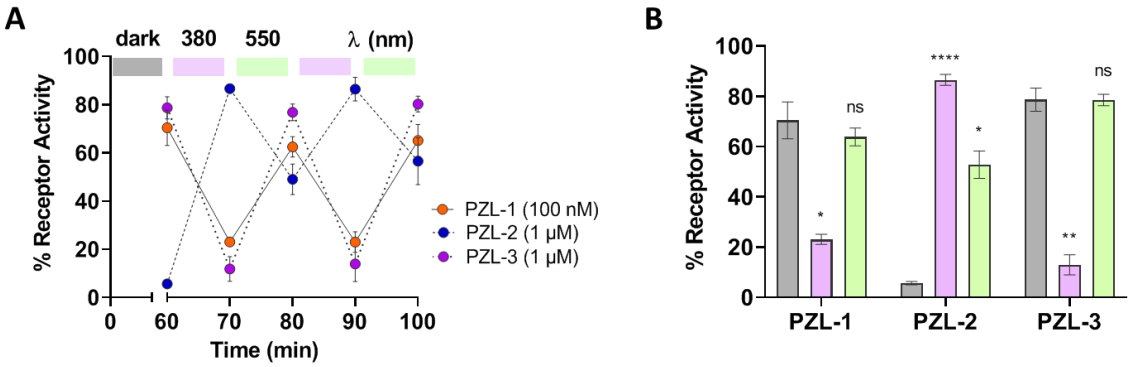

Figure 78. Real-time optical control of β_1-AR using PZLs 1-3. (A) Time course quantification of intracellular cAMP in cells treated with 100 nM **PZL-1**(orange dots), 1 µM **PZL-2** (blue dots) and 1 µM **PZL-3** (purple dots). Purple and green boxes correspond to 10 min illumination breaks using 380 nm and 550 nm lights respectively. (B) β_1-AR functional activity values for **PZL-1** to **-3** measured for the different light conditions. Data are shown as the mean ± SEM of three independent experiments. Statistical differences from dark results are denoted for adjusted p values as follows: * p<0.05, **p<0.01 and ****p<0.0001.

To sum up, we have developed three ligands (**PZLs**) that display different pharmacological behaviors towards the two subtypes of beta-adrenoceptors studied. Both **PZL-1** and **PZL-2** were detected as β_2-AR inhibitors and β_1-AR agonists or partial agonists in the studied biological systems. However, light-dependent properties of the two structural isomers were opposing; **PZL-1** was more active in its *trans*- isomeric form and **PZL-2** behaved as a *cis*-on compound. Additionally, the modulation of the target receptors exerted by the two ligands was reversible upon illumination cycles in cultured cells. Finally, **PZL-3** arose as a very promising compound as it selectively targeted β_1 adrenoceptors in a reversible manner with light. This *p*-AB behaves as a *trans*-on partial agonist for β_1-AR while displaying very low and non-switchable antagonistic activity towards β_2-AR. As a consequence of the results obtained with **PZL-3**, the development of β_1-AR selective photoswitchable ligands was then explored.

2.2 β_1-AR selective photoswitches

As previously stated, beta-blockers are widely used drugs that allow treatment of several and varied diseases. Their use is especially common for the treatment of cardiac conditions due to the inhibition of cardiac β-AR responses in the heart (mainly attributed to β_1-AR modulation). However, a main side effect appears as a consequence of non-selective inhibition of β_2-AR in the airways, which results in bronchospasm.[46] For this reason, molecules exhibiting β_1-AR selectivity should be more cardio-selective and consequently offer a lower side-effect profile. Additionally, the development of β_1-AR selective molecules that could be modulated with spatiotemporal precision would provide tools with great value for both research and clinical

applications. Taking into account the promising results obtained with compound **76**, we aimed to develop photochromic ligands with a good β_1/β_2 selectivity profile.

2.2.1 Design and synthesis of compounds 83 and 84

It is well described that β_1-AR and β_2-AR are highly similar in sequence and structure.[47] However, despite their high homology, numerous agonists and antagonists selective for β_1AR or β_2AR have been discovered.[47–49] An evaluation of the chemical structures of β_1AR selective antagonists highlighted that the oxyaminoalcohol substructure is repeatedly positioned in *para*- with respect to the other substituents of the phenyl ring (Figure 79).

This was consistent with the results obtained for the first series of photochromic ligands, where the *para*-substituted azobenzene **76** was the only ligand that showed selectivity towards the β_1 receptor subtype. Additionally, it is worth noting that CGP 20712A presents the highest β_1/β_2 selectivity ratio. This molecule is very large, and its hydrophobic moiety is constituted by two aromatic rings, resembling a *para*-substituted azobenzene. Consequently, two *para*-substituted azobenzenes **83** and **84** were proposed as potential β_1AR selective photoswitchable ligands (Figure 79). **83**, which presents a *para*-monosubstituted azobenzene, was proposed due to its synthetic accessibility. In **84**, a methoxy group was introduced in the 4-position of the phenyl ring. The introduction of an electron-donating group (EDG) is expected to shift the π-π* transition towards the visible range of the spectrum.

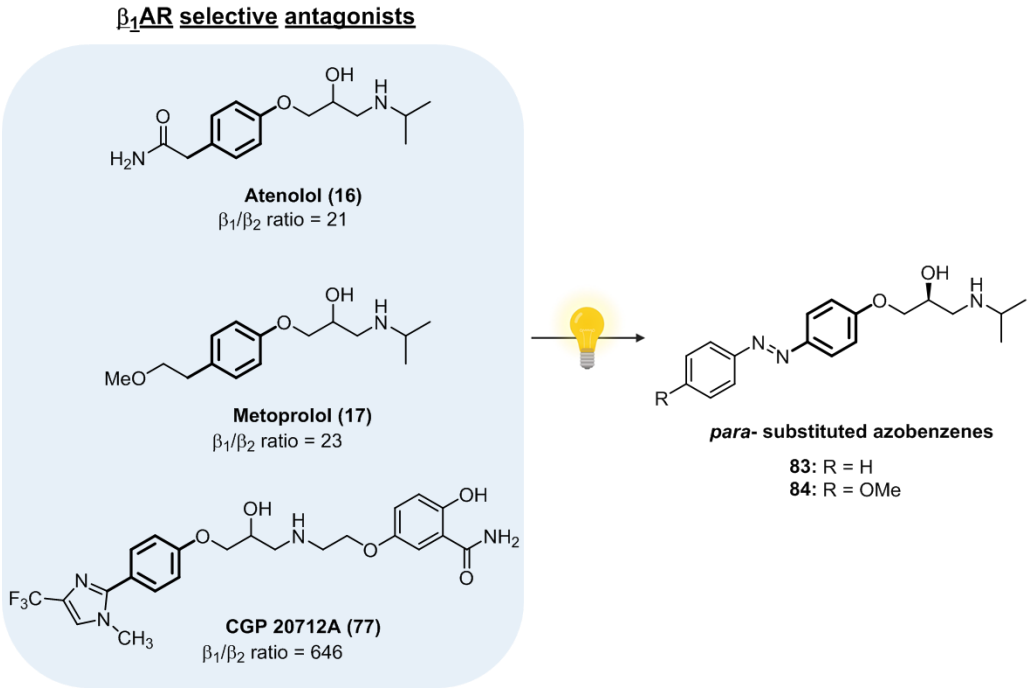

Figure 79. Design of selective photoswitches targeting β_1-AR. Left panel, prototypical β_1-adrenoceptor selective ligands and their β_1/β_2 log K_D ratios.[49] Right panel, designed photoswitchable ligands through the application of the azologization strategy.

The synthetic route followed to produce *para*-azobenzenes **83** and **84** is analogous to the one described for compound **76** (Scheme 12). Direct diazotization of *p*-methoxyaniline **78** followed by reaction with phenol yielded phenolic intermediate **80**. Intermediate **79** was obtained commercially. Both phenolic azobenzenes were alkylated by direct reaction with (*R*)-

epichlorohydrin using butanone as a solvent, which proceeded with inversion of configuration to yield (*S*)-oxiranes **81** and **82**.[41] The resulting epoxides were finally opened by nucleophilic attack of isopropylamine, and the desired products (**83** and **84**) were obtained.

Scheme 12. Synthesis of β_1-AR selective azobenzenes 83 and 84.[a]

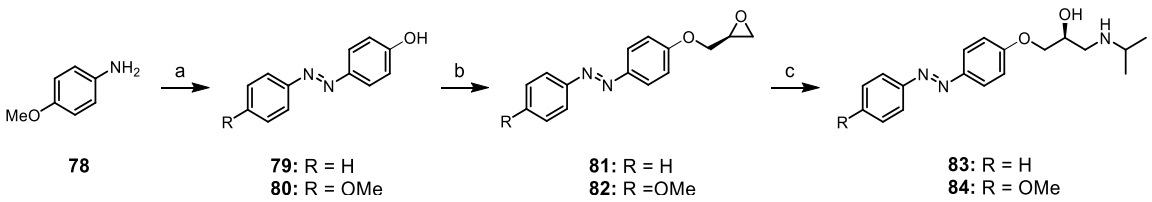

[a] Reagents and conditions: (a) (I) $NaNO_2$, aq HCl, 0ºC, 5 min; (II) Phenol, aq NaOH, 0ºC, 30 min 79%; (b) (*R*)-Epichlorohydrin, K_2CO_3, butanone, reflux, 24-48h, 90%; (c) i-PrNH_2, 2-12h, r.t or MW, 24-62%.

2.2.2 Photochemical evaluation of azobenzenes 83 and 84

Once the target compounds **83** and **84** had been synthesized, we focused our attention on their photochemical behavior. The presence of the azobenzene moiety in both ligands allows the existence of the compounds in two distinct isomeric forms, as previously mentioned. These two isomeric states can be reversibly interconverted through the application of light by direct excitation of their azoaromatic units (Figure 80). Most of the experiments performed to photochemically characterize the two compounds were carried in aqueous buffer (0.5 % DMSO) in order to reproduce the conditions that will be thereafter used in biological assays.

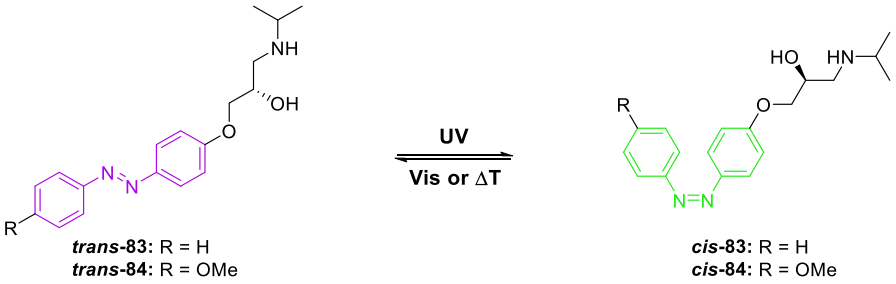

Figure 80. Photoinduced isomerization of *p*-ABs 83 and 84.

In order to determine the optimal photoisomerization wavelengths, UV-Vis spectra of the two compounds were recorded in dark and after continuous illumination with different wavelengths for 3 minutes (Figure 81A and B).

The absorption spectra of the *trans* isomer, displayed an intense absorption band at 346 nm and 358 nm for **83** and **84** respectively, which is associated with the allowed π-π* transition of the *trans*-azobenzene chromophore. Additionally, both dark spectra showed a broad shoulder between 400-450 nm that corresponds to the n-π* transition, forbidden by symmetry. It is worth noting that the additional EDG in **84** causes an energetic decrease of the π-π* transition, resulting in a bathochromic shift of the absorption band and higher overlapping with the n-π* transition (Figure 81B).

Excitation of the compounds to their *cis* isomers was achieved upon illumination with 365 nm for **83** and 365/380 nm indistinctively for **84**. The absorbance spectrum of the two *cis* azobenzenes showed a clear decrease and hypsochromic shift of the π-π* transition and a

slight increase and bathochromic shift of the n-π* band. Back isomerization to the thermodynamically stable *trans* configuration was achieved upon illumination at 530 nm for both compounds (Figure 81A and B).

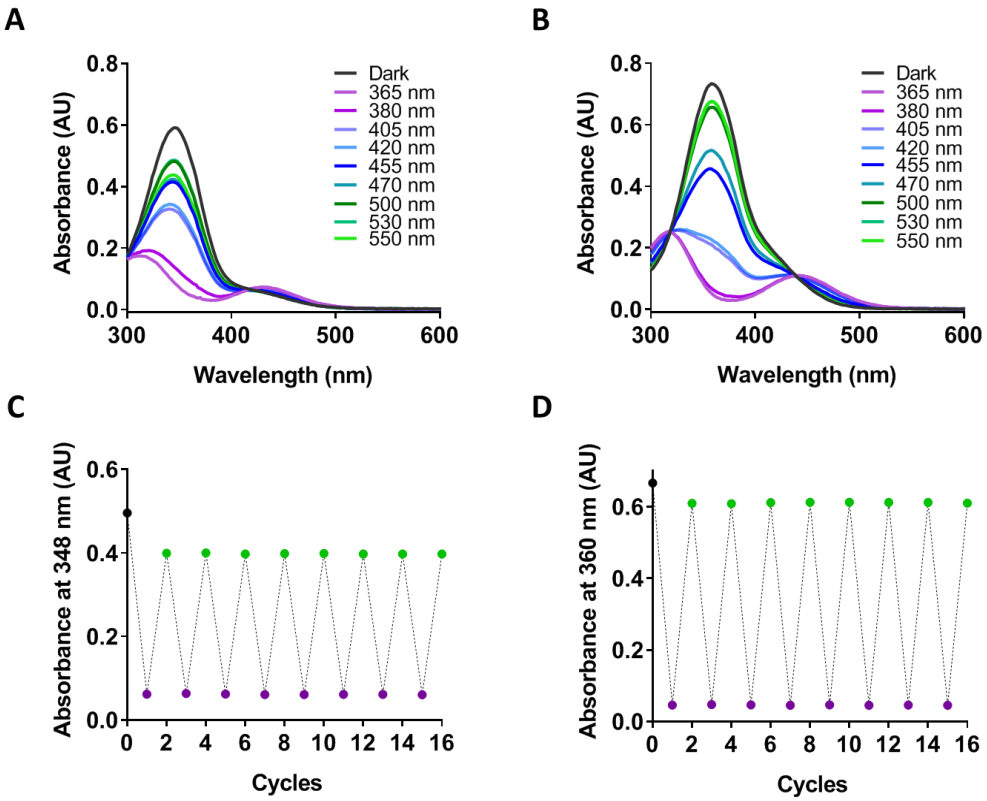

Figure 81. UV-Vis absorption spectra and isomerization cycles of 83 and 84. UV-Vis absorption spectra of a 50 µM solution of **83** (A) and **84** (B) in Epac buffer (0.5% DMSO) under different light conditions. Multiple cis/trans isomerization cycles (380/530 nm) of **83** (C) and **84** (D).

Furthermore, both compounds showed reversible photoisomerization through the application of several light cycles (380/530 nm), which confirms the stability of the two compounds to prolonged illuminations (Figure 81C and D).

Thermal relaxation of the *cis* isomers was also evaluated at 25ºC. Samples of **83** and **84** were illuminated for 3 min at 380 nm and absorbance spectra were periodically measured in dark conditions until complete back-isomerization was achieved (Figure 82).

Cis→*trans* thermal isomerization resulted in a gradual increase and bathochromic shift of the π-π* transition band of both compounds (Figure 82A and C). Plotting the absorbance changes at the λ_{max} and fitting the curve to an exponential growth function, half-life times of the two *cis* isomers were determined (Figure 82B and D).

Both compounds showed long *cis*-state thermal stability, with half-life times of 38.3 h and 11.5 h for **83** and **84** respectively. Compound **84**, that presents an additional methoxy group in the 4-position of the phenyl ring, showed a noticeably faster thermal relaxation compared to the monosubstituted *para*-AB **83**. The presence of an additional EDG causes a modest decrease in the thermal isomerization barrier by increasing the electron density in the π* orbital; this results in a higher rate of *cis*→*trans* thermal relaxation. [50]

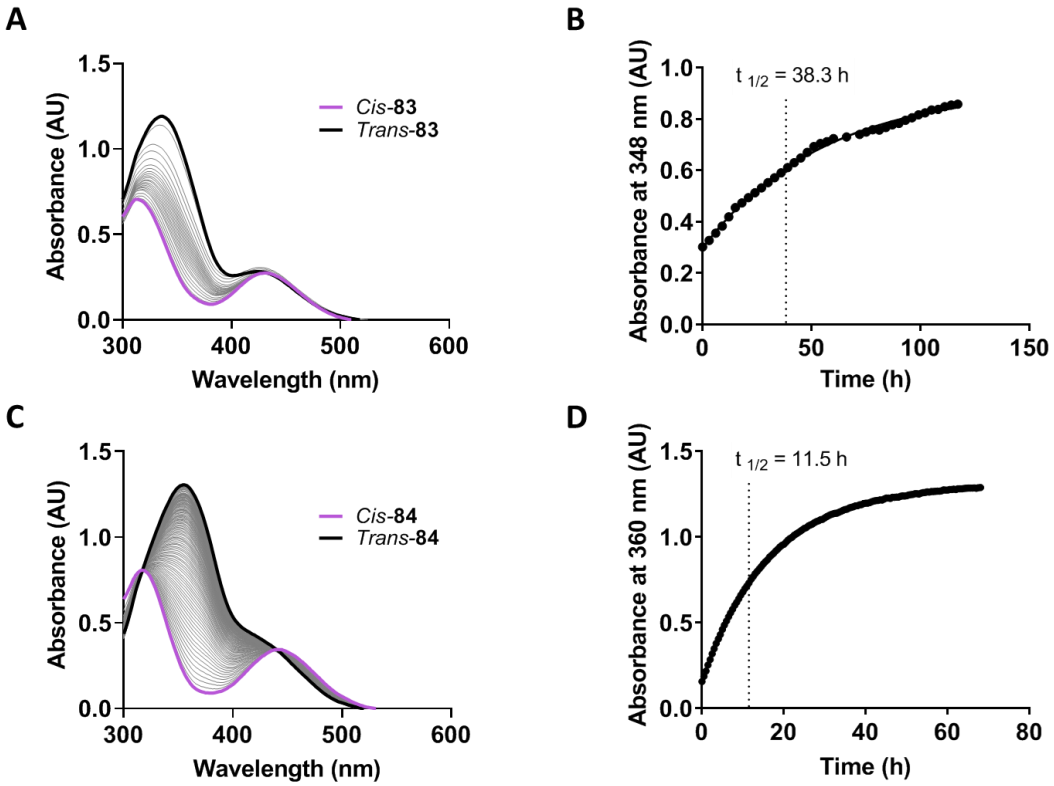

Figure 82. Thermal relaxation of 83 and 84. Changes in the UV-Vis spectra due to thermal relaxation of the *cis* isomer and half-lifetime estimation of *cis*-**83** (A, B) and *cis*-**84** (C, D). 50 µM aqueous samples of the studied compound were continuously illuminated at 380 nm for 3 minutes; measurements were collected at 25 ºC with the ThermoEvolution 350 spectrophotometer.

In the last series of UV-Vis experiments, photoinduced isomerization cycles were recorded continuously, which allowed the determination of isomerization rates (Figure 83 and Table 16).

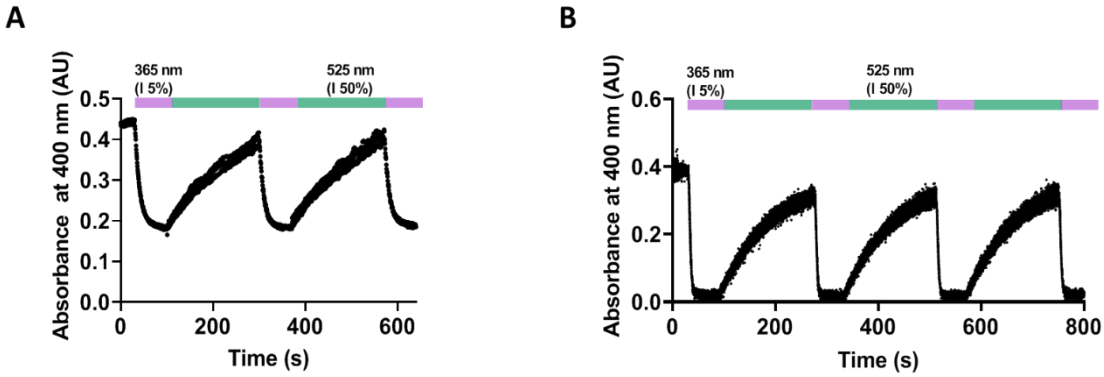

Figure 83. Continuous *cis/trans* isomerization cycles. Multiple *cis*/*trans* isomerization cycles (365/525 nm) of **83** (A) and **84** (B) were performed. Absorbance was measured continuously with the Thermo Fisher Evolution 350 spectrophotometer, even during the application of light. Light was applied from top using the CoolLED system, set at the intensities depicted in the figure.

Similarly to what we observed with **PZLs 1-3**, both ligands showed faster isomerization rates for the *cis*→*trans* transition (Figure 83). While excitation to the *cis*-AB occurred with a τ of 3-8 seconds, back-isomerization to the *trans*-AB required 1-2 minutes and increased light potency (50 %) (Table 16). Interestingly, **84** presents higher rates for both isomerization transitions.

This can also be attributed to the energetic effects of this additional EDG in a *para*- position with respect to the N=N bond.

Table 16. Kinetics of the light-driven isomerization of 83 and 84[a]

Compound	$\tau_{trans \rightarrow cis}$[a] (s)	$\tau_{cis \rightarrow trans}$[a] (s)
83	7.4	122.1
84	2.9	69.0

[a] Determined at 50 µM in aqueous buffer + 0.5 % DMSO, 25 ºC.

Finally, relative concentrations of the two isomers in equilibrium at PSS_{365} and PSS_{525} was determined by ^{1}H NMR spectroscopy (Figure 84). Upon illumination with 365 nm, all signals present in the dark spectra were shifted, which confirmed the excitation of the compounds to the *cis* isomer. AB-**83** did not present a singlet signal and therefore, one of the aromatic signals was used for the isomeric quantification (Figure 84A). On the other hand, the methyl signal of **84** was used for the relative quantification of the two isomers (Figure 84B).

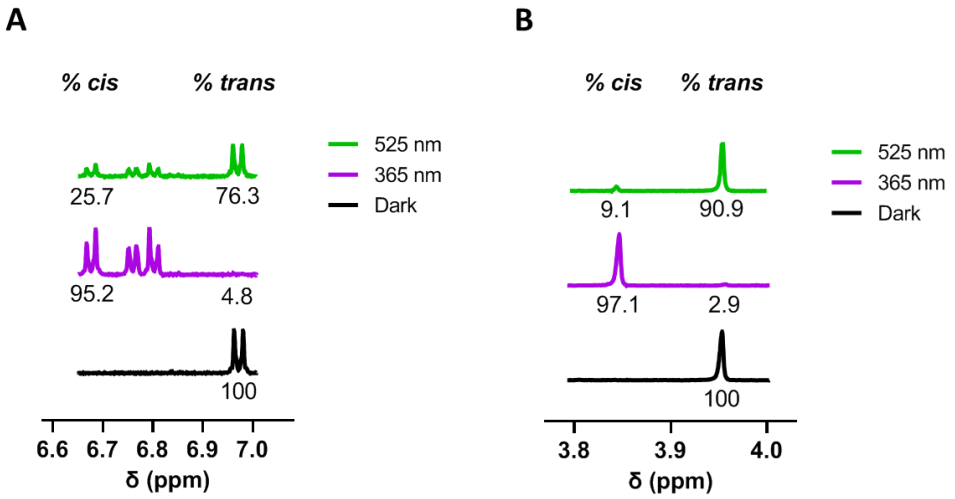

Figure 84. Photostationary state (PSS) quantification by ^{1}H-NMR. The proportions of *cis* and *trans* isomers of **83** (A) and **84** (B) in D_2O at PSS_{365} and PSS_{525} were determined by ^{1}H NMR. Samples were continuously illuminated for 3 min using 365nm and 525 nm light.

Both compounds showed almost quantitative conversion (< 95%) to the *cis* isomer upon illumination at 365 nm. Illumination at 525 nm triggered the *cis*→*trans* isomerization in both compounds. For *p*-AB **84**, 90.9% of the thermostable *trans* isomer was recovered upon illumination. Nevertheless, the photoinduced back-isomerization of *cis*-**83** was not as efficient, with only 76.3% of the *trans* isomer quantified at PSS_{525}. This lower efficiency appears as a consequence of the n-π* band overlapping in the absorbance spectra of the two photoisomers of **83** (Figure 82A).

Photochemical properties of the developed azobenzenes (**83** and **84**) are summarized in Table 17. Both compounds present similar properties in general; however, the introduction of a methoxy group in **84** has a significant increase on the thermal relaxation rate of the *cis*-**84**.

Table 17. Photochemical properties of azobenzenes 83 and 84[a]

Compound	λ_{trans}[a] (nm)	λ_{cis}[a] (nm)	$t_{½}$[a] (h)	PSS_{365}[b] (%*cis*)	PSS_{530}[b] (% *trans*)
83	346	430	38.3	95.2	76.3
84	358	440	11.5	97.1	90.9

[a] Determined at 50 µM in aqueous buffer + 0.5 % DMSO, 25 ºC. [b] PSS state areas were determined at 12 ºC by ^{1}H-NMR after illumination (380/550 nm) of a 100 µM sample in D_2O.

2.2.3 *In vitro* photopharmacological evaluation of compounds 83 and 84

Following the photochemical characterization of *p*-ABs **83** and **84**, we decided to evaluate the pharmacological properties of the two photochromic ligands in cultured cells. In particular, we were especially interested to see if the compounds showed good selectivity towards β_1-AR, which was our main objective when the compounds were designed.

Photoswitchable modulation of β_2-AR

Functional β_2-AR activity of the two *p*-AB, **83** and **84**, was assessed using HEK293-H188 M1 cells, following the protocol described for the first family of photochromic ligands. Inhibitory dose-response curves of the ligands were obtained with a constant concentration of cimaterol (3 nM), both in the dark and upon illumination at 380 nm (Figure 85 and Table 18).

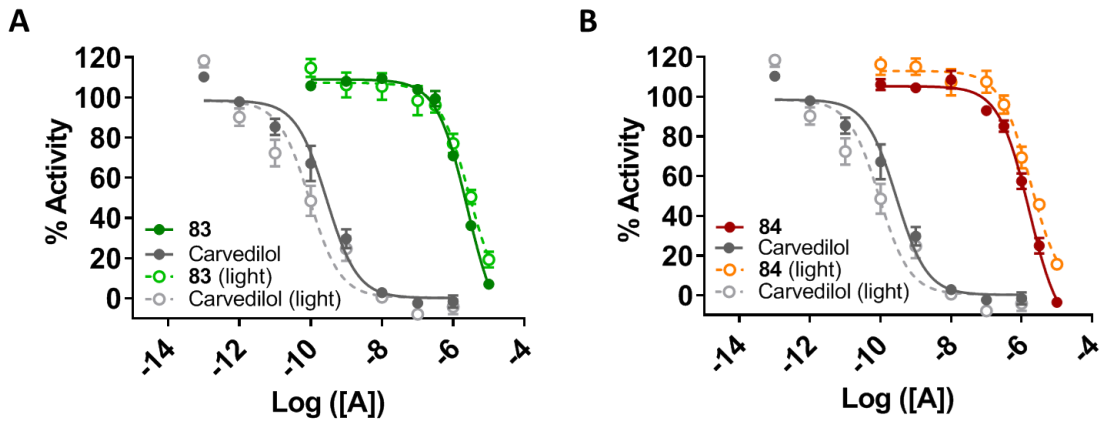

Figure 85. Light-dependent β_2-AR inhibition of 83 and 84. Dose-response curves of **83** (A) and **84** (B) with a constant concentration of the agonist cimaterol (3 nM) in the dark and under constant violet light (380 nm). Data are shown as the mean ± SEM of four independent experiments in duplicate.

Interestingly, both compounds showed a similar pharmacological profile, with low inhibitory potency (within the µM range) and no significant changes in the functional activity triggered by the application of light (Figure 85 and Table 18).

Table 18. Pharmacological data of photoswitches 83 and 84 for β_2AR.

	DARK		LIGHT			
Cmpd	**IC_{50} (μM)**	**SEM**	**IC_{50} (μM)**	**SEM**	**PPS[a]**	**SEM**
83	2.45	0.33	2.86	0.39	1.08	0.23
84	1.65	0.26	1.78	0.18	1.17	0.33
Carvedilol	0.00029	0.12	0.000086	0.10	0.33	0.18

[a] PPS refers to Photoinduced Potency Shift which is the relation between the measured IC_{50} in light and dark conditions respectively.

The low inhibitory potency observed for the two *p*-AB constituted a promising start, considering that both ligands were designed to selectively target β_1-AR. To complete the characterization of their relatively poor β_2-AR antagonism, dose-response curves of cimaterol were recorded in the presence or absence of a constant concentration of the photochromic ligands under different illumination conditions (Figure 86). DR curves of the agonist were treated with 1 μM of the photoswitchable ligands, which approximately corresponds to their IC_{50} values.

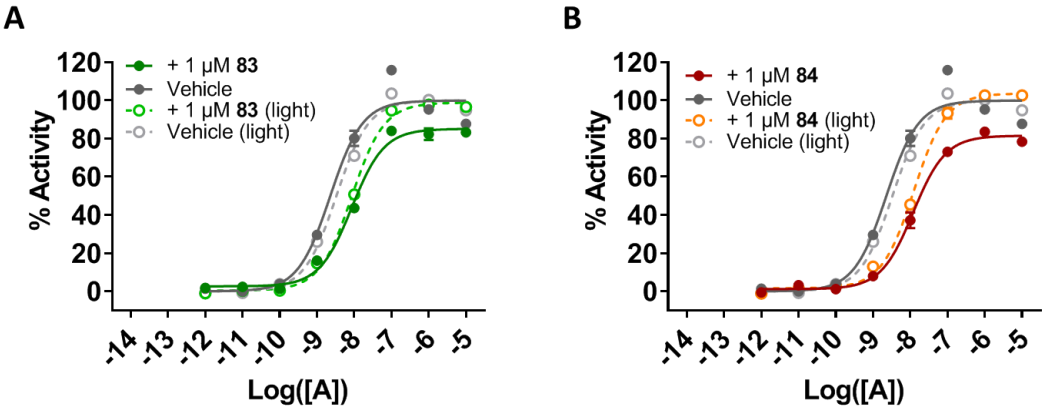

Figure 86. Light-dependent β_2-AR inhibition of 83 and 84. Dose-response curves of the agonist cimaterol with a constant concentration (1 μM) of the photochromic ligands **83** (A) and **84** (B) in the dark and under constant violet light (380 nm). Data are shown as the mean ± SEM of four independent experiments in duplicate.

Results showed that the addition of a constant concentration of **83** and **84** caused a slight shift on the agonistic curve, which was identical for the two photoisomers. This was consistent with the absence of photoinduced-shift observed in the *p*-AB dose-response curves. Nevertheless, both compounds showed an unusual light-dependent effect, which was more marked in the results obtained for compound **84**. Cimaterol dose-response curves treated with ABs **83** and **84** in the dark presented a reduction in the E_{max} of 15% and 20% respectively. This effect was reversed when compounds were illuminated at 380 nm (Figure 86). Photoinduced modulation of the E_{max} can be attributed to non-competitive antagonism of *trans* isomers, but it can also be consequence of a hemi-equilibria, where the assay time has been insufficient for the equilibration of agonist, antagonist and receptor in the cellular system.

To further investigate this unusual light-dependent effect, agonist dose-response curves were performed in the dark and upon illumination at 380 nm with different constant concentrations of **84** (0.6 to 16 µM) (Figure 87).

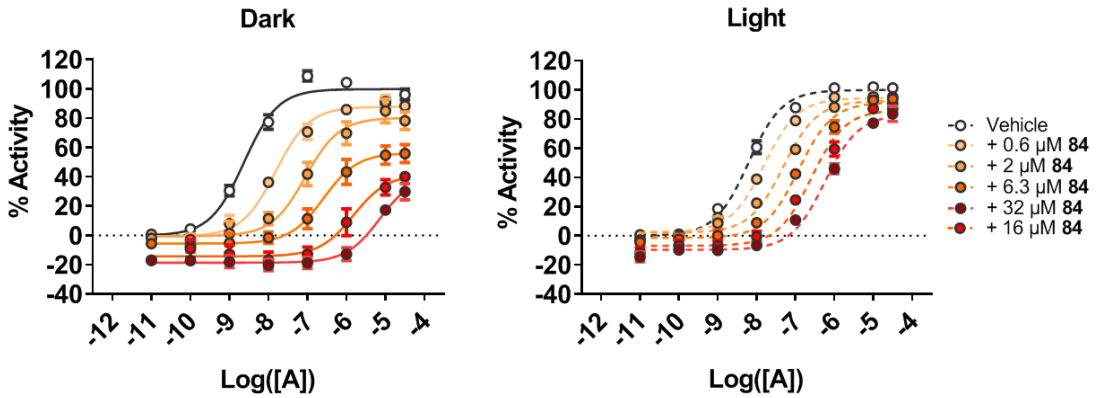

Figure 87. Antagonistic activity of 84. Dose-response curves of cimaterol with different concentrations of **84** under dark conditions or after 380 nm light illumination. Each data point represents the mean and SEM of three experiments performed in duplicate.

Results showed that both isomers of the studied azobenzene are inverse agonists, as they can reduce the basal activity of the system up to 20% (Figure 87). Additionally, agonistic curves treated with **84** upon illumination showed parallel displacement of the DR at higher concentrations of antagonist and no diminution of the E_{max} (Figure 87). This antagonistic behavior is consistent with orthosteric competitive antagonism.[51] When the same experiment was performed in dark conditions, increasing concentrations of **84** shifted the agonist DR curves according to competitive kinetics; however, a significant and progressive diminution of the E_{max} was also observed (Figure 87). The combination of these two characteristic behaviors suggested that the system in dark conditions was in hemi-equilibria.[51]

To confirm this hypothesis and exclude the possibility of noncompetitive antagonism exerted by the *trans* isomer, we performed a Schild analysis (Figure 88). Schild analysis refers to the use of the equation derived by Arunlakshana and Schild to construct linear plots (Eq. 1).[52]

$$\text{Log (DR-1)} = \text{Log [A]} - \text{Log } K_A \qquad \text{(Eq.1)}$$

DR refers to dose ratios, which is the relation between the EC_{50} of the agonist measured in the presence or in the absence of antagonist. Thus, for every concentration of antagonist [A] studied in the experiment depicted in Figure 87, a corresponding DR was calculated. Results were then plotted as a linear regression of log (DR-1) upon log [A] (Figure 88). This pharmacological tool can be used to quantify the affinity of competitive antagonists and to define the mechanism of action of the studied antagonist. Affinity estimation of the ligand can be extracted from the intercept of the Schild regression to the X axis, as it corresponds to the pK_B. However, this affinity estimation is only valid if the Schild regression is linear with a slope of unity, which corresponds to the plot of ideal competitive antagonism. Figure 88 shows that only illuminated **84** presents an ideal Schild regression and thus, we could only estimate the pK_B of *cis*-**84**.

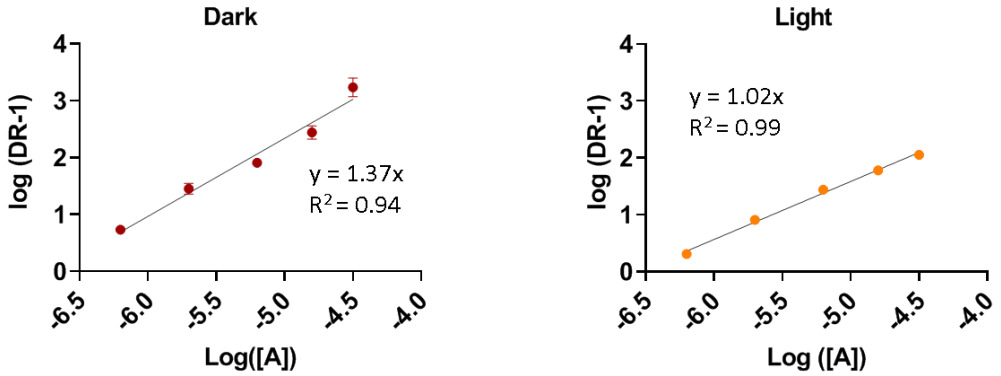

Figure 88. Schild regression of 84. Schild regression of the data extracted from experiments depicted in Figure 87, both in dark and light conditions. Each data point represents the mean and SEM of three experiments performed in duplicate.

On the other hand, we were mostly interested in the capability offered by Schild analysis of unveiling nonequilibrium conditions, as this would confirm if the *trans*-**84** is in hemi-equilibria as hypothesized. Left panel in Figure 88 showed a linear correlation between log (DR-1) and log [**84**] with slope significantly greater than unity, a behavior that is probably attributed to an inadequate equilibration time for *trans*-**84**.[51] In consequence, Schild analysis highlighted that while *cis*-**84** has reached an equilibrium with the biological system after 45 minutes of incubation, the *trans* isomer requires longer equilibration times. This might be attributed to the large and planar geometry of *trans*-**84**, which may difficult the access of this isomer to the binding pocket.

To sum up, the two *p*-AB developed showed poor β_2-AR antagonistic activity and no light-dependent pharmacological effects. Therefore, both ligands displayed so far, the desired pharmacological properties towards β_2-AR, as they were designed to selectively target the β_1-AR subtype.

Photoswitchable modulation of β_1-AR

Finally, β_1-AR photopharmacological properties of **83** and **84** were evaluated in cultured cells. HEK-293 ^{i}SNAP β_1AR H188 cells were used, and assays were performed following the protocol established for the characterization of β_1-AR photopharmacology of the first series of azobenzenes.

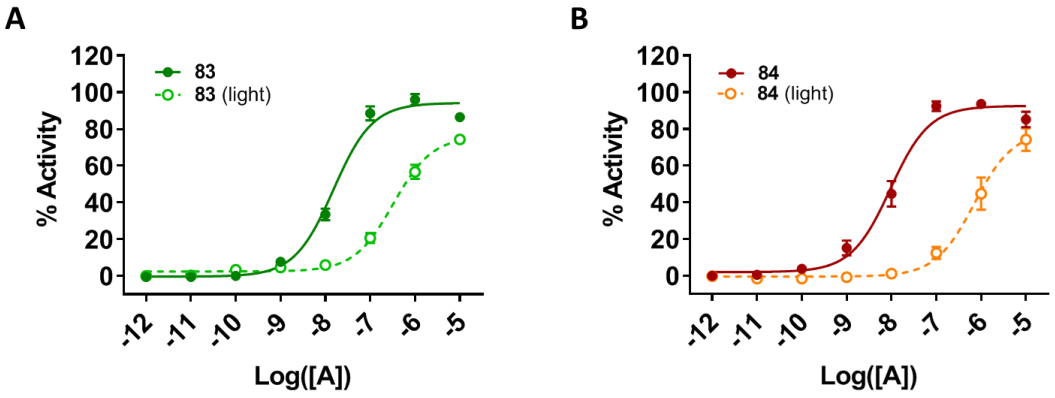

Figure 89. Light-dependent β_1-AR activation of 83 and 84. Dose-response curves of **83** (A) and **84** (B) in the dark and under constant violet light (380 nm). Data are shown as the mean ± SEM of three to five independent experiments in duplicate.

Results showed that the *trans* isomers of both, **83** and **84**, displayed good agonistic activity with an EC_{50} in the nanomolar range. Application of UV light (380 nm) triggered a significant decrease in the EC_{50} of both photoswitchable ligands, which appoints them as *trans*-on compounds (Figure 89, Table 19).

Table 19. Pharmacological data of photoswitches 83 and 84 for β_1-AR.

	DARK		LIGHT			
Cmpd	**EC_{50} (nM)**	**SEM**	**EC_{50} (nM)**	**SEM**	**PPS[a]**	**SEM**
83	15.14****	1.42	331.13	77.76	20.08	6.06
84	8.79****	2.89	762.08	169.61	83.03	39.06

[a] PPS refers to Photoinduced Potency Shift which is the relation between the measured EC_{50} in light and dark conditions respectively. Statistical differences from light EC_{50} values are denoted for adjusted p values as follows: ****p<0.0001.

In addition, both compounds presented very good light-dependent modulation of β_1-AR, with photoinduced shifts of 20 and 83 for **83** and **84** respectively (Table 19). However, **84** was particularly promising, as it allowed modulation of the activation state of β_1-AR from 100% to almost 0% through the application of light at 100 nM concentrations.

Additionally, it is worth noting that even though both compounds behaved as full agonists in the developed system, it is very likely that they are partial agonists for the reasons previously discussed with **PZLs 1-3**. In order to evaluate if the developed azobenzenes are full or partial agonists, dose-response curves of cimaterol and of methoxy substituted AB **84** were performed in iSNAP β_1-AR HEK cells with two different expression levels (induced with 0.01 µM and 0.003 µM doxycycline for 24h respectively) (Figure 90).[51]

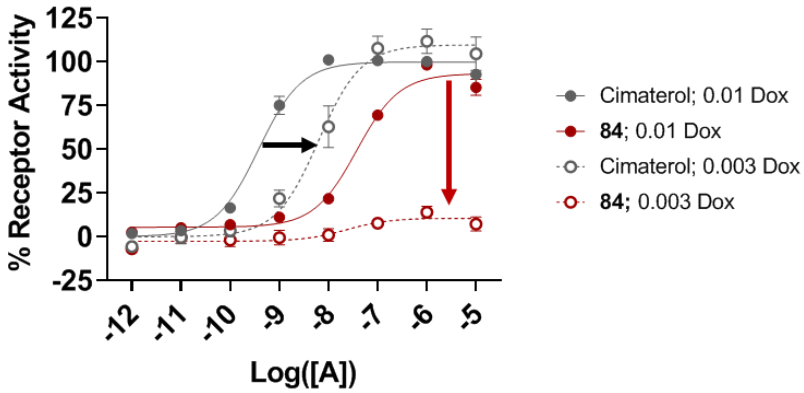

Figure 90. β_1-AR functional assays performed in differently induced HEK293 iSNAP β_1-AR cells stably transfected with an Epac cAMP biosensor. Dose-response curves of the agonist cimaterol and *p*-AB **84** were performed using cells with different induction conditions: 0.01 dox and 0.003 dox respectively. Data are shown as the mean ± S.E.M of three independent experiments performed in duplicate.

Results showed that the use of cells with lower expression levels only shifted the dose-response curve of full agonist cimaterol, thus significantly increasing the EC_{50} measured in this system (Figure 90). Meanwhile, changes in the expression levels of β_1-AR significantly affected the E_{max} values of the dose-response curve registered for AB **84**, which was almost detected as

a flat line when tested in cells induced with 0.003 μM doxycycline; nevertheless, EC_{50} values of **84** were unaltered by the different β_1-AR expression levels (Figure 90). These results evidence that *p*-AB **84** is a very partial agonist, which essentially behaves as an antagonist in physiological systems with low receptor expression.[51,53]

When assessing the differences in functional activities for β_1- and β_2-AR, the two *p*-AB displayed good β_1-AR selectivity in their *trans* isomeric form (Table 20). T*rans*-**83** displayed a β_1/ β_2 selectivity ratio of 161.8 and *trans*-**84** of 187.7, both notably higher than the selectivity ratios reported for β_1-AR selective ligands atenolol and metoprolol, for instance. On the other hand, the *cis* isomers of the two compounds showed moderate modulation of the two adrenoceptor subtypes, and β_1/ β_2 estimated selectivity ratios were 8.6 and 2.3 for **83** and **84** respectively. The fact that good β_1 selectivity is achieved when the compound is disposed in its longer isomeric form is in good agreement with the molecular mechanisms of β_1/β_2 subtype selectivity recently reported. Both β_1AR and β_2AR present the same residues at the orthosteric site, only some residues at the edge of the pocket are different. Thus, large ligands may directly interact with these residues resulting in a differential modulation of the two receptor subtypes.[47]

Table 20. Selectivity ratios of the *p*-AB (83 and 84).[a]

	DARK	LIGHT
Cmpd	**β_1 vs β_2**	**β_1 vs β_2**
83	161.8	8.6
84	187.7	2.3

[a] A ratio of 1 implies no receptor selectivity for a receptor subtype over another.

Finally, studies were performed in order to assess the dynamic and reversible modulation of the target receptors with light in living cells. In these experiments, both compounds enabled good modulation of the activation state of β_1-AR in living cells through the application of light cycles (Figure 91).

Results showed that both **83** and **84** displayed similar agonistic effects in the dark, with 85% and 90% of receptor activation respectively. When violet light was applied to the biological system, a significant decrease in the activation state of β_1-AR was measured for the two azobenzenes, implying that their *cis* isomers present reduced agonism. Therefore, the two compounds have an analogous and very similar light-dependent pharmacology; considering that their *trans* isomeric form showed higher agonistic potency, both **83** and **84** are very good *trans*-on compounds (Figure 91). However, the methoxy- substituted compound **84** presents slightly better photopharmacological properties, as it allows dynamic modulation of β_1-AR activation from 90% in its *trans* form to approximately 6% upon light application (Figure 91B). In consequence, *p*-AB **84** is a particularly ideal photoswitchable ligand, which enables an almost complete ON/OFF modulation of β_1-AR with the external application of light. On the other hand, AB **83** shows a violet light-triggered activity decrease of approximately 65%, which

can be almost completely reversed upon illumination with green light (550 nm). Therefore, the developed ligands show good and reversible photopharmacological properties towards β_1-AR.

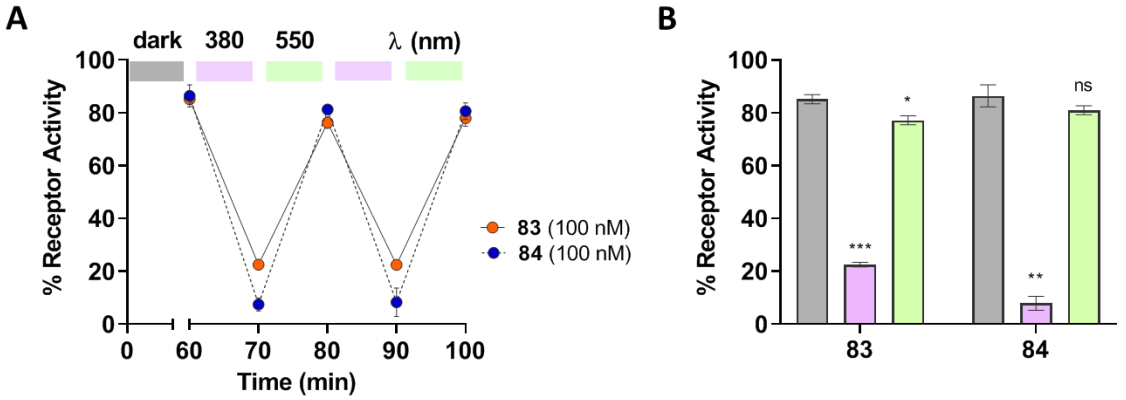

Figure 91. Real-time optical control of β_1-AR enabled by *p*-ABs 83 and 84. (A) Time course quantification of intracellular in the presence of 100 nM **83** (orange dots) and 100 nM **84** (blue dots). Purple and green boxes correspond to 10 min illumination breaks using 380 nm and 550 nm lights respectively. (B) β_1-AR functional activity values obtained for *p*-ABs **83** and **84** measured under different illumination conditions. Data are shown as the mean ± SEM of three independent experiments. Statistical differences from dark results are denoted for adjusted p values as follows: * p<0.05, **p<0.01 and ***p<0.001.

In conclusion, we have successfully developed the first photoswitchable ligands that enable a selective and reversible modulation of β_1-AR with the application of light. Both **83** and **84** are *trans*-on compounds with partial agonistic behavior in the nanomolar range. The application of UV light (380 nm) triggers excitation of the ligands to their *cis* isomeric forms, which display significantly lower agonistic activities towards β_1-AR. Therefore, the development of these ligands constitutes a valuable tool to better discern the role of β_1-AR in physiological systems. Furthermore, these ligands should particularly modulate the cardiac function with the application of light, taking into account that β_1-AR are mainly expressed in the cardiac tissue.

2.2.4 Light-dependent modulation of the cardiac output in zebrafish larvae

In order to assess the potential of the developed *p*-ABs, our best β_1-AR hit (**84**) was tested in zebrafish larvae (7 dpf). In particular, the capability of this photochromic ligand to modulate the cardiac rhythm through the application of light was evaluated (Figure 92). Zebrafish larvae were exposed to different treatments (1% DMSO, 25 µM **84** and 10 µM carvedilol) under dark conditions for 1.5 h and the cardiac rhythm of the larvae was monitored using a camera coupled to a microscope. Additionally, light-triggered effects on the cardiac rhythm were assessed; the different experimental groups were kept in dark conditions for 1 h and illuminated for 1 min with 380 nm light. Immediately after light application, a significant increase in heart rate was detected in control larvae; this undesired light-dependent event in control animals can be attributed to the physiological alteration induced by a visual stimulus, such as larvae illumination with 380 nm light. In order to assess light-dependent effects related to treatment with *p*-AB **84**, animals were left to acclimate for 30 min prior to heart monitorization, which reduced non-specific alterations of the cardiac rhythm induced by the visual stimulus, considering that zebrafish have specific UV light photoreceptors. [54]

Results showed that treatment of the larvae with *trans*-**84** caused a significant reduction of the cardiac rhythm; this decrement in the heart rate was partial in comparison to results obtained with the beta-blocker carvedilol. Interestingly, when animals exposed to **84** were illuminated with 380 nm light, the measured heart rate had been restored to control levels. These results are in good agreement with the data obtained *in vitro*, where **84** is a partial agonist with a good *trans*-on behavior. Importantly, no significant differences were observed between the control groups in dark conditions and after light application. Moreover, when larvae were treated with non-photoswitchable antagonist carvedilol, a significant reduction in the cardiac rhythm was measured, and no changes were detected between the groups kept in dark conditions and illuminated with UV light. All these controls confirm that light-triggered differences observed in animals exposed to **84** are a consequence of the different pharmacological behavior described for the two photoisomers of AB **84**.

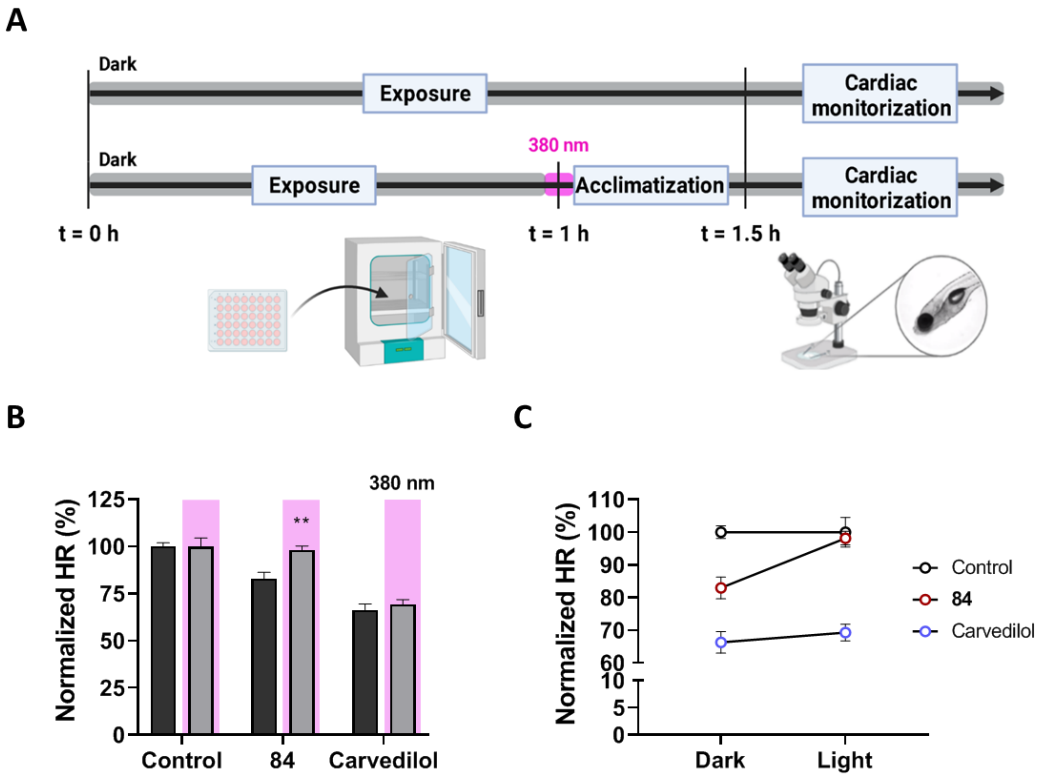

Figure 92. Optical modulation of the cardiac frequency tested using *p*-AB 84 in zebrafish larvae. (A) Schematic representation of the followed protocol to assess cardiac modulation through the application of light. (B) Normalized cardiac frequency of the different experimental groups (1% DMSO N=16-21, 25 µM **84** N=16-21 and 10 µM carvedilol N=16-21) in the dark and after illumination with 380 nm light for 1 min. Purple boxes correspond to results after illumination with 380 nm for 1 min. Statistical differences between the different illumination conditions are denoted for adjusted p values as follows: **p<0.01 (C) Direct comparison of the light-induced changes in the normalized heart rate of zebrafish larvae in the distinct experimental groups (1% DMSO N=16-21, 25 µM **84** N=16-21 and 10 µM carvedilol N=16-21). Data are shown as the mean ± SEM of two independent experiments.

Therefore, these experiments highlight the potential of the developed AB (**83** and **84**), which enable a selective modulation of β_1-AR and allow cardiac control, both through the application of light. This constitutes the first proof of concept for selective optical modulation of β_1-AR, which highlight the enormous potential of the developed molecular tools for future research applications in a variety of fields.

2.3 Conclusions

The first proof of concept for β-AR photopharmacology is presented in this chapter. Following the azologization strategy, the hydrophobic moiety present in the majority of β-AR antagonists was substituted for a *p*-acetamido azobenzene, which led to the development of three photochromic ligands named **Photoazolol-1**, **-2**, and **-3**. Interestingly, **PZLs-1-3**, which are structural isomers, showed different light-regulated pharmacological properties and different selectivity towards the two studied beta-AR subtypes. *Trans*-**PZL-1** was found to be the most active isomer for both β_1- and β_2-AR, whereas for **PZL-2**, higher antagonism was observed on its *cis* form; however, both **PZL-1** and **PZL-2** showed higher functional activities for beta-2. For **PZL-3**, which incorporates the oxyaminoalcohol moiety in *para*, selective *trans*-on modulation of β_1-AR was described. In addition, antagonistic behavior was detected when ligands were tested against β_2-AR, while compounds were identified as agonists or partial agonists for β_1-AR. This can be attributed to the different receptor expression levels found in the cellular systems used to functionally characterize ligands towards the two subtypes of β-AR.

Taking into account the results obtained for **PZL-3**, two *para*-substituted azobenzenes (**83** and **84**) were synthesized to selectively target β_1-AR. The two ligands displayed good β_1-AR selectivity, with nanomolar agonistic activities detected for their *trans*-isomers. The application of violet light significantly decreased the agonism in both **83** and **84**, highlighting a *trans*-on behavior. For *p*-AB **84**, additional experiments were performed with cells expressing different levels of β_1-AR, which highlighted the partial agonistic nature of this photochromic ligand. The promising *in vitro* light-dependent results of **84** as a β_1-AR selective ligand were extrapolated to assess its potential to optically modulate living animals. Experiments performed in zebrafish larvae (7 dpf) showed that animals exposed to *trans*-**84** experienced a significant reduction of the cardiac rhythm. When animals exposed to AB **84** were illuminated for 1 minute at 380 nm, the cardiac rate was restored to control levels, which is in good agreement with the results obtained in cells. Of note, we demonstrated that dynamic control of the two studied receptors *in vitro* with the application of light is possible for all the developed molecules.

Therefore, we have developed several chemical probes with complementary and reversible photochromic behavior. Additionally, ligands that selectively target both receptor subtypes (β_1- and β_2-AR) have also been described, which opens the door to a broad range of future research applications. Overall, these potent tools enable the control of prototypical class A GPCRs, enlarging the photopharmacological toolbox of compounds targeting the GPCR large family of proteins, which includes a substantial number of therapeutic targets.

Chapter 3. Towards red-shifted azobenzenes targeting β-AR: an improved photochemical profile for therapeutic applications

Abstract

[redacted]

[redacted]

[redacted]

[redacted]

[redacted]

[redacted]

[redacted]	[redacted]	[redacted]	[redacted]	[redacted]	[redacted]
[redacted]	[redacted]	[redacted]	[redacted]	[redacted]	[redacted]
[redacted]	[redacted]	[redacted]	[redacted]	[redacted]	[redacted]
[redacted]	[redacted]	[redacted]	[redacted]	[redacted]	[redacted]

[redacted]

[redacted]

[redacted]

[redacted] [redacted]

[redacted]

[redacted]

[redacted]

[redacted]

[redacted]

[redacted]

[redacted]

[redacted]

[redacted]

[redacted]

[redacted]

[redacted]

[redacted]

[redacted]

[redacted]

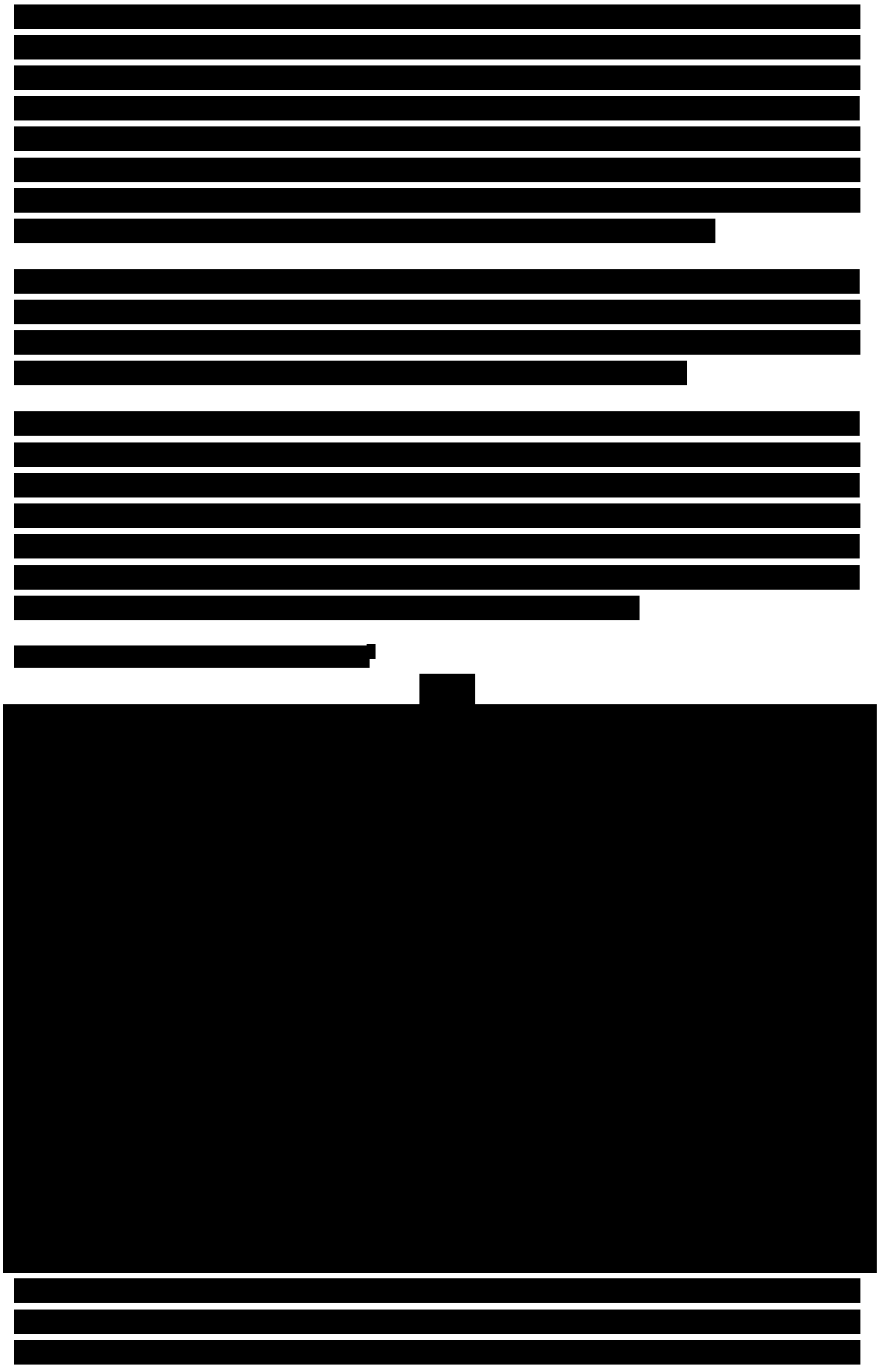

[redacted]

[redacted]

[redacted]

[redacted]

[redacted]

[redacted]

[redacted]	[redacted]	[redacted]	[redacted]	[redacted]	[redacted]
[redacted]	[redacted]	[redacted]	[redacted]	[redacted]	[redacted]
[redacted]	[redacted]	[redacted]	[redacted]	[redacted]	[redacted]
[redacted]	[redacted]	[redacted]	[redacted]	[redacted]	[redacted]
[redacted]	[redacted]	[redacted]	[redacted]	[redacted]	[redacted]
[redacted]	[redacted]	[redacted]	[redacted]	[redacted]	[redacted]
[redacted]	[redacted]	[redacted]	[redacted]	[redacted]	[redacted]

[redacted]

[redacted]

[redacted]

[redacted]

[redacted]

[redacted]

[redacted]

[redacted]

[redacted]

[redacted]

[redacted]

3.3 Towards the development of fluorinated azobenzenes targeting β-AR

3.3.1 Design and synthesis

[redacted]

In another strategy for red-shifting azobenzenes which has gained popularity, the n – π* absorption bands of the two photoisomers get separated through tetra-*ortho* substitution with heteroatoms. This approach has been successfully reported for -chloro[57,63], -alcoxy[64] and -fluoro[58,65] substituted azobenzenes among others; tetra-*ortho* halogenated compounds isomerize in the red range of the visible spectrum and have longer thermal relaxation times, thus providing ideal molecular tools for the study of physiological systems with spatiotemporal precision. Taking into account the results reported in the literature for these scaffolds, we proposed that introducing fluorine groups in the chemical structure of **Photoazolols 1-3** would provide good, red-shifted ligands targeting β-adrenoceptors.

Fluorine was selected as the optimal substituent considering that its bulkiness is similar to hydrogen, thus minimally altering the photopharmacological activities of **PZLs 1-3**. However, the synthetic approaches to produce *ortho*-fluoroazobenzenes based in **PZLs** presented several difficulties and it was not certain that the compounds would maintain their pharmacological behavior. For these reasons, prior to the development of *ortho*-fluoroazobenzenes based in **PZLs**, we decided to evaluate the effects of substituting an -H for a -F in the molecular scaffold of **PZL-1** as a proof of concept. The fluorinated analogue of **PZL-1** was designed with the fluorine atom in *para*- with respect to the molecular fingerprint due to its synthetic accessibility (Scheme 15).

Scheme 15. Synthesis of azobenzene 107.[a]

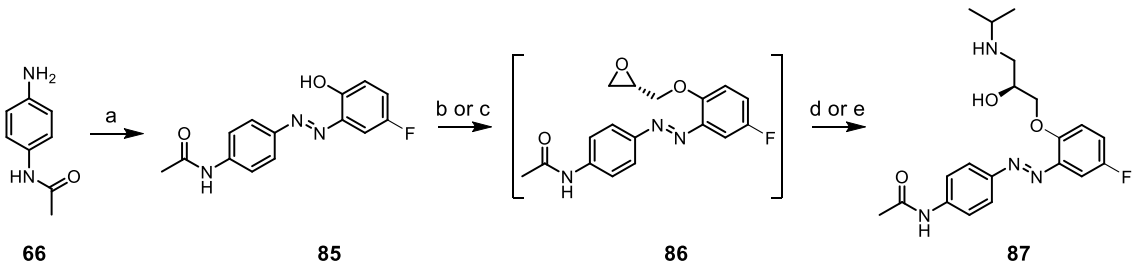

[a] Reagents and conditions: (a) (I) $NaNO_2$, aq HCl, 0ºC, 5 min; (II) 4-Fluorophenol, aq NaOH, 0ºC, 30 min 30%; (b) (*R*)-Epichlorohydrin, K_2CO_3, butanone, reflux, 24-48h, 81%; (c) (2*S*)-Glycidyltosylate, K_2CO_3, DMF, r.t, 12h; (d) i-$PrNH_2$, 12h, r.t, 15% ; (e) i-$PrNH_2$, 90ºC, 48h, 26%.

Direct diazotization of *p*-acetamidoaniline (**66**) followed by reaction with 4-fluorophenol yielded phenolic intermediate **105** with moderate yields (30%). Reaction of 4-fluorophenol with the diazonium salt can only occur in the 2- position considering that the para- position is already substituted. Phenolic azobenzene **105** was then alkylated by direct reaction with (*R*)-epichlorohydrin to provide (*S*)-oxirane **106**, as previously described. The epoxide was finally

opened by nucleophilic attack of isopropylamine, which provided **107**. However, when the enantiomeric purity of the final product was evaluated, racemization was detected. As previously stated, the reaction of (*R*)-epichlorohydrin with phenolic azobenzenes only racemizes when the phenol group is located in an *ortho*- position with respect to the N=N bond. To obtain **107** with good enantiomeric purity, a one pot reaction using (2*S*)-glycidyltosylate and isopropylamine was performed.

3.3.2 Photochemical characterization

Following the synthesis, compound **107** was photochemically characterized to assess the differences introduced by fluorine substitution with respect to the photophysical properties reported for **PZL-1**. A complete characterization was performed in an identical manner to the characterization described for **PZLs** or *p*-AB **83** and **84** (Figure 112). Table 25 also summarizes the photochemical properties of fluorinated compound **87**.

The optimal wavelength to trigger excitation of *trans*-**87** to its cis isomer was 385 nm. Back-isomerization was achieved through application of green light (525/550 nm) (Figure 112B). The compound was found to be stable and displayed reversible isomerization through the application of several light cycles (Figure 112E). Unfortunately, the appropriate isomerization wavelengths for **87** are identical to the wavelengths described for **PZL-1**, indicating that the introduction of a single fluorine has not induced notable photochemical changes.

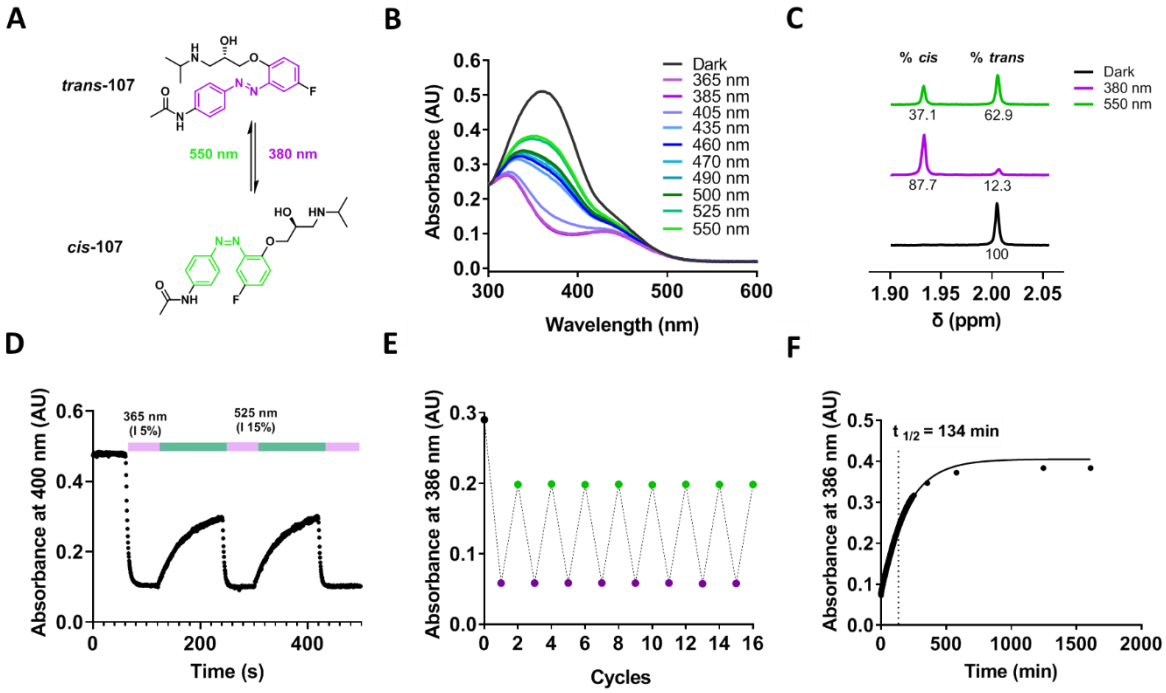

Figure 112. Photochemical characterization of 107 (50 µM in 0.5% DMSO Buffer). (A) 2D chemical structures of the photoisomers of **107**. (B) UV-Vis spectra of the azobenzene under different light conditions. (C) Photostationary state (PSS) quantification by ^{1}H-NMR. (D) Multiple *cis*/*trans* isomerization cycles (365/525 nm) of **107** were performed. Absorbance at 400 nm was measured continuously with the Thermo Fisher Evolution 350 spectrophotometer, even during the application of light. (E) Multiple *cis*/*trans* isomerization cycles show the stability of the compound over 45 minutes of light application. (E) Half-lifetime estimation of *cis*-**107** at 25 ºC; absorbance was measured at 386 nm.

Table 25. Photochemical properties of azobenzene 107[a]

Compound	λ_{trans}[a] (nm)	λ_{cis}[a] (nm)	$t_{½}$[a] (min)	PSS_{365}[b] (%*cis*)	PSS_{530}[b] (% *trans*)
107	360	430	134.0	87.7	62.9

[a] Determined at 50 µM in aqueous buffer + 0.5 % DMSO, 25 ºC. [b] PSS state areas were determined at 12 ºC by ^{1}H-NMR after illumination (380/550 nm) of a 100 µM sample in D_2O.

The small effects caused by mono-fluorination of the AB can be attributed to the fact that only one -F atom was introduced in *meta-* with respect to the azo bridge, which usually displays low frontier orbital coefficients. When the absorbance spectra of **107** and **PZL-1** were superposed, we observed that fluorination had broadened the band corresponding to the π-π* transition and increased the intensity of the n-π* band (Figure 113). The described changes in the absorbance spectrum of **107** resulted in an increased overlapping of the n-π* bands of the two photoisomers, which difficulted its light-triggered back-isomerization. In particular, only 63% of *trans*-**107** was quantified at PSS_{550}, which is lower compared to the PSS_{550} *trans*-**PZL-1** (Figure 112C, Table 25).

Additionally, thermal relaxation of *cis*-**107** was found to be notably slower, with a half-lifetime of 134 min compared to the 74 min estimated for *cis*-**PZL-1**. This increase in the half-life time of the *cis* isomer can be explained through the EW properties of fluorine atoms. Fluorine atoms can donate electrons through induction; however, due to their high electronegativity they are overall considered electron-withdrawing groups. Introducing an EWG in the molecular scaffold of **PZL-1** lowers the energy of the *cis* n orbital causing an increase in its stability and thermal relaxation times.[58]

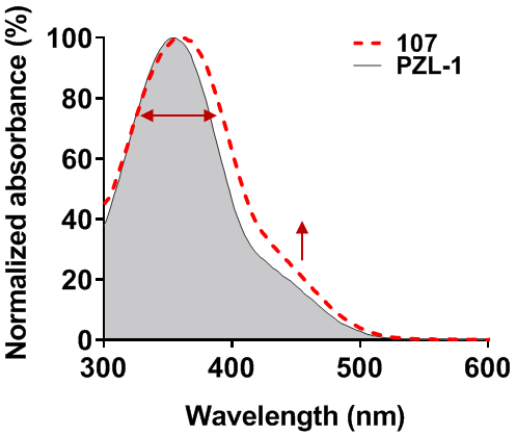

Figure 113. Superposed absorption spectra of fluorinated 107 and PZL-1. Absorbance spectra of the two compounds were normalized; 100% and 0% absorbances were attributed to the maximal and minimal absorbance values of each spectrum respectively.

3.3.3 Photopharmacological characterization

Finally, we evaluated the impact of fluorinating **PZL-1** on the pharmacological properties. For this reason, inhibitory dose-response curves of **107** in both dark and after illumination (380 nm) were performed in the β_2-AR cellular system (Figure 114A). Results showed that

fluorinated **107** displayed good inhibitory potency, within the nanomolar range (Table 26). Application of light triggered a 22-fold decrease in the antagonistic activity of the studied compound, which highlighted it as a *trans*-on photoswitch. Therefore, the light-dependent pharmacological behavior of **107** towards β_2-AR is very similar to the behavior described for **PZL-1**. This suggested that the introduction of several fluorine atoms in the azobenzene moiety should afford red-shifted compounds with similar photopharmacological properties to **PZL-1**.

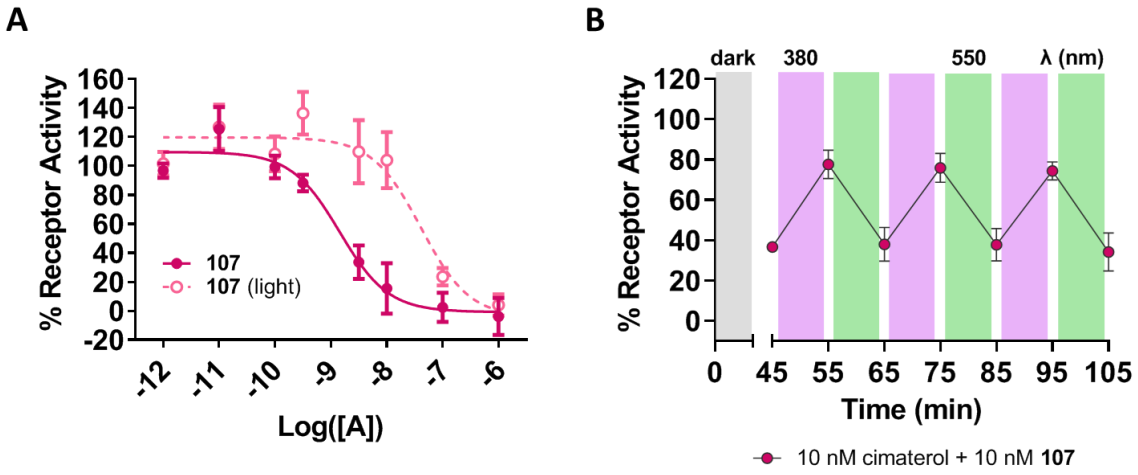

Figure 114. Light-dependent β_2-AR inhibition of 107. (A) Dose-response curves of **107** with a constant concentration of the agonist cimaterol (3 nM) in the dark and under constant violet light (380 nm). (B) Time course quantification of intracellular cAMP challenged with the β-AR agonist cimaterol in the presence of **107**. Purple and green boxes correspond to 10 min illumination breaks using 380 nm and 550 nm lights respectively. Data are shown as the mean ± SEM of four independent experiments in duplicate.

Table 26. Pharmacological data of azobenzene 107 for β_2AR.

	DARK		LIGHT			
Cmpd	**IC_{50} (nM)**	**SEM**	**IC_{50} (nM)**	**SEM**	**PPS[a]**	**SEM**
107	1.61***	0.71	36.29	10.41	22.42	17.57

[a] PPS refers to Photoinduced Potency Shift which is the relation between the measured EC_{50} in light and dark conditions respectively. Statistical differences from light IC_{50} values are denoted for adjusted p values as follows: ***p<0.001.

Additionally, reversible modulation of the activation state of β_2-AR was achieved through the application of light cycles in cultured cells (Figure 114B). After incubating compound **107** (10 nM) with the studied cells for 45 min in dark conditions, the activation state of beta-2 was reduced to 38%. Application of violet light (380 nm) triggered a significant increase on the receptor activity that could be reversed through application of green light.

Finally, the activity of **107** in the dark and after illumination at 380 nm was also assayed in HEK-293 ^{i}SNAP β_1AR (Figure 115, Table 27). *Trans*-**107** behaved as a partial agonist with an EC_{50} of 289 nM. Upon illumination, the agonistic activity was significantly reduced to the µM range, which highlighted that the fluorinated compound presents a *trans*-on photopharmacological behavior.

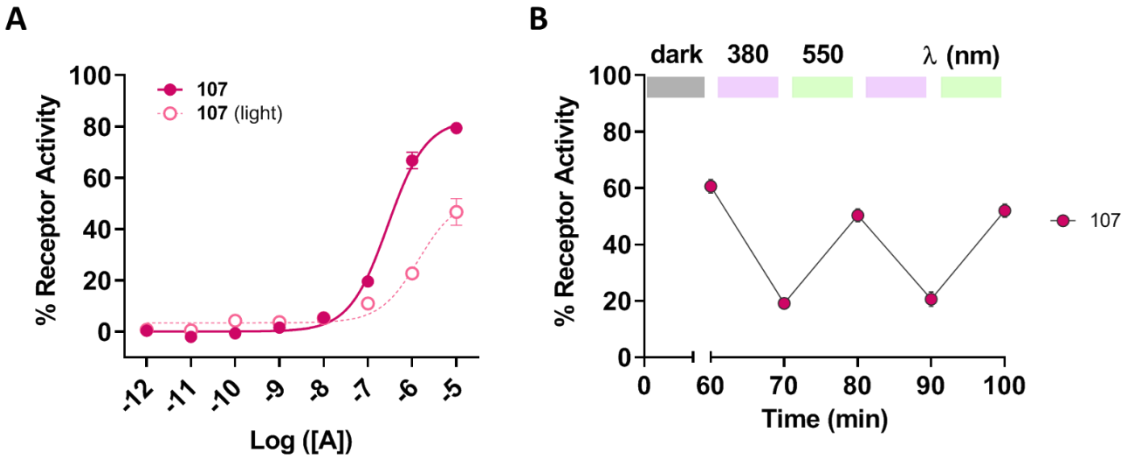

Figure 115. Light-dependent β_1-AR activation of 107. (A) Dose-response curves of **107** in the dark and under constant violet light (380 nm). (B) Time course quantification of intracellular cAMP challenged with the β-AR agonist cimaterol in the presence of **107**. Purple and green boxes correspond to 10 min illumination breaks using 380 nm and 550 nm lights respectively. Data are shown as the mean ± SEM of three to five independent experiments in duplicate.

Table 27. Pharmacological data of compound 107 for β_1AR.

	DARK		LIGHT			
Cmpd	**EC_{50} (nM)**	**SEM**	**EC_{50} (nM)**	**SEM**	**PPS[a]**	**SEM**
107	289.07***	22.29	1272.77	291.14	4.25	1.23

[a] PPS refers to Photoinduced Potency Shift which is the relation between the measured EC_{50} in light and dark conditions respectively. Statistical differences from light EC_{50} values are denoted for adjusted p values as follows: ***p<0.001.

Interestingly, while the introduction of a fluorine in the molecular scaffold of **PZL-1** had no substantial effects on the β_2-AR inhibitory activity, β_1-AR agonism detected for both photoisomers of **107** was found to be notably lower. In consequence, the developed compound presents better selectivity towards the beta-2 subtype, which increased as a result of fluorinating the 5- position of the phenyl ring with respect to the N=N bond (Table 28). The selectivity towards β_2-AR is especially high for the *trans*- isomer, with a β_1/β_2 selectivity ratio of 179.5.

Table 28. Selectivity ratios of the 107.[a]

	DARK	LIGHT
Cmpd	**β_1 vs β_2**	**β_1 vs β_2**
107	179.5	35.07

[a] A ratio of 1 implies no receptor selectivity for a receptor subtype over another.

Therefore, we have successfully developed a fluorinated analogue of **PZL-1** to evaluate how the introduction of a fluorine affects the photochemical and photopharmacological properties of this azobenzene. We observed only small variations in the absorption spectrum of *trans*-**107**, and no modification of the optimal isomerization wavelengths was achieved with the introduction of one fluorine atom. Interestingly, the compound retained its β_2-AR photopharmacological behavior but displayed better selectivity towards this receptor subtype. Lower *trans*-on β_1-AR partial agonism was detected for **107**, which was attributed to the mono-fluorination of the azobenzene scaffold. In light of these results, further research efforts should be conducted in the future to develop *ortho*-fluorinated azobenzenes based in **PZLs**, as they are expected to be red-shifted and potentially maintain the desired photopharmacological properties.

3.4 Conclusions

[redacted]

Chapter 4. Structural studies of β-AR using synthetic photoswitches: understanding light-triggered protein changes

Abstract

In Chapters 2 and 3 of the present thesis, we have reported the development of several photoswitchable compounds targeting β-adrenoceptors. Different photophysical, photopharmacological and selectivity profiles were encountered among the described ligands, which compose a varied and useful toolbox of molecules for the study of β-AR.

A wide number of applications can be explored using the developed ligands. For instance, in previous chapters we explored the use of photochromic ligands to optically control β-AR *in vitro* and *in vivo*. Studying receptor pharmacology constitutes one of the most common applications reported for synthetic photoswitches as it can provide relevant knowledge for the development of improved drugs, among others. In addition, understanding the interactions between ligands and receptors at molecular level has proven to be very useful in drug discovery. However, this type of knowledge is still lacking in photopharmacology, especially regarding the dynamics that receptor and photoswitches undergo upon light application. Recently, the light-dependent capabilities offered by photoswitchable ligands have been applied to the field of structural biology, which have allowed to better understand the dynamic processes occurring after light application in certain systems.[66] Additionally, some studies have reported the binding modes of the two photoisomers of an AB with the studied receptor.[67,68]

In this context, **the aim of this chapter was to crystallize both β_1-AR and β_2-AR with one of the *trans*-on compounds** from our library of photochromic ligands. After crystallization, we intended to **perform conventional X-Ray Crystallography experiments with the obtained crystals in the dark and after illumination** with the appropriate wavelength to evaluate the light-induced structural changes in our target receptors.

Firstly, receptor expression was optimized for the different constructs of β_1-AR and β_2-AR. Next, purification protocols were established and optimized for the different membrane proteins. Finally, crystallization trials were set up using purified protein bound to **PZL-1**, and preliminary crystals were obtained for the ultra-stable (US) construct of β_1-AR. However, we did not manage to obtain diffraction-quality crystals, which are required to perform X-Ray Crystallography experiments.

The work reported in this Chapter was performed as part of a 6-months research stay at the Paul Scherrer Institut, based in Villigen (Switzerland). Research was performed in collaboration with Robin Stipp and under the supervision of Dr. Jörg Standfuss and Dr. Steffen Brüenle.

4.1 Reviewing structural biology studies that use photoswitchable ligands

The field of photopharmacology has very limited knowledge on the structural aspects of light-triggered events that lead to changes in the biological activity of the studied system.

There are only a few examples reporting crystal structures of soluble proteins in complex with synthetic photoswitchable ligands in their *trans* isomeric form. These studies did not actually explore the light-induced changes in the structure of target proteins nor the binding mode of the *cis* isomers.[69–71] It was only in a study published in 2021, that the binding mode of the two photoisomers of optojasp-8 (**OJ8**) to the globular protein F-acting was determined by cryo-EM (Figure 116). This provided detailed structural information that allowed to better understand the increased functional activity of *cis*-**OJ8** and can be used in the future to design improved photochromic ligands targeting F-actin.[68]

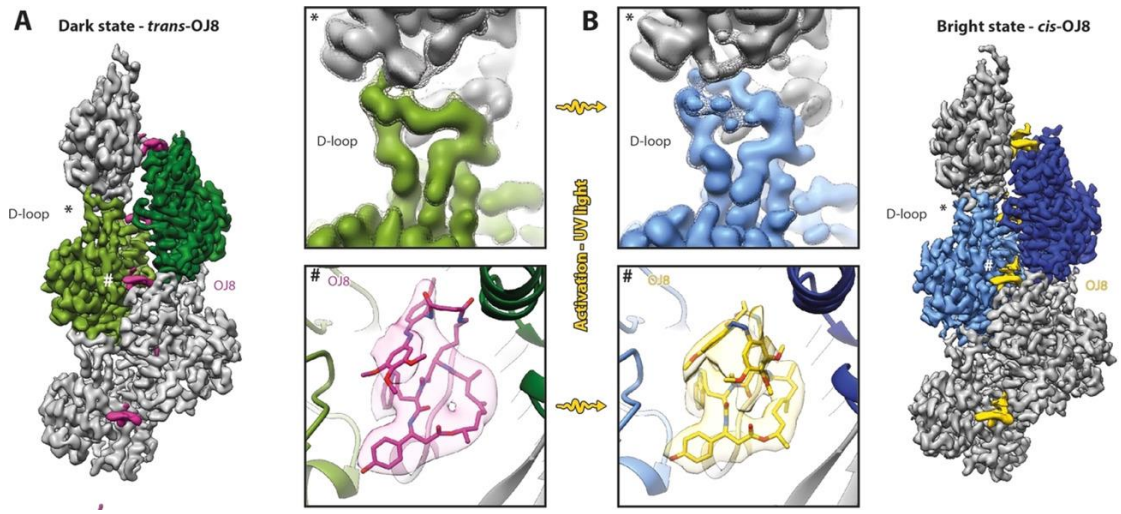

Figure 116. Cryo-EM structures of F-actin bound to OJ8. (A) Dark state, trans-OJ8 is represented in magenta, and (B) bright state, cis-OJ8 represented in yellow. Reproduced from Pospich (2021).

In addition, two examples of protein crystallization with synthetic photoswitches were recently reported. In a first example, crystal structures of the glutamate transporter homologue Glt_{Tk} were solved bound to an azo derivative of the ligand TBOA, both in *trans* and *cis* configurations. The differences reported in the binding modes of the two photoisomers provided an explanation for the light-triggered functional modulation observed *in vitro*. *Trans p*-OMe-azo-TBOA, which is the most active isomer, shows an additional H-bond with the binding pocket. This indicates that this isomeric configuration has higher affinity towards the studied receptor and consequently displays better inhibitory properties.[67] Finally, a recent study on the different mGluR activation modes, described the binding mode of *trans*-alloswitch-1, an $mGlu_5$ photoswitchable NAM, to a thermostabilized $mGlu_5$ 7TM (Figure 117).[72]

Finally, the novel field of time-resolved (TR) crystallography has been applied to study the protein dynamics of bacteriorhodopsin, among other proteins, after light excitation of retinal, its endogenous photoswitch. This research provided series of snapshots within the femtosecond range that allowed to follow light-induced protein dynamics due to the transition of *trans*-retinal to its excited *cis* isomer.[66]

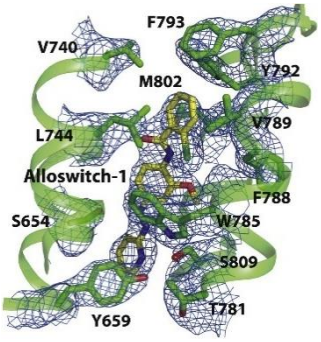

Figure 117. X-ray structure of alloswitch-1 bound to $mGlu_5$ TM7. Alloswitch-1 is represented in yellow. Reproduced from Nasrallah (2021).

Therefore, the combination of structural biology with photochromic ligands is arising as a powerful approach to study the molecular mechanisms that drive the distinct pharmacological responses of synthetic and natural azobenzenes before and after light application. It can provide novel information on the relevant structural features that lead to receptor activation. Moreover, it can unravel the succession of events triggered by light, which is still unknown. Overall, this innovative approximation can potentially impact both structural biology and photopharmacology. For these reasons, we decided to use the photoswitches developed in the present thesis to perform structural studies in collaboration with the Standfuss group.

4.2 Crystallization of β_1-AR bound to a *trans*-on synthetic photoswitch

To produce β_1-AR for crystallization, we used two different DNA constructs that encoded our target receptor. These constructs, named β_1-AR JM50 and TS β_1-AR, were kindly provided by Dr. Roger Benoit (Paul Scherrer Institut). Both constructs had been previously reported and used in structural biology studies, which implied that they had been appropriately modified to improve their stability and assist crystallization (see Introduction, section 2.1).[73,74] However, only β_1-AR JM50 or β_1-AR Ultra-stable (US) has been crystallized so far.[73]

A

B

Name	Construct name	Expression system	Origin	Protein Tag	Point mutations	Truncations	Crystal structure
β_1-AR US	β_1-AR JM50	Mammalian cells	Turkey	Strep and GFP	9	C-terminus, N-terminus and ICL-3	Yes. PDB ID: 4VBN
β_1-AR Shin	TS-β_1-AR	Mammalian cells	Turkey	Strep and GFP	10	C-terminus, N-terminus and ICL-3	No

Figure 118. β_1-AR constructs used for crystallization purposes. (A) Schematic representation of the two β_1-AR constructs employed. (B) Summary of characteristics of β_1-AR Ultrastable (US) and β_1-AR Shin.

The two available constructs, β_1-AR US and β_1-AR Shin are very similar and share a general schematic representation (Figure 118A). In fact, they are both derived from the turkey β_1-AR44-m23 mutant, used in crystallographic studies. Compared to the wild-type receptor, both

mutants have truncated carboxy and amino termini, as well as the ICL3 to reduce their inherent flexibility. Additionally, the two constructs incorporate a Strep tag and a Histidine tag to assist protein purification processes. Green Fluorescent Protein (GFP) has also been introduced to facilitate protein expression evaluation in HEK293 cells. The main difference between β_1-AR US and β_1-AR Shin is that while the ultra-stable construct presents nine point mutations, the Shin mutant has an additional neutral mutation (D200E) (Figure 118B). The reasons that led us to use of two different β_1-AR mutants for crystallization purposes are the following:

1) It is not certain if β_1-AR US will be flexible enough to allow photoisomerization studies in protein crystals bound to a synthetic photoswitch.
2) β_1-AR Shin has been used in protein dynamic studies, which ensures a certain degree of receptor flexibility; however, this construct has never been crystallized.

Therefore, each β_1-AR variant displayed its advantages and inconveniences, which enforced the decision of using them both to get better chances of achieving our project objectives.

4.2.1 Expression optimization of two β_1-AR mutants in mammalian cells

In order to express the two recombinant variants of β_1-AR, HEK293 GnTI- cells were used. These cells do not have N-acetylglucosaminyltransferase I (GnTI) activity, thus lacking the presence of complex N-glycans. HEK293 GnTI- cells are extremely useful to express recombinant proteins as they ensure high protein expression levels and homogeneous protein N-glycosylation. Initially, we followed an identical purification protocol for the two receptor mutants, which was already established in the Standfuss group (Figure 119). Firstly, a polyclonal stable cell line was generated for each inducible β_1-AR construct. Adherent cells were scaled up and then transferred into suspension, which constituted a more efficient approach for large-scale protein production. Once we had grown enough cells (2-6 L cell culture, 2 million cells/mL) we induced them using tetracycline (3 mg/mL for 72 h) to achieve receptor expression, harvested them by centrifugation and flash froze the resulting cell pellets.

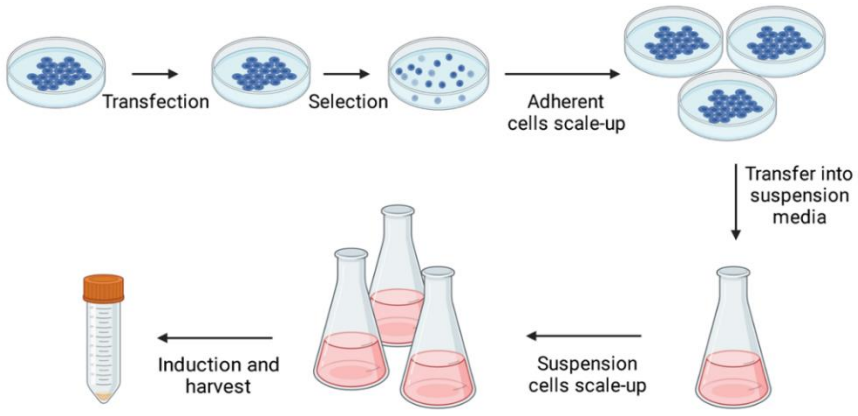

Figure 119. Cellular scale-up and protein induction flowchart. This succession of processes is a standard procedure to produce large amounts of mammalian cell pellets containing the protein of interest. Created with Biorender.

However, we observed that β_1-AR US cells did not grow well in suspension, compared to the cell line containing β_1-AR Shin. Additionally, significant differences were observed between receptor expression levels in the two cell lines after induction (Figure 120). Fluorescence

microscopy images showed that most β_1-AR Shin cells were highly fluorescent (Figure 120B), in contrast to β_1-AR US cells, which displayed low and localized fluorescence (Figure 120A). The differences in fluorescence detected visually were further confirmed by the fluorescence intensity values obtained for the two analyzed images. β_1-AR Shin cells presented ten times more fluorescence than β_1-AR US cells (Figure 120C). Therefore, the described protocol was only considered appropriate for large-scale production of the β_1-AR Shin mutant.

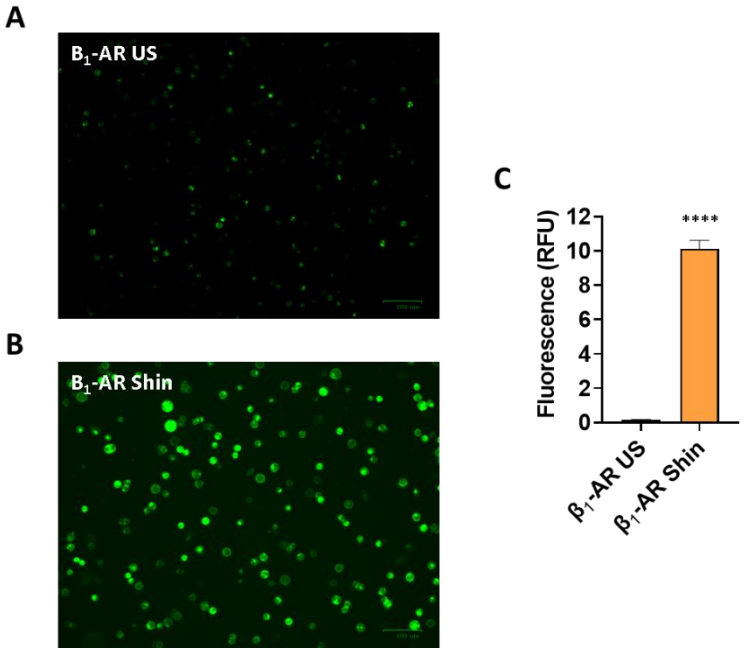

Figure 120. Protein expression comparison between HEK293 β_1-AR US and HEK293 β_1-AR Shin induced in suspension. Fluorescence microscopy images of HEK293 β_1-AR US cells (A) and HEK293 β_1-AR Shin cells (B) in suspension after induction using 3 mg/mL of tetracycline for 72 h. (C) Fluorescence intensities measured for the two different constructs of β_1-AR expressed in HEK293 GnTI- cells. Fluorescence was analyzed from different microscopy images using ImageJ. Each expression test was performed twice. Statistical differences from dark Tm values are denoted for adjusted p values as follows: **** $p<0.0001$.

Considering the difficulties experienced with the growth of β_1-AR US cells in suspension and the low protein expression detected after induction, we decided to use an alternative approach to produce large amounts of protein (Figure 121). We decided to upscale the β_1-AR ultra-stable polyclonal cell line in adherence and directly induce cells in culture plates.

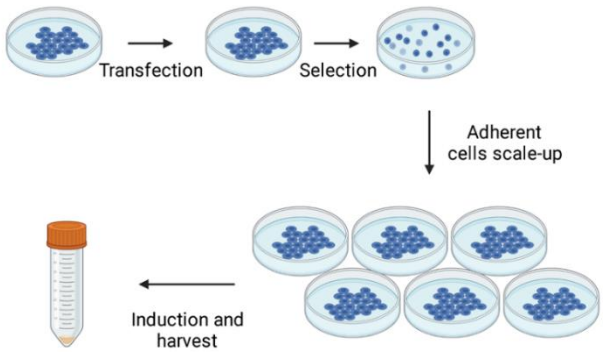

Figure 121. Cellular scale-up and protein induction in adherence. HEK293 β_1-AR US cells were scaled-up and induced in adherence, which showed improved protein expression compared to the standard protocol. Created with Biorender.

Additionally, we performed β_1-AR US expression tests in adherent cells to establish their optimal induction conditions. Different induction times (24-96 h) and different tetracycline concentrations (1.5, 3 or 6 mg/mL) were evaluated (Figure 122).

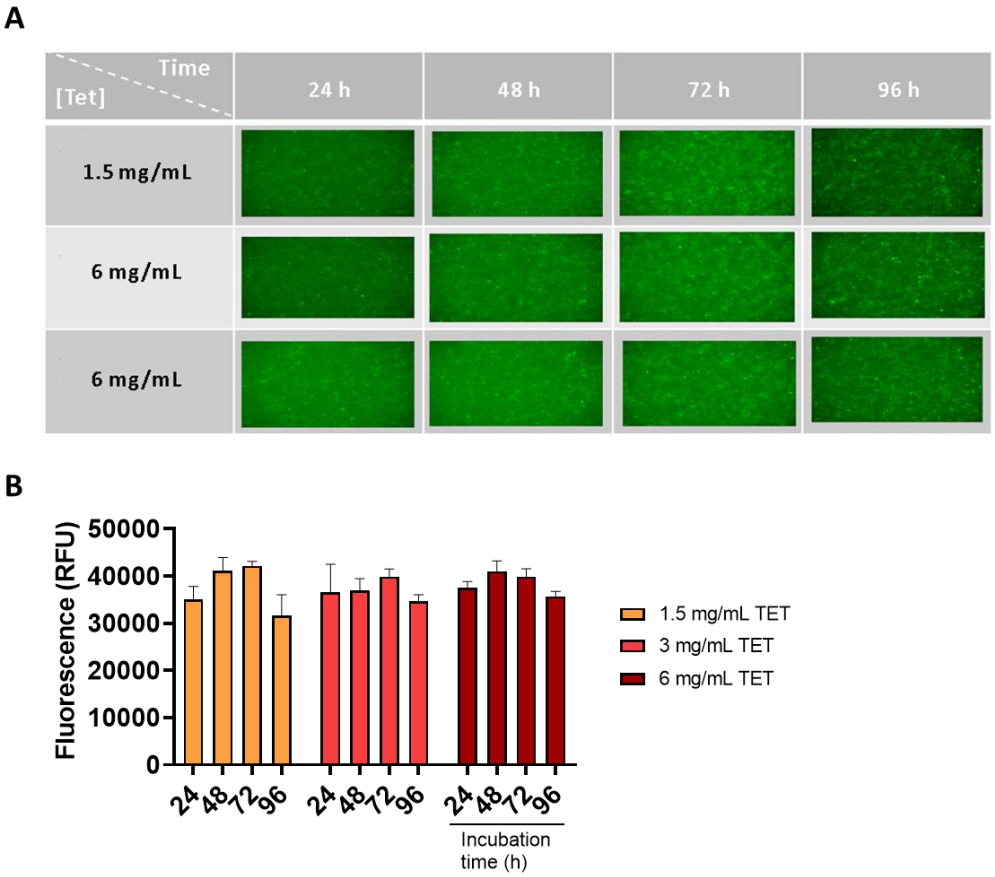

Figure 122. Expression optimization of HEK293 β_1-AR US cells in adherence. (A) Fluorescence microscopy images from the different expression tests performed. (B) Fluorescence intensities measured for the different expression conditions evaluated. Fluorescence was analyzed from different microscopy images using ImageJ. Each expression test was performed in duplicate.

Results obtained from the expression tests did not show significant differences between the tested concentrations of tetracycline (Figure 122B). On the other hand, cells induced with 1.5 and 3 mg/mL of TET showed that optimal expression was achieved after 72 h incubation; longer incubation times resulted in slight decreases in the measured fluorescence. Finally, tests performed using 6 mg/mL of TET showed maximal fluorescence after 48 h; as previously mentioned, longer incubation times led to slight decreases in protein expression. Nevertheless, it is worth noting that fluorescence variations observed for the different incubation times are rather modest. Taking into account the obtained results, induction of cells in adherence was thereafter performed using 1.5 mg/mL of TET for 72 h.

Therefore, expression of the β_1-AR US recombinant receptor in adherent cells showed better results than induction of the polyclonal cell line in suspension. However, this protocol is notably longer, tedious, and highly expensive, which also questions its long-term viability.

4.2.2 Optimization and protocol development for the purification of apo β_1-AR

After establishing and optimizing expression of the two β_1-AR constructs in HEK293 cells, purification of the two empty recombinant receptors (apo β_1-AR) was conducted. Considering that the two variants of β_1-AR are highly stabilized and very similar, purification of apo β_1-AR for the two constructs was performed following an identical protocol (Materials & Methods, section 4.2.4).

Briefly, membranes were prepared from cell pellets expressing our target receptor. Following membrane preparation, the target protein was solubilized in Dodecyl Maltoside (DDM) (1 %). Solubilized membranes were then purified through Streptavidin Affinity Chromatography (AC). β_1-AR variants directly eluted from AC were then treated overnight with His-tagged human Rhinovirus 3C protease (HRV 3C), to cleave off the GFP tag. Then, a reverse immobilized metal ion affinity chromatography (IMAC) was performed to remove the protease. Finally, the protein containing solution was concentrated and purified by Size Exclusion Chromatography (SEC), which yielded the apo form of the two β_1-AR variants.

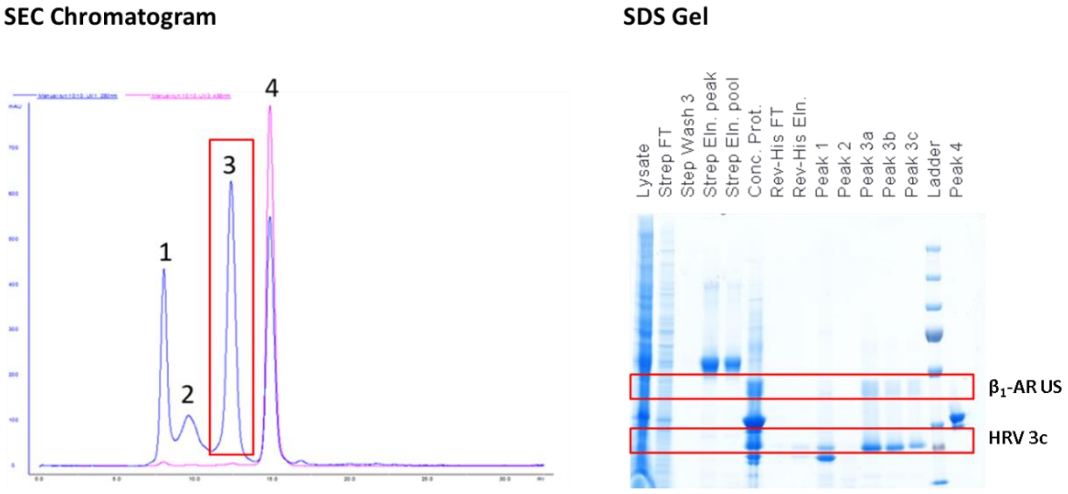

Figure 123. Purification of apo β_1-AR US. Results from the purification are summarized in a SEC Chromatogram and an SDS gel.

Results from the purification of β_1-AR US are shown in Figure 123. SEC chromatogram shows that four different elution peaks were obtained in the last purification step. The first peak is known as void peak and contains protein aggregates formed during the purification and concentration processes. Additionally, the fourth peak corresponded to GFP elution (left panel). To identify which fractions contained β_1-AR US and its purity, aliquots from the different stages of the purification were analyzed by SDS gel (right panel). From the SDS gel we could observe that good amounts of relatively pure protein were obtained from the Streptavidin chromatography. In addition, we identified that the third peak of the SEC corresponded to the protein of interest. However, the β_1-AR US eluted from the SEC displayed an additional band in the SDS gel, which evidenced the presence of a lower molecular weight protein. This same band was also observed in the first two elution peaks of the SEC and was identified as remaining protease. This purification yielded 2 mg of purified protein from a 2 L cell pellet. Even if the results obtained from this purification are not ideal, we decided to carry

on with ligand characterization and crystallization trials, as the main impurity is a soluble protein (HRV 3C) that is not expected to interfere with the following steps.

On the other hand, results from the purification of β_1-AR Shin are depicted in Figure 124. The void peak overlapped with the β_1-AR Shin elution peak (left panel), which difficulted the separation of the different protein components in the mixture by SEC. In addition, the obtained chromatogram showed a notably large void peak, indicating that apo β_1-AR Shin forms aggregates more easily compared to β_1-AR US. SDS gel analysis identified the presence of some impurities in the β_1-AR Shin eluate obtained after Size Exclusion Chromatography, as lower molecular weight bands were observed (right panel). Among the impurities, we identified the presence of the protease, as described in the purification of β_1-AR US. Only 0.6 mg of purified protein were isolated from a 2 L cell pellet. The low yield obtained in this purification was attributed to the high aggregation levels observed for β_1-AR Shin.

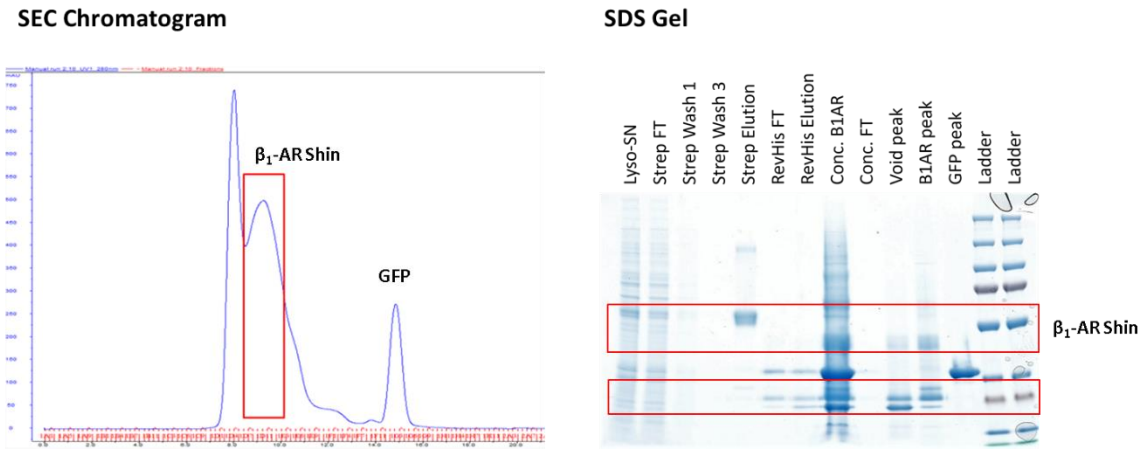

Figure 124. Purification of apo β_1-AR Shin. Results from the purification are summarized in a SEC Chromatogram and an SDS gel.

In order to improve the purity and yield of the final eluate of β_1-AR Shin, we performed a purification that incorporated a few changes in the previously described protocol (Figure 125).

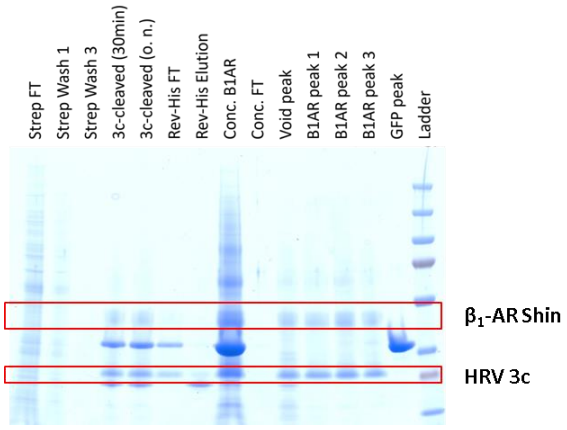

Figure 125. Purification of apo β_1-AR Shin with an improved protocol. Results from the purification are shown in the obtained analytical SDS gel.

Firstly, 1 % of glycerol was added to the protein solution prior to the overnight treatment with protease. The addition of glycerol is meant to reduce undesired hydrophobic interactions of

β_1-AR Shin with other small proteins such as the protease. Moreover, concentration of the protein solution prior to SEC purification was handled carefully, centrifuging the mixture at lower speed in order to reduce aggregation processes. SDS gel analysis showed that the isolated fractions containing β_1-AR Shin displayed a significantly improved purity profile (Figure 125). Additionally, the yield was also notably better, as 1.2 mg of protein were obtained from a 2 L of cell pellet. Nevertheless, all elution fractions still presented a band that corresponded to the protease. β_1-AR Shin isolated from this purification was used to characterize the photoswitchable ligands and perform crystallization trials.

Considering that the protease band has been detected in all protein batches isolated so far, we hypothesized that the HRV 3c used in the performed purifications is strongly interacting with the target receptors, thus hampering its removal. Future purifications should be performed with an alternative protease to evaluate if the final purity of β_1-AR can be improved.

4.2.3 Evaluation of ligand-receptor interactions using Thermal Shift Assays (TSA)

After the purification of the apo β_1-AR variants, biophysical assays were performed to evaluate the interactions between the developed photoswitchable ligands and the studied receptors. Particularly, fluorescence-based Thermal Shift Assays (TSA) were conducted, which detect the melting temperature (Tm) of proteins under different conditions (see Introduction, section 2.3.7). It is well known that most ligands can stabilize their target receptors upon binding, thus increasing their melting temperature in a concentration dependent manner. Therefore, this type of assay is widely used to detect ligand-receptor interactions. Additionally, ligand-induced thermostabilization can be crucial when attempting to crystallize a protein, as the formation of crystal contacts requires a relatively stable system. This is especially relevant in GPCRs, which have only been crystallized bound to a stabilizing ligand.

To further study the interactions established between the developed photoswitches and β_1-AR, we tested our ligands in Thermal Shift Assays (Figures 126 and 127). Moreover, a careful evaluation of the results obtained in these assays provided key information that assisted the selection of the optimal photoswitchable ligand to perform crystallization trials. TSA assays were performed using CPM [7-diethylamino-3-(40-maleimidylphenyl)-4-methylcoumarin] as a fluorogenic dye. This compound, specifically reacts with free cysteine residues to form fluorescent adducts, thus revealing the temperature at which buried cysteines become solvent-accessible due to denaturation. [redacted]

Results obtained for the tested compounds towards the two β_1-AR mutants are very similar, thus corroborating that the highly thermostabilized receptor and the more dynamic variant are similar models for crystallization purposes (Figures 126 and 127). One of the main differences that can be detected is the higher Tm measured for apo β_1-AR US in comparison to the melting temperature detected for β_1-AR Shin, 66ºC and 51ºC respectively. This notably higher denaturation temperature is a result of the increased thermostability of the ultrastable mutant. Interestingly, *o*-ABs **PZL-1** and **107** showed the best thermostabilization profile, with

melting temperatures between 75ºC and 81ºC. This significant increase in the measured melting temperature is very similar to the one observed for the non-photoswitchable beta-blocker propranolol. This suggests that *o*-ABs and propranolol interact with the receptor in a similar manner.

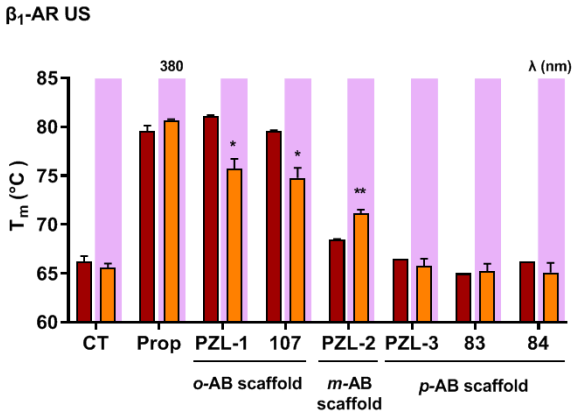

Compound	Tm Dark (ºC)	Tm Light (ºC)
CT	66.2 ± 0.5	65.6 ± 0.4
Prop	79.6 ± 0.6	80.6 ± 0.3
PZL-1	81.1 ± 0.1	75.7 ± 1.0
107	79,5 ± 0.1	74.8 ± 1.0
PZL-2	68,4 ± 0.1	71.1 ± 0.4
PZL-3	66,5 ± 0.1	65.8 ± 0.7
83	65 ± 0.1	65.2 ± 0.8
84	66,2 ± 0.1	65.1 ± 1.0

Figure 126. Thermal Shift Assays performed for β_1-AR US treated with UV-absorbing photoswitches. Histogram shows the Tm of β_1-AR US upon binding to propranolol (Prop), **PZLs 1-3**, compound **107** and *p*-ABs **83** and **84** under dark (red bars) and after illumination with violet light (380 nm). All compounds were tested at 100 µM concentrations. Purple boxes correspond to data obtained from illuminated samples (380 nm). Mean values ± SEM for the tested compounds upon different light conditions are summarized in the table. Data are shown as the mean ± SEM of three to five independent experiments performed in triplicate. Statistical differences from dark Tm values are denoted for adjusted p values as follows: *p<0.05, ** p<0.01.

When assays were performed under constant illumination with 380 nm a significant decrease was measured for the Tm of the two ABs, which is consistent with the *trans*-on nature of **PZL-1** and **107**. However, it is important to note that this assay is not appropriate for a robust detection of light-induced differences, as the temperature of the biological system is progressively increased during the assay, thus favoring thermal relaxation of *cis* ABs. On the other hand, *m*-AB **PZL-2** only showed a significant shift in the Tm upon illumination, which is consistent with the *cis*-on behavior described for this compound in Chapter 2.

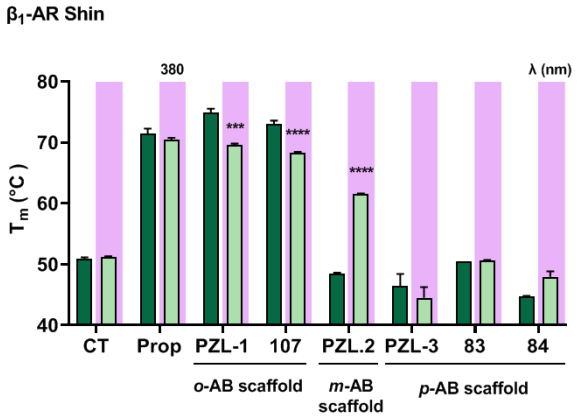

Compound	Tm Dark (ºC)	Tm Light (ºC)
CT	50.9 ± 0.2	51.2 ± 0.1
Prop	71.4 ± 0.8	70.5 ± 0.3
PZL-1	74.9 ± 0.6	69.6 ± 0.2
107	73.0 ± 0.5	68.2 ± 0.2
PZL-2	48.5 ± 0.1	61.5 ± 0.1
PZL-3	46.5 ± 1.9	44.5 ± 1.8
83	50.5 ± 0.1	50.6 ± 0.1
84	44.7 ± 0.2	48.0 ± 0.9

Figure 127. Thermal Shift Assays performed for β_1-AR Shin variant treated with UV-absorbing photoswitches. Histogram shows the Tm of β_1-AR Shin upon binding to propranolol (Prop), **PZLs 1-3**, compound **107** and *p*-ABs **83** and **84** under dark and after illumination with violet light (380 nm). All compounds were tested at 100 µM concentrations. Purple boxes correspond to data obtained from illuminated samples (380 nm). Mean values ± SEM for the tested compounds upon different light conditions are summarized in the table. Data are shown as the mean ± SEM of three to five independent experiments performed in triplicate. Statistical differences from dark Tm values are denoted for adjusted p values as follows: ***p<0.001, **** p<0.0001.

Finally, no ligand-induced thermostabilization nor light-dependent effects were detected for all *p*-ABs tested (**PZL-3**, **83** and **84**). This was rather surprising, as *p*-ABs have shown β_1-AR selectivity with a good *trans*-on behavior. These results could indicate that *p*-AB bind to the receptor via a completely different mode that does not stabilize the receptor. However, further pharmacological and *in silico* assays should be performed in order to confirm this hypothesis.

Overall, we identified that *o*-ABs **PZL-1** and **107** constitute the most promising ligands to attempt crystallization trials for both β_1-AR variants, as they stabilize the receptor to the same levels as propranolol, which has already been co-crystalized with β_2-AR.[75]

Finally, measuring melting temperatures of the target receptor for increasing concentrations of the tested ligand also allows to estimate relative ligand binding affinities (K_D).[76] Binding affinities towards the two β_1-AR variants were estimated for our two photoswitchable hits (**PZL-1** and **107**) and the non-photoswitchable ligand propranolol (Figure 128, Table 29).

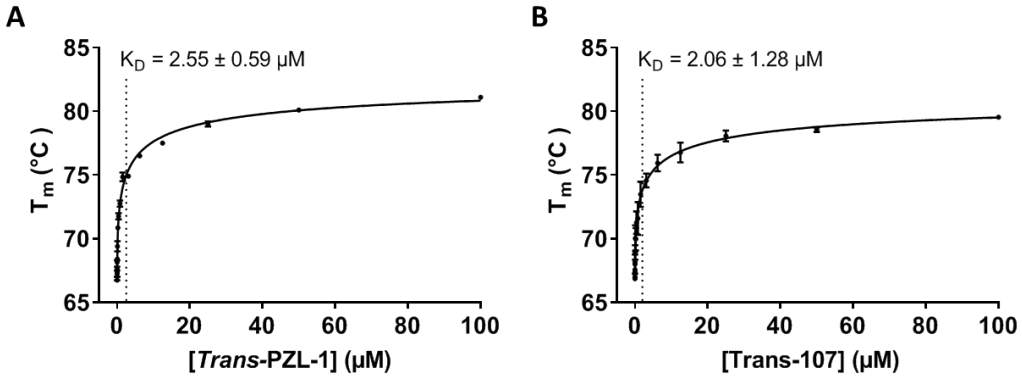

Figure 128. Affinity constants (K_D) of PZL-1 and 107 towards β_1-AR US determined by TSA. Melting temperatures of the target receptor treated with increasing concentrations of each azobenzene are represented. Data are shown as the mean ± SEM of three independent experiments performed in triplicate.

Results showed that all compounds display similar binding affinities, within the micromolar range. This is consistent with the proposed hypothesis, which suggests a similar binding mode for *o*-ABs and propranolol to β-AR. In addition, similar values were also estimated for the two β_1-AR mutants, which further corroborated that the two recombinant receptors constitute similar models (Table 29).

Table 29. Summary of TSA determined affinities for the two β_1-AR variants studied.

Compound	K_D (µM) β_1-AR US	K_D (µM) β_1-AR Shin
Propranolol	1.53 ± 0.13	1.45 ± 0.26
PZL-1	2.55 ± 0.59	1.25 ± 0.61
107	2.06 ± 1.28	2.30 ± 1.03

Finally, results obtained in TSA for the tested photoswitches were summarized in Table 30, which assisted the selection of the best ligand to attempt crystallization. From this table we identified that **PZL-1** constituted the best candidate, as it has good solubility in aqueous media and induces high receptor thermal stabilization in dark conditions.

Table 30. Summary of properties of the tested photoswitches in TSA.

Scaffold	Compound	Solubility	Tm-Shift	Photoinduced Tm-Shift	*Cis-/trans-* on
Ortho-	**PZL-1**				*Trans*-on
	107				
Meta-	**PZL-2**				*Cis*-on
Para-	**PZL-3**				*Trans*-on
	83				
	84				

4.2.4 Crystallization trials using β_1-AR bound to Photoazolol-1

Finally, LCP crystallization trials were conducted for both β_1-AR variants bound to **PZL-1** (Materials & Methods, Section 4.2.4). Several crystallization plates were set for both constructs based on reported conditions (Figure 129A);[77–79] preliminary crystals were obtained for β_1-AR US (Figure 129B). Nevertheless, the small size and poor geometry of the obtained crystals was unsuitable for X-Ray Crystallography experiments. Optimization of crystallization conditions should be performed to obtain diffraction-quality crystals.

A

	β_1-AR US	β_1-AR Shin
Crystallization plates	9	8
Crystallization conditions	864	768
Observed crystals	Yes	No

B

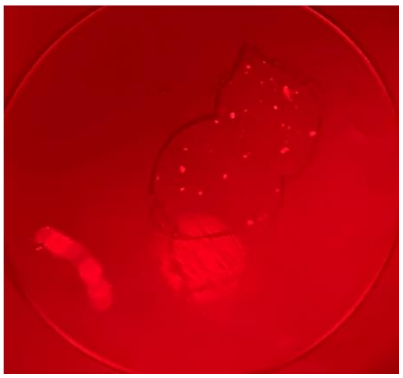

Figure 129. Crystallization trials of the two β_1-AR mutants with PZL-1. (A) Summary of crystallization trials. (B) Preliminary crystals of β_1-AR US bound to PZL-1.

On the other hand, crystals could not be obtained with any of the crystallization conditions explored for the β_1-AR Shin mutant bound to **PZL-1**. Despite the resemblances observed for this construct with the ultra-stable variant, β_1-AR Shin has a more dynamic and flexible nature, which might make it more challenging or even impossible to crystallize.

To sum up, the structure of β_1-AR bound to **PZL-1** could not be determined by X-Ray Crystallography, as only preliminary crystals could be produced for β_1-AR US. Further optimization of the crystallization conditions for β_1-AR US should be performed to obtain diffraction-quality crystals that allow to conduct structural studies of the target protein bound to our photoswitchable ligand **PZL-1**.

4.3 Crystallization of β_2-AR bound to a *trans*-on synthetic photoswitch

Crystallization of wild-type β_2-AR has not been possible so far due to the inherent flexibility of this receptor. However, there are several β_2-AR engineered constructs reported in the literature that have enabled the obtention of high-resolution crystal structures. To pursue the crystallization of β_2-AR bound to one of the developed photoswitches, we used one of the reported engineered constructs, known as β_2-AR-T4L (Figure 130).[62,80–82] β_2-AR-T4L presents a truncated C-terminus and displays a fusion protein that replaces the flexible ICL3. Introducing a T4 lysozyme (T4L) in replacement of ICL3 restricts the movement of the transmembrane helices and simultaneously provides a polar surface that can facilitate the formation of crystal contacts. This expression construct, designed to be expressed in insect cells, also presents a Flag tag to assist protein purification (Figure 130). [80]

A

B

Name	Construct name	Expression system	Origin	Protein Tag	Point mutations	Truncations	Crystal structure
β_2-AR	β_2-AR T4L	Insect cells	Human	Flag	3	C-terminus and ICL-3 replaced for T4L	Yes. PDB ID: 2RH1

Figure 130. β_2-AR construct used for crystallization purposes. (A) Schematic representation of the β_2-AR-T4L chimera employed. (B) Summary of construct characteristics.

4.3.1 Expression optimization of β_2-AR in insect cells

In order to express β_2-AR-T4L in insect cells, we used the commercial bac-to-bac expression system.[83] This viral system uses a baculovirus containing the gene that encodes the protein of interest. The baculovirus has strong infectivity against insect cells, which produce the target protein upon infection (Figure 131).

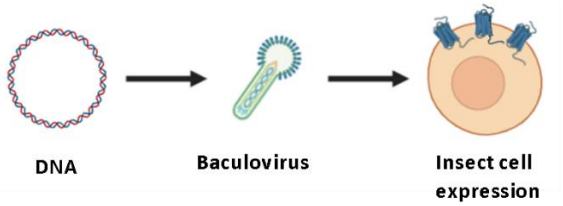

Figure 131. General scheme for viral insect cell expression systems. The gene of interest is inserted in a baculovirus that is then used to infect insect cells, which upon infection can express the target receptor.

Firstly, the recombinant bacmid was produced in *E. coli* DH10Bac cells. Once the recombinant bacmid was isolated, insect cells were transfected and recombinant viruses, named V_0, were produced within a week. V_0 was harvested by centrifugation and used to scale up the volume of recombinant virus available. Virus upscaling was achieved by performing two sequential *Sf9* cell infections with increasing cell volumes (10 and 100 mL respectively), which enabled the production of higher volumes of recombinant viruses. We managed to isolate 100 mL of V_2,

which were thereafter used to produce large volumes of cells expressing the target receptor for purification purposes (see Materials & Methods, Section 4.2.5).

Virus production was progressively followed by an assessment of the morphology and viability of the infected cells (Figure 132). Infected *Sf9* cells displayed an increased size, with their diameter changing from 15 µm in healthy cells to 18 µm upon infection (Figure 132). Additionally, virus production induces cellular death and causes a significant decrease in the measured viability. This parameter was determinant to assess if the cellular infection was progressing adequately. The recombinant virus was only harvested after cell viability was lower than 25 % to ensure maximal virus production.

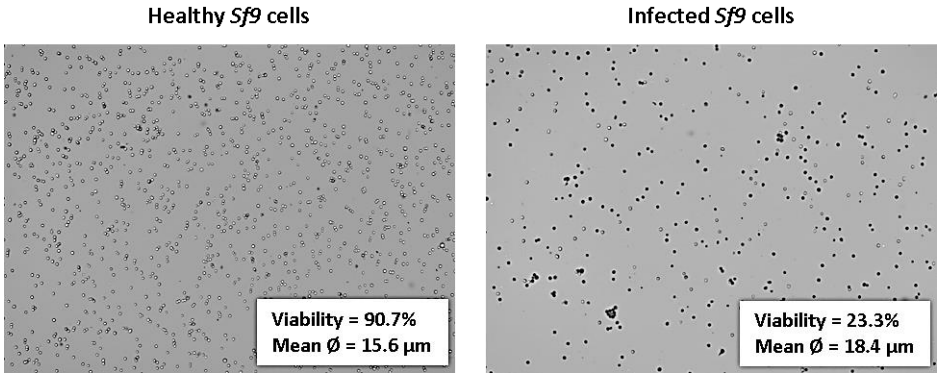

Figure 132. Morphological and viability differences between healthy and infected *Sf9* cells. Cellular viability was assessed using trypan blue to stain dead cells. Mean cell diameter analysis was performed using the DeNovix CellDrop cell counter.

At this point, we evaluated the optimal conditions to achieve maximal β_2-AR-T4L expression in *Sf9* cells. Four distinct 50 mL flasks containing $2 \cdot 10^6$ cells/mL were used (Figure 133A). We evaluated two distinct time conditions (48h and 72h) and two V_2 concentrations (0.5 % and 1 %) (Figure 133A). Cells from the different expression conditions tested were harvested, and protein levels were analyzed by western blot (Figure 133B). Results highlighted that optimal expression was achieved after infection of *Sf9* cells with 1 % of V_2 for 48 h. Consequently, we used these expression conditions to produce large amounts of β_2-AR-T4L in *Sf9* cells for purification purposes.

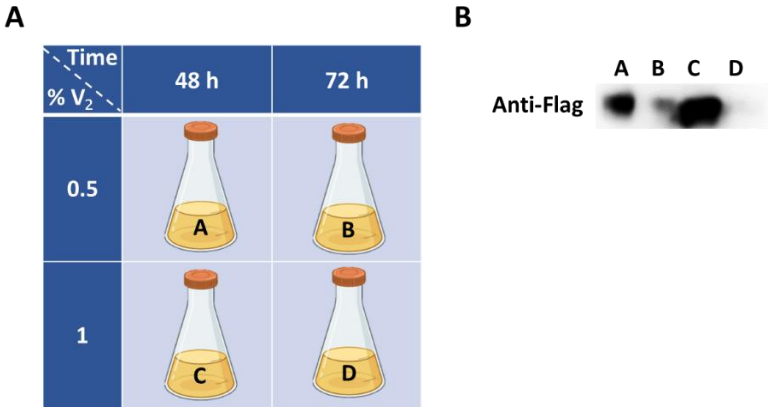

Figure 133. Expression optimization of HEK293 β_1-AR US cells in adherence. (A) Schematic representation of the infecting conditions explored. Each flask contained 50 mL of *Sf9* cells at $2 \cdot 10^6$ cells/mL density. (B) Western blot results detected Flag-containing proteins from the different expression tests carried.

4.3.2 Purification of apo β_2-AR

Following the optimization of β_2-AR expression in insect cells, we proceeded to its purification. Initially, we aimed to purify apo receptor, as the empty protein is required to characterize ligand-receptor interactions in Thermal Shift Assays.

Purification of apo-β_2-AR started with lysis and solubilization of a 2L cell pellet. Solubilized membranes were directly applied to a Flag affinity column. Fractions eluted from the affinity chromatography were concentrated and further purified by Size Exclusion Chromatography (SEC). Results from this purification are depicted in Figure 134.

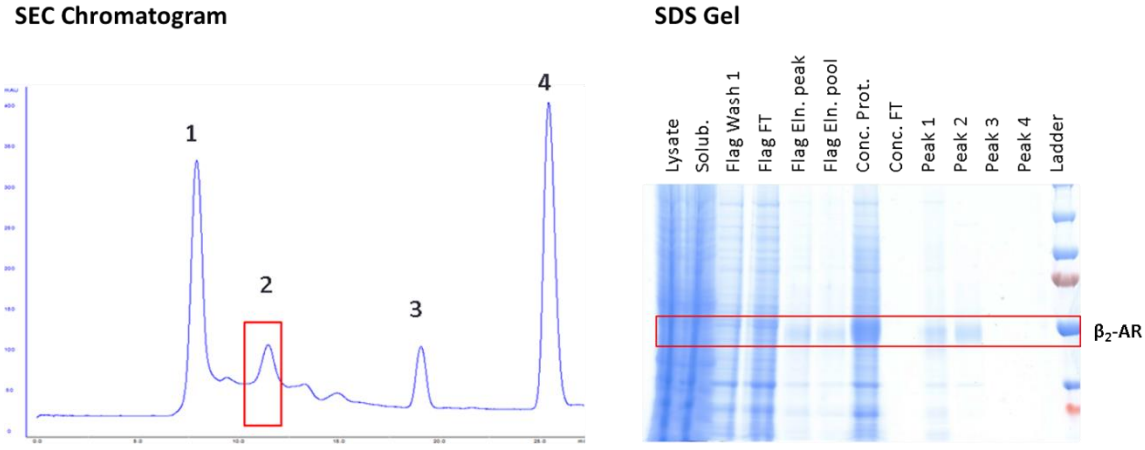

Figure 134. Purification of apo β_2-AR-T4L. Results from the purification are reported in a SEC Chromatogram and an SDS gel.

Considering that the β_2-AR construct employed is not highly thermostable, purification of apo-β_2-AR-T4L resulted in high levels of protein aggregation. This could be detected by the presence of a large void peak in the SEC chromatogram (Figure 134, left panel). In addition, SDS gel analysis of aliquots extracted from the different purification steps showed that pure apo-β_2-AR-T4L was eluted in the second peak of the SEC. This small peak contained only 0.2 mg of protein, which was sufficient to perform Thermal Shift Assays. However, the yield of this purification was very low as a consequence of the instability of apo-β_2-AR-T4L, which indicated that this protein should be purified bound to a stabilizing ligand in order to obtain higher amounts of the receptor.

4.3.3 Evaluation of ligand-receptor interactions using Thermal Shift assays (TSA)

Following the purification of apo-β_2-AR, we evaluated the ligand-induced thermostabilization effects of UV-absorbing photoswitches. Thermal Shift Assays were performed as previously described for β_1-AR, under dark conditions and after illumination with 380 nm (Figure 135). As previously mentioned, β_2-AR-T4L does not have many thermostabilizing mutations, and consequently displays a lower melting temperature (approximately 42ºC) compared to β_1-AR US and β_1-AR Shin constructs (with Tm above 50ºC). Other than that, TSA results obtained for β_2-AR-T4L are very similar to those obtained for β_1-AR (Figure 135).

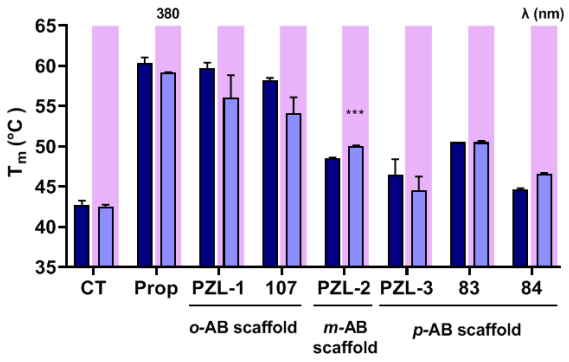

Compound	Tm Dark (ºC)	Tm Light (ºC)
CT	42.7 ± 0.6	42.5 ± 0.2
Prop	60.3 ± 0.8	59.2 ± 0.3
PZL-1	59.7 ± 0.7	56.0 ± 2.8
107	58.2 ± 0.3	54.1 ± 2.0
PZL-2	48.5 ± 0.1	50.1 ± 0.1
PZL-3	46.5 ± 1.9	44.5 ± 1.8
83	50.5 ± 0.1	50.5 ± 0.2
84	44.6 ± 0.8	46.6 ± 0.6

Figure 135. Thermal Shift Assays performed for β_2-AR-T4L treated with UV-absorbing photoswitches. Histogram shows the Tm of β_2-AR upon binding to propranolol (Prop), **PZLs 1-3**, compound **107** and *p*-ABs **83** and **84** under dark and after illumination with violet light (380 nm). All compounds were tested at 100 µM concentrations. Purple boxes correspond to data obtained from illuminated samples (380 nm). Mean values ± SEM for the tested compounds upon different light conditions are summarized in the table. Data are shown as the mean ± SEM of three to five experiments performed in triplicate.

o-ABs **PZL-1** and **107** were identified as the best hits to attempt β_2-AR-T4L crystallization, considering that both compounds induce good thermal stabilization of the receptor in their *trans* form. Upon illumination, the measured melting temperature was slightly reduced, which is consistent with their *trans*-on behavior Surprisingly, light-induced changes in the measured Tm were generally poor and not significant. This could be attributed to the higher flexibility and dynamism of this recombinant receptor, which might increase the binding/unbinding kinetic rates of the system. Additionally, this type of experiment does not provide accurate results on the behavior of *cis*- isomers, as previously mentioned. In fact, it is very likely that higher differences exist between the melting temperatures measured for β_2-AR-T4L under dark and light conditions, when treated with the studied ABs. *Meta*-AB **PZL-2** showed a moderate shift in the measured Tm, which was slightly increased upon illumination. This was consistent with the *cis*-on behavior described *in vitro* for this compound. Finally, *p*-ABs **PZL-3** and **84** did not induce thermal stabilization of the target receptor in none of their two isomeric forms. This was consistent with the minor antagonism and negligible light-dependency described for these ligands in β_2-AR functional assays. However, compound **83** showed a thermal stabilization of 8ºC, that did not change upon illumination. This was rather surprising, considering that this compound did not show relevant antagonism towards β_2-AR in cell-based functional assays.

Additionally, binding affinities were estimated for the two *ortho*-ABs and propranolol, which served as control. Results showed that both *o*-ABs and propranolol displayed higher affinity towards β_2-AR, considering that estimated K_D values were found to be in the nanomolar range. Compound **107** showed an analogous behavior to the non-switchable beta-blocker propranolol, with similar K_D values and Tm increases measured for these two ligands (Figures 136B and C). On the other hand, we identified that **PZL-1** interacted with the receptor with higher affinity (Figure 136A); however, this ligand induced similar levels of receptor thermostabilization compared to propranolol and AB **107** (Figures 135 and 136).

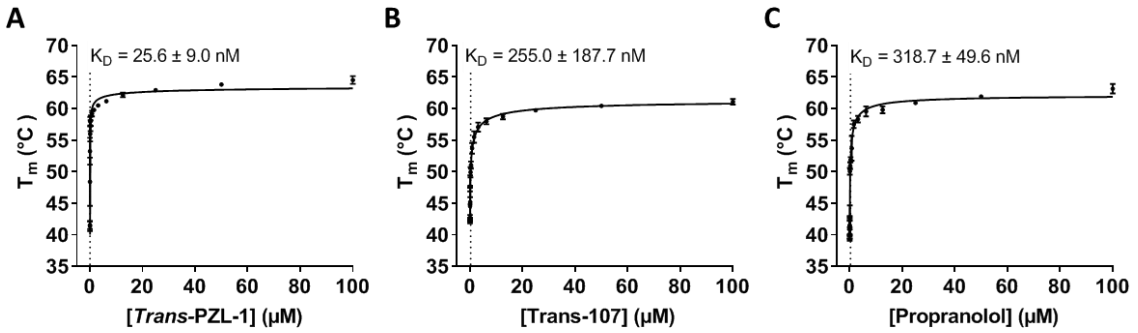

Figure 136. Affinity constants (K_D) of PZL-1 (A), 107 (B) and propranolol (C) towards β_2-AR determined by TSA. Melting temperatures of the target receptor treated with increasing concentrations of each azobenzene are represented. Data are shown as the mean ± SEM of three independent experiments performed in triplicate.

Overall, we concluded that the best photoswitchable ligand to attempt β_2-AR crystallization was **PZL-1**. This ligand was described as a good *trans*-on antagonist towards β_2-AR *in vitro* and showed excellent thermal stabilization of the receptor upon binding. Additionally, estimated K_D values evidenced that the compound binds to the receptor with high affinity, even higher than propranolol, which was tested as a non-switchable positive control. Therefore, there are good chances that crystallization of β_2-AR-T4L bound to **PZL-1** can be achieved.

4.3.4 Optimization and protocol development for the purification of β_2-AR bound to PZL-1

In order to produce β_2-AR-T4L bound to **PZL-1** to attempt crystallization, we followed a protocol reported in many structural biology papers (see Materials & Methods, 4.2.5).[62,80,81] Firstly, the cell pellet expressing β_2-AR-T4L was subjected to lysis and solubilization with DDM (1 %). The resulting protein solution was directly applied to a Flag affinity column. Eluted fractions containing the target receptor were further purified through an alprenolol sepharose column, which was performed at room temperature due to the slow binding/unbinding kinetics of the system. This purification step removes non-functional receptor, as only functional β_2-AR can bind to the ligand alprenolol, which is linked to the chromatographic resin. The target receptor was eluted from the sepharose resin bound to alprenolol, considering that high concentrations of this ligand were used to outcompete binding of β_2-AR to the resin. To obtain β_2-AR-T4L bound to **PZL-1**, the protein solution was applied to a Flag affinity column, where ligand exchange was performed. The protein solution obtained from the last Flag AC was treated with PNGase F to remove glycosylation sites, which can hamper crystal formation. Finally, β_2-AR-T4L bound to **PZL-1** was carefully concentrated.

Even though we were following a reported protocol, optimization was required for this complex purification, as the first purification attempts yielded negligible amounts of target protein. We identified that the main problem of the purification protocol described for β_2-AR-T4L relied on the alprenolol sepharose step, that had to be conducted at room temperature. It is well known that keeping a protein solution at room temperature for too long can be a cause of protein degradation. For this reason, we had to fine tune the loading and elution times of the protein solution to the alprenolol sepharose column, as we observed that most protein was degraded if this step was performed as reported. Optimization led us to reduce the loading and elution times from 3 h to 1 h. Nevertheless, significant protein loss was still

detected in this step, which indicated that high amounts of non-functional receptor are produced in insect cells.

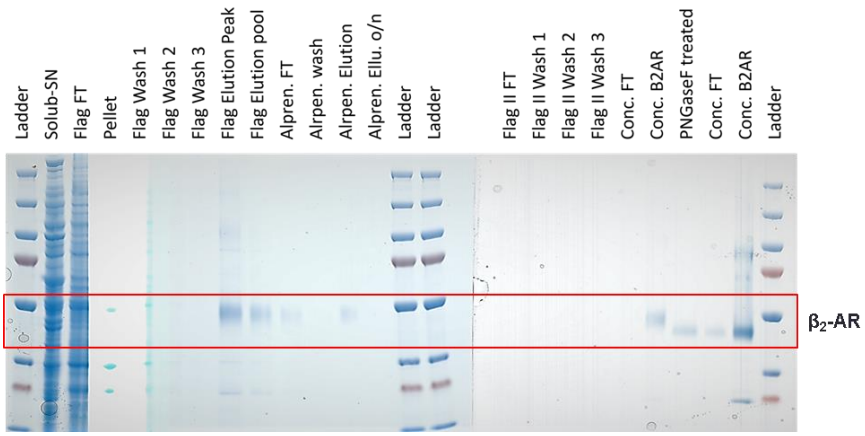

Figure 137. Purification of β_2-AR-T4L bound to PZL-1. Results from the purification are shown in an SDS-gel.

SDS gel analysis of the best purification results obtained during protocol optimization showed that we could finally obtain relatively pure β_2-AR-T4L bound to **PZL-1** (Figure 137). Nevertheless, the yield from the improved protocol was still very low, as we were only able to obtain 0.4 mg of the protein of interest from 2L of cell culture. Therefore, further optimization is required for this particular purification, taking into account that greater amounts of protein are required to initiate crystallization trials.

4.4 Conclusions and future perspectives

In conclusion, we have successfully established the expression and purification of two different constructs of β_1-AR for crystallization purposes. Nevertheless, expression of β_1-AR US should be improved, considering that large-scale protein expression in suspension cells did not work well and the alternative procedure established is very costly and time-consuming. Thermal Shift Assays identified that *ortho*-ABs **PZL-1** and **107** constitute the best candidates to attempt crystallization, as both ligands induced good receptor stabilization. In addition, TSA confirmed the *cis*-on behavior of *meta*-AB **PZL-2**, as it significantly increased thermal stabilization of the receptor upon illumination. On the other hand, *p*-ABs (**PZL-3**, **83**, and **84**) did not induce thermal stabilization of the receptors under dark or light conditions. These results were surprising considering that the ligands behaved as selective *trans*-on partial agonists towards β_1-AR functional assays. Further studies should be conducted to shed light on a possible new binding mode for these ligands.

Preliminary crystals were obtained for the β_1-AR US recombinant receptor bound to **PZL-1**; however, further screening of crystallization conditions should be performed to obtain diffraction-quality crystals. Contrarily, no crystal hits were obtained for β_1-AR Shin, a more flexible recombinant receptor that might be more difficult to crystallize.

On the other hand, we successfully established the optimal expression conditions of β_2-AR-T4L in *Sf9* cells. Apo-β_2-AR was purified and used to evaluate the ligand-receptor interactions with the photoswitchable ligands developed during the present thesis. **PZL-1** was identified as the best candidate to attempt crystallization of this receptor, as it induced good thermal

stabilization in its *trans* isomeric form. Nevertheless, purification of β_2-AR-T4L bound to **PZL-1** was found to be challenging and complex, even if the protocol is reported in several publications. Optimization was conducted but only low amounts of the target protein were obtained, which limited the project progress. Crystallization trials could not be performed due to the insufficient amounts of purified protein obtained. In consequence, further optimization of the purification protocol is required to be able to progress to protein crystallization tests.

Even If the main objective of this Chapter could not be achieved during the 6-months research stay conducted, a long-term collaboration has been established between the MCS group (IQAC-CSIC, Barcelona) and the Standfuss group (PSI, Villigen). For this reason, a Ph.D. student is currently optimizing the crystallization conditions of β_1-AR US-**PZL-1**. In addition, the Standfuss group is also focusing on the optimization of β_2-AR-T4L-**PZL-1** purification. They have managed to obtain sufficient amounts of pure protein bound to the photochromic ligand and have initiated crystallization trials. Once appropriate crystals are obtained for the two adrenoceptor subtypes bound to **PZL-1**, conventional X-Ray crystallography experiments with crystals kept in dark conditions or exposed to illumination with UV light (380 nm) will be performed. This is expected to provide relevant information on light-induced structural changes for the different recombinant receptors. Moreover, it might highlight the binding mode differences existing between the two photoisomers of **PZL-1**, which can help to better understand the differences observed in cell-based functional assays.

References

1. Ellis-Davies, G. C. R. Caged compounds: photorelease technology for control of cellular chemistry and physiology. *Nature Methods* **4**, 619–628 (2007).

2. Ellis-Davies, G. C. R. Useful Caged Compounds for Cell Physiology. *Accounts of Chemical Research* **53**, 1593–1604 (2020).

3. Adams, S. R. & Tsien, R. Y. Controlling Cell Chemistry with Caged Compounds. *Annual Review of Physiology* **55**, 755–784 (1993).

4. KOSHIMIZU, T. Carvedilol selectively inhibits oscillatory intracellular calcium changes evoked by human alpha1D- and alpha1B-adrenergic receptors. *Cardiovascular Research* **63**, 662–672 (2004).

5. Wisler, J. W. *et al.* A unique mechanism of beta-blocker action: Carvedilol stimulates beta-arrestin signaling. *Proceedings of the National Academy of Sciences* **104**, 16657–16662 (2007).

6. Kim, J. *et al.* The β-arrestin-biased β-adrenergic receptor blocker carvedilol enhances skeletal muscle contractility. *Proceedings of the National Academy of Sciences* **117**, 12435–12443 (2020).

7. Chan, H. C. S., Filipek, S. & Yuan, S. The Principles of Ligand Specificity on beta-2-adrenergic receptor. *Scientific Reports* **6**, 34736 (2016).

8. Warne, T., Edwards, P. C., Leslie, A. G. W. & Tate, C. G. Crystal Structures of a Stabilized β1-Adrenoceptor Bound to the Biased Agonists Bucindolol and Carvedilol. *Structure* **20**, 841–849 (2012).

9. Josa-Culleré, L. & Llebaria, A. In the Search for Photocages Cleavable with Visible Light: An Overview of Recent Advances and Chemical Strategies. *ChemPhotoChem* **5**, 296–314 (2021).

10. Klán, P. *et al.* Photoremovable Protecting Groups in Chemistry and Biology: Reaction Mechanisms and Efficacy. *Chemical Reviews* **113**, 119–191 (2013).

11. Ricart-Ortega, M., Font, J. & Llebaria, A. GPCR photopharmacology. *Molecular and Cellular Endocrinology* **488**, 36–51 (2019).

12. Schönleber, R. O., Bendig, J., Hagen, V. & Giese, B. Rapid photolytic release of cytidine 5'-diphosphate from a coumarin derivative: a new tool for the investigation of ribonucleotide reductases. *Bioorganic & Medicinal Chemistry* **10**, 97–101 (2002).

13. Weinrich, T., Gränz, M., Grünewald, C., Prisner, T. F. & Göbel, M. W. Synthesis of a Cytidine Phosphoramidite with Protected Nitroxide Spin Label for EPR Experiments with RNA. *European Journal of Organic Chemistry* **2017**, 491–496 (2017).

14. Slanina, T. *et al.* In Search of the Perfect Photocage: Structure–Reactivity Relationships in *meso* -Methyl BODIPY Photoremovable Protecting Groups. *Journal of the American Chemical Society* **139**, 15168–15175 (2017).

15. Stiles, G. L., Caron, M. G. & Lefkowitz, R. J. Beta-adrenergic receptors: biochemical mechanisms of physiological regulation. *Physiological Reviews* **64**, 661–743 (1984).

16. Klarenbeek, J., Goedhart, J., van Batenburg, A., Groenewald, D. & Jalink, K. Fourth-Generation Epac-Based FRET Sensors for cAMP Feature Exceptional Brightness, Photostability and Dynamic Range: Characterization of Dedicated Sensors for FLIM, for Ratiometry and with High Affinity. *PLOS ONE* **10**, e0122513 (2015).

17. Bell, R. M., Mocanu, M. M. & Yellon, D. M. Retrograde heart perfusion: The Langendorff technique of isolated heart perfusion. *Journal of Molecular and Cellular Cardiology* **50**, 940–950 (2011).

18. Bruegmann, T. *et al.* Optogenetic defibrillation terminates ventricular arrhythmia in mouse hearts and human simulations. *Journal of Clinical Investigation* **126**, 3894–3904 (2016).

19. Crocini, C., Ferrantini, C., Pavone, F. S. & Sacconi, L. Optogenetics gets to the heart: A guiding light beyond defibrillation. *Progress in Biophysics and Molecular Biology* **130**, 132–139 (2017).

20. Koopman, C. D., Zimmermann, W. H., Knöpfel, T. & de Boer, T. P. Cardiac optogenetics: using light to monitor cardiac physiology. *Basic Research in Cardiology* **112**, 56 (2017).

21. Quinn, T. A. *et al.* Electrotonic coupling of excitable and nonexcitable cells in the heart revealed by optogenetics. *Proceedings of the National Academy of Sciences* **113**, 14852–14857 (2016).

22. Wang, Y. *et al.* Optogenetic Control of Heart Rhythm by Selective Stimulation of Cardiomyocytes Derived from Pnmt+ Cells in Murine Heart. *Scientific Reports* **7**, 40687 (2017).

23. Riefolo, F. *et al.* Optical Control of Cardiac Function with a Photoswitchable Muscarinic Agonist. *Journal of the American Chemical Society* **141**, 7628–7636 (2019).

24. Gauthier, P. T. & Vijayan, M. M. A rapid zebrafish embryo behavioral biosensor that is capable of detecting environmental β-blockers. *Environmental Pollution* **250**, 493–502 (2019).

25. Faria, M. *et al.* Development of a vibrational startle response assay for screening environmental pollutants and drugs impairing predator avoidance. *Science of The Total Environment* **650**, 87–96 (2019).

26. Randlett, O. *et al.* Distributed Plasticity Drives Visual Habituation Learning in Larval Zebrafish. *Current biology : CB* **29**, 1337-1345.e4 (2019).

27. Best, J. D. *et al.* Non-associative learning in larval zebrafish. *Neuropsychopharmacology : official publication of the American College of Neuropsychopharmacology* **33**, 1206–1215 (2008).

28. Murnane, K. S. *et al.* The adrenergic receptor antagonist carvedilol interacts with serotonin 2A receptors both in vitro and in vivo. *Pharmacology, biochemistry, and behavior* **181**, 37–45 (2019).

29. Xu, X.-L. *et al.* Effects of carvedilol on M2 receptors and cholinesterase-positive nerves in adriamycin-induced rat failing heart. *Autonomic Neuroscience* **130**, 6–16 (2006).

30. Montezinho, L. P. *et al.* The interaction between dopamine D_2-like and beta-adrenergic receptors in the prefrontal cortex is altered by mood-stabilizing agents. *Journal of Neurochemistry* **96**, 1336–1348 (2006).

31. Reznikoff, G. A., Manaker, S., Rhodes, C. H., Winokur, A. & Rainbow, T. C. Localization and quantification of beta-adrenergic receptors in human brain. *Neurology* **36**, 1067–1067 (1986).

32. Barisione, G., Baroffio, M., Crimi, E. & Brusasco, V. Beta-Adrenergic Agonists. *Pharmaceuticals* **3**, 1016–1044 (2010).

33. Napolitano, A., Manini, P. & d'Ischia, M. Oxidation Chemistry of Catecholamines and Neuronal Degeneration: An Update. *Current Medicinal Chemistry* **18**, 1832–1845 (2011).

34. Sun, K. *et al.* Efficient synthesis of D_6-clenproperol and D_6-cimaterol using deuterium isopropylamine as labelled precursor. *Journal of Labelled Compounds and Radiopharmaceuticals* **59**, 552–556 (2016).

35. ASATO, G. *et al.* Repartitioning agents: 5-(1-Hydroxy-2-(isopropylamino)ethyl)anthranilonitrile and related phenethanolamines: Agents for promoting growth, increasing muscle accretion and reducing fat deposition in meat-producing animals. *Agricultural and Biological Chemistry* **48**, 2883–2888 (1984).

36. Muralidharan, S. & Nerbonne, J. M. Photolabile "caged" adrenergic receptor agonists and related model compounds. *Journal of Photochemistry and Photobiology B: Biology* **27**, 123–137 (1995).

37. Chan, H. C. S., Filipek, S. & Yuan, S. The Principles of Ligand Specificity on beta-2-adrenergic receptor. *Scientific Reports* **6**, 1–11 (2016).

38. Shonberg, J., Kling, R. C., Gmeiner, P. & Löber, S. GPCR crystal structures: Medicinal chemistry in the pocket. *Bioorganic and Medicinal Chemistry* **23**, 3880–3906 (2015).

39. Broichhagen, J., Frank, J. A. & Trauner, D. A Roadmap to Success in Photopharmacology. *Accounts of Chemical Research* **48**, 1947–1960 (2015).

40. Mehvar, R. & Brocks, D. R. Stereospecific pharmacokinetics and pharmacodynamics of beta-adrenergic blockers in humans. *Journal of Pharmacy and Pharmaceutical Sciences* vol. 4 185–200 (2001).

41. McClure, D. E., Arison, B. H. & Baldwin, J. J. Mode of Nucleophilic Addition to Epichlorohydrin and Related Species: Chiral Aryloxymethyloxiranes. *Journal of the American Chemical Society* vol. 101 3666–3668 (1979).

42. Klunder, J. M., Ko, S. Y. & Sharpless, K. B. Asymmetric Epoxidation of Allyl Alcohol: Efficient Routes to Homochiral B-Adrenergic Blocking Agents. *Journal of Organic Chemistry* **51**, 3710–3712 (1986).

43. Baker, J. G. *et al.* Novel selective β1-adrenoceptor antagonists for concomitant cardiovascular and respiratory disease. *FASEB Journal* **31**, 3150–3166 (2017).

44. Sandoz, G., Levitz, J., Kramer, R. H. & Isacoff, E. Y. Optical Control of Endogenous Proteins with a Photoswitchable Conditional Subunit Reveals a Role for TREK1 in GABAB Signaling. *Neuron* **74**, 1005–1014 (2012).

45. Cherezov, V. *et al.* High-resolution crystal structure of an engineered human β2-adrenergic G protein-coupled receptor. *Science* **318**, 1258–1265 (2007).

46. Lewis, R. v. & Lofthouse, C. Adverse Reactions with B-Adrenoceptor Blocking Drugs An Update. *Drug Safety* **9**, 272–279 (1993).

47. Wu, Y., Zeng, L. & Zhao, S. Ligands of Adrenergic Receptors: A Structural Point of View. *Biomolecules* **11**, 936 (2021).

48. Baker, J. G. The selectivity of *β* -adrenoceptor antagonists at the human *β* 1, *β* 2 and *β* 3 adrenoceptors. *British Journal of Pharmacology* **144**, 317–322 (2005).

49. Louis, S. N. S., Nero, T. L., Iakovidis, D., Jackman, G. P. & Louis, W. J. LK 204–545, a highly selective β1-adrenoceptor antagonist at human β-adrenoceptors. *European Journal of Pharmacology* **367**, 431–435 (1999).

50. Bandara, H. M. D. & Burdette, S. C. Photoisomerization in different classes of azobenzene. *Chem. Soc. Rev.* **41**, 1809–1825 (2012).

51. Kenakin, T. P. Orthosteric Drug Antagonism. in *A Pharmacology Primer* (Elsevier, 2014). doi:10.1016/B978-0-12-407663-1.00006-5.

52. ARUNLAKSHANA, O. & SCHILD, H. O. SOME QUANTITATIVE USES OF DRUG ANTAGONISTS. *British Journal of Pharmacology and Chemotherapy* **14**, (1959).

53. Kenakin, T. P. Agonists. in *A Pharmacology Primer* (Elsevier, 2014). doi:10.1016/B978-0-12-407663-1.00005-3.

54. Zang, J. & Neuhauss, S. C. F. Biochemistry and physiology of zebrafish photoreceptors. *Pflügers Archiv - European Journal of Physiology* **473**, 1569–1585 (2021).

55. McMillan, T. J. *et al.* Cellular effects of long wavelength UV light (UVA) in mammalian cells. *Journal of Pharmacy and Pharmacology* **60**, 969–976 (2010).

56. Weissleder, R. A clearer vision for in vivo imaging. *Nature Biotechnology* **19**, 316–317 (2001).

57. Lameijer, L. N. *et al.* General Principles for the Design of Visible-Light-Responsive Photoswitches: Tetra- *ortho* -Chloro-Azobenzenes. *Angewandte Chemie International Edition* **59**, 21663–21670 (2020).

58. Knie, C. *et al. ortho* -Fluoroazobenzenes: Visible Light Switches with Very Long-Lived *Z* Isomers. *Chemistry - A European Journal* **20**, 16492–16501 (2014).

59. Dong, M., Babalhavaeji, A., Samanta, S., Beharry, A. A. & Woolley, G. A. Red-Shifting Azobenzene Photoswitches for in Vivo Use. *Accounts of Chemical Research* **48**, 2662–2670 (2015).

60. Aleotti, F. *et al.* Spectral Tuning and Photoisomerization Efficiency in Push–Pull Azobenzenes: Designing Principles. *The Journal of Physical Chemistry A* **124**, 9513–9523 (2020).

61. Xu, X. *et al.* Binding pathway determines norepinephrine selectivity for the human β1AR over β2AR. *Cell Research* **31**, 569–579 (2021).

62. Liu, X. *et al.* Mechanism of intracellular allosteric β2AR antagonist revealed by X-ray crystal structure. *Nature* **548**, 480–484 (2017).

63. Konrad, D. B. *et al.* Computational Design and Synthesis of a Deeply Red-Shifted and Bistable Azobenzene. *Journal of the American Chemical Society* **142**, 6538–6547 (2020).

64. Samanta, S. *et al.* Photoswitching Azo Compounds in Vivo with Red Light. *Journal of the American Chemical Society* **135**, 9777–9784 (2013).

65. Leistner, A. *et al.* Fluorinated Azobenzenes Switchable with Red Light. *Chemistry – A European Journal* **27**, 8094–8099 (2021).

66. Nogly, P. *et al.* Retinal isomerization in bacteriorhodopsin captured by a femtosecond x-ray laser. *Science* **361**, (2018).

67. Arkhipova, V. *et al.* Structural Aspects of Photopharmacology: Insight into the Binding of Photoswitchable and Photocaged Inhibitors to the Glutamate Transporter Homologue. *Journal of the American Chemical Society* **143**, 1513–1520 (2021).

68. Pospich, S. *et al.* Cryo-EM Resolves Molecular Recognition Of An Optojasp Photoswitch Bound To Actin Filaments In Both Switch States. *Angewandte Chemie International Edition* **60**, 8678–8682 (2021).

69. Morgan, H. P. *et al.* The Trypanocidal Drug Suramin and Other Trypan Blue Mimetics Are Inhibitors of Pyruvate Kinases and Bind to the Adenosine Site. *Journal of Biological Chemistry* **286**, 31232–31240 (2011).

70. Schehr, M. *et al.* 2-Azo-, 2-diazocine-thiazols and 2-azo-imidazoles as photoswitchable kinase inhibitors: limitations and pitfalls of the photoswitchable inhibitor approach. *Photochemical & Photobiological Sciences* **18**, 1398–1407 (2019).

71. DuBay, K. H. *et al.* A Predictive Approach for the Optical Control of Carbonic Anhydrase II Activity. *ACS Chemical Biology* **13**, 793–800 (2018).

72. Nasrallah, C. *et al.* Agonists and allosteric modulators promote signaling from different metabotropic glutamate receptor 5 conformations. *Cell Reports* **36**, 109648 (2021).

73. Miller-Gallacher, J. L. *et al.* The 2.1 Å Resolution Structure of Cyanopindolol-Bound β1-Adrenoceptor Identifies an Intramembrane Na+ Ion that Stabilises the Ligand-Free Receptor. *PLoS ONE* **9**, e92727 (2014).

74. Isogai, S. *et al.* Backbone NMR reveals allosteric signal transduction networks in the β1-adrenergic receptor. *Nature* **530**, 237–241 (2016).

75. Ishchenko, A. *et al.* Toward G protein-coupled receptor structure-based drug design using X-ray lasers. *IUCrJ* **6**, 1106–1119 (2019).

76. Bai, N., Roder, H., Dickson, A. & Karanicolas, J. Isothermal Analysis of ThermoFluor Data can readily provide Quantitative Binding Affinities. *Scientific Reports* **9**, 2650 (2019).

77. Warne, T., Edwards, P. C., Leslie, A. G. W. & Tate, C. G. Crystal Structures of a Stabilized β1-Adrenoceptor Bound to the Biased Agonists Bucindolol and Carvedilol. *Structure* **20**, 841–849 (2012).

78. Sato, T. *et al.* Pharmacological Analysis and Structure Determination of 7-Methylcyanopindolol–Bound β_1-Adrenergic Receptor. *Molecular Pharmacology* **88**, 1024–1034 (2015).

79. Warne, T., Serrano-Vega, M. J., Tate, C. G. & Schertler, G. F. X. Development and crystallization of a minimal thermostabilised G protein-coupled receptor. *Protein Expression and Purification* **65**, 204–213 (2009).

80. Cherezov, V. *et al.* High-Resolution Crystal Structure of an Engineered Human β_2-Adrenergic G Protein–Coupled Receptor. *Science* **318**, 1258–1265 (2007).

81. Rasmussen, S. G. F. *et al.* Crystal structure of the β2 adrenergic receptor–Gs protein complex. *Nature* **477**, 549–555 (2011).

82. Wacker, D. *et al.* Conserved Binding Mode of Human β_2 Adrenergic Receptor Inverse Agonists and Antagonist Revealed by X-ray Crystallography. *Journal of the American Chemical Society* **132**, 11443–11445 (2010).

83. Luckow, V. A., Lee, S. C., Barry, G. F. & Olins, P. O. Efficient generation of infectious recombinant baculoviruses by site-specific transposon-mediated insertion of foreign genes into a baculovirus genome propagated in Escherichia coli. *Journal of Virology* **67**, 4566–4579 (1993).

CONCLUSIONS

The conclusions elicited from the present thesis are summarized below, ordered according to their corresponding Chapter.

Chapter 1. Caged ligands targeting β-AR: an irreversible approach to optically control physiological systems.

1. We described the first diffusible caged antagonist targeting β-AR. The incorporation of the coumarin-4-yl protecting group to the beta-blocker carvedilol yielded Caged-Carvedilol. Photolytic release of the bioactive molecule could be achieved through illumination with blue light (405 nm).

2. Caged-Carvedilol did not inhibit β-AR in cell-based functional assays. Upon illumination, carvedilol was photolytically released, thus significantly reducing the activation state of β-AR. This evidenced the success of the conducted caging strategy, which enabled the control of β-AR *in vitro* through the application of light.

3. The developed photoactivatable molecule was used to evaluate the light-triggered modulation of the cardiac frequency in two different physiological systems. Studies were performed using perfused mice hearts and 7dpf zebrafish larvae. In both cases, the cardiac frequency was only significantly reduced on experimental groups treated with illuminated Caged-Carvedilol, thus confirming the potential of the developed molecular tool for research or therapeutic applications.

4. Behavioral studies conducted in zebrafish larvae showed that only illuminated Caged-Carvedilol triggered a reduction in the startle response to a vibrational stimulus. Additionally, delayed non-associative learning was observed for experimental groups treated with illuminated C-C. This opens up new avenues for the use of the developed ligand in research studies that aim to unravel the role of beta-blockers in the brain.

5. A caged analogue of the β-AR agonist cimaterol was synthesized following the caging strategy employed for Caged-Carvedilol. However, photochemical characterization highlighted that the photolytic reaction that releases cimaterol was occurring in an unexpected manner. Only minor amounts of the bioactive molecule were released upon illumination, and most of the molecule was degraded in an undesired reaction.

Chapter 2. Development of the first photoswitchable ligands to reversibly control β-AR function with light.

1. We described the first photoswitchable ligands targeting β-AR: **Photazolols 1-3** (**PZLs 1-3**). These structural isomers display a *p*-acetamido azobenzene that substitutes the hydrophobic moiety present in all β-AR antagonists. Photoisomerization could be achieved through the application of UV (380 nm) or green (550 nm) light.

2. Despite the existing structural similarities between **PZLs 1-3**, different photopharmacological and selectivity profiles were observed *in vitro*. **PZL-1** was found to behave as a *trans*-on compound in both β_1- and β_2-AR functional assays. *Meta*-AB **PZL-2** behaved as a *cis*-on compound against the two receptor subtypes studied. Both **PZL-1** and **PZL-2** showed higher functional activities towards the beta-2 subtype.

3. **PZL-3**, which incorporates the oxyaminoalcohol moiety in *para*, displayed selective *trans*-on modulation of β_1-AR. This compound behaved as a partial agonist. When tested in β_2-AR functional assays, negligible and non-switchable antagonism was detected.

4. Two *para*-substituted azobenzenes (**83** and **84**) were synthesized to selectively target β_1-AR. The two compounds inhibited β_2-AR with low potency, with IC_{50} values obtained in the micromolar range for the different photoisomers. When compounds were tested against β_1-AR nanomolar agonistic activities were detected for their *trans*-isomers. Upon illumination, Photoinduced Potency shifts of 20 and 83-fold were measured for ABs **83** and **84** respectively, highlighting the *trans*-on nature of the ligands. Additional *in vitro* assays evidenced that both ligands are partial agonists with low efficacy. Therefore, both **83** and **84** displayed β_1-AR selectivity.

5. Results obtained i*n vivo* further confirmed the selectivity of *p*-ABs towards β_1-AR. After zebrafish larvae were exposed to *p*-OMe AB **84** in dark conditions, they showed reduced cardiac frequencies compared to control groups. On the other hand, when larvae were exposed to illuminated **84** (at 380 nm) they presented restored cardiac rhythms, which were not significantly different from control groups.

Chapter 3. Towards red-shifted azobenzenes targeting β-AR: an improved photochemical profile for therapeutic applications.

1. [redacted]

2. [redacted]

3. [redacted]

[redacted]

4. [redacted]

5. A fluorinated analogue of **PZL-1** was produced as a proof of concept for the future development of red-shifted tetra-*ortho* fluorinated ABs. Substituting hydrogen for a fluorine atom in the azobenzene moiety did not dramatically alter the reference light-dependent pharmacological properties.

Chapter 4. Structural studies of β-AR using synthetic photoswitches: understanding light-triggered protein changes.

1. Expression and purification of two different β_1-AR recombinant proteins were successfully established for crystallization purposes. Nevertheless, cellular expression of the β_1-AR US variant should be improved, considering that large-scale protein expression in suspension cells proved unsuccessful and the established alternative is not appropriate for long-term usage.

2. Optimal expression conditions of β_2-AR-T4L in *Sf9* cells were determined, which allowed producing high amounts of target protein in insect cells. Apo-β_2-AR was purified with low yields due to the low thermostabilization of this receptor in the absence of a ligand. Low amounts of protein were isolated when β_2-AR-T4L was purified bound to **PZL-1** following a reported protocol for crystallization purposes. Even after optimizing the bottleneck steps in the protocol, we did not achieve to purify enough β_2-AR-T4L-**PZL-1** to set crystallization trials.

3. Thermal Shift Assays (TSA) performed independently for the three recombinant proteins studied concluded that *ortho*-ABs **PZL-1** and **107** constitute the best candidates to attempt crystallization of β-AR. The two ligands induced noticeable thermal stabilization upon binding to either of the three recombinant receptors.

4. TSA confirmed the *cis*-on behavior of *meta*-AB **PZL-2**, considering that it significantly increased thermal stabilization of the receptor upon illumination for the three recombinant proteins tested. On the other hand, *p*-ABs (**PZL-3**, **83**, and **84**) did not induce thermal stabilization of any of the tested receptors under dark or light conditions. These results were surprising considering that the ligands behaved as

selective *trans*-on partial agonists towards β_1-AR functional assays. Further studies should be conducted to shed light on a possible new binding mode for these ligands.

5. Preliminary crystals were obtained for the β_1-AR US recombinant receptor bound to **PZL-1**. However, optimization of the crystallization conditions should be performed to obtain diffraction-quality crystals. Contrarily, no crystal hits were obtained for β_1-AR Shin, a more flexible recombinant receptor that might be difficult to crystallize.

MATERIALS & METHODS

Materials & Methods contents

1 Synthetic chemistry

1.1 Materials and Methods

1.1.1 Chemicals and solvents

All starting materials were obtained from commercial sources and used without further purification unless otherwise stated. Anhydrous solvents were obtained from a solvent purification system (*PureSolv-EN*^{TM}) and kept under a nitrogen atmosphere.

1.1.2 Reaction monitoring

Reactions were monitored by thin layer chromatography (TLC) on silica gel (60F, 0.2 mm, ALUGRAM Sil G/UV_{254} *Macherey-Nagel*) and visualized with 254 nm UV light.

1.1.3 Microwave reactions

Reactions under microwave irradiation were carried out in a *CEM Discover Focused™* Microwave reactor. This instrument is constituted by a continuous focused microwave power delivery system with selectable power output (0-300 W). Reactions were performed in 10 mL sealed glass vessels. Temperature of the vessel content was monitored using an IR sensor and the indicated temperature corresponds to the maximal temperature reached during each experiment. Reaction vessels were magnetically stirred by means of a rotating magnetic plate located below the floor of the microwave cavity. The specified time corresponds to the total irradiation time. Efficient cooling was accomplished by means of pressurized air during entire experiment.

1.1.4 Compound purification

Flash column chromatography was carried using silica-gel 60 (*Panreac*, 40-63 µm mesh) or by means of a *Biotage* Isolera One automated system with *Biotage* SNAP columns.

1.1.5 Nuclear Magnetic Resonance (NMR)

Nuclear Magnetic Resonance (NMR) spectroscopy was performed using a *Varian-Mercury 400 MHz* spectrometer. Chemical shifts are reported in δ (ppm) relative to the residual non-deuterated solvent signal (Chloroform-*d* δ = 7.26 ppm (^{1}H), δ = 77.16 ppm (^{13}C); DMSO-*d6* δ = 2.50 ppm (^{1}H), δ = 39.51 ppm (^{13}C), Methanol-*d4* δ = 4.87 ppm, δ = 3.31 ppm (^{1}H), δ = 49.3 ppm (^{13}C)). The following abbreviations have been used to designate multiplicities: s=singlet, d=doublet, t=triplet, q=quadruplet, h=heptet, m=multiplet, br=broad signal, dd=doublet of doublet, ddd=doublet of doublet of doublet, dddd=doublet of doublet of doublet of doublet, dt=doublet of triplet, qd=quadruplet of doublet. Coupling constants (*J*) are reported in Hz.

1.1.6 Infrared Spectra (IR)

IR spectra were recorded neat or dissolved in $CHCl_3$ using *Thermo Nicolet Avatar 360 FT-IR* Spectrometer.

1.1.7 Melting Points (mp)

Melting points were measured with *Melting Point B-545 (Büchi)*.

1.1.8 Optical rotation ([α]D)

Optical rotation values were measured in a *Perkin-Elmer 341* polarimeter with the indicated solvents. $[\alpha]_D$ values are reported in degrees and calculated as *c* x 100 / (*d* x *m*) where *c* is the concentration of the sample in g/100 mL, *d* is the optical way in dm and *m* is the measured value (mean of 5 measurements).

1.1.9 Chiral HPLC

Chiral analytical HPLC was performed on a *Thermo Ultimate 3000SD* (*Thermo Scientific Dionex*) coupled to a *Dionex VWD-3400-RS* detector (*Thermo Scientific*; λ = 362 nm). As chiral HPLC column, a Phenomenex Lux Amylose-2 (4.6 x 250 mm, 5 µM) was used. Enantiomeric excess was determined using the following binary systems: (S1) 0.25% IPA + 0,3 % DEA + 0,1 % HF in ACN, isocratic; 0.5 mL/min; (S2) 0.5% IPA + 0.1 % DEA + 0.1 % HF in ACN, isocratic; 0.6 mL/min; (S3) 1.5 % IPA + 0.1 % DEA in ACN, isocratic; 0.5 mL/min; (S4) 10 % IPA in Hexane + 0.1% DEA, isocratic; 1.0 mL/min; (S5) 5 % IPA in ACN + 0.1% DEA, isocratic; 0.5 mL/min.

1.1.10 High-resolution mass spectra (HRMS)

High-resolution mass spectra (HRMS) and elemental composition were performed on a FIA (Flux Injected Analysis) with Ultrahigh-Performance Liquid Chromatography (UPLC) *Aquity (Waters)* coupled to LCT Premier Orthogonal Accelerated Time of Flight Mass Spectrometer (TOF) (*Waters*). Data from mass spectra was analyzed by electrospray ionization in positive and negative mode using MassLynx 4.1 Software (*Waters*). Spectra were scanned between 50 and 1500 Da with values every 0.2 seconds and peaks are reported as *m/z*.

1.1.11 Final compound purity

Purity of final compounds was determined by High-Performance Liquid Chromatography (HPLC). Analytical HPLC was performed on a *Thermo Ultimate 3000SD* (*Thermo Scientific Dionex*) coupled to a PDA detector and Mass Spectrometer *LTQ XL ESI-ion trap* (*Thermo Scientific)* (HPLC-PDA-MS)) or on a *Waters 2795 Alliance* coupled to a DAD detector (*Agilent 1100*) and an *ESI Quattro Micro* MS detector (*Waters*); HPLC columns used were *ZORBAX Eclipse Plus C18* (4.6x150mm; 3.5µm) and *ZORBAX Extend-C18* (2.1 x 50 mm, 3.5 µm) respectively. HPLC purity was determined using the following binary solvent system: 5% acetonitrile in 0.05% formic acid for 0.5 minutes, from 5 to 100% acetonitrile in 5 minutes, 100% acetonitrile for 1.5 minutes, from 100 to 5% acetonitrile in 2 minutes and 5% acetonitrile for 2 minutes. The flow rate was 0.5 mL/min, column temperature was fixed to 35 ºC and wavelengths from 210-600 nm were registered.

1.2 Synthetic procedures

1.2.1 Synthesis of caged compounds

7-(Diethylamino)-2-oxo-2*H*-chromene-4-carbaldehyde (51)

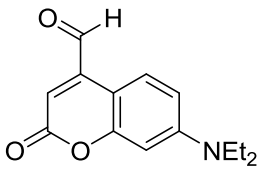

Selenium dioxide (7.10 g, 63.9 mmol) and 7-(diethylamino)-4-methyl-2H-chromen-2-one (5.10 g, 22.05 mmol) were suspended in xylene (315 mL). The reaction mixture was heated to reflux and stirred vigorously for 5 days under an argon atmosphere. The mixture was then filtered through celite and concentrated under reduced pressure to yield aldehyde (**51**) (5.2 g, 96 % yield) as a dark oil.

^{1}H NMR (400 MHz, Chloroform-*d*) δ = 10.02 (s, 1H), 8.29 (d, *J* = 9.2 Hz, 1H), 6.62 (dd, *J* = 9.2, 2.6 Hz, 1H), 6.51 (d, *J* = 2.6 Hz, 1H), 6.45 (s, 1H), 3.42 (q, *J* = 7.1 Hz, 4H), 1.21 (t, *J* = 7.1 Hz, 6H). The described NMR is in good agreement with the data reported in the literature.[1]

7-(Diethylamino)-4-(hydroxymethyl)-2*H*-chromen-2-one (52)

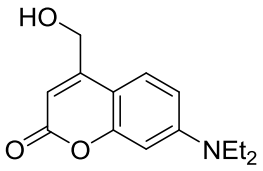

A solution of **51** (3.5 g, 14.27 mmol) in methanol (30 mL) was cooled down in an ice bath. Sodium borohydride (540 mg, 14.27 mmol) was then added slowly and the reaction was left to stir overnight. Water (200 mL) was added and the solution was neutralised using 1N HCl. The brown aqueous solution was extracted using EtOAc (3 x 250 mL). The organic phases were poured together, washed with brine and dried over Na_2SO_4. The solvent was removed *in vacuo* to yield **52** (3 g, 85% yield) as a brown oil.

^{1}H NMR (400 MHz, Chloroform-*d*) δ = 7.32 (d, *J* = 9.0 Hz, 1H), 6.57 (dd, *J* = 9.0, 2.6 Hz, 1H), 6.51 (d, *J* = 2.6 Hz, 1H), 6.26 (t, *J* = 1.3 Hz, 1H), 4.83 (d, *J* = 4.7 Hz, 2H), 3.41 (q, *J* = 7.1 Hz, 4H), 1.20 (t, *J* = 7.1 Hz, 6H). The NMR spectrum is in good agreement with that reported in the literature.[2]

4-(Bromomethyl)-7-(diethylamino)-2*H*-chromen-2-one (53):

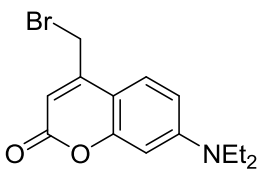

Triethylamine (0.789 mL, 5.66 mmol) was added to a solution of **52** (700 mg, 2.83 mmol) in DCM (12 mL) and the mixture was cooled down in an ice bath. Methanesulfonyl chloride (486 mg,

4.25 mmol) was added dropwise and the reaction was stirred for 2 hours. The mixture was quenched with saturated $NaHCO_3$ (25 mL). The organic solution was isolated, dried over Na_2SO_4 and concentrated under vacuum. The obtained crude product was dissolved in THF (12 mL) and treated with LiBr (983 mg, 11.32 mmol). The reaction was concentrated after 2 hours, DCM was added and the solution was washed with brine, dried over Na_2SO_4 and concentrated under vacuum. **53** (230 mg, 26 % yield) was isolated as a brown solid.

^{1}H NMR (400 MHz, Chloroform-*d*) δ = 7.50 (d, *J* = 8.8 Hz, 1H), 6.64 (d, *J* = 8.8 Hz, 1H), 6.53 (s, 1H), 6.14 (s, 1H), 4.40 (s, 2H), 3.42 (q, *J* = 7.1 Hz, 4H), 1.22 (t, *J* = 7.1 Hz, 6H). The described NMR is in good agreement with the data reported in the literature.[3]

4-(((3-((9*H*-Carbazol-4-yl)oxy)-2-hydroxypropyl)(2-(2-methoxyphenoxy)ethyl)amino)methyl)-7-(diethylamino)-2*H*-chromen-2-one (Carvedilol-Caged, 54):

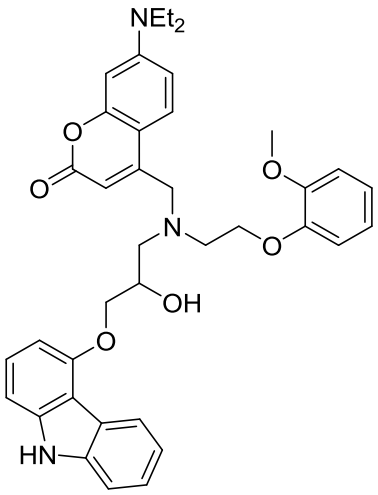

1-((9*H*-Carbazol-4-yl)oxy)-3-((2-(2-methoxyphenoxy)ethyl)amino)propan-2-ol (**11**) (260 mg, 0.640 mmol) was dissolved in DMF (1.5 mL). 4-(Bromomethyl)-7-(diethylamino)-2*H*-chromen-2-one (**53**) (198 mg, 0.64 mmol) and triethylamine (90 µL, 0.64 mmol) were added and the mixture was stirred at room temperature for 24h. The solvent was removed under reduced pressure. DCM (20 mL) was added and the organic solution was washed with brine, dried and concentrated under vacuum to yield a brown solid. The crude product was further purified by silica gel column chromatography (DCM:EtOAc ,95:5) to yield 250 mg (62 % yield) of Carvedilol-Caged (**54**).

^{1}H NMR (400 MHz, Chloroform-*d*) δ = 8.22 (s, 1H), 8.20 (s, 1H), 7.59 (d, *J* = 9 Hz, 1H), 7.41-7.30 (m, 2H), 7.23 (t, *J* = 8 Hz, 1H), 7.16 (t, *J* = 7.4 Hz, 1H), 7.01 (d, *J* = 8 Hz, 1H), 6.95-6.81 (m, 4H), 6.50 (d, *J* = 8 Hz, 1H), 6.39 (d, *J* = 2.6 Hz, 1H), 6.25 (s, 1H), 6.22 (s, 1H), 4.36 (br, 1H), 4.27-4.21 (m, 1H), 4.20-4.12 (m, 3H), 4.04-3.82 (m, 2H), 3.79 (s, 3H), 3.56-3.44 (m, 1H), 3.33 (q, *J* = 7.1 Hz, 4 H), 3.18-2.98 (m, 3H), 1.15 (t, *J* = 7.1 Hz, 6H). **^{13}C NMR** (101 MHz, Chloroform-*d*) δ = 162.3, 156.5, 155.2, 150.5, 149.6, 148.1, 141.0, 138.8, 126.7, 126.0, 125.0, 122.9, 122.6, 121.5, 120.9, 119.7, 113.1, 112.7, 111.6, 110.2, 109.2, 108.5, 107.8, 103.9, 101.2, 97.6, 70.1, 68.3, 66.9, 58.2, 57.5, 55.8, 54.2, 44.8, 12.6. **HRMS** (ESI+): m/z calcd for $C38H42N3O6^+$ $[M + H]^+$ = 636.3074; found 636.3073.

1-(4-Amino-3-bromophenyl)ethenone (59)

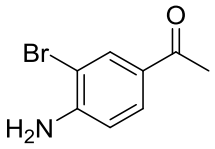

1-(4-Aminophenyl)ethanone (2.0 g, 14.8 mmol) was taken up in ACN (10 mL) and the solution was cooled in an ice bath. NBS (2.63 g, 14.8 mmol) dissolved in ACN (24 mL) was then added dropwise. The resulting mixture was left to stir overnight at room temperature. The reaction was concentrated in vacuo and the crude product dissolved in EtOAc. The organic solution was subjected to multiple washings using $NaHCO_3$, brine and water, dried over $MgSO_4$, filtered and evaporated in vacuo to yield (**59**) as a brown oil (3.05 g, 96 % yield).

^{1}H NMR (400 MHz, Chloroform-*d*) δ = 8.06 (d, *J* = 2.0 Hz, 1H), 7.74 (dd, *J* = 8.5, 2.0 Hz, 1H), 6.74 (d, *J* = 8.5 Hz, 1H), 2.50 (s, 3H). The obtained NMR is in good agreement with that reported in the literature.[4,5]

5-Acetyl-2-aminobenzonitrile (60)

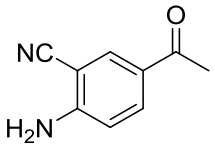

1-(4-Amino-3-bromophenyl)ethanone (**59**) (2.50 g, 11.68 mmol) was taken up in *N,N*-dimethylformamide (15 mL) under an inert atmosphere. Copper (I) cyanide (1.25 g, 14.01 mmol) was then added, and the reaction mixture was refluxed for 6 h. After cooling, the mixture was poured into water (200 mL) and the obtained precipitate was filtered off and dried. Compound **60** was isolated as a yellow solid (1.50 g, 80 % yield).

^{1}H NMR (400 MHz, DMSO-d_6) δ = 8.06 (d, *J* = 2.0 Hz, 1H), 7.83 (dd, *J* = 8.9, 2.0 Hz, 1H), 6.91 (s, 2H), 6.79 (d, *J* = 8.9 Hz, 1H), 2.42 (s, 3H). The described NMR is in good agreement with the data reported in the literature.[4,5]

2-Amino-5-(2-bromoacetyl)benzonitrile (61)

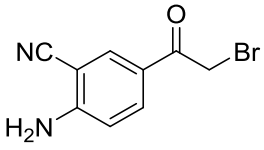

5-Acetyl-2-aminobenzonitrile (**60**) (122 mg, 0.762 mmol) and $CuBr_2$ (8.4 g, 37.6 mmol) were dissolved under a dry nitrogen atmosphere in a 1:1 mixture of $CHCl_3$ and EtOAc (10 mL). The reaction mixture was stirred for 30 minutes at 70°C; ethanol (2 mL) was then added dropwise for 30 minutes. After the addition, the mixture was stirred for 2 hours at 70ºC. The reaction was

then filtered and the obtained solution was washed with brine (3 × 50 mL), dried over anhydrous $MgSO_4$, and concentrated in vacuum to yield **61** (160 mg, 88 % yield).

^{1}H NMR (400 MHz, DMSO-d_6) δ = 8.13 (d, *J* = 2.2 Hz, 1H), 7.83 (dd, *J* = 9.0, 2.2 Hz, 1H), 7.06 (s, 2H), 6.79 (d, *J* = 9.0 Hz, 1H), 3.13 (s, 2H). The NMR spectrum is in good agreement with the data reported in the literature. [4,5]

2-Amino-5-(1-hydroxy-2-(isopropylamino)ethyl)benzonitrile (6)

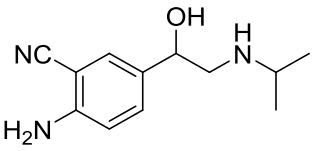

2-Amino-5-(2-bromoacetyl)benzonitrile (**61**) (500 mg, 2.09 mmol) was taken up in EtOH (10 mL) and the solution was cooled down in an ice bath. Isopropylamine (358 µl, 4.18 mmol) was added and the mixture was left to stir for 30 minutes. The mixture was then stirred for 2h at 60ºC under nitrogen. The mixture was cooled down at 0ºC and $NaBH_4$ (127 mg, 3.35 mmol) was added portion wise. After the addition, the reaction was left to stir for 4h at r.t. Water (10 mL) was added, and the resulting mixture was acidified with HCl to get the product in the aqueous phase. The aqueous solution was washed with EtOAc (3 x 50 mL). The aqueous phase contained the desired product was then basified using NaOH and extracted with EtOAc (3 x 50 mL). The organic phases were poured together, dried over $MgSO_4$, filtered and evaporated in vacuo. Further purification was achieved by reverse phase chromatography (95:5 water 0.1% NH4OH : ACN 0.1% NH_4OH to 100% ACN 0.1% NH_4OH). Cimaterol (**6**) was isolated as a white solid (75 mg, 16%).

^{1}H NMR (400 MHz, Methanol-d_4) δ = 7.35 (d, *J* = 2.0 Hz, 1H), 7.33 (dd, *J* = 8.5, 2.0 Hz, 1H), 6.81 (d, *J* = 8.5 Hz, 1H), 4.61 (dd, *J* = 8.8, 4.2 Hz, 1H), 2.87 (h, *J* = 6.3 Hz, 1H),), 2.74 (dd, *J* = 12.0, 4.2 Hz, 1H), 2.69 (dd, *J* = 12.0, 8.8 Hz, 1H), 1.10 (d, *J* = 6.3 Hz, 3H), 1.08 (d, *J* = 6.3 Hz, 3H). The described NMR is in good agreement with the data reported in the literature.[5]

2-Amino-5-(2-(((7-(diethylamino)-2-oxo-2*H*-chromen-4-yl)methyl)(isopropyl)amino)-1-hydroxyethyl)benzonitrile (62)

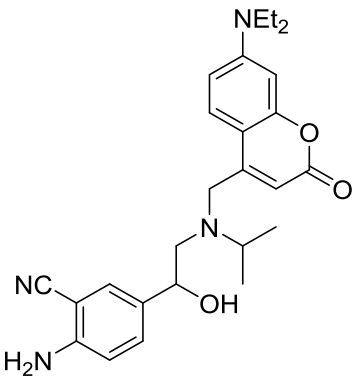

2-Amino-5-(1-hydroxy-2-(isopropylamino)ethyl)benzonitrile (**6**) (50 mg, 0.23 mmol) was dissolved in DMSO (1.5 mL) and triethylamine (32 µl, 0.23 mmol) was added. The mixture was left to stir for 10' and 4-(bromomethyl)-7-(diethylamino)-2*H*-chromen-2-one (**53**) (70.7 mg, 0.23 mmol) was added. The reaction mixture was left to stir for 5 days at room temperature avoiding light exposure. The crude was directly purified with column chromatography (4:1 EtOAc:Hexane). The appropriate fractions were poured together and concentrated under reduced pressure avoiding light exposure. **62** was isolated as a pale-yellow oil (8 mg, 7.8 % yield).

^{1}H NMR (400 MHz, DMSO-d_6) δ = 7.43 (d, *J* = 9.0 Hz, 1H), 7.19 (d, *J* = 2.0 Hz, 1H), 7.14 (dd, *J* = 8.6, 2.0 Hz, 1H), 6.60 (d, *J* = 8.6 Hz, 1H), 6.48 (dd, *J* = 9.0, 2.6 Hz, 1H), 6.38 (d, *J* = 2.6 Hz, 1H), 6.03 (s, 1H), 4.47 (s, 2H), 4.35 (dd, *J* = 8.5, 5.0 Hz, 1H), 3.74–3.57 (m, 2H), 3.30 (q, *J* = 7.0 Hz, 4H), 2.94 (p, *J* = 6.6 Hz, 1H), 2.48–2.43 (m, 2H), 1.10 (t, *J* = 7.0 Hz, 6H), 1.04 (d, *J* = 6.6 Hz, 3H), 0.91 (d, *J* = 6.6 Hz, 3H). **^{13}C NMR** (101 MHz, DMSO-d_6) δ = 202.2, 187.2, 167.0, 161.6, 155.8, 151.1, 150.6, 132.8, 130.6, 126.6, 118.8, 115.3, 113.8, 108.6, 107.6, 97.1, 71.3, 52.5, 51.2, 44.4, 18.3, 17.7, 12.8.

1.2.2 Synthesis of UV-absorbing azobenzenes

1-Methoxy-3-nitrosobenzene (64)

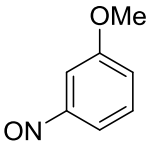

A solution of Oxone (11.0 g, 17.9 mmol) in water (20.3 ml) was added slowly to a solution of 3-methoxyaniline (1.0 ml, 8.1 mmol) in DCM (20.3 mL). The reaction mixture was stirred vigorously at room temperature for approximately 2h. The two phases were thereafter separated, and the aqueous layer was further extracted with DCM (15 mL x 3). The combined organic layers were washed with HCl (1 M), saturated Na_2CO_3 and brine. The organic extracts were dried over anhydrous $MgSO_4$, filtered and evaporated under reduced pressure. The crude mixture was purified by flash column chromatography (hexane) and 1-methoxy-3-nitrosobenzene **64** (510 mg, 49%) was isolated as a green-red oil.

^{1}H NMR (400 MHz, Chloroform-*d*) δ = 8.03 (ddd, *J* = 8, 2, 1.2 Hz, 1H), 7.59 (t, *J* = 8 Hz, 1H), 7.26 (ddd, *J* = 8, 2, 1.2 Hz, 1H), 6.89 (t, *J* = 2Hz, 1H), 3.85 (s, 3H). The described NMR is in good agreement with the data reported in the literature.[6]

***N*-(4-((3-Methoxyphenyl)diazenyl)phenyl)acetamide (65)**

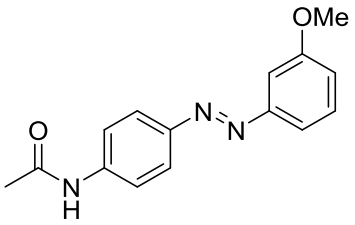

A suspension of 1-methoxy-3-nitrosobenzene (**64**) (510 mg, 3.7 mmol) and *N*-(4-aminophenyl)acetamide (559 mg, 3.7 mmol) in AcOH (7,4 mL) was left to stir overnight at room temperature. The crude was further purified by column chromatography (EtOAc:Hexane 1:3) and compound **65** was isolated as an orange solid (410 mg, 41%), m.p.145.6-145.8 ºC.

^{1}H NMR (400 MHz, Chloroform-*d*) δ = 7.92 (d, *J* = 8.8 Hz, 2H), 7.68 (d, *J* = 8.8 Hz, 2H), 7.53 (ddd, *J* = 8, 1.6, 0.8 Hz, 1H), 7.44– 7.43 (m, 1H), 7.42 (t, *J* = 8 Hz, 1H), 7.32 (br, 1H), 7.03 (ddd, *J* = 8, 2.6, 0.8 Hz, 1H), 3.90 (s, 3H), 2.23 (s, 3H). **^{13}C NMR** (101 MHz, Chloroform-*d*) δ = 168.1, 160.5, 154.1, 149.1, 140.6, 129.9, 124.2, 119.8, 117.8, 117.2, 105.7, 55.6, 25.0. **IR** (neat): υ = 3298, 3252, 3190, 3125, 3064, 3004, 2937, 2833, 1665, 1590, 1544, 1501, 1406, 1319, 1264, 1148, 1123, 1041, 1031, 846, 782, 681. **HRMS** (ESI +): *m/z* calcd for $C_{15}H_{16}N_3O_2^+$ $[M+H]^+$ = 270.1243; found 270.1263.

***N*-(4-((4-Hydroxyphenyl)diazenyl)phenyl)acetamide (67)**

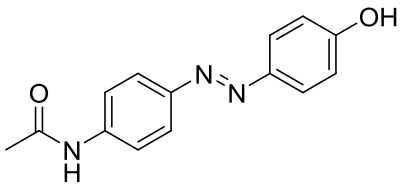

N-(4-Aminophenyl)acetamide (3.82 g, 25.4 mmol) was taken up in water (16.2 mL) and the solution was cooled down to -10 ºC. HCl (15.5 mL, 509 mmol) was added carefully, and the mixture was left to stir for 5 minutes. A solution of sodium nitrite (3.95 g, 57.2 mmol) in water (24.2 mL) was then added dropwise through an addition funnel, keeping the temperature below 5º C. The reaction was stirred for 10 minutes. In parallel, we prepared a solution of phenol (4.79 g, 50.9 mmol) in NaOH 10% (32.3 mL) and water (24.2 mL). This mixture was thereafter stirred vigorously and cooled down to -10º C in an ice bath. The freshly prepared diazonium salt was kept cold to avoid degradation and was added very slowly on top of the phenolic solution. A red precipitate was formed immediately. The reaction mixture was allowed to stand in an ice-bath for 30 min with occasional stirring, filtered, washed with water and dried. Phenol **67** was isolated (4.1 g, 63%) as a brown solid and no further purification was required, m.p.181.9-184ºC.

^{1}H NMR (400 MHz, DMSO-d_6) δ = 10.24 (s, 1H), 7.82 – 7.71 (m, 6H), 6.92 (d, *J* = 8.4 Hz, 2H), 2.08 (s, 3H). **^{13}C NMR** (101 MHz, DMSO-d_6) δ = 168.6, 160.5, 147.5, 145.3, 141.5, 124.5, 123.0, 119.1, 115.9, 24.1. The NMR data are in good agreement with the literature.[7] **IR** (neat): υ = 3346, 3049, 2998, 2796, 2595, 1651, 1584, 1530, 1503, 1405, 1371, 1228, 1142, 835. **HRMS** (ESI +): *m/z* calcd for $C_{14}H_{14}N_3O_2^+$ $[M+H]^+$ = 256.1086; found 256.1061.

***N*-(4-((3-Hydroxyphenyl)diazenyl)phenyl)acetamide (68)**

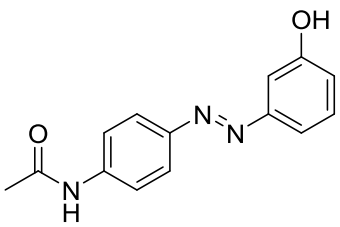

A solution of *N*-(4-((3-methoxyphenyl)diazenyl)phenyl)acetamide **65** (450 mg, 1.7 mmol) in DCM (16.7 mL) was cooled down to 0°C and kept under a nitrogen atmosphere. BBr_3 (1 M in DCM, 11.7 mL, 11.7 mmol) diluted in CH_2Cl_2 (6.3 mL) was added carefully and the mixture was left to warm up and kept under constant stirring for 24h. The reaction was terminated by the addition of water (50 mL). The mixture was left to stir for 1h before the addition of 100 mL EtOAc/MeOH (10:0.1). The two phases were separated, and the aqueous phase was further extracted with EtOAc (3 x 25 mL). The combined organic extracts were dried over Na_2SO_4, filtered and concentrated under vacuum to yield an orange solid. Further purification was carried by column chromatography (EtOAc:Hexane 1:3) and **68** was isolated as an orange solid (407 mg, 95%), m.p. 200.5-200.6 ºC.

^{1}H NMR (400 MHz, Methanol-d_4) δ = 7.86 (d, *J* = 8.8 Hz, 2H), 7.75 (d, *J* = 8.8 Hz, 2H), 7.39 (dt, *J* = 7.9, 1.5 Hz, 1H), 7.34 (t, *J* = 7.9 Hz, 1H), 7.29 (dd, *J* = 2.4, 1.7 Hz, 1H), 6.92 (ddd, *J* = 7.9, 2.4, 1.2 Hz, 1H), 2.17 (s, 3H). **^{13}C NMR** (101 MHz, Methanol-d_4) δ = 171.8, 159.4, 155.4, 150.0, 142.8, 130.9,124.6, 121.0, 119.1, 116.5, 108.8, 24.0. **IR** (neat): υ = 3404, 3066, 3018, 2860, 2725, 1660, 1602, 1585, 1525, 1504, 1469, 1435, 1407, 1389, 1307, 1258, 1236, 1157, 881, 840. **HRMS** (ESI +): *m/z* calcd for$C_{14}H_{14}N_3O_2^+$ $[M+H]^+$ = 256.1086; found 256.1096.

***(S)*-*N*-(4-((4-(Oxiran-2-ylmethoxy)phenyl)diazenyl)phenyl)acetamide (69)**

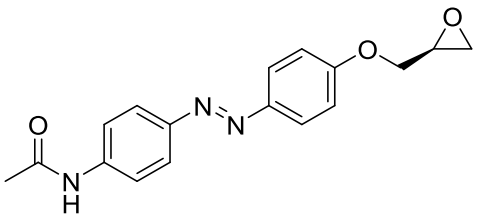

*N-(*4-((4-Hydroxyphenyl)diazenyl)phenyl)acetamide **67** (1.17 g, 4.6 mmol) was taken up in anhydrous butanone (11.5 mL). K_2CO_3 (1.9 g, 13.8 mmol) was added and the suspension was left to stir for 10 minutes. (*R*)-epichlorohydrin (1.8 ml, 22.9 mmol) was finally added and the reaction was heated to reflux overnight. An orange precipitate was observed. The suspension was thereafter filtered, washed with acetone (3 x 20 mL) and dried. Further purification was achieved by column chromatography (EtOAc:Hexane 1:6) and oxirane **69** was isolated as a red solid (842 mg, 59%), m.p. 182.1-183.9 ºC.

^{1}H NMR (400 MHz, DMSO-d_6) δ = 10.25 (s, 1H), 7.77-7.86 (m, 6H), 7.15 (d, *J* = 8.8 Hz, 2H), 4.45 (dd, *J* = 11.7, 2.6 Hz,1H), 3.94 (dd, *J* = 11.7, 6.6 Hz, 1H), 3.36-3.40 (m, 1H), 2.87 (t, *J* = 4.7 Hz, 1H), 2.74 (dd, *J* = 4.7, 2.6 Hz,1H), 2.09 (s, 3H). **^{13}C NMR** (101 MHz, DMSO-d_6) δ = 168.7, 160.5, 147.4, 146.4, 141.8, 124.2, 123.3, 119.1, 115.1, 69.4, 49.6, 43.8, 24.2. **IR** (neat): υ = 3302, 3258, 3192, 3126, 3074, 3004, 2912, 1667, 1591, 1539, 1497, 1367, 1299, 1255, 1242, 1152, 1031, 845, 826. **HRMS** (ESI +): *m/z* calcd for $C_{17}H_{18}N_3O_3^+$ $[M+H]^+$ = 312.1348; found 312.1329. **$[\alpha]_D^{25}$** = + 2.6 (c = 1.0, $CHCl_3$). (*R*)-**69** (703 mg, 90 %) was produced following the same protocol but using (*S*)-epichlorohydrin (1.2 mL, 15.7 mmol).

***(S)*-*N*-(4-((3-(Oxiran-2-ylmethoxy)phenyl)diazenyl)phenyl)acetamide (70)**

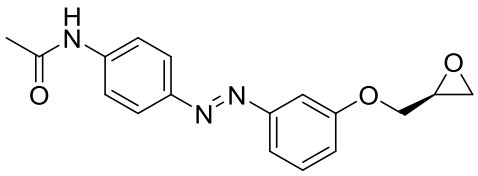

N-(4-((3-hydroxyphenyl)diazenyl)phenyl)acetamide **68** (250 mg, 0.98 mmol), was taken up in anhydrous butanone (9.8 mL). K_2CO_3 (406 mg, 2.94 mmol) was added and the suspension was left to stir for 10 minutes. (*R*)-epichlorohydrin (384 µL, 4.90 mmol) was finally added and the reaction was heated to reflux overnight. An additional equivalent of (*R*)-2-(chloromethyl)oxirane and K_2CO_3 was added and the mixture was left to stir for 24h. An orange precipitate was formed. The suspension was thereafter filtered and washed with acetone (3 x 10 mL). Oxirane **70** was isolated as a red oil (304 mg, 100%).

^{1}H NMR (400 MHz, Chloroform-*d*) δ = 7.91 (d, *J* = 8.8 Hz, 2H), 7.67 (d, *J* = 8.8 Hz, 2H), 7.55 (ddd, *J* = 8.0, 1.7, 1 Hz, 1H), 7.43 (dd, *J* = 2.6, 1.7 Hz,1H), 7.41 (t, *J* = 8.0, 1H), 7.05 (ddd, *J* = 8.0, 2.6, 1 Hz, 1H), 4.33 (dd, *J* = 11.1, 3.1 Hz, 1H), 4.05 (dd, *J* = 11.1, 5.6 Hz, 1H), 3.38-3.42 (m,1H), 2.94 (dd, *J* = 5, 4.1 Hz, 1H), 2.80 (dd, *J* = 5, 2.6 Hz, 1H), 2.22 (s, 3H). **^{13}C NMR** (101 MHz, Chloroform-*d*) δ = 168.5, 159.3, 154.0, 149.0, 140.7, 130.0, 124.2, 119.8, 118.3, 117.9, 106.3, 69.0, 50.2, 44.9, 25.0. **IR** ($CHCl_3$): υ = 3311, 3193, 3126, 3065, 3006, 2928, 1672, 1596, 1538, 1503, 1406, 1371, 1317, 1302, 1259, 1150, 1123, 1037, 848, 753, 684. **HRMS** (ESI +): *m/z* calcd for $C_{17}H_{18}N_3O_3^+$ $[M+H]^+$ = 312.1348; found 312.1374. **$[\alpha]^{25}_D$** = + 5.6 (c = 1.0, $CHCl_3$). Racemic **70** (35 mg, 91 %) was produced following the same protocol but using racemic epichlorohydrin (0.048 mL, 0.6 mmol).

***N*-(4-Nitrosophenyl)acetamide (71)**

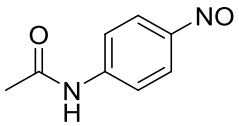

Oxone (35.0 g, 56.9 mmol) was taken up in water (288 mL) and stirred vigorously at room temperature. Potassium carbonate (11.8 g, 85 mmol) was thereafer added slowly and the resulting mixture was directly poured to a solution of N-(4-aminophenyl)acetamide (4) (4.27 g, 28.4 mmol) in water (423 mL). The reaction was left to stir for 10 minutes at room temperature and a green precipitate was formed. The suspension was then filtered and dried. *N*-(4-Nitrosophenyl)acetamide (**71**) was isolated as a green solid (4.27 g, 91%) and was used without further purification on the following reaction.

^{1}H NMR (400 MHz, DMSO-d_6) δ = 10.61 (br, 1H), 7.90-7.84 (m, 4H), 2.14 (s, 3H). The NMR spectra is in good agreement to that reported in the literature.[8]

***N*-(4-((2-Hydroxyphenyl)diazenyl)phenyl)acetamide (72)**

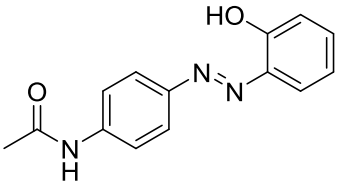

A suspension of 2-aminophenol (1.064 g, 9.8 mmol) and *N*-(4-nitrosophenyl)acetamide (**71**) (1.6 g, 9.8 mmol) in AcOH (19.5 mL) was left to stir at room temperature for 48h. The solvent was thereafter removed under reduced pressure to yield a black slurry. The residue was purified by column chromatography (EtOAc:Hexane 1:3) and the product was isolated as a red solid (410 mg, 16%), m.p. 151.6-152.3 ºC.

^{1}H NMR (400 MHz, Chloroform-*d*) δ = 12.85 (s, 1H), 7.91 (dd, *J* = 8.1, 1.7 Hz, 1H), 7.86 (d, *J* = 8.8 Hz, 2H), 7.69 (d, *J* = 8.8 Hz, 2H), 7.33 (ddd, *J* = 8, 7.5, 1.7 Hz, 1H), 7.07 (ddd, *J* = 8, 7.5, 1.1 Hz, 1H), 7.02 (dd, *J* = 8.1, 1.1 Hz, 1H), 2.23 (s, 3H). **^{13}C NMR** (101 MHz, Chloroform-*d*) δ = 152.6, 149.7, 143.8, 142.9, 137.2, 132.0, 131.7, 124.4, 124.2, 119.7, 117.9, 114.9, 110.2, 29.7. **IR** (neat): υ = 3274, 3203, 3119, 2926, 1672, 1596, 1541, 1503, 1423, 1332, 1319, 1305, 1266, 843, 760, 751. **HRMS** (ESI +): *m/z* calcd for $C_{14}H_{14}N_3O_2^+$ $[M+H]^+$ = 256.1086 found 256.1079.

***(S)*-*N*-(4-((2-(Oxiran-2-ylmethoxy)phenyl)diazenyl)phenyl)acetamide (73)**

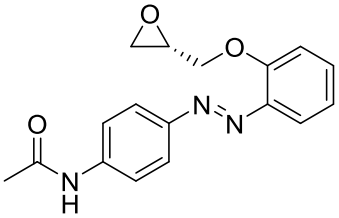

Method A: *N*-(4-((2-hydroxyphenyl)diazenyl)phenyl)acetamide **72** (110 mg, 0.4mmol), was taken up in anhydrous butanone (4.3 mL). K_2CO_3 (179 mg, 1.3 mmol) was added and the suspension was left to stir for 10 minutes. (*R*)-epichlorohydrin (0.169 mL, 2.2 mmol) was finally added and the reaction was heated to reflux overnight. An orange precipitate had been formed. The suspension was thereafter filtered and washed with acetone (3 x 10 mL). Oxirane (*S*)- **73** was isolated as a red oil (98 mg, 73%).

^{1}H NMR (400 MHz, Chloroform-*d*) δ = 7.91 (d, *J* = 8.8 Hz, 2H), 7.67 (d, *J* = 8.8 Hz, 2H), 7.66 (dd, *J* = 8.4, 1.6 Hz, 1H), 7.30 (br, 1H), 7.40 (ddd, *J* = 8.4, 7.2, 1.6 Hz, 1H), 7.12 (dd, *J* = 8.4, 1.2 Hz, 1H), 7.06 (ddd, *J* = 8.4, 7.2, 1.2 Hz, 1H), 4.46 (dd, *J* = 11.2, 3.1 Hz, 1H), 4.22 (dd, *J* = 11.2, 5.2 Hz, 1H), 3.44-3.48 (m, 1H), 2.93 (dd, *J* = 5.2, 4 Hz, 1H), 2.85 (dd, *J* = 5.2, 2.6 Hz, 1H), 2.22 (s, 3H). **^{13}C NMR** (101 MHz, Chloroform-*d*) δ = 168.4, 156.2,149.6, 143.0, 140.5, 132.2, 124.3, 122.0, 119.8, 117.3, 115.7, 70.9, 50.5, 45.0, 25.0. **HRMS** (ESI +): *m/z* calcd for $C_{17}H_{18}N_3O_3^+$ $[M+H]^+$ = 312.1348; found 312.1317.

Method B: *N*-(4-((2-Hydroxyphenyl)diazenyl)phenyl)acetamide **72** (65 mg, 0.2 mmol) was taken up in anhydrous DMF (5 mL). Potassium carbonate (34 mg, 0.2 mmol) was then added to the solution and the mixture was left to stir under nitrogen for 10 minutes. (2*S*)-Glycidyltosylate

(46.5 mg, 0.2 mmol) was then added and the reaction left to stir overnight at room temperature. Oxirane **73** was not isolated and used directly on the subsequent step of the one-pot rection.

(*S*)-*N*-(4-((2-(2-Hydroxy-3-(isopropylamino)propoxy)phenyl)diazenyl)phenyl)acetamide (74)

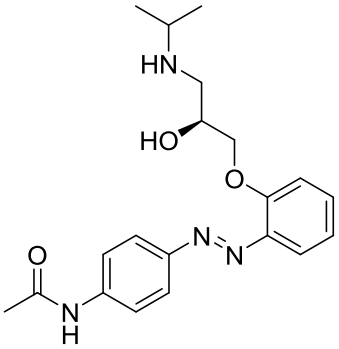

Method A: (*S*)-*N*-(4-((2-(Oxiran-2-ylmethoxy)phenyl)diazenyl)phenyl)acetamide (**73**) (36 mg, 0.1mmol) was dissolved in isopropylamine (0.5 mL, 5.8mmol) and the reaction mixture was stirred at room temperature overnight. The reaction mixture was concentrated under reduced pressure yielding 42 mg (100%) of an orange oil identified as product. Chiral HPLC showed the compound was partially racemized when obtained by reaction with (*R*)-epichlorohydrin. Chiral HPLC (system 1): t_R = 15.0 min, ee 45%.

Method B: Oxirane **73** formed via the reaction of 10 with (2*S*)-Glycidyltosylate (Method B) was directly reacted with isopropylamine (0.175 ml, 2 mmol) in a one-pot reaction and the mixture was heated up to 90ºC for 48h. The reaction was then dried under vacuum and water (20 mL) was added. The obtained solution was neutralized using 2 N NaOH and extracted using EtOAc (3 x 20 mL). The organic fractions were poured together, dried over anhydrous Na_2SO_4, filtered and concentrated under reduced pressure. The product was further purified by automated column chromatography (Water:ACN 95:5 - 0:100 + 0.05% HCOOH). The desired fractions were lyophilized to yield an orange solid, which was found to be the formate salt of **74**. Neutralization was achieved through an aqueous work-up using 1 N NaOH and EtOAc. **74** was isolated as an orange oil (25 mg, 33 %).

^{1}H NMR (400 MHz, Chloroform-*d*) δ = 7.87 (d, *J* = 8.8 Hz, 2H), 7.67 (d, *J* = 8.8 Hz, 2H), 7.65 (dd, *J* = 8, 1.7 Hz, 1H), 7.59 (br, 1H), 7.41 (ddd, *J* = 8.4, 7.4, 1.7 Hz, 1H), 7.11 (dd, J = 8.4, 1.2 Hz, 1H), 7.06 (ddd, *J* = 8, 7.4, 1.2 Hz, 1H), 4.26 – 4.14 (m, 3H), 2.92 (dd, *J* = 12.1, 3.9 Hz, 1H), 2.88 – 2.81 (m, 2H), 2.21 (s, 3H), 1.07 (d, *J* = 6.3 Hz, 6H). **^{13}C NMR** (101 MHz, Chloroform-*d*) δ = 168.6, 156.1, 149.4, 143.2, 140.7, 132.4, 124.2, 122.2, 119.9, 117.8, 116.4, 73.8, 68.5, 49.3, 49.2, 24.9, 22.8, 22.7. **IR** ($CHCl_3$): υ = 3255, 2984, 1673, 1589, 1539, 1501, 1486, 1372, 1320, 1303, 1280, 1239, 1148, 1109, 1036, 846, 749, 665. **HRMS** (ESI +): *m/z* calcd for $C_{20}H_{27}N_4O_3^+$ $[M+H]^+$ = 371.2083; found 371.2064. **Chiral HPLC** (system 1): t_R = 14.9 min, ee 93%. **$[\alpha]^{25}_D$** = - 61.4 (c = 1.0, MeOH).

((*S*)-*N*-(4-((3-(2-Hydroxy-3-(isopropylamino)propoxy)phenyl)diazenyl)phenyl)acetamide (75)

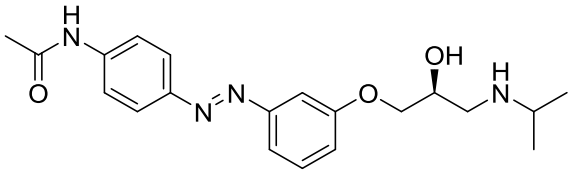

(*S*)-*N*-(4-((3-(Oxiran-2-ylmethoxy)phenyl)diazenyl)phenyl)acetamide **70** (250 mg, 0.8 mmol) was dissolved in isopropylamine (3.4 mL, 40.1 mmol) and the reaction mixture was stirred at room temperature overnight. The solution was concentrated under reduced pressure and purified by reverse phase automated column chromatography (Water:ACN 95:5 – 0:100 + 0.05% HCOOH). The desired fractions were lyophilized to yield an orange solid, which was found to be the formate salt of **75**. Neutralization was achieved through an aqueous work-up using 1 N NaOH and EtOAc. **75**was isolated as an orange oil (97.6 mg, 29 %).

^{1}H NMR (400 MHz, Chloroform-*d*) δ = 7.90 (d, *J* = 8.8, 2H), 7.67 (d, *J* = 8.8, 2H), 7.54 (ddd, *J* =8, 1.8, 1 Hz, 1H), 7.43 (dd, *J* = 1.8, 2.6 Hz, 1H), 7.40 (t, *J* = 8Hz, 1H), 7.04 (ddd, J = 8, 2.6, 1.0 Hz, 1H), 4.07 (s, 3H), 2.90-2.95 (m, 1H), 2.86 (septet, *J* = 6.3 Hz, 1H), 2.79-2.73 (m, 1H), 2.22 (s, 3H), 1.11 (d, *J* = 6.3 Hz, 6H). **^{13}C NMR** (101 MHz, Chloroform-*d*) δ = 168.5, 159.5, 154.0, 149.0, 140.7, 130.0, 124.2, 119.8, 118.1, 117.7, 106.3, 70.8, 68.5, 49.3, 49.2, 24.9, 23.2, 23.1. IR ($CHCl_3$): υ = 3305, 3195, 3125, 3065, 2967, 1673, 1594, 1539, 1503, 1405, 1370, 1317, 1303, 1257, 1215, 1150, 1127, 1037, 848, 749, 683. **HRMS** (ESI +): *m/z* calcd for $C_{20}H_{27}N_4O_3^+$ $[M+H]^+$ = 371.2083; found 371.2091. **Chiral HPLC** (system 2): t_R = 28.8 min, ee 88%. **$[\alpha]^{25}_D$** = -3.6 (c = 1.0, MeOH). Racemic **75** (15 mg, 36 %) was synthesised from racemic **70** (35 mg, 0.1 mmol) as described above.

***(S)*-*N*-(4-((4-(2-Hydroxy-3-(isopropylamino)propoxy)phenyl)diazenyl)phenyl)acetamide (76)**

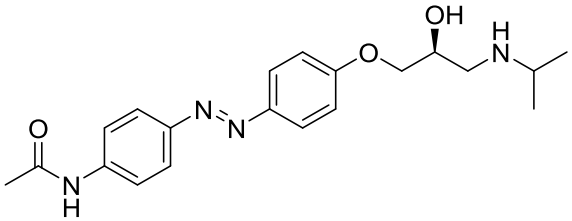

(*S*)-*N*-(4-((4-(Oxiran-2-ylmethoxy)phenyl)diazenyl)phenyl)acetamide **69** (206 mg, 0.7 mmol) was dissolved in isopropylamine (2.8 mL, 33.1 mmol), and the reaction mixture was irradiated for 90 minutes in the microwave (100ºC, 200 psi, 200W). CH_2Cl_2 (5 mL) was added to the orange solution and a precipitate was formed. The suspension was filtered, washed with DCM (3 x 5 mL) and dried. **76**was obtained as an orange solid (137 mg, 56 % yield), m.p. 159.5-163.2 ºC.

^{1}H NMR (400 MHz, Methanol-d_4) δ = 7.87 (d, *J* = 8.8 Hz, 2H), 7.84 (d, *J* = 8.8 Hz, 2H), 7.73 (d, *J* = 8.8 Hz, 2H), 7.09 (d, *J* = 8.8 Hz, 2H), 4.13–4.02 (m, 3H), 2.94 – 2.87 (m, 2H), 2.72 (dd, *J* = 12, 8.2 Hz, 1H), 2.16 (s, 3H), 1.13 (d, *J* = 3.6 Hz, 3H), 1.12 (d, *J* = 3.6 Hz, 3H). **^{13}C NMR** (101 MHz, Methanol-d_4) δ = 171.8, 162.7, 150.2, 148.4, 142.3, 125.5, 124.3, 121.0, 115.9, 72.2, 69.6, 50.6, 50.0, 24.0, 22.4, 22.3. **IR** (neat): υ = 3302, 3132, 2972, 2840, 1668, 1597, 1521, 1499, 1373, 1251, 1151, 1105, 1018, 845, 835. **HRMS** (ESI +): *m/z* calcd for $C_{20}H_{27}N_4O_3^+$ $[M+H]^+$ = 371.2083; found

371.2065. **Chiral HPLC** (system 3): t_R = 9.2 min, ee 99%. **[α]$^{25}_D$** = +6.6 (c = 1.0, MeOH). (*R*)-enantiomer of **76** (33 mg, 23%) was synthesised from (*R*)-**69** (123 mg, 0.4 mmol) as described above. **Chiral HPLC** (system 3): t_R = 9.6 min, ee 98%.

***(E)*-4-((4-Methoxyphenyl)diazenyl)phenol (80)**

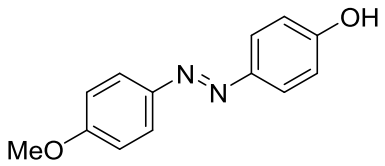

4-methoxyaniline (500 mg, 4.1 mmol, 1.0 eq) was taken up in water (4 mL) and cooled down in an ice bath. HCl (2.1 mL) was then added slowly and the solution was stirred for 10 min at 0ºC.

A solution of sodium nitrite (630 mg, 9.1 mmol, 2.25 eq) in water (6 mL) was then added dropwise and the mixture was left to stir for 10 more minutes in an ice bath. The resulting red slurry was finally added slowly on top of an ice-cold solution of phenol (764 mg, 8.1 mmol, 2.0 eq) in NaOH 10% (8 mL) and the reaction was left to stir for 1 h. A brown precipitate had been formed. The suspension was filtered off with cold water and dried to yield 730 mg of **80** (yield = 79 %), m.p. 139.5 - 139.6 ºC.

^{1}H NMR (400 MHz, Chloroform-*d*) δ = 7.89 (d, *J* = 8.8 Hz, 2H), 7.84 (d, *J* = 8.8 Hz, 2H), 7.00 (d, *J* = 8.8 Hz, 2H), 6.94 (d, *J* = 8.8 Hz, 2H), 3.89 (s, 3H). Spectroscopic data is in agreement with that reported in the literature.[9]

***(S,E)*-1-(4-(Oxiran-2-ylmethoxy)phenyl)-2-phenyldiazene (81)**

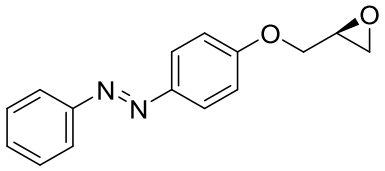

(*E*)-4-(phenyldiazenyl)phenol (200 mg, 1.01 mmol, 1.0 eq) was taken up in butanone (3 mL) in a nitrogen atmosphere. Potassium carbonate (418 mg, 3.03 mmol, 3.0 eq) was added and the reaction was left to stir for 10 minutes. (*R*)-epichlorohydrin (0.396 ml, 5.04 mmol, 5 eq) was finally added and the reaction was heated to reflux and left to stir overnight. The reaction mixture was filtered and the precipitate washed with acetone (10 mL x 3). The resulting solution was dried under reduced pressure to yield a brown oil. The crude product was further purified by column chromatography (hexane/EtOAc 3:1). Oxirane **81** was isolated as an orange solid (703 mg, 90% yield), m.p. 85 - 87 ºC.

^{1}H NMR (400 MHz, Chloroform-*d*) δ = 7.92 (d, *J* = 9.1 Hz, 2H), 7.88 (dd, *J* = 7.2, 2 Hz, 2H), 7.55-7.48 (m, 2H), 7.48-7.39 (m, 1H), 7.04 (d, *J* = 9.1 Hz, 2H), 4.32 (dd, *J* = 11.0, 3.0 Hz, 1H), 4.03 (dd, *J* = 11.0, 5.7 Hz, 1H), 3.40 (m, 1H), 2.94 (dd, *J* = 4.8, 4.0 Hz, 1H), 2.79 (dd, *J* = 4.9, 2.6 Hz, 1H). **^{13}C NMR** (101 MHz, Chloroform-*d*) δ = 161.0, 152.8, 147.4, 130.6, 129.2, 124.9, 122.7, 115.0, 69.1, 50.1, 44.8. **IR** (neat): *υ* = 3066, 3003, 2919, 2874, 1603, 1580, 1497, 1242, 1142, 1027, 835, 764, 689. **HRMS** (ESI +): *m/z* calcd for $C_{15}H_{15}N_2O_2^+$[M + H]$^+$ = 255.1134; found 255.1121. **[α]$^{25}_D$** = + 7.6

(c = 1.6, MeOH). (*R*)-**81** (981 mg, 96 %) was produced following the same protocol but using (*S*)-epichlorohydrin (1.6 mL, 15.7 mmol).

***(S,E)*-1-(4-Methoxyphenyl)-2-(4-(oxiran-2-ylmethoxy)phenyl)diazene (82)**

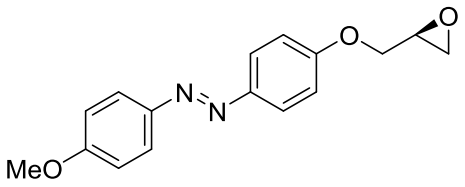

(*E*)-4-((4-Methoxyphenyl)diazenyl)phenol (**80**) (630 mg, 2.8 mmol, 1.0 eq) was taken up in Butanone (6 mL). Potassium carbonate (1.1 g, 8.3 mmol, 3.0 eq) was then added to the solution and the mixture was left to stir under nitrogen for 10 min. (*R*)-epichlorohydrin (1.08 mL, 13.8 mmol, 5.0 eq) was then added and the reaction was heated to reflux and left to stir overnight. The mixture was filtered, and the precipitate washed with acetone (3 x 20 mL). The obtained red solution was evaporated under reduced pressure to yield **82** (703 mg, 2.47 mmol, 90 % yield) as a brown solid, m.p. 130.3 – 131.6 ºC.

^{1}H NMR (400 MHz, Chloroform-*d*) δ = 7.88 (d, *J* = 8.8 Hz, 2H), 7.87 (d, *J* = 8.8 Hz, 2H), 7.02 (d, *J* = 7.6 Hz, 2H), 7.00 (d, *J* = 7.6 Hz, 2H), 4.31 (dd, *J* = 11.0, 2.6 Hz, 1H), 4.03 (dd, *J* = 11.0, 5.8 Hz, 1H), 3.89 (s, 3H), 3.39 (ddt, J = 5.8, 4.2, 2.6 Hz, 1H), 2.94 (dd, *J* = 4.9, 4.2 Hz, 1H), 2.79 (dd, *J* = 4.9, 2.6 Hz, 1H). **^{13}C NMR** (101 MHz, Chloroform-*d*) δ= 161.8, 160.5, 147.5, 147.2, 124.5, 124.5, 115.0, 114.3, 69.1, 55.7, 50.2, 44.8. **IR** (neat): *υ* = 3096, 3076, 3014, 2928, 2840, 1600, 1580, 1495, 1238, 1148, 1026, 840. **HRMS** (ESI +): *m/z* calcd for $C_{16}H_{17}N_2O_3^+$[M + H]$^+$ = 285.1239; found 285.1332. **[α]$^{25}_D$**= + 7.5 (c = 4.6, MeOH).

***(S,E)*-1-(Isopropylamino)-3-(4-(phenyldiazenyl)phenoxy)propan-2-ol (83)**

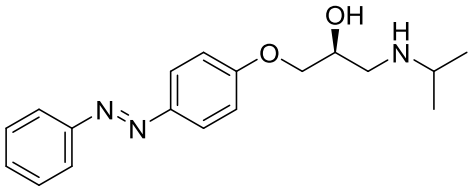

Oxirane **80** (100 mg, 0.39 mmol, 1.0 eq) was dissolved in isopropylamine (1.68 mL) in a sealed microwave tube and heated at 40ºC for 72 h. The reaction mixture was then concentrated under reduced pressure. The isolated crude was purified by column chromatography (10 % MeOH in DCM, 1 % Ammonia) and azobenzene **83** was isolated as a yellow solid (30 mg, 24 % yield), m.p. 108.4–109.8 ºC.

^{1}H NMR (400 MHz, Methanol-d_4) δ = 8.52 (s, 1H), 7.91 (d, *J* = 9.0 Hz, 2H), 7.84 (d, *J* = 9.0, 2H), 7.53–7.41 (m, 3H), 7.12 (d, *J* = 9.0 Hz, 2H), 4.24 (dtd, *J* = 9.6, 5.4, 3.1 Hz, 1H), 4.13 ((dd, *J* = 9.6, 5.4 Hz, 1H), 4.09 (dd, *J* = 8.3, 5.4 Hz, 1H), 3.40 (h, *J* = 6.6 Hz, 1H), 3.25 (dd, *J* = 12.6, 3.1 Hz, 1H), 3.11 (dd, *J* = 12.6, 9.6 Hz, 1H), 1.34 (dd, *J* = 6 .6 Hz, 3H), 1.33 (dd, *J* = 6 .6 Hz, 3H). **^{13}C NMR** (101 MHz, Methanol-d_4) δ = 168.8, 161.1, 152.6, 147.2, 130.3, 128.8, 124.3, 122.1, 114.6, 70.0, 65.7, 50.4, 18.2, 17.7. **IR** (neat): *υ* = 3303, 3070, 2964, 2922, 2870, 1600, 1582, 1501, 1250, 1141, 837,

689. **HRMS** (ESI +): *m/z* calcd for $C_{18}H_{24}N_3O_2^+[M + H]^+$ = 314.1869; found 314.1896. **[α]$^{25}_D$**= + 10.5 (c = 2.5, MeOH). (*R*)-enantiomer of **83** (101 mg, 59 %) was synthesised from (*R*)-**80** (140 mg, 0.55 mmol) as described above. **Chiral HPLC** (system 4): t_R = 14.4 min, ee 93%.

***(S,E)*-1-(Isopropylamino)-3-(4-((4-methoxyphenyl)diazenyl)phenoxy)propan-2-ol (84)**

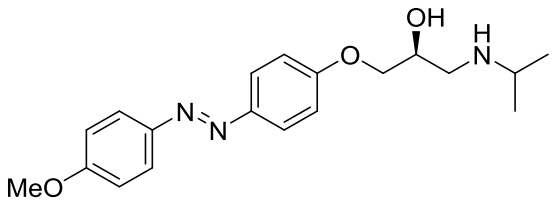

Oxirane **82** (200 mg, 0.70 mmol, 1.0 eq) was dissolved in isopropylamine (3 mL) and the reaction was heated to reflux for 48 h. The reaction mixture was then concentrated *in vacuo*. The crude material was then purified by column chromatography (10% MeOH in DCM, 1 % ammonia) and azobenzene **84** isolated as a yellow solid (150 mg, 62.1 % yield), m.p. 137.2–137.6 ºC.

^{1}H NMR (400 MHz, DMSO-d_6) δ = 7.85 (d, *J* = 9.1 Hz, 2H), 7.84 (d, *J* = 9.1 Hz, 2H), 7.12 (d, *J* = 9.1 Hz, 2H), 7.11 (d, *J* = 9.1 Hz, 2H) , 4.08 (dd, *J* = 9.1, 4.1 Hz, 1H), 4.04-3.94 (m, 2H), 3.86 (s, 3H), 2.90 (h, *J* = 6.3 Hz, 1H), 2.83 (dd, *J* = 12.1, 3.7 Hz, 1H), 2.72 (dd, *J* = 12.1, 7.1 Hz, 1H), 1.07 (d, 6.3 Hz, 6H). **^{13}C NMR** (101 MHz, DMSO-d_6) δ= 161.50, 160.84, 146.21, 124.15, 115.09, 114.57, 70.91, 67.42, 55.63, 48.75, 21.71. **IR** (neat): *υ* = 3316, 2964, 2927, 2835, 1595, 1581, 1495, 1238, 1146, 1025, 841. **HRMS** (ESI +): *m/z* calcd for $C_{19}H_{26}N_3O_3^+[M + H]^+$ = 344.1974; found 344.1942. **[α]$^{25}_D$**= + 1.72 (c = 2.5, MeOH).

[redacted]

[redacted]

[redacted]

[redacted]

[redacted]

[redacted]

[redacted]

[redacted]

[redacted]

[redacted]

[redacted]

[redacted]

[redacted]

[redacted]

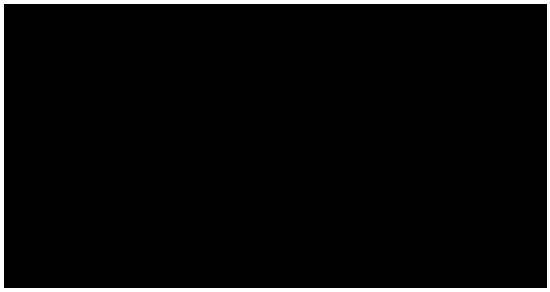

[redacted]

[redacted]

[redacted]

***(E)-N*-(4-((5-Fluoro-2-hydroxyphenyl)diazenyl)phenyl)acetamide (105)**

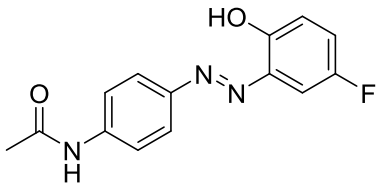

N-(4-Aminophenyl)acetamide (3.22 g, 21.4 mmol) was taken up in MeOH (20.4 mL) and the solution was cooled down to -0 ºC. HCl (4.6 mL, 152 mmol) was added carefully, and the mixture was left to stir for 5 minutes. A solution of sodium nitrite (1.47 g, 21.4 mmol) in water (5.1 mL) was then added dropwise through an addition funnel, keeping the temperature below 5º C. The reaction was stirred for 10 minutes. In parallel, we prepared a solution of 4-fluorophenol (2.0 g, 17.8 mmol) and sodium acetate (4.4 g, 53.5 mmol) in water (10.2 mL). This mixture was thereafter stirred vigorously and cooled down to -10º C in an ice bath. The freshly prepared diazonium salt was kept cold to avoid degradation and was added very slowly on top of the phenolic solution. A red precipitate was formed immediately. The reaction mixture was allowed to stand in an ice-bath for 30 min with occasional stirring, filtered, washed with water and dried. Phenol **105** was isolated (1.5 g, 30 % yield) as a brown solid and no further purification was required, m.p. 190.6 -191.3 ºC.

^{1}H NMR (400 MHz, Methanol-d_4) δ = 7.93 (d, *J* = 8.9 Hz, 2H), 7.79 (d, *J* = 8.9 Hz, 2H), 7.58 (dd, *J* = 9.1, 3.2 Hz, 1H), 7.16 (ddd, *J* = 9.1, 4.8, 3.2 Hz, 1H), 7.01 (dd, *J* = 9.1, 4.8 Hz, 1H), 2.19 (s, 3H). **^{13}C NMR** (101 MHz, Methanol-d4) δ = 171.9, 157.6 (d, *J* = 235.7 Hz), 151.1, 148.5, 143.5, 138.74 (d, *J* = 8.1 Hz), 124.7, 121.1, 120.7 (d, *J* = 23.8 Hz), 119.9 (d, *J* = 7.9 Hz), 113.9 (d, *J* = 23.9 Hz), 24.0. **IR** (neat): *υ* = 3298, 3189, 3129, 3062, 2919, 2850, 1673, 1598, 1540, 1491, 1423, 1370, 1254, 788. **HRMS** (ESI +): *m/z* calcd for $C_{14}H_{13}N_3O_2F^+$ $[M+H]^+$ = 274.0992; found 274.0955.

***(S,E)-N*-(4-((5-Fluoro-2-(oxiran-2-yloxy)phenyl)diazenyl)phenyl)acetamide (106)**

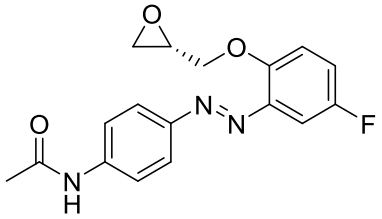

Method A: Phenol **105** (275 mg, 1 mmol) was taken up in anhydrous butanone (10 mL). K_2CO_3 (417 mg, 3.0 mmol) was added and the suspension was left to stir for 10 minutes. (*R*)-epichlorohydrin (0.4 mL, 5.0 mmol) was finally added and the reaction was heated to reflux overnight. An orange precipitate had been formed. The suspension was thereafter filtered and washed with acetone (3 x 10 mL). Oxirane (*S*)-**106** was isolated as a red solid (270 mg, 81 %), m.p. 170.5 – 172.3 ºC.

^{1}H NMR (400 MHz, Chloroform-*d*) δ = 7.90 (d, *J* = 8.8 Hz, 2H), 7.65 (d, *J* = 8.8 Hz, 2H), 7.40 (dd, *J* = 8.4, 1.6 Hz, 2H), 7.09 (dd, *J* = 5.8, 2.0 Hz, 2H), 4.44 (dd, *J* = 11.4, 2.8 Hz, 1H), 4.15 (dd, *J* = 11.4, 5.2 Hz, 1H), 3.43 (br, 1H), 2.91 (t, *J* = 5.2, 1H), 2.86 (dd, *J* = 5.0, 2.8 Hz , 1H), 2.19 (s, 3H). **^{13}C NMR** (101 MHz, Chloroform-*d*) δ = 168.3, 158.0 (d, *J* = 235.7 Hz), 152.7, 149.1, 143.4, 140.8, 124.4,

121.7, 118.3 (d, *J* = 23.8 Hz), 117.5 (d, *J* = 8.0 Hz), 103.5 (d, *J* = 23.9 Hz), 72.0, 50.3, 44.6, 24.8. **IR** (neat): *υ* = 3313, 3190, 3125, 3066, 2919, 2850, 1673, 1594, 1540, 1502, 1408, 1371, 1317, 1302, 1263, 1148, 848. **HRMS** (ESI +): *m/z* calcd for $C_{17}H_{17}N_3O_3F^+$ $[M+H]^+$ = 330.1254; found 330.1219. **[α]$^{25}_D$**= + 41.8 (c = 1.0, MeOH).

Method B: *(E)-N*-(4-((5-fluoro-2-hydroxyphenyl)diazenyl)phenyl)acetamide **105** (907 mg, 3.3 mmol) was taken up in anhydrous DMF (10 mL). Potassium carbonate (550 mg, 4.0 mmol) was then added to the solution and the mixture was left to stir under nitrogen for 10 minutes. (2*S*)-Glycidyltosylate (909 mg, 4.0 mmol) was then added and the reaction left to stir overnight at room temperature. Oxirane **106** was not isolated and used directly on the subsequent step of the one-pot rection.

***(S,E)-N*-(4-((5-Fluoro-2-(2-hydroxy-3-(isopropylamino)propoxy)phenyl)diazenyl)phenyl)acetamide (107)**

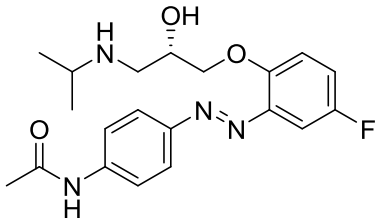

Method A: *(S,E)-N*-(4-((5-Fluoro-2-(oxiran-2-yloxy)phenyl)diazenyl)phenyl)acetamide **106** (50 mg, 0.15 mmol) was dissolved in isopropylamine (0.65 mL, 7.6 mmol) and the reaction mixture was stirred at room temperature overnight. The solution was concentrated under reduced pressure and the crude obtained purified by column chromatography (90:10 EtOAc:MeOH). Compound **107** was isolated as a red oil (9 mg, 15 % yield).

Method B: Oxirane **106** formed via the reaction of **105** with (2*S*)-Glycidyltosylate (Method B) was directly reacted with isopropylamine (2.85 ml, 33.2 mmol) in a one-pot reaction and the mixture was heated up to 90ºC for 48h. The reaction was then dried under vacuum and water (20 mL) was added. The obtained solution was neutralized using 2 N NaOH and extracted using EtOAc (3 x 20 mL). The organic fractions were poured together, dried over anhydrous Na_2SO_4, filtered and concentrated under reduced pressure. The product was further purified by automated column chromatography (Water:ACN 95:5 - 0:100 + 0.05% HCOOH). The desired fractions were lyophilized to yield a highly hygroscopic orange solid, which was found to be the formate salt of **107**. (375 mg, 26 % yield).

^{1}H NMR (400 MHz, Methanol-d_4) δ = 8.56 (s, 1H), 7.92 (d, *J* = 9.0 Hz, 2H), 7.80 (d, *J* = 9.0 Hz, 2H), 7.44 (dd, *J* = 9.4, 2.9 Hz, 1H), 7.32–7.27 (m, 2H), 4.37–4.19 (m, 3H), 3.41 (h, *J* = 6.5 Hz, 1H), 3.35 (dd, *J* = 12.7, 2.8 Hz, 1H), 3.23 (dd, *J* = 12.7, 8.6 Hz, 1H), 2.20 (s, 3H), 1.34 (d, *J* = 6.5 Hz, 3H), 1.33 (d, *J* = 6.5Hz, 3H). **^{13}C NMR** (101 MHz, Methanol-d_4) δ = 171.9, 170.2, 158.1, 155.0 (d, *J* = 209.0 Hz), 150.3, 144.5 (d, *J* = 5.2 Hz), 143.5, 125.0, 121.6, 119.6 (d, *J* = 24.2 Hz), 118.3 (d, *J* = 8.2 Hz), 104.3 (d, *J* = 24.8 Hz), 73.9, 67.2, 51.8, 24.0, 19.6, 19.0. **IR** (neat): *υ* = 3253, 3186, 3113, 3050, 2983, 2919, 2849, 2787, 2708, 1592, 1545, 1496, 1371, 1319, 1265, 1147, 752. **HRMS** (ESI +): *m/z* calcd for $C_{20}H_{26}N_4O_3F^+$$[M + H]^+$ = 389.1989; found 389.2015. **[α]$^{25}_D$**= - 115.4 (c = 1.0, MeOH).

2 Photochemistry

2.1 Instruments

2.1.1 HPLC

HPLC-MS was performed on a *Thermo Ultimate 3000SD* (*Thermo Scientific Dionex*) coupled to a PDA detector and Mass Spectrometer *LTQ XL ESI-ion trap* (*Thermo Scientific).* The ESI source was set in positive mode for the different experiments.

HPLC analysis was carried using a Waters Alliance 2695 Separation module coupled to a Waters 2487 Dual λ Absorbance Detector.

2.1.2 Light sources

Mono-channel LED

When illumination was applied to a single well, a LED light source (pE-4000, CoolLED) connected to a liquid light guide (pE-1906, CoolLED) was used. Characterization of the light source is reported in Table 31.

Table 31. CoolLED characterization. Potency evaluation at different wavelengths and intensities. [a]

λ = 405 nm	
Intensity	**Potency (mW/mm²)**
5	0.51
10	0.96
25	2.01
50	2.10
100	3.28

Intensity = 50 %	
λ (nm)	**Potency (mW/mm²)**
365	1.04
385	2.60
405	2.10
435	0.72
460	2.17
470	1.02
490	0.95
500	0.3
525	0.36
550	1.57

[a] Potencies were measured using a Thorlabs PM100D power energy meter connected to a standard photodiode power sensor (S120VC).

96-well LED array plate

When illumination was applied to 96-well plates, a 96-LED array plate (LEDA Teleopto) connected to a LED array driver (LAD-1, Teleopto) was used. The potencies associated to each wavelength (continuous mode at 13.3 V) are summarized in Table 32.

Table 32. 96-well LED array plate potencies at different wavelengths. [a]

Voltage = 13.3 V	
λ (nm)	**Potency (mW/mm²)**
365	0.11
380	0.12
405	0.20
420	0.15
455	0.18
500	0.12
530	0.10
550	0.15

[a] Potencies were measured using a Thorlabs PM100D power energy meter connected to a standard photodiode power sensor (S120VC).

2.1.3 Spectrophotometers

Plate reader

Absorbance measurements in plates were performed using a Tecan Spark 20M Multimode Microplate reader. 96-well transparent plates were used (Deltalab).

Cuvette spectrophotometer

Absorbance measurements in cuvettes were performed using the Thermo Fisher Evolution 350 UV-Vis spectrophotometer. A 10-mm Quartz Suprasil ultra micro cell (Helma Analytics) was used.

2.1.4 Nuclear Magnetic resonance (NMR)

NMR data was acquired using a Bruker Avance-III 500 MHz spectrometer equipped with a z-axis pulsed field gradient triple resonance (^{1}H, ^{13}C, ^{15}N) TCI cryoprobe. 1D ^{1}H spectra were acquired at 285 K with 32 scans using the pulse sequence zgesgppe (water signal suppressed using excitation sculpting and perfect echo) extracted from the Bruker library. Every sample was locked, tuned and shimmed prior to acquisition. Chemical shifts (δ) are quoted in ppm and referenced to the corresponding deuterated solvent.

2.2 Methods for the characterization of caged compounds

2.2.1 Absorption spectra

UV-Vis spectra were recorded using the Spark microplate reader. All samples were prepared at 50 µM of compound in PBS (30 % DMSO) and absorbances were measured between 600 nm and 250 nm with 2 nm fixed intervals. Transparent 96-well plates (200 µL of compound solution/well)

were used and illumination at 405 nm was applied from top using the CoolLED pE-4000 light source (continuous mode, 5 % intensity).

2.2.2 Evaluation of compound stability to light

The stability of the active compounds to light was qualitatively evaluated by HPLC-MS. A 10 µM solution of carvedilol (**11**) (1 % DMSO in PBS) was illuminated at 405 nm using the CoolLED light source (set at 25 % and 50 % intensity) in continuous mode. Different illumination times up to 3 minutes were evaluated. Samples were thereafter analyzed by HPLC-MS (Table 33).

Table 33. HPLC-MS method to analyze carvedilol (11).

Eluent A: 0.05 % formic acid in ACN

Eluent B: 0.05 % formic acid in H_2O

Column: *ZORBAX Eclipse Plus C18* (4.6x150mm; 3.5µm)

Column T: 35ºC

Time (min)	Flow (mL/min)	%A	% B
0	0.9	23	77
3	0.9	30	70
5	0.9	35	65
6	0.9	100	0
8	0.9	100	0
9	0.9	23	77
11	0.9	23	77

0.5 mg/mL solutions of cimaterol (**6**) and isoprenaline (**4**) (1 % DMSO in PBS) were illuminated using the CoolLED pE-4000 light source (set at 25 % and 50 % intensity) in continuous mode. Illuminations were performed for 30 min, 1 h, 1 h 30 min and 2 h. Samples were analyzed by HPLC-MS using the method described in Table 34.

Table 34. HPLC-MS method to analyze isoprenaline (4) and cimaterol (6).

Eluent A: 0.1 % NH_4OH in ACN

Eluent B: 0.1 % NH_4OH in H_2O

Column: *Acclaim Mixed-Mode HILIC-1* (3x50mm; 3.0 µm)

Column T: 35ºC

Time (min)	Flow (mL/min)	%A	% B
0	0.6	23	77
3	0.6	30	70
6	0.6	35	65

2.2.3 Uncaging quantification

Preparation of stock solutions and calibration curves

10 mM stock solutions of carvedilol (**11**), cimaterol (**6**) and their caged analogues **54** and **62** were prepared in DMSO. All solutions were stored at -20 ºC and brought to room temperature in dark conditions before usage.

The calibration standard curve of carvedilol (**11**) comprised concentrations between 0.2 – 10 µM. The stock solution (10 mM) was diluted 1:100 with water. The obtained solution (100 µM) was subsequently diluted with water to a final concentration of 50 µM. Using this working solution, intermediate dilutions were prepared in the range of 5-25 µM. From these intermediate solutions we finally obtained the calibration curve solutions that were analyzed by HPLC-MS.

The calibration standard curve of **54** comprised concentrations between 2 – 15 µM. The stock solution (10 mM) was diluted 1:100 with water. The obtained solution (100 µM) was subsequently diluted to intermediate working solutions in the range of 20-75 µM. From these intermediate solutions we finally obtained the calibration curve solutions that were analyzed by HPLC-MS.

The calibration curve of cimaterol (**6**) was prepared by sequential dilution of the stock solution using 1% DMSO in PBS. The analyzed solutions comprised concentrations between 250 - 1 µM.

Chromatographic and mass spectrometric conditions

Chromatographic separations of carvedilol (**11**) and **54** were performed using the HPLC-MS method described in Table 33. Quantification was performed using single reaction monitoring (SRM) mode with the transition of m/z 407.3 → 222.1 ± 2, 224.1 ± 2 and 283.1 ± 2 for carvedilol, m/z 658.1 → 423 ± 26, 475 ± 2, 513.5 ± 19, 534.3 ± 2, 590.6 ± 2, 640.4 ± 2 and 654.4 ± 2 for C-C. The optimal source parameters were set as follows: sheath gas flow 60, aux gas flow 10, sweep gas flow 10, capillary temperature 300 ºC, source voltage 3 kV, capillary voltage 42 V and tube lens 110 V. The compound dependent parameter normalized collision energy (CE) was set at 20 % for both compounds. The compound dependent parameter normalized Act Q was set at 0.25 % for the two compounds. The compound dependent parameter Act Time was set at 30 ms for carvedilol and C-C.

Chromatographic separations of cimaterol (**6**) and its caged analogue **62** were performed using the Waters HPLC instrument with the method summarized in Table 35. Measurements were collected at two different wavelengths: 210 nm to detect cimaterol and 385 nm to detect 62.

Table 35. HPLC method to analyze cimaterol (6) and 62.

Eluent A: 0.1 % formic acid in ACN

Eluent B: 0.1 % formic acid in H_2O

Column: *Agilent Ecliplse Plus C18* (4.6x75mm; 3.5µm)

Column T: 35ºC

Time (min)	Flow (mL/min)	%A	% B
0	1.0	5	95
5	1.0	90	10
7	1.0	90	10
8	1.0	100	0
10	1.0	100	0
11	1.0	5	95
15	1.0	5	95

Uncaging protocol

A 100 µM Carvedilol-Caged (**54**) solution (10 % DMSO) was illuminated for the studied times using the CoolLED light source (405 nm, 10 % intensity). The sample was thereafter diluted to 10 µM in water (1 % DMSO) and analyzed by HPLC-MS.

The cimaterol caged (**62**) stock solution (10 mM) was diluted to a 100 µM concentration (1 % DMSO in PBS). This solution was continuously illuminated using the CoolLED light source (405 nm, 10 % intensity) for the studied times (0 - 20 min). The samples were then analyzed by HPLC.

2.3 Methods for the characterization of azobenzenes

2.3.1 Absorption spectra

UV-Vis absorbance spectra were recorded using the Spark microplate reader. All samples were prepared with 50 µM of compound in 0.5 % DMSO in Buffer and 100 % DMSO. Samples were measured between 600 nm and 300 nm with 2 nm fixed intervals in 96-well transparent plates (200 µL of compound solution/well). Illumination at the different wavelengths was achieved using the CoolLED pE-4000 light source, set at 50 % intensity. The liquid light guide accessory was pointed directly towards the well containing the studied sample for 3 minutes in continuous mode.

2.3.2 Reversibility and repeatability of isomerization

Multiple *trans/cis* isomerization cycles were registered by measuring absorbance of 50 µM samples (0.5 % DMSO in Buffer and 100 % DMSO) at a fixed wavelength in dark and after 3 minutes of continuous illumination with the optimal wavelengths (Table 36). Light was applied using the CoolLED light source and measurements were performed with the Spark microplate reader.

Continuous measurements of *trans/cis* isomerization cycles were performed using the Evolution 350 spectrophotometer. Samples (50 µM, 0.5 % DMSO in Buffer and 100 % DMSO) contained in a cuvette were continuously measured at a fixed wavelength in the dark and while illuminated (Table 36). Several isomerization cycles were performed, and isomerization half-life for each compound was calculated by plotting absorbance versus time and by fitting the obtained curve to an exponential decay function using GraphPad prism version 8.1.2 (San Diego, CA).

2.3.3 Kinetics of *cis* to *trans* isomerization

Thermal relaxation studies were performed at 25ºC by prolonged absorbance measuring (in dark conditions) after samples (50 µM, 0.5 % DMSO in Buffer and 100 % DMSO) had been subjected to 3 min illuminations at the appropriate wavelength (Table 36). Samples were illuminated using the CoolLED light system and measurements were collected using the Spark microplate reader. The relaxation half-life of the compounds was calculated by plotting absorbance readings at a fixed wavelength versus time and by fitting the obtained curve to an exponential decay function using GraphPad prism version 8.1.2 (San Diego, CA). The measured wavelength corresponded to the point where maximum difference in absorbance was observed for *trans* and *cis* isomers (Table 36).

Table 36. Summary of illumination conditions and measured λ of the developed azobenzenes.

UV Azobenzenes				Vis Azobenzenes			
Compound	**$\lambda_{trans\rightarrow cis}$ (nm)**	**$\lambda_{cis\rightarrow trans}$ (nm)**	**Measured λ (nm)**	**Compound**	**$\lambda_{trans\rightarrow cis}$ (nm)**	**$\lambda_{cis\rightarrow trans}$ (nm)**	**Measured λ (nm)**
74	385	550	364	**96**	435	365	422
75	385	550	364	**97**	435	550	422
76	385	550	364	**98**	435	550	418
83	365/ 385	550	360	**99**	435	365	422
				100	435	365	422
84	365/ 385	550	360	**101**	435	530	422
107	385	550	386	**102**	435	530	422
				103	435	530	416
				104	435	530	416

2.3.4 ^{1}H-NMR Photostationary State Determination

External light was applied continuously for 3 minutes using the 96-well LED array plate. Samples were prepared from a concentrated stock solution (10 mM in d_6-DMSO) by dilution in deuterated water (100 μM final). ^{1}H NMR spectra of the compound in dark conditions was initially recorded. The sample was thereafter illuminated in the NMR tube with the optimal *trans→cis* isomerization wavelength. ^{1}H NMR spectra were continuously collected over a period of 10-15 minutes in order to ensure there was no variation on PSS quantification attributed to thermal relaxation. The sample contained in the NMR tube was finally illuminated using the appropriate wavelength to trigger the *cis→trans* transition. ^{1}H NMR spectra were again collected over a period of 10-15 minutes to ensure the accuracy of PSS determination.

3 Photopharmacology

3.1 *In vitro* assays

3.1.1 Cell Culture and transfection

To evaluate the activity of the ligands towards β-AR, two different stable expressing cell lines were established. HEK-293 cells, which endogenously express β_2-AR were transfected with the Epac-SH[188] biosensor (1 µg H188 DNA) from Kees Jalink group (Netherlands Cancer Institute) using X-tremeGENE 9 (Sigma-Aldrich, 3:1 X-tremeGENE/DNA ratio) as a transfecting agent. Transfection was carried in 6-well Clear TC-treated Multiple Well Plates (Corning) at a density of 500.000 cells/well. Cells were left to grow for 48h before the selection process was started. The medium was then changed to complete DMEM containing 0.5 mg/mL of Geneticin in order to only select transfected cells containing the Neomycin resistant gene from the plasmid. Two weeks after, cells were passaged and diluted in decreasing densities in a transparent 96-well plate (limited dilution cloning) using cell culture medium enriched with 0.5 µg/mL of G-418. Single cell colonies were isolated from this process, grown, and their functional activity was assessed with the agonist cimaterol (see below). Cells obtained following this protocol, named HEK293-H188 M1, were thereafter to evaluate the functional activity of β_2-AR. On the other hand, to evaluate the functional activity of β_1-AR, iSNAP β_1-AR HEK-293 cells were used. These cells, kindly provided by Dr. Karen Martinez (University of Copenhagen), can express β_1-AR upon induction with tetracycline. A polyclonal stable cell line with the Epac sensor, named iSNAP β_1-AR HEK-293, was established following the transfection and selection protocols previously described. Both cell lines were found to be fluorescent when excited at 485nm indicating the incorporation of the sensor. HEK293 cells stably expressing the Epac-SH[188] cAMP biosensor were maintained at 37ºC, 5% CO_2 in 4,5 g/L D-glucose Dulbecco's Modified Eagle Medium (DMEM, GIBCO) supplied with 10% heat inactivated FBS (GIBCO) and 1% penicillin-streptomycin (10,000 U/mL, GIBCO). In the case of HEK293 iSNAP β_1AR H188 cells, the medium was additionally supplemented with Hygromycin B (100 µg/mL) and Blasticidin (15 µg/mL) since this cell line is also stable for the expression of the human ADRB1. All cell lines were split when reaching 75-90% confluence and detached by trypsin digestion.

3.1.2 General Methods

In vitro assays were carried out using HEK-293 cells endogenously expressing β_2AR or HEK-293 iSNAP β_1AR, which can express β_1AR upon induction. Both cell lines were also stably expressing the cAMP FRET biosensor. All assays were performed at room temperature. Adherent cells were grown in T-175 flasks or 150-mm dishes to 75-90% confluence. Cells were detached by rinsing once with PBS (GIBCO), followed by incubation with Trypsin-EDTA (Sigma-Aldrich) for 5 minutes until detachment of cells was observed. Cells were then centrifugated; in parallel, 10 µL of the single cell suspension were counted using a Neubauer Chamber. The supernatant was carefully removed, and cells were resuspended in DMEM complete medium to obtain a cell solution with 1.0 x 10^6 cells/mL. 100,000 cells per well were seeded in a transparent 96-well microplate (Thermo Scientific Nunc Microwell) and left at 37ºC with 5% CO_2 for approximately 24h. In the case of assays performed using HEK-293 iSNAP β_1AR, receptor was induced by addition of 0.01

µg/mL doxycycline to the medium for 18-24 h. cAMP EPAC sensor buffer (14 mM NaCl, 50 nM KCl, 10 nM $MgCl_2$, 10 nM $CaCl_2$, 1 mM HEPES, 1.82 mg/mL Glucose, pH 7.2) was used as the assay medium in all FRET-based experiments. In assays performed using the HEK-293 H188 M1 cell line, cAMP EPAC sensor buffer was supplemented with 100 µM IBMX. Fluorescence values were measured using a Tecan Spark M20 multimode microplate reader equipped with the Fluorescence Top Standard Module with defined wavelength settings (excitation filter 430/20 nm and emission filters 485/20 nm and 535/25 nm). FRET ratio was calculated as the ratio of the donor emission ($td^{cp173}V$, 485 nm) divided by the acceptor emission (mTurq2Δ, 535 nm). The FRET ratio was normalized to the effect of the buffer (0%) and the maximum response obtained with cimaterol (100%). External light was applied using the 96-well LED array plate (LEDA Teleopto). Each set of experiments was performed three to five times with each concentration in duplicate or triplicate.

3.1.3 Stable cell line characterization

A 96-well plate with the three isolated HEK293 stable cell lines (HEK293-H188 M1, M2 and M3) was produced as described above. Cimaterol Dose-Response solutions were prepared in a pre-plate using cAMP EPAC sensor buffer containing 100 µM IBMX. Culture medium was removed by inversion and 90 µL of assay medium containing IBMX were added to the adherent cells. 10 µL of the different concentrations of agonist were then added and cells were left to incubate for 15 minutes at 25 ºC. Fluorescence measurements were performed immediately after. To evaluate the sensor expression stability over time, two separate batches of cells stably expressing the biosensor were maintained under different selection conditions over four weeks. One of the batches was kept in DMEM complete medium, and the other in medium supplemented with 0.5 mg/mL G-418. The two cell batches were assayed (cimaterol Dose-Response assays) every week in order to assess the stability of sensor expression in a non-selective culture medium. No differences in activity were detected for more than a month. After these results, cells were maintained in DMEM complete medium with no additional antibiotics.

Characterization of the HEK-293 iSNAP β_1AR H188 stable cell line included an evaluation of receptor expression levels. Cells were induced with different concentrations of doxycycline (1-0.004 µg/mL) for 24 h. Cimaterol Dose-Response curves were performed as described for the characterization of HEK293-H188 M1 cells in cAMP EPAC buffer with no IBMX. The optimal conditions to work with these cells are achieved after 24 h induction with 0.01 µg/mL doxycycline.

FRET ratios were calculated and normalized to the effect of assay buffer (0%) and the maximum response obtained by cimaterol (100%). The experiments were performed in duplicate per cell line.

3.1.4 Cimaterol-stimulated Assays

In order to perform *in vitro* assays with Carvedilol-Caged (**54**), 10 µM aliquots of the compound were pre-illuminated for different times using the CoolLED light source (set at 10 % intensity). Differently illuminated **54** samples were then pre-incubated with the HEK293-H188 M1 cells for 15 min. The agonist cimaterol was then added (final concentration of 10 nM) and the plate was

incubated for 30 min. Fluorescence values were measured using the Spark microplate reader for 30 minutes (Figure 138).

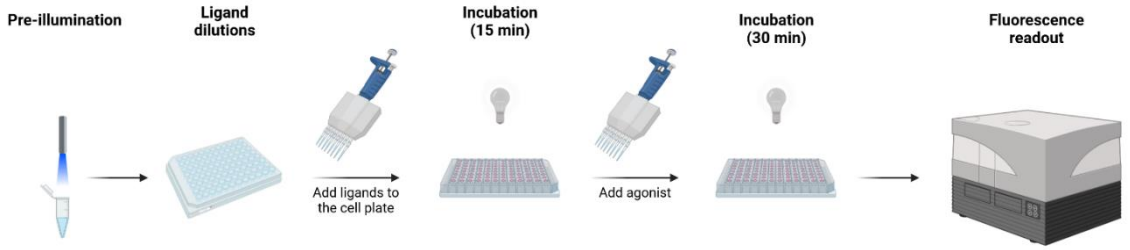

Figure 138. Flowchart of the protocol to assay caged compounds *in vitro.*

To perform cimaterol-stimulated assays with the azobenzene ligands in HEK293-H188 M1 cells we prepared two different plates, one for each light condition. For all assays, both plates were left to incubate with the studied compounds for 45 minutes at room temperature. To induce photoswitching, the "light plate" was exposed to continuous illumination (380 or 405 nm) during the incubation time using the LED array plate (LEDA Teleopto). Fluorescence values were thereafter measured for 30 minutes (Figure 139). Dose-response curves for each compound were obtained using a constant concentration of the agonist cimaterol (3.16 nM). To see the effect of the antagonists on the agonist dose-response, dose-response curves for cimaterol were prepared in combination with different constant concentrations of the photoswitchable compound.

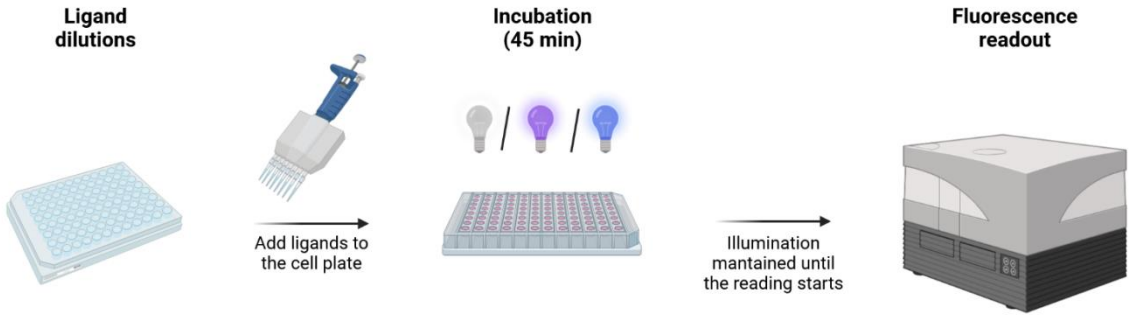

Figure 139. Flowchart of the protocol to assay photoswitchable ligands *in vitro.*

In order to evaluate the activity of the developed azobenzenes in the HEK293 iSNAP β_1AR cell line, only one plate was used to evaluate both light conditions. Cells were treated with a constant concentration of cimaterol (3.16 nM) and different concentrations of the studied azobenzenes to produce dose-response curves. Compounds were incubated with the cells for 45 min in the dark at room temperature. Fluorescence values were thereafter measured. The same plate was then continuously illuminated for 45 min (380/405 nm) using the Teleopto LED array system. Fluorescence values were measured again.

3.1.5 Forskolin-stimulated Assays

To evaluate that the activity of the synthesized photoswitchable antagonists was directly linked to β_2-AR, we stimulated the cells using forskolin, a described activator of adenyl cyclase. For each

experiment, we prepared two different plates containing HEK293 H188-M1 cells, one for each light condition. Dose-response curves for each compound were obtained using a constant concentration of forskolin (10 µM). Dose-response curves of forskolin were also evaluated with a constant concentration of the photoswitchable compounds. Both plates were left to incubate with the assayed compounds for 45 minutes at room temperature. In order to induce photoswitching, the "light plate" was exposed to continuous illumination (380 nm) using the LED array plate (LEDA Teleopto) during the incubation time. Fluorescence values were thereafter recorded for 30 minutes.

3.1.6 Real-Time Assays

Assays to assess the dynamic control of receptor activity were carried out using a constant concentration of azobenzene and cimaterol. Response of the cells with buffer and buffer supplemented with cimaterol was also evaluated. Cells were left to incubate with the compounds for 45 minutes and fluorescence was measured. Then, the plate was continuously illuminated with light at 380 nm or 405 nm for 10 minutes and fluorescence values were recorded. Immediately after, the plate was illuminated in continuous mode for 10 minutes with light at 550 nm or 365 nm and fluorescence was measured. Two additional light cycles were applied to ensure the reversibility in receptor activity triggered by light was reproducible over time.

3.2 *Ex-vivo* assays

3.2.1 Langendorff heart experiments

Adult female C57BL/6J mice (25-30 g, 9-11 weeks old) were anesthetized with sodium pentobarbital (1.5 g/kg, I.P.) and submitted to a bilateral thoracotomy. Whole hearts were quickly excised and retrogradely perfused through the aorta with an oxygenated (95% O_2 : 5% CO_2) Krebs solution at 37ºC (118 mM NaCl, 4.7 mM KCl, 1.2 mM $MgSO_4$, 1.8 mM $CaCl_2$, 25 mM $NaHCO_3$, 1,2 mM KH_2PO_4, and 11 mM glucose, pH 7.4) in a constant flow Langendorff system as previously described. Flow was initially adjusted to produce a perfusion pressure of 80-90 mmHg (normoxic conditions). Left ventricular (LV) pressure was monitored with a water-filled latex balloon connected to a pressure transducer, placed in the left ventricle and inflated to obtain a LV end-diastolic pressure (LVEDP) between 6 and 8 mmHg. Perfusion pressure was monitored through a lateral access into the cannula. All signals were recorded in a computer using a ML119 PowerLab interface and Chart 5.0 software (AdInstruments). After 35 min of equilibration, isolated mice hearts were treated with normoxic Krebs or with Krebs containing 25 µM carvedilol caged, or 25 µM of illuminated carvedilol caged (405 nm, 2 x 2.5 min). After 30 minutes, 0.1 µM isoprenaline was added to all hearts for the next 10 min. Changes in heart rate were continuously monitored for an additional 30 minutes. The present study conforms to European

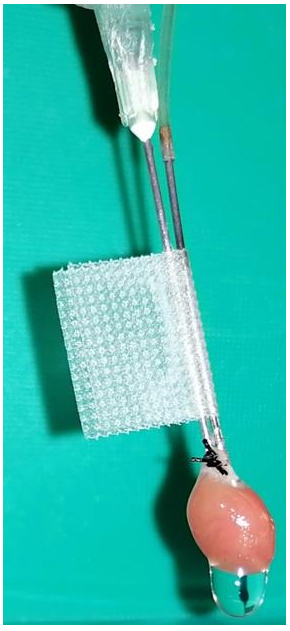

Figure 140. Experimental set up to measure the cardiac effects of carvedilol and its caged analogue 54 using perfused mice hearts.

legislation (Directive 2010/63/EU) on the protection of animals used for scientific purposes and the NIH Guide for the Care and Use of Laboratory Animals (NIH publications Nº. 85-23, revised 1996, updated in 2011), and was approved by the Ethics Committee of Vall d'Hebron Research Institute (reference 22/20 CEEA).

3.3 *In vivo* assays

3.3.1 Fish Husbandry and Larvae Production

Adult wild-type zebrafish were purchased from EXOPET (Madrid, Spain) and maintained in fish water (reverse-osmosis purified water containing 90 µg/mL of Instant Ocean (Aquarium Systems) and 0.58 mM $CaSO_4 \cdot 2H_2O$) at 28 ± 1°C in the Research and Development Center of the Spanish Research Council (CID-CSIC) facilities under standard conditions. Embryos were obtained by in-tank group breeding with a 5:3, female:male ratio per tank. Breeding tanks are homemade and include a solid external tank and an internal plastic net (Figure 141). Embryos deposited in the bottom of the tank were collected and maintained in 500 mL glass containers at 1 individual/mL density in fish water at 28.5 °C on a 12 light:12 dark photoperiod. Larvae were not fed before or during the experimental period. All procedures were approved by the Institutional Animal Care and Use Committees at the CID-CSIC and conducted in accordance with the institutional guidelines under a license from the local government (agreement number 9027).

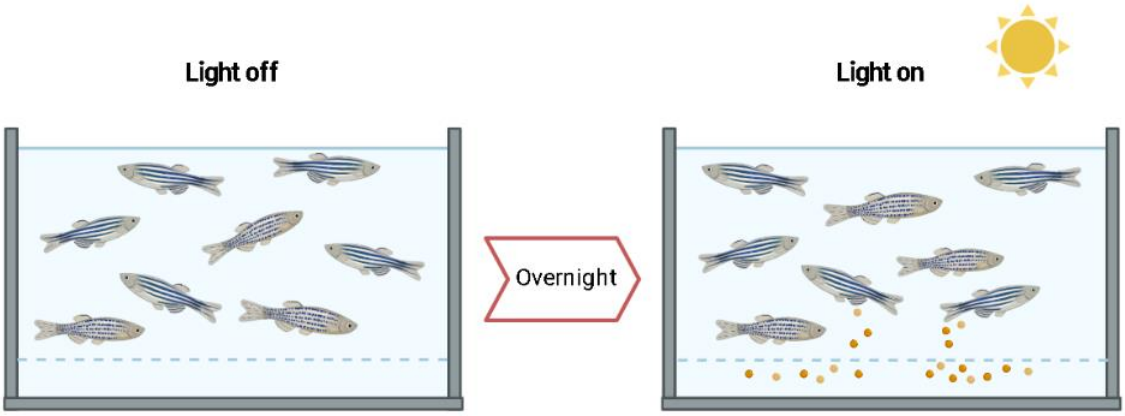

Figure 141. Experimental set up to obtain zebrafish larvae.

3.3.2 Behavioral Assays in Zebrafish larvae

Exposures were conducted in 48-well microplates containing 1 larva per well and 1 mL of working solution (total 48 larvae per plate). 7 dpf (days post fertilization) larvae were used for all experiments. After 1 h of exposure at 28.5°C (POL-EKO APARATURA Climatic chamber KK350), behavior was directly tested without further manipulation. Behavioral assays were performed using a DanioVision system running an Ethovision XT 13 software (Noldus). Larvae were acclimated in the dark for 10 min before video recording. Video tracking conditions included a further 10 min cycle under dark conditions followed by a 50-second stimulus period which consisted of the delivery of 50 tapping stimuli every second. Tapping stimulus was selected at the highest intensity (intensity level: 8). Trials were performed at 28°C with near-infrared light

and videos were recorded at 30 frames per second and the responses were analyzed using the EthoVision XT 13 software (Noldus).

Basal locomotor activity (BLA)

The BLA is defined as the total distance (cm) traveled by the larvae during a period of 10 min of under dark conditions. This parameter was analyzed for each individual larva from the initial 10 min of video tracking.[11,12]

Vibrational startle response (VSR)

The VSR assay is based on the escape response evoked in zebrafish larvae by a tapping stimulus. VSR was analyzed for each individual larva by measuring the distance traveled (cm) over the 1 s period following each stimulus. The VSR assay allows to obtain two behavior responses: The "Startle Response" and the "Habituation". The startle response is defined as the total distance moved (cm) in response to the first stimulus. The habituation evaluates a form of non-associative learning, defined as the area under the curve (AUC) of plots of distance moved by larvae during the delivery of 50 consecutive tapping stimuli relative to the response to the first stimulus.[11]

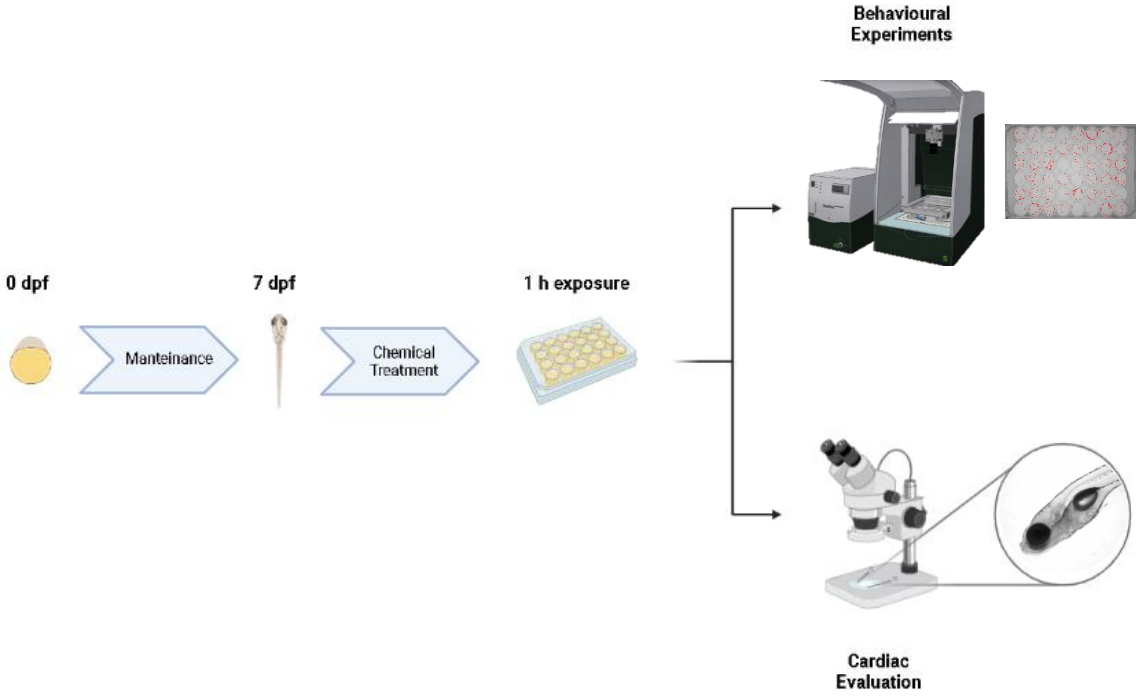

Figure 142. Protocol flowchart for the experiments performed to assay photoactivatable compounds with zebrafish larvae.

3.3.3 Cardiac frequency monitorization in zebrafish larvae

Zebrafish larvae were observed under a Motic SMZ-171 dissecting microscope fitted with a GigE camera (iDS - Imaging Development Systems GmbH). Heart rates were measured in 8 to 10 larvae from each experimental condition. Larvae were placed over 3% methylcellulose with a drop of medium water and positioned on the left side. Videos were recorded for 30 seconds

using uEye Cockpit application (iDS software) at a frame rate of 40 fps. Videos were then analyzed with a MATLAB algorithm (version R2010b, MathWorks, USA) to obtain heart beats per minute for each individual. The program was based on a code to measure the heart rate from a video of a human fingertip captured with a smartphone camera (GitHub: uavster/Video2HeartRate). Briefly, after the video is recorded the brightness signal of the heart region is computed as pixel variations between frames. Then, a band-pass filter is applied (Butterworth filter) to attenuate all frequencies outside the interest band and a Fourier transform is calculated using the Fast Fourier Transform (FFT) algorithm to translate the signal from the time domain to the frequency domain. Finally, the maximum FFT amplitude is obtained, and the corresponding frequency transformed to beats per minute (BPM).

Assay protocol to test caged compounds

To assess differential cardiac modulation enabled by caged and uncaged compounds, zebrafish larvae (7 dpf) were exposed to the tested ligands as previously described (Behavioral Assays, section 3.3.2) (Figure 142).

Assay protocol to test photoswitchable ligands

To assess differential cardiac modulation enabled by the two photoisomers of AB **84**, zebrafish larvae (7 dpf) were exposed to the tested compound for 1.5 h, at 28.5°C (POL-EKO APARATURA Climatic chamber KK350). The different experimental groups, control (1 % DMSO) and 25 µM of AB **84** (15-20 individuals) were kept in 6-well plates for the incubation. Two different plates of zebrafish larvae were used to test both, dark and light conditions. The dark experimental group was kept in dark conditions for 1.5 h and cardiac rhythm was then monitored for each larva. The light plate was incubated in dark conditions for 1 h and illuminated continuously for 1 min using 380 nm light (13.3 V). As we observed that light significantly increased the cardiac rhythm of control larvae, an acclimatation period was added after illumination, where larvae were kept in dark conditions for 30 min prior to cardiac monitorization.

3.4 Data analysis

All experiments were analyzed using GraphPad Prism 8.1.1 (GraphPad Software, San Diego, CA). Data are always presented as the mean ± SEM unless otherwise stated. Statistical differences were considered significant when $p < 0.05$ unless otherwise stated.

For the analysis of *in vitro* assays, stimulation Dose-Response data was fitted using the log (agonist) vs. response (three parameters) function. Inhibition Dose-Response data was fitted using the log(antagonist) vs. response (three parameters) function. Statistical analysis comparing the EC_{50} or IC_{50} values of the compounds in dark and light conditions was performed by unpaired Student's t-test.

To see the effect of the antagonists on the agonist dose−response, dose−response curves for cimaterol were prepared in combination with different constant concentrations of the photoswitchable compound. Statistical analysis of the differences between the vehicle and the assayed concentrations of photochromic ligand was achieved by pairwise comparisons based on the extra sum-of-squares F test for Log(EC_{50}). The obtained p-values were corrected using a

multiple testing method known as the false discovery rate (FDR).[13] Differences between curves with an equal concentration of azobenzene under the different light conditions were analyzed via an extra sum-of-squares F test followed by an FDR test.

Statistical analysis comparing the three light conditions in Real Time Assays was performed by a one-way ANOVA followed by Tukey's multiple comparisons test.

For the analysis of the *ex-vivo* experiments, statistical differences were assessed by repeated measures ANOVA (MANOVA) and Tukey's *post hoc* test.

For the analysis of the *in vivo* experiments, statistical differences were assessed by performing a one-way ANOVA followed by Tukey's multiple comparisons test.

4 Structural Biology

4.1 Materials

4.1.1 Constructs

Two different β_1-AR constructs were used, both provided by the Benoit's group (Paul Scherrer Institut, Switzerland). The turkey (*Meleagris gallopavo*) ultra-stable β_1-AR construct is identical to that crystalized, β_1AR-JM50.[14] This construct contained nine thermostabilizing point mutations and truncations at the N terminus, inner loop 3, and C terminus in order to favor crystallization.[14] On the other hand, we also used a less thermostabilized turkey construct, described in the literature as TS-β_1AR.[15] As compared to the wild type, TS-β_1AR contains truncations at the amino and carboxy termini and intracellular loop (ICL3), nine thermostabilizing point mutations, three further point mutations and a C-terminal hexahistidine tag.[15] Nevertheless, this construct has never been used for crystallization purposes.

As a β_2AR construct, an amino-terminally fused T4 lysozyme–β_2AR construct with β_2AR truncated in position 365 (T4L–β_2AR) was used. T4L–β_2AR has been previously crystallized and its complete sequence is described in the literature.[16]

4.1.2 Buffers and solutions

Name	Ingredients	Concentration
Membrane preparation:		
Low salt buffer	HEPES (NaOH) pH 7.5	10 mM
	$MgCl_2$	10 mM
	KCl	20 mM
	Complete protease inhibitor (Roche)	1/100 mL
High salt buffer	HEPES (NaOH) pH 7.5	10 mM
	$MgCl_2$	10 mM
	KCl	20 mM
	NaCl	1 M
	Complete protease inhibitor (Roche)	1/100 mL
β_1AR purification:		
Solubilization buffer	HEPES (NaOH) pH 7.5	50 mM
	NaCl	150 mM
	DDM	0.03 % (w/v)
	Complete protease inhibitor (Roche)	1/100 mL
Strep wash buffer	HEPES (NaOH) pH 7.5	50 mM
	NaCl	150 mM
	DDM	0.03 % (w/v)
	Complete protease inhibitor (Roche)	1/100 mL

Strep elution buffer	HEPES (NaOH) pH 7.5	50 mM
	NaCl	150 mM
	DDM	0.03 % (w/v)
	Desthiobiotin	5 mM
	Complete protease inhibitor (Roche)	1/100 mL
Talon A	HEPES (NaOH) pH 7.5	50 mM
	NaCl	150 mM
	DDM	0.03 % (w/v)
Talon B	HEPES (NaOH) pH 7.5	50 mM
	NaCl	150 mM
	Desthiobiotin	500 mM
	DDM	0.03 % (w/v)
SEC buffer	HEPES (NaOH) pH 7.5	25 mM
	NaCl	150 mM
	DDM	0.03 % (w/v)

β_2AR purification:

Lysis buffer	Tris pH 7.4	10 mM
Solubilization buffer	HEPES (NaOH) pH 7.5	20 mM
	NaCl	100 mM
	$CaCl_2$	10 mM
	DDM/CHS	1/0.2 % (w/v)
	Complete protease inhibitor (Roche)	1/100 mL
Flag wash buffer	HEPES (NaOH) pH 7.5	20 mM
	NaCl	100 mM
	$CaCl_2$	10 mM
	DDM/CHS	0.1/0.02 % (w/v)
	Complete protease inhibitor (Roche)	1/100 mL
Flag elution buffer	HEPES (NaOH) pH 7.5	20 mM
	NaCl	100 mM
	DDM/CHS	0.1/0.02 % (w/v)
	Flag peptide	0.3 mg/mL
	EDTA	5 mM
	Complete protease inhibitor (Roche)	1/100 mL

Flag ligand-exchange buffer	HEPES (NaOH) pH 7.5	20 mM
	NaCl	100 mM
	$CaCl_2$	10 mM
	DDM/CHS	0.1/0.02 % (w/v)
	Photoswitchable 74	100 µM
	Complete protease inhibitor (Roche)	1/100 mL
Alprenolol wash buffer	Tris pH 7.4	10 mM
	NaCl	100 mM
	DTT	50 µM
	DDM/CHS	0.1/0.02 % (w/v)
	Complete protease inhibitor (Roche)	1/100 mL
Alprenolol elution buffer	Tris pH 7.4	10 mM
	NaCl	100 mM
	DTT	50 µM
	Alprenolol	300 µM
	DDM/CHS	0.1/0.02 % (w/v)
	Complete protease inhibitor (Roche)	1/100 mL

4.1.3 Chromatographic material

Column	Material	Manufacturer
β_1AR purification:		
Streptavidin Affinity Column	Streptavidin magnetic beads	ThermoFischer
Reverse IMAC	Ni-NTA Sepharose	IBA Lifesciences
Preparative SEC	HiLoad Superdex 200 10/300GL	GE Healthcare
B_2AR purification:		
Flag Affinity Column	Anti-Flag M1 Sepharose	Sigma-Aldrich
Alprenolol Affinity Column	Alprenolol Agarose	Cell Mosaic

4.1.4 Crystallization screens

Crystallization screens were acquired commercially or prepared using the screen builder Formulator (Formulatrix).

Commercial Matrix screens:	MemMeso, Molecular Dimensions
	Memgold, Molecular Dimensions
	JBS-LCP, Jena Bioscience

4.2 Methods

4.2.1 Sodium dodecyl polyacrylamide gel electrophoresis (SDS-PAGE)

SDS-PAGE runs were performed using commercial NuPAGE Bis-Tris 4-12 % gels (Invitrogen) and its 20X NuPAGE MOPS SDS running buffer (Invitrogen). The running buffer was diluted 20 times with water. Protein samples (12.5 µL) were mixed with 2.5 µL of 5X sample loading buffer (225 mM Tris (HCl) pH 6.8, 50 % glycerol (v/v), 5 % SDS (w/v), 0.05 % bromophenol blue (w/v), 250 mM DTT). Following a few minutes incubation, 12.5 µL of each sample were loaded into the sample wells. Additionally, 4 µL of Precision Plus Marker (BioRad) were added to have a molecular weight standard. 200 V current was applied for 40 min and the gel was immediately stained using InstantBlue stain (Expedeon).

4.2.2 Western Blot

SDS-PAGE

The first step of the procedure consisted in running an SDS-PAGE gel as described above.

Transfer of protein from gel to membrane

A PVDF membrane (Roche) was shortly pre-soaked in 100 % MeOH before soaking it in Transfer buffer 1X (30.3 mg/mL Tris, 143.75 mg/mL, 20 % (v/v) MeOH). Filter papers and blotting pads were also soaked in Transfer buffer 1X. The sandwich containing the SDS-PAGE gel was then prepared and the proteins were transferred into the PVDF membrane for 22 min at 100 V. After the run, the membrane was washed 3 times for 5 min with 0.1 % Tween 20 in TBS 1X (20 mM Tris-HCl pH 8.0 and 125 nM NaCl in MQ Water).

Immunodetection

The membrane containing the transferred proteins was incubated in blocking buffer (5 % milk in 0.1 % Tween 20 in TBS 1 X) for 1 h. Primary antibodies (1:1000) were incubated with the blocked membrane overnight at 4ºC under gentle agitation. β_2-AR was detected by incubating the membrane with anti-mouse IgG (1:30000) for 1 h at room temperature under gentle agitation. Chemiluminescence was achieved with treatment of the membrane with ECL Western Blotting substrate (GE Healthcare) and using the C-Digit Blot scanner (LI-COR Biosciences).

4.2.3 Bicinchoninic acid (BCA) protein assay

Basis

The BCA protein assay takes advantage of the biuret reaction, in which the proteins reduce the cupric ion (Cu^{2+}) to cuprous ion (Cu^{+}) when they are found in alkaline medium. The presence of cuprous ion can be thereafter detected by the addition of bicinchoninic acid (BCA). Two molecules of BCA chelate one Cu^{+} and form a purple-colored complex. This complex is water-soluble and exhibits a strong linear absorbance at 562 nm with increasing protein concentrations. Therefore, this is a colorimetric method that shows good sensitivity and low interference with the environment. In order to quantify the protein concentration, a standard curve is usually prepared using bovine serum albumin (BSA).

Procedure

A standard curve with concentrations in the range 125-2000 µg/mL was prepared from a 2 mg/mL BSA stock solution by dilution with MQ water. 10 µL of each protein solution, including the problem sample were added to a transparent 96-well plate. BCA working reagent was prepared by mixing 50 parts of reagent A with 1 part of reagent B (Pierce BCA Protein Assay Kit, Thermo Fischer). 200 µL of the mix were added to the wells containing the protein solution. The 96-well plate was homogenized and incubated at 37ºC for 30 min. Absorbance measures at 562 nm were performed using the NanoDrop One spectrophotometer (Thermo Fischer). From the absorbance measures of the calibration curve, the protein concentration of the problem sample was determined.

4.2.4 β_1-adrenoceptor production, purification and crystallization

Receptor expression

Both β_1-AR constructs were expressed in HEK293 GnTI- cells. The same procedures were conducted to obtain two stable cell lines that express each variant of β_1-AR upon induction.

Bacterial transformation and DNA purification

E. coli competent cells (100 µL) were mixed with 1 µL of each plasmid. The resulting mixture was incubated in ice for 5 min. Competent cells were then heat-shocked for 30 s at 42ºC with no shaking. The mixture was then placed on ice for an additional 2 min. 800 µL of pre-warmed LB media were added to the cells and the solution was spread in an LB plate containing ampicillin (25 µg/mL). The plate was inverted and incubated at 37 ºC overnight. A single colony was then picked from the LB plate and introduced in 150 mL of LB media containing ampicillin. The bacterial culture was incubated overnight at 37ºC on a shaker set at 200 rpm. Plasmid purification was achieved using the Nucleospin Plasmid EasyPure kit (Macherey-Nagel) following the instructions of the supplier. Purified DNA was quantified using the NanoDrop One spectrophotometer (Thermo Scientific) at 260/280 ratios. The ratio of absorbance between 260 and 280 nm is used to assess the purity of the DNA. A ratio of ~1.8 indicates the isolated DNA has an acceptable purity. Lower values for this parameter suggest there are contaminants such as proteins or phenols that strongly absorb at 280 nm.

Generation of a polyclonal stable HEK cell line

HEK293 GnTI- cells were grown in a 10 cm plate up to 80 % confluency. Two Eppendorf tubes were prepared containing 18 µL Lipofectamine 2000 (Invitrogen) in 375 µL Opti-Mem 1X (Invitrogen) and 6 µg of the β_1-AR plasmid in 15 µL P3000 and 375 µL Opti-Mem. The components of the two Eppendorf tubes were mixed and incubated at room temperature for 20 min. The resulting mixture was added dropwise to the cells and left to incubate for 24 h at 37ºC and 5 % CO_2. Selection was then initiated and the media was changed for complete DMEM containing 0.1 mg/mL of Zeocin (InvivoGen) and 0.005 mg/mL of Blasticidin (InvivoGen). Cells were maintained in these conditions and a polyclonal stable cell line was stablished for each construct.

Cell upscaling and expression induction

In order to obtain sufficient material to purify the receptor of interest, high amounts of cells expressing the target protein had to be produced. Upscaling was initiated in adherence, where 15 cm plates were continuously expanded. When eight 15 cm plates were 90% confluent, cells were put into suspension using 200 mL of PEM media (Gibco) supplemented with 10 % FBS, 1% P/S, 1% GlutaMAX (Gibco), 0.1 mg/mL Zeocin and 0.005 mg/mL Blasticidin. Suspension cells were grown under constant stirring in 2 L conical flasks, at 37ºC and 5% CO_2. Cells were maintained at $1 \cdot 10^6$ cells/mL densities by direct dilution using complete PEM media. When 800 mL of cells at $2 \cdot 10^6$ cells/mL were obtained they were induced by addition of 400 µL tetracycline (6 mg/mL stock) and left to incubate for 72 h under constant stirring at 37ºC and 5% CO_2. Expression of the receptor of interest was assessed by GFP fluorescence microscopy.

<u>Purification of β_1-AR expressed in HEK293 cells</u>

Both β_1-AR constructs were purified following the same general protocol (Figure 143).

Membrane preparation

All steps were carried at 4ºC unless otherwise stated. Cells were thawed and immediately re-suspended in low salt buffer. The amount of buffer added was chosen to achieve a cell to buffer ratio of 1:10. Cell membranes were disrupted by dounce homogenization in portions of 50 mL (20 strokes/portion). The homogenized material was then spun down using an ultracentrifuge (45000 rpm, 45 min, 4ºC, Himac CP-NX, Hitachi, rotor Ti45). The obtained supernatant was discarded and membranes were gently resuspended in low salt buffer using the Ultra Turrax (IKA). Extensive membrane washing was achieved by performing repeated resuspension and ultracentrifugation cycles. Two additional washings were performed with high salt buffer and one last wash was carried using low salt buffer. Purified membranes were resuspended in low salt buffer to a concentration of 1 mg/mL, flash frozen in liquid nitrogen and stored at -80ºC.

Streptavidin Affinity Chromatography

In order to continue with the protein purification, membranes were thawed and resuspended in solubilization buffer. The mixture was briskly stirred at 4ºC for 1-2 h and the solubilized receptor was isolated by ultracentrifugation (45000 rpm, 45 min, 4ºC, Himac CP-NX, Hitachi, rotor Ti45). Solubilized membranes were then purified through an affinity chromatography. The solution was incubated with 3 mL of Streptavidin beads for 1 h (4ºC, 500 rpm). Following the binding process, the mixture was poured into a glass column support that allowed separation of the supernatant from the beads. The beads containing the receptor of interest were then washed with 3 CV of Strep wash buffer. Finally, 3 CV of Strep elution buffer were added, the beads were resuspended and left to incubate for 40 min. Elution was collected in 1 mL fractions. Fractions were pooled according to protein concentration measured with the NanoDrop One spectrophotometer (Thermo Scientific).

Protease cleavage and reverse IMAC

The eluted receptor was then treated with His-tagged human Rhinovirus 3C protease (HRV 3C) (in-house) in order to cleave off the GFP. Protease was added in a 1:10 protease:receptor ratio and it was left to incubate with the receptor overnight at 4ºC. To remove the protease, a reverse immobilized metal ion affinity chromatography (IMAC) was performed. The receptor-protease mixture was incubated with the Ni-NTA resin for 1 h at 4ºC. The supernatant containing the target receptor was then isolated.

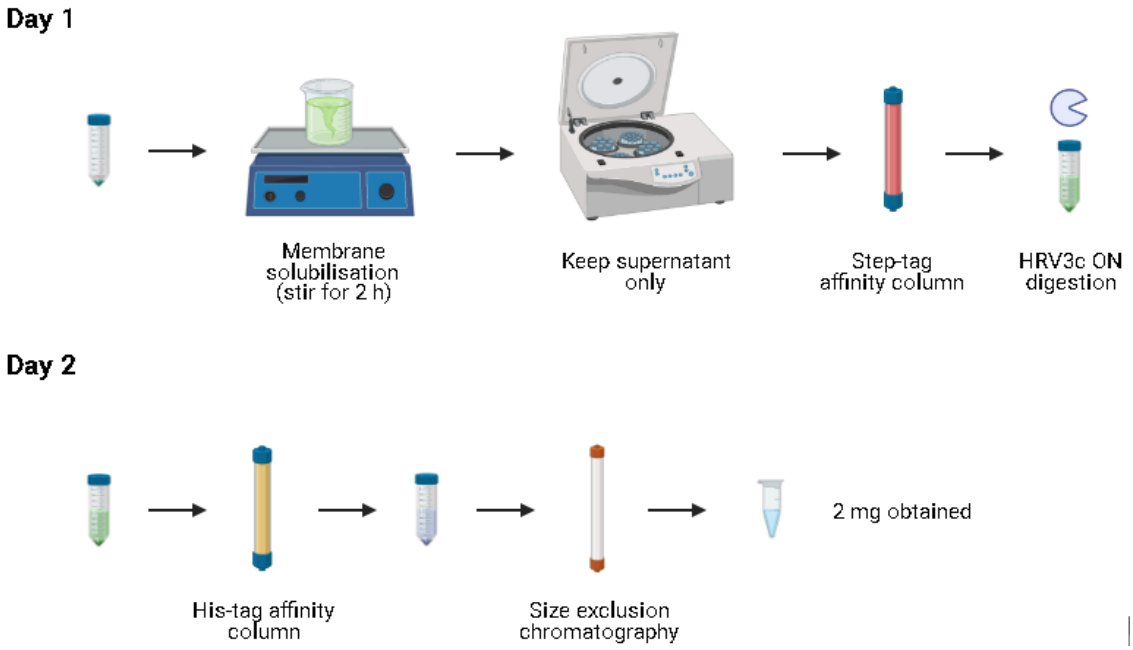

Figure 143. Protocol flowchart followed for the purification of β_1-AR

Size exclusion chromatography (SEC)

The last step on the purification was achieved by size exclusion chromatography (SEC). A Superdex 200 10/300GL (CV = 24 mL) was connected to an FPLC system (ÄKTA prime, GE Healthcare). The column was washed with MQ water to remove the storage conditions and equilibrated with 2CV of SEC buffer. Protein solution was concentrated by centrifugation (2000 g, 3 min intervals, 4ºC, Eppendorf 5801 R) to a final volume of < 0.5 mL using a 100 kDa cut-off ultrafiltration concentrator (Vivaspin20$_{MWCO100000}$, Sartorius Stedium). The concentrated sample was then spun down (15000 g, 1 min, 4ºC, Eppendorf 5424 R) to remove aggregates and loaded onto the column using a 0.5 mL loop. The purification was carried at 0.4 mL/min and 200 µL fractions were collected in 96-well plates. Fractions containing the protein of interest were pooled and purity was assessed by SDS-PAGE. Purified receptor was finally flash frozen with liquid nitrogen and stored at -80ºC.

<u>Lipidic Cubic Phase Crystallization</u>

Protein was treated with 100 µM 74 and left to incubate for 30 min on ice. Ligand-bound receptor was then concentrated to a final concentration of 8-20 mg/mL using a 100 kDa cut-off

ultrafiltration concentrator (Vivaspin20$_{MWCO100000}$, Sartorius Stedium). Receptor was reconstituted into lipidic cubic phase using monoolein (1-(9Z-octadecenoyl)-rac-glycerol, MAG 9.9, MO). The receptor-monoolein mixture was effected by coupling two Hamilton syringes and a homogeneous lipidic cubic phase was achieved by pushing the syringe plungers back and forth for several mixing steps. The final concentration of the mixture was 2:3 protein to monoolein ratio. Lipidic reconstitution and following steps were carried at > 20ºC.

Crystallization trials were set in 96-well glass sandwich plates (Laminex, Molecular Dimensions) using a dispensing robot (Crystal Gryphon LCP, Art Robbins Instruments) with a humidity chamber set at 70 % humidity. 5-15 nL LCP drops were dispensed onto the Laminex glass base and layered with 800 nL of precipitant solution. When the 96 drops had been dispensed, the base was immediately sealed using a Laminex glass cover. Plates were incubated at 20ºC for at least 7 days.

4.2.5 β_2-adrenoceptor production and purification

Receptor expression

Virus production

The viruses containing the β_2AR construct were produced using the Bac-to-Bac Baculovirus Expression System (Invitrogen).[17]

Commercially bought *E. coli DH10 Bac* cells (Invitrogen) were used for bacmid production. These cells were transformed by electroporation with 100 ng of the custom plasmid that contains the gene of interest in a pFastBac vector (Invitrogen). Cells were left to incubate at 37ºC overnight and then they were plated in 10 cm agar plates containing ampicillin (100 µg/mL), kanamycin (50 µg/mL), gentamycin (10 µg/mL), tetracycline (10 µg/mL), IPTG (0.5 mM) and X-Gal (80 µL added of a 20 mg/mL stock). Plates were incubated overnight at 37ºC. Colonies were selected depending on their color white/blue. White colonies were picked, considering that they are expressing the recombinant Bacmid, and were re-streaked in a new plate and incubated overnight at room temperature. Colonies that stayed white were picked and incubated in 50 mL of 2xTY medium at 37ºC and shaken at 200 rpm. Bacmid DNA was isolated using the Nucleospin Plasmid EasyPure kit (Macherey-Nagel).

Bacmid DNA was used to transfect insect *Spodoptera frugiperda (Sf9)* cells which subsequently produced the virus of interest. $0.7 \cdot 10^6$ cells/mL were seeded in a 6-well plate in *Sf900*-III medium (Gibco). Transfection was conducted following the CellFectin protocol, where 2 µg of DNA in 100 µL of medium were mixed with 8 µL of CellFectin in 100 µL of medium. The mixture was incubated for 30 min at room temperature and then it was added dropwise to the cells. The plate was sealed and cells were incubated for 5 h at 27ºC. Finally, medium was changed and cells were left to incubate for 5 days at 27ºC. In this time, cell viability noticeably decreased and cell diameter was increased, indicating that virus has been produced. Supernatant was collected and spun down (800 g, 5 min) and V_0 virus (2 mL) was isolated and stored in the dark at 4ºC. V_0 was then used to amplify the amount and potency of the virus. 1 mL of V_0 was used to infect 10 mL of $0.7 \cdot 10^6$ cells/mL contained in a T-25 flask. Cells were incubated for 3-5 days at 27ºC under constant agitation. Supernatant was collected and spun down (800 g, 5 min) and V_1 (10 mL) was

obtained. 10 mL of V_1 were then used to treat 100 mL of $0.7 \cdot 10^6$ cells/mL contained in a 200 mL conical flask. After 3-5 days supernatant was spun down (800 g, 10 min) and V_2 (100 mL) was obtained (Figure 144). V_2 virus was stored t 4ºC in the dark and used in the large-scale expression of β_2AR.

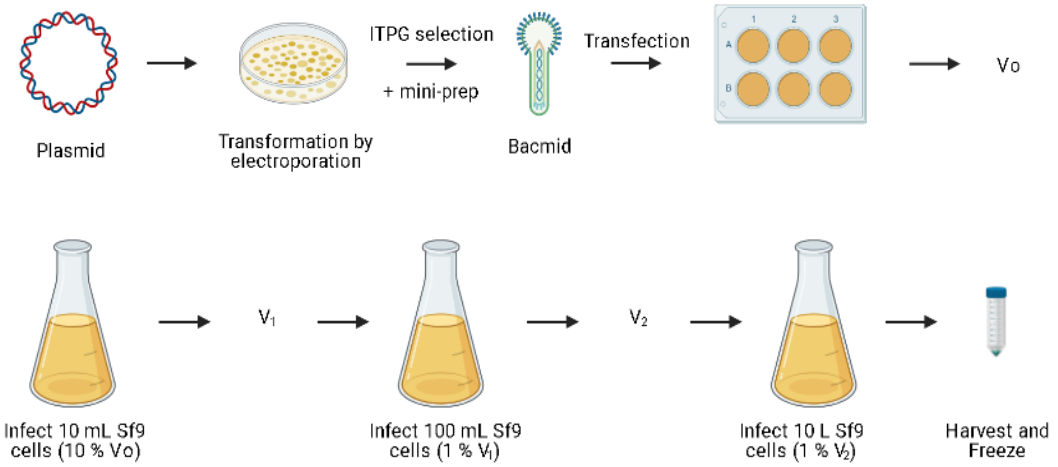

Figure 144. Protocol flowchart followed for the production and amplification of a baculovirus containing the gene of interest.

Virus Titration

With the objective to establish the correct conditions for large-scale expression of the target receptor, small-scale expression tests were conducted. For that we used four different 200 mL conical flasks containing 50 mL cells at a $2 \cdot 10^6$ cells/mL in *Sf900*-III medium (Gibco). Two of the flasks were infected with 0.5 % (v/v) V_2 and the other two were treated with 1 % volume of infection (VOI). Cells were shaken at 27ºC and 120 rpm for 48 h or 72 h. Cells were harvested by centrifugation (2000 g, 10 min, 4 ºC, Eppendorf 5801 R), lysed using a hypotonic buffer and solubilized in buffer containing 1% DDM. Expression levels were analyzed by performing a western blot as previously described. The best fermentation conditions were obtained when cells were treated with a VOI of 0.5 % for 48 h.

Fermentation of Sf9 cells

Fermentation was conducted in 2L heat-sterilized conical flasks. 800 mL cells at a $2 \cdot 10^6$ cells/mL in *Sf900*-III medium (Gibco) were infected with 0.5 % (v/v) V_2 and shaken at 27ºC and 120 rpm for 48 h. Cell pellets were harvested by centrifugation (5000 rpm, 20 min, 4ºC, Sorvall RC 3B Plus), flash frozen with liquid nitrogen and stored at -80ºC until further used.

<u>Purification of β_2-AR expressed in insect cells</u>

Lysis and solubilization

All steps were carried at 4 ºC unless otherwise stated. Frozen cell pellets expressing β_2AR were thawed and resuspended in lysis buffer (100 mL per 1L cell culture). The suspension was stirred at 4ºC for 10 min to ensure cell lysis. Cell membranes were then ultracentrifuged (40000 rpm, 20 min, 4ºC, Himac CP-NX, Hitachi, rotor Ti45) and the supernatant was discarded. Isolated

membranes were directly resuspended in solubilization buffer using the Ultra Turrax. The resulting mixture was left to stir for 1 h (4ºC, 500 rpm) and the solubilized receptor was isolated by ultracentrifugation (45000 rpm, 45 min, 4ºC, Himac CP-NX, Hitachi, rotor Ti45).

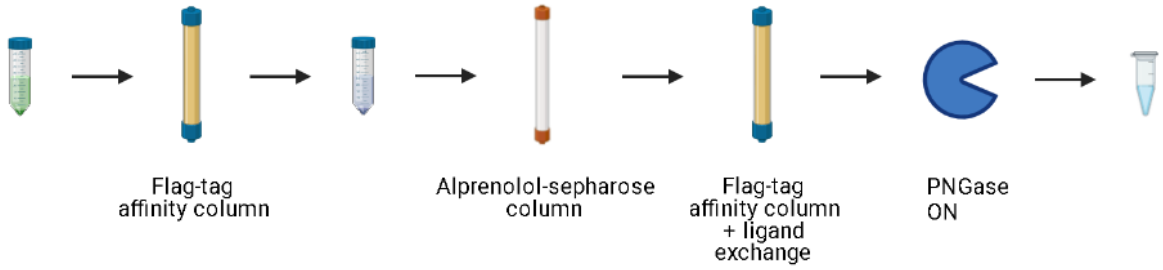

Figure 145. Protocol flowchart for the purification of β_2-AR bound to a ligand of interest.

Flag Affinity Chromatography

The first step of the purification consisted in an affinity chromatography. The solution was loaded using an automatic pump to 3 mL of anti-Flag M1 beads over the course of 2 h. Following the binding, the beads which have receptor of interest bound were washed three times with 1 CV of Flag wash buffer. Finally, portions of 2 mL of Flag elution buffer were added to the beads until no additional receptor was eluted. Elution was collected in 1 mL fractions. Fractions were pooled according to protein concentration measured with the NanoDrop One spectrophotometer (Thermo Scientific).

To purify the apo-receptor, the following step in the purification consisted in a SEC. This step was performed as described for the purification of the β_1AR.

Alprenolol-sepharose Affinity Chromatography

Purification of β_2AR for crystallization purposes continued with an alprenolol-sepharose affinity chromatography. Loading of the solubilized receptor was carried at room temperature over the course of 45 min. The beads (30 mL) were then washed with cold alprenolol wash buffer (3 x 3 CV). The target receptor was finally eluted by pumping 100 mL of alprenolol elution buffer at room temperature over the course of 1h. The elute was immediately cooled down to 4ºC and treated with PNGase F overnight.

Flag AC and ligand exchange

The last step of the β_2AR purification consisted in a Flag affinity chromatography, carried in the same manner as described above with one additional step. Before the elution, when the receptor is bound to the beads and to the ligand alprenolol, a ligand exchange step was performed. The beads were washed and incubated for 30 min with Flag ligand exchange buffer, containing 100 µM of the photoswitch 74. Elution was collected in 1 mL fractions. Fractions were pooled according to protein concentration measured by a BCA assay, as described above. BCA assay was performed to avoid the interference caused by the aromatic ligand on the NanoDrop measurements.

4.2.6 Thermal Shift Assays

To measure receptor melting temperature when bound to the photoswitches, 59 µL of purified apo-receptor at a concentration of 0.524 mM were dispensed into a 96 well PCR plate kept in ice. 1.51 µL of photoswitchable compound stock solution (4 mM) were added to each well, to give a final concentration of 100 µM. The plate was sealed and left to incubate with the evaluated compounds for 30 min on ice either in the dark or illuminated (365 nm or 455 nm). CPM (*N*-[4-(7-diethylamino-4-methyl-3-coumarinyl)phenyl]maleimide) dye stock solution (3 mg/mL in DMSO) was diluted 1:100. 5.14 µL of the diluted solution were added to each well and mixed thoroughly. Out of each well, triplicates of 20 µL were distributed into 0.1 mL Rotor-Gene Q tubes (QIAGEN). Melting profiles were recorded using a real-time PCR machine (Rotor-Gene Q, QIAGEN) with temperature ramping from 25ºC to 95ºC in 1ºC steps, with 4 s pause after each step. Measurements were set at an excitation λ of 365 ± 20 nm and emission λ of 460 ± 20 nm. For compounds that showed a good increase in the melting temperature of the protein, additional experiments were performed to estimate its affinity. The same protocol was followed, the only difference was that a range of final concentrations from 100 µM to 0.0002 µM were evaluated for each of the interesting compounds.

References

1. Goegan, B., Terzi, F., Bolze, F., Cambridge, S. & Specht, A. Synthesis and Characterization of Photoactivatable Doxycycline Analogues Bearing Two-Photon-Sensitive Photoremovable Groups Suitable for Light-Induced Gene Expression. *ChemBioChem* **19**, 1341–1348 (2018).

2. Schönleber, R. O., Bendig, J., Hagen, V. & Giese, B. Rapid photolytic release of cytidine 5'-diphosphate from a coumarin derivative: a new tool for the investigation of ribonucleotide reductases. *Bioorganic & Medicinal Chemistry* **10**, 97–101 (2002).

3. Weinrich, T., Gränz, M., Grünewald, C., Prisner, T. F. & Göbel, M. W. Synthesis of a Cytidine Phosphoramidite with Protected Nitroxide Spin Label for EPR Experiments with RNA. *European Journal of Organic Chemistry* **2017**, 491–496 (2017).

4. Sun, K. *et al.* Efficient synthesis of D_6 -clenproperol and D_6 -cimaterol using deuterium isopropylamine as labelled precursor. *Journal of Labelled Compounds and Radiopharmaceuticals* **59**, 552–556 (2016).

5. ASATO, G. *et al.* Repartitioning agents: 5-(1-Hydroxy-2-(isopropylamino)ethyl)anthranilonitrile and related phenethanolamines: Agents for promoting growth, increasing muscle accretion and reducing fat deposition in meat-producing animals. *Agricultural and Biological Chemistry* **48**, 2883–2888 (1984).

6. Molander, G. A. & Cavalcanti, L. N. Nitrosation of Aryl and Heteroaryltrifluoroborates with Nitrosonium Tetrafluoroborate. *The Journal of Organic Chemistry* **77**, 4402–4413 (2012).

7. Lerch, M. M., Hansen, M. J., Velema, W. A., Szymanski, W. & Feringa, B. L. Orthogonal photoswitching in a multifunctional molecular system. *Nature Communications* **7**, 12054 (2016).

8. Bujak, K. *et al.* Azopolymers with imide structures as light-switchable membranes in controlled gas separation. *European Polymer Journal* **118**, 186–194 (2019).

9. Renier, O. *et al.* Photoisomerization and Mesophase Formation in Azo-Ionic Liquids. *Crystal Growth & Design* **20**, 214–225 (2020).

10. SAWICKI, E. & GERBER, D. The Physical Properties of Aminoazobenzene Dyes. II. Further Studies of the Basicity [1]. *The Journal of Organic Chemistry* **21**, 410–412 (1956).

11. Faria, M. *et al.* Screening anti-predator behaviour in fish larvae exposed to environmental pollutants. *Science of The Total Environment* **714**, 136759 (2020).

12. Faria, M. *et al.* Zebrafish Models for Human Acute Organophosphorus Poisoning. *Scientific Reports* **5**, 15591 (2015).

13. Yoav Benjamini & Yosef Hochberg. Controlling the False Discovery Rate: A Practical and Powerful Approach to Multiple Testing. *Journal of the Royal Statistical Society* **57**, 289–300 (1995).

14. Miller-Gallacher, J. L. *et al.* The 2.1 Å Resolution Structure of Cyanopindolol-Bound β1-Adrenoceptor Identifies an Intramembrane Na+ Ion that Stabilises the Ligand-Free Receptor. *PLoS ONE* **9**, e92727 (2014).

15. Isogai, S. *et al.* Backbone NMR reveals allosteric signal transduction networks in the β1-adrenergic receptor. *Nature* **530**, 237–241 (2016).

16. Rasmussen, S. G. F. *et al.* Structure of a nanobody-stabilized active state of the β2 adrenoceptor. *Nature* **469**, 175–180 (2011).

17. Luckow, V. A., Lee, S. C., Barry, G. F. & Olins, P. O. Efficient generation of infectious recombinant baculoviruses by site-specific transposon-mediated insertion of foreign genes into a baculovirus genome propagated in Escherichia coli. *Journal of Virology* **67**, 4566–4579 (1993).